

**A Thesis Submitted for the Degree of PhD at the University of Warwick**

**Permanent WRAP URL:**

<http://wrap.warwick.ac.uk/111392>

**Copyright and reuse:**

This thesis is made available online and is protected by original copyright.

Please scroll down to view the document itself.

Please refer to the repository record for this item for information to help you to cite it.

Our policy information is available from the repository home page.

For more information, please contact the WRAP Team at: [wrap@warwick.ac.uk](mailto:wrap@warwick.ac.uk)

**REPRODUCED  
FROM THE  
BEST  
AVAILABLE  
COPY**

OXYGEN AND SULPHUR ADSORPTION ON CYLINDRICAL CRYSTALS OF  
COPPER AND NICKEL.

An Auger electron spectroscopy study.

By Alistair Fullerton Armitage

Submitted for the degree of Ph.D.

University of Warwick, August 1982.

The research reported in this thesis was performed at the  
Department of Physics, University of Warwick, Coventry, England.

## TABLE OF CONTENTS

CHAPTER 1 : INTRODUCTION		Page
1.1	Introduction.	1
1.2	Segregation and adsorption.	3
1.3	The effect of surface structure.	4
	References.	6
CHAPTER 2 : EXPERIMENTAL TECHNIQUES		
2.1	U.H.V. system.	8
2.2	Mounting of specimen.	8
2.3	Manipulator and computer link-up.	9
2.4	Mass spectrometer.	10
2.5	Sulphur source :	10
	A. Solid-state electrochemical cell.	10
	B. Operating conditions.	11
	C. Cell design.	11
	D. Experimental procedure.	12
2.6	Electron guns.	13
2.7	Hemi-cylindrical mirror analyser.	14
2.8	Electronics.	15
2.9	Sample preparation.	16
2.10	Bakeout and bombardment.	18
2.11	Quantitative Auger electron spectroscopy.	21
	References.	26
CHAPTER 3 : CHOICE OF SYSTEM		
3.1	Introduction.	28
3.2	Bismuth in copper.	31
3.3	Carbon and sulphur in polycrystalline nickel.	34
3.4	Nickel hemisphere.	45
3.5	The cylinder.	48
	References	50



CHAPTER 4 : BACKSCATTERING AND CRYSTAL MOUNTING	Page
4.1 Cylindrical system.	52
4.2 Electron channelling effects.	55
4.3 Diffraction in copper and nickel.	62
4.4 Distortions.	63
4.5 Oxide layer on nickel.	67
References.	69

CHAPTER 5 : OXYGEN ON COPPER	
5.1 Previous work.	71
5.2 Calibration of Auger peak heights.	74
5.3 Results.	75
5.4 Discussion.	78
5.5 Adsorption kinetics of low index faces.	79
5.6 Adsorption kinetics models.	83
Model 1.	83
Model 2.	86
General result.	87
5.7 Conclusions.	89
References.	91

CHAPTER 6 : OXYGEN ON NICKEL	
6.1 Previous work.	93
6.2 Calibration of Auger peak heights.	95
6.3 Results.	97
6.4 Discussion :	99
6.4.1 Chemisorption.	99
6.4.2 Oxide film growth.	101
6.4.3 Nucleation of oxidation.	103
References.	106

CHAPTER 7 : SULPHUR ADSORPTION	Page
7.1 Sulphur on copper.	107
7.2 Segregation.	108
7.3 Results and discussion : S on Cu.	109
7.4 Sulphur on nickel.	113
7.5 Results and discussion : S on Ni.	114
References.	117

CHAPTER 8 : CONCLUSION	119
References.	124

#### Appendix A

Integration of the equation for the sticking factor.	125
--	-----

#### Appendix B

Integration of equation 5.9.	127
------------------------------	-----

## FIGURES AND TABLES

	Page
1.1 Energy level diagram.	3
1.2 Possible routes for adsorption/segregation.	3
2.1 Ultra-high vacuum system.	8
2.2 Cross-section of U.H.V. chamber.	8
2.3 Sample mounting assembly.	8
2.4 Sample mount for single crystal sample.	9
2.5 Sample mount for polycrystalline sample.	9
2.6 Specimen manipulator assembly.	9
2.7 Typical mass spectra.	10
2.8 Flux of sulphur generated by solid-state cell.	11
2.9 Flux of sulphur as a function of temperature.	11
2.10 Sulphur source.	11
2.11 Distribution of sulphur on cylinder.	12
2.12 Cross-section of electron gun.	13
2.13 Auger electron yield at different beam energies.	13
2.14 Hemi-cylindrical mirror analyser.	14
2.15 Schematic diagram of electronics.	15
2.16 Auger spectra of Ni before and after cleaning.	16
2.17 Schematic diagram of U.H.V. system.	17
2.18 Sample temperature as a function of time.	18
2.19 Pressure during an oxygen exposure experiment.	19
2.20 Undifferentiated Auger spectra.	23
2.21 Differentiated Auger spectra.	23
2.22 Build up of carbon contamination.	24
2.23 Auger spectra from scanning round a cylinder.	25

	page
3.1 Possible routes for segregation/adsorption	28
TABLE 3.1 : Types of experiment.	29
3.2 Histogram of Bi concentration at Cu grain boundaries.	31
3.3 Segregation of Bi in Cu.	32
3.4 Histogram of Bi segregation to Cu grain surfaces.	32
3.5 Segregation of S in Ni at 950°C.	36
3.6 Segregation of S in Ni at 1100°C.	36
3.7 Segregation of S at 800°C (position 1).	36
3.8 Segregation of S at 800°C (position 2).	36
3.9 Build up of a sub-surface depletion layer	38
TABLE 3.2 : Ratio of S to Ni for two different grains.	40
3.10 Equilibrium ratio of S to Ni as a function of temp.	40
3.11 Langmuir plot for S on Ni.	41
3.12 Carbon Auger peak.	42
3.13 S and C build up on Ni (position 1).	42
3.14 S and C build up on Ni (position 2).	42
3.15 S and C build up on Ni (position 3).	42
3.16 C on Ni at 672°C.	43
3.17 C on Ni at 684°C.	43
3.18 C on Ni at 697°C.	43
3.19 C on Ni at 709°C.	43
3.20 C on Ni at 647°C.	43
3.21 nickel crystal.	45
3.22 Ni Auger peak round the hemispherical crystal.	45
3.23 C and S on the nickel crystal	45
3.24 Ratio of S to Ni Auger peaks.	46

	page
4.1 Faces present on the cylindrical crystal.	52
4.2 The 6 sites of high coordination.	53
4.3 Typical face in the $\langle 110 \rangle$ zone.	53
4.4 Plot of the $C_7$ site density.	53
4.5 The four key faces.	54
4.6 Proportion of the four key faces present.	54
4.7 Variation of crystal current and elastic and Auger peaks.	55
4.8 variation in the elastic peak round the crystal.	56
4.9 Variation in the Cu Auger peaks round the crystal.	58
4.10 Variation in the secondary electron signal.	59
4.11 Comparison of elastic peak variation in Cu and Ni.	62
4.12 Comparison of the crystal current in Cu and Ni.	62
4.13 Variation of crystal current during argon ion cleaning.	63
4.14 Polar plot of crystal current.	63
4.15 Schematic diagram of cylinder rotation.	64
4.16 Polar plot of elastically scattered electron peak.	65
4.17 Correction to allow for eccentric rotation.	66
4.18 Variation round crystal of Auger peaks.	67
5.1 Polar plot of oxygen on copper	75
5.2 Oxygen on two different copper cylinders.	76
5.3 Oxygen coverage at different exposures.	77
5.4 Oxygen coverage at different exposures.	77
5.5 Oxygen coverage on the three low index faces.	77
5.6 Oxygen coverage on flat low index faces.	77
5.7 Comparison of results from cylinder and flat crystals.	77
5.8 Oxygen coverage compared with $C_7$ site density.	79

	page
5.9 Proportion of the four key faces present.	79
5.10 Habraken's data.	81
5.11 Test of equations for low index faces.	81
5.12 Comparison of equations with Habraken's results.	82
TABLE 5.1 : Initial sticking factors	85
5.13 Calculated oxygen coverages (model 1).	86
5.14 Calculated oxygen coverages (model 1).	86
5.15 Calculated oxygen coverages (model 2).	88
5.16 Calculated oxygen coverages (model 2).	88
5.17 Comparison of models 1 and 2.	89
5.18 Comparison of models 1 and 2.	89
5.19 Coverage at two Langmuirs compared with model 1.	89
6.1 Oxygen adsorption on Ni (100) and (110).	97
6.2 Oxygen on Ni (110).	97
6.3 Results from cylinder compared with flat crystals.	98
6.4 Low coverage of oxygen on nickel.	98
6.5 Oxygen coverages at increasing exposures.	98
6.6 Oxygen coverages at increasing exposures.	98
TABLE 6.1 : Coverage after chemisorption stage.	100
TABLE 6.2 : Coverage after oxide film growth.	102
6.7 Predicted oxygen coverage.	102
6.8 Predicted oxygen coverage.	102
6.9 Comparison of cylinder and flat crystals.	103

	page
5.9 Proportion of the four key faces present.	79
5.10 Habraken's data.	81
5.11 Test of equations for low index faces.	81
5.12 Comparison of equations with Habraken's results.	82
TABLE 5.1 : Initial sticking factors	85
5.13 Calculated oxygen coverages (model 1).	86
5.14 Calculated oxygen coverages (model 1).	86
5.15 Calculated oxygen coverages (model 2).	88
5.16 Calculated oxygen coverages (model 2).	88
5.17 Comparison of models 1 and 2.	89
5.18 Comparison of models 1 and 2.	89
5.19 Coverage at two Langmuirs compared with model 1.	89
6.1 Oxygen adsorption on Ni (100) and (110).	97
6.2 Oxygen on Ni (110).	97
6.3 Results from cylinder compared with flat crystals.	98
6.4 Low coverage of oxygen on nickel.	98
6.5 Oxygen coverages at increasing exposures.	98
6.6 Oxygen coverages at increasing exposures.	98
TABLE 6.1 : Coverage after chemisorption stage.	100
TABLE 6.2 : Coverage after oxide film growth.	102
6.7 Predicted oxygen coverage.	102
6.8 Predicted oxygen coverage.	102
6.9 Comparison of cylinder and flat crystals.	103

	page
7.1 Sulphur coverage on copper.	110
7.2 Cu Auger peak after sulphur exposure.	110
7.3 Crystal current after increasing S exposures.	110
7.4 Cu Auger peak before and after oxygen exposure.	110
7.5 Low coverages of sulphur on copper.	111
7.6 Cu Auger peak after increasing S exposures.	111
7.7 Sulphur coverage on nickel.	114
7.8 Sulphur coverage on nickel after low exposure of S.	114
7.9 Sulphur coverage on nickel after low exposure of S.	114
7.10 Ni Auger peak after increasing S exposures.	115
7.11 Elastic peak after increasing S exposures.	115
8.1 Initial sticking factor as a function of coordination.	122



ACKNOWLEDGEMENTS.

With many thanks to all those who helped.....

Phil Woodruff for many hours of time and discussion.

Stan Simpson for technical help.

Pete Johnson for teaching me how to drive a U.H.V. system.

Liz Armitage for typing and keeping me going.

Bill Cant for typing.

John Forty for some excellent advice.

Dave Andrews for the design of the sulphur gun.

Those, too numerous to mention, who took the time to talk.

The financial help of the S.E.R.C. and INCO Europe Ltd. in the form of a C.A.S.E. award is most gratefully acknowledged. The use of the facilities of the Physics Department at warwick university is also gratefully acknowledged.

"Facts are chiels that winna ding and downa be disputed."

R. Burns

## SUMMARY

The research reported in this thesis is concerned with the adsorption (and segregation) of oxygen and sulphur to copper and nickel surfaces. Auger electron spectroscopy (a highly surface-specific technique) has been used to provide quantitative measurements of the constituents at various metal surfaces.

The segregation of impurities to polycrystalline nickel surfaces is reported first. The competition for surface sites between carbon and sulphur was observed to occur in a different manner on different grains. The equivalence of segregation and adsorption was demonstrated for sulphur on nickel.

The polycrystalline samples presented only a limited range of surfaces for examination. Work on a hemispherical nickel crystal (which presented all possible orientations for examination) was limited by experimental difficulties in determining the exact surface orientation being sampled at any instant.

The largest part of the research reported in this thesis was on cylindrical crystals of copper and nickel. By careful choice of the cylinder axis, a sample could be cut with a surface structure that varied in a well-controlled manner.

The adsorption of oxygen on copper turned out to be strongly dependent on the copper surface structure. The initial rate of chemisorption varied linearly with the step density. In contrast, the chemisorption of oxygen on nickel was not greatly affected by variations in the surface structure. However, at higher exposures of oxygen, an oxide film developed at a rate that did depend on the surface structure of the sample.

The adsorption of sulphur from a beam of  $S_2$  molecules proceeded quite differently. On a copper cylinder a bulk sulphide grew in a manner that did not seem to be influenced by the substrate surface structure. On nickel, the initial adsorption of sulphur did vary slightly with surface structure, but the later growth of a bulk sulphide did not.

### PUBLICATIONS

Parts of the work reported in this thesis have been published as follows:-

Chapter 4 : A.F.Armitage, D.P.Woodruff, & P.D.Johnson,

Surf. Sci. 100 (1980) L483

Chapter 5 : A.F.Armitage, D.P.Woodruff & P.D.Johnson,

Proc. 4th Intern. Conf. on Solid Surfaces

(Suppl. Le Vide, Les Couches Minces Vol 1, p.271)

A.F.Armitage & D.P.Woodruff,

Surf. Sci. 114 (1982) 414

Chapters 5&6: A.F.Armitage, H.T.Liu & D.P.Woodruff,

Vacuum 31 (1981) 519

Chapter 6 : H.T.Liu, A.F.Armitage & D.P.Woodruff,

Surf. Sci. 114 (1982) 431

impurity elements in solid solution in a metal accumulate at defect sites if the temperature of the metal is high enough for diffusion to occur. These defect sites may be dislocations, grain boundaries, or free surfaces. Such segregation can lead to the build-up of very high concentrations of impurities at grain boundaries, even when the bulk concentration of the impurity is very small (several parts per million). The concentration of impurities leads to a reduction in the ductility of many metals, a process known as grain boundary embrittlement. Grain boundary embrittlement has been observed for such segregants as sulphur in nickel<sup>1,2</sup> or copper<sup>3</sup>, bismuth in copper<sup>4</sup>, and sulphur and tin in iron<sup>5</sup>. These studies have been reviewed by Sear<sup>6</sup>.

It is often impossible to reduce the amount of impurities in the bulk to a sufficiently low concentration to avoid segregation occurring during heat treatment or in normal service life. This makes it important to be able to identify segregating species, and to try and reach a better understanding of the segregation process.

In a system (such as bismuth in copper) where severe embrittlement occurs, the segregants can be studied by fracturing the sample in an ultra-high vacuum (U.H.V.). This exposes the grain boundaries for examination by Auger Electron Spectroscopy (A.E.S.), a technique sensitive enough to be able to detect fractions of a monolayer of atoms on a surface.

Unfortunately, many systems cannot be examined by these means because impurity segregation to grain boundaries does not embrittle the material enough to allow the sample to be fractured in a U.H.V. system. This may occur even when the grain boundary segregation

is sufficient to significantly affect the properties of the material. In such cases, information can be gained more readily by examining segregation to a free surface of the material rather than to the inaccessible grain boundaries. Such an approach has been adopted by Lea and Seah who studied the segregation of tin in iron at grain boundaries<sup>7</sup>, and at free surfaces<sup>8</sup>.

A theoretical description of segregation was provided first for grain boundaries by McLean<sup>9</sup>. The relation between surface and grain boundary segregation has been treated by Seah and Lea<sup>10</sup>. The kinetics and equilibria of surface segregation have been extensively dealt with<sup>11,12,13</sup>. In particular, Rowlands and Woodruff<sup>14</sup> have introduced a theory for surface segregation which specifically includes the difference between the binding energy at the surface and in the bulk. This model describes the kinetics of segregation in binary and ternary systems, and includes the effects of evaporation from the surface and of saturation in the surface layer.

If the driving force for segregation is the lower binding energy that exists at the surface, then variations in the binding energy may cause variations in the kinetics and equilibria of segregation. These variations in surface binding energy might arise from variations in the surface site geometry associated with surfaces of varying crystallographic orientation. This thesis is devoted to the study of such variations in crystals of copper and nickel, using Auger Electron Spectroscopy to detect segregated, or adsorbed, atoms on the crystal surfaces.

## 1.2 EXPERIMENTAL ROUTES

Gibbs<sup>12</sup> was the first to recognise that there is no real distinction between segregation and adsorption. Figure 1.1 shows the relationship between adsorption and segregation on an energy level diagram. Both adsorption and segregation occur because the internal energy of the system can be reduced when atoms of B bind to surface sites on A, rather than occupying positions in the bulk of A. The energy levels of B in the vapour phase, and B in solution in A, are fixed. However, the energy level of B on the surface of A will vary depending on the orientation of the surface of A (and hence on the surface site geometry). This means that the energy of adsorption and the energy of segregation will vary in a related manner, although the fractional variation will generally be larger for the energy of segregation. The orientation dependence of the surface binding energy can therefore be studied by examining either segregation or adsorption.

Figure 1.2 shows the three possible routes that can be studied (adsorption from the gas phase directly to grain boundaries is obviously impossible). All three routes may shed light on orientation dependence of binding energies, but route 1 has the disadvantage that it is experimentally difficult to determine the orientation of grain boundaries. For this reason, this thesis is largely concerned with routes 2 and 3, i.e. segregation and adsorption to a free surface. The choice of which of these two routes should be studied is governed mainly by experimental considerations, as is the choice of what form the free surface should take.

The reasons for adopting a particular experimental route and type of free surface will be dealt with in chapter 3.

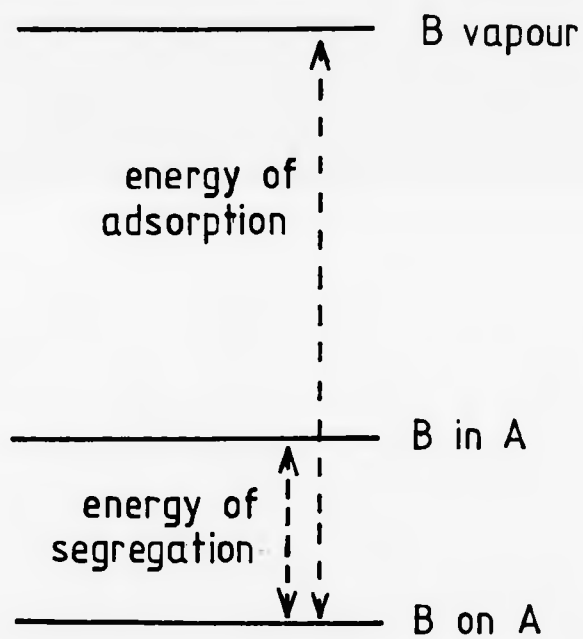


fig. 1.1 Energy level diagram illustrating the relationship between adsorption and segregation.

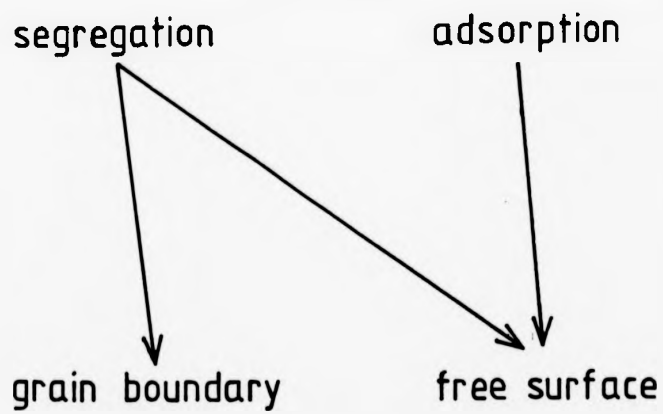


FIG. 1.2 The three possible routes for adsorption or segregation.



The effect of surface orientation (i.e. surface structure) on adsorption has been noted for many systems. For example, Tammann<sup>18</sup> noticed that the oxidation colours were different on different grains of polycrystalline copper. In a classic study, Gwathmey and coworkers<sup>17-19</sup> measured the thickness of an oxide film on a spherical copper crystal and on a spherical crystal cut with flat low-index faces. They found that the oxidation rate varied greatly between surfaces of different orientation.

More recent work has concentrated on measurements of the sticking factor of various systems (i.e. the fraction of gas molecules arriving at a surface that actually stick). For oxygen adsorption on freshly cleaved surfaces of silicon, Ibach et al.<sup>20</sup> found that the sticking factor increased exponentially with step density by more than two orders of magnitude. Hopster, Ibach and Comsa<sup>21</sup> found that the adsorption of oxygen on platinum followed a similar pattern, with the sticking factor varying exponentially with the step density.

A different type of surface structure dependent behaviour is shown by tungsten. Besocke and Berger<sup>22</sup> found that the initial sticking factor of oxygen on tungsten varied linearly with step density. On the other hand, King<sup>23</sup> has found that the sticking factor for nitrogen on tungsten varies not with the step density but with the density of (001) type sites. Apparently the (001) sites provide a favourable structure for the activated complex leading to nitrogen dissociation.

The effect of stepped surfaces on the physical and chemical properties of a material have been reviewed by Wagner<sup>24</sup>. He points out that the theoretical calculation of adsorption kinetics is not easy, even for well-characterised faces of low Miller index.

It is therefore necessary, when considering the effects of step density on the adsorption kinetics, to use qualitative arguments. Gwathney outlines two approaches as follows:

The exponential variation of the sticking factor in some systems (oxygen on silicon, oxygen on platinum) can be explained by considering the dipole moment at the edge of steps. These dipole moments lower the electrostatic potential experienced by the precursor molecule, and this in turn lowers the activation barrier for chemisorption.

The linear dependence of the sticking factor on the step density (as observed in such systems as oxygen on tungsten) is more easily explained by the presence of unsaturated bonds at atoms on the edges of steps. Free valence orbitals promote adsorption at step edges, or at any part of the surface that is rough on an atomic scale (e.g. at defect sites and kinked steps).

The systems studied in greatest detail in this thesis (oxygen on copper or nickel) will be seen to fall into the second category, with sticking factors varying approximately linearly with step density. This variation in step density is affected by the particular geometry chosen for the sample surface. Gwathney and co-workers<sup>17-19</sup> used a spherical crystal with all possible surface orientations. In practice, there are experimental difficulties in studying such a sample. For most of the work in this thesis a cylindrical sample was used, as this provided a practical compromise between the spherical sample and the flat crystal faces which have been the subject of most recent work. The cylinder provides a good range of surface orientations (i.e. of step density) in a well defined and easily studied manner. It was found that cylinders were ideal subjects for studying the effects of step density variations.

#### CHAPTER 1: REFERENCES

1. J. H. Westbrook & D. L. Wood, Nature **192** (1961) 1280.
2. S. Floreen & J. H. Westbrook, Acta. Met. **17** (1969) 1175.
3. S. P. Clough & D. F. Stein, Scripta Metall. **9** (1975) 1163.
4. E. Voce & A. P. C. Hallows, J. Inst. Metals **73** (1947) 323.
5. A. P. Seah & E. D. Hondros, Proc. R. Soc. A. **335** (1973) 191.
6. A. P. Seah, Surf. Sci. **53** (1975) 168.
7. C. Lea & A. P. Seah, Scripta Metall. **9** (1975) 583.
8. C. Lea & A. P. Seah, Phil. Mag. **35** (1977) 213.
9. D. McLean, "Grain boundaries in metals", Oxford (Clarendon Press) 1957.
10. A. P. Seah & C. Lea, Phil. Mag. **31** (1975) 627.
11. A. Lagües & J. L. Domange, Surf. Sci. **47** (1975) 77.
12. H. P. Stüwe & I. Jager, Acta Met. **24** (1976) 605.
13. S. Hofmann & J. Erlewein, Surf. Sci. **77** (1978) 591.
14. G. Rowlands & D. P. Woodruff, Phil. Mag. A. **40** (1979) 459.
15. J. W. Gibbs. Reprinted in "J. W. Gibbs, The scientific papers", Dover, New York (1961).
16. G. Tammann, J. Inst. Metals **44** (1930) 29.
17. A. T. Gwathmey & A. F. Benton, J. Chem. Phys. **8** (1940) 431.
18. A. T. Gwathmey & A. F. Benton, J. Phys. Chem. **46** (1942) 969.
19. F. W. Young Jr., J. V. Cathcart & A. T. Gwathmey, Acta Met. **4** (1956) 145.
20. H. Ibach, K. Horn, R. Dorn & H. Lüth, Surf. Sci. **38** (1973) 433.
21. H. Hopster, H. Ibach & G. Comsa, J. Catalysis **46** (1977) 37.

22. K. Besocke & S. Berger, Proc. 7th Intern. Vac. Congr. & 3rd Intern. Conf. on Solid Surfaces (Vienna, 1977), vol. ii, p. 893.
23. D. A. King, Proc. 7th Intern. Vac. Congr. & 3rd Intern. Conf. on Solid Surfaces (Vienna, 1977), vol. ii, p. 769.
24. H. Wagner, Springer tracts in modern physics, vol. 85, p. 190 (Springer-Verlag, Berlin & New York).

## CHAPTER 2 : EXPERIMENTAL TECHNIQUES

### 2.1 : U.H.V. SYSTEM

The experiments were carried out in a stainless steel Ultra-high vacuum system (fig.2.1) which was initially pumped by a rotary pump. Pumping was done in the low pressure range by an ion pump, a titanium sublimation pump and an oil diffusion pump. In the pressure range  $10^{-4}$  to  $10^{-11}$  torr the pressure could be measured by a Bayard-Alpert type ion gauge (V.G.Ltd.). The experimental chamber is shown in cross-section in fig.2.2. The crystal is positioned so that argon ion bombarding, sulphur dosing, and Auger electron spectroscopy (using normal or grazing incidence electron beams) can be carried out. A baffle could be rotated to screen the sample from either the argon ion or sulphur beams.

### 2.2 : MOUNTING OF SPECIMEN

The specimen mounting system had to be capable of rigidly holding a cylindrical sample without obscuring the outer cylindrical face. In order to anneal the specimen after argon ion cleaning some method of heating the sample had also to be provided. In practice slightly different mounting systems were used depending on the size of the sample and the heating requirements. Nickel samples had to be heated to temperatures in the region of  $1100^{\circ}\text{C}$ , whereas it was never necessary to heat copper samples to above  $700^{\circ}\text{C}$ . The cross-section of a typical mounting system is shown in fig.2.3. The most important feature of all the mounting systems used was that the heating current was carried by a tungsten heating filament inserted in the centre of a hollow cylindrical sample. The return current passed symmetrically through the sample itself so that there were no current loops present to cause stray magnetic fields. Using this system, Auger electron spectroscopy could be

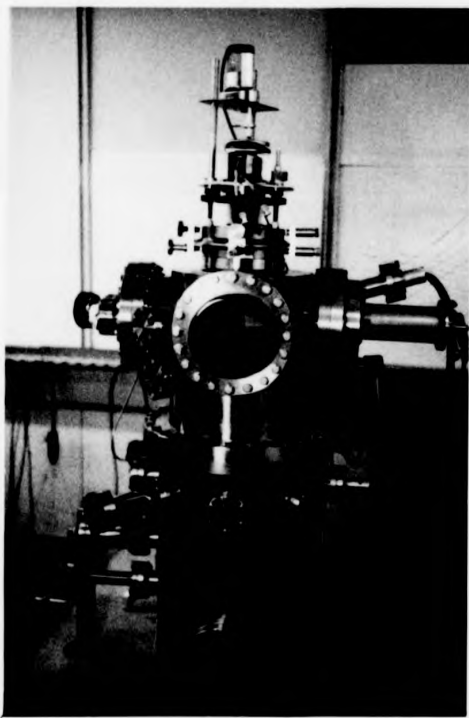


FIG. 2.1 Ultra-high vacuum chamber.

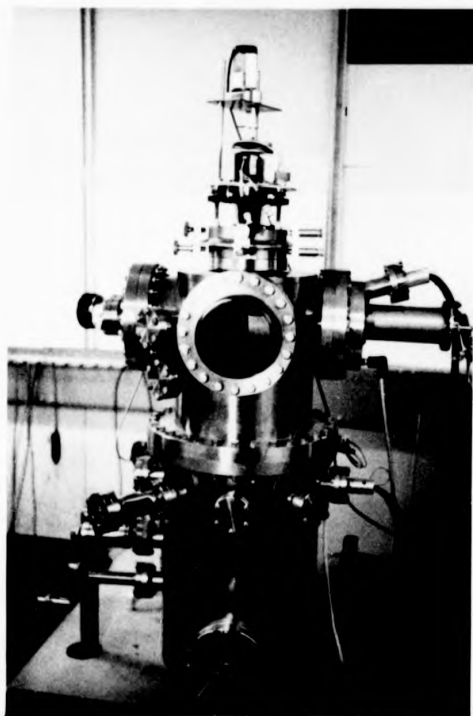


FIG. 2.1 Ultra-high vacuum chamber.

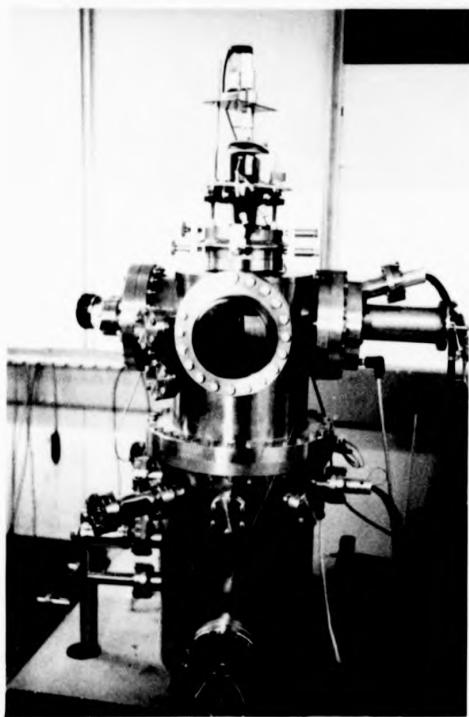


FIG. 2.1 Ultra-high vacuum chamber.



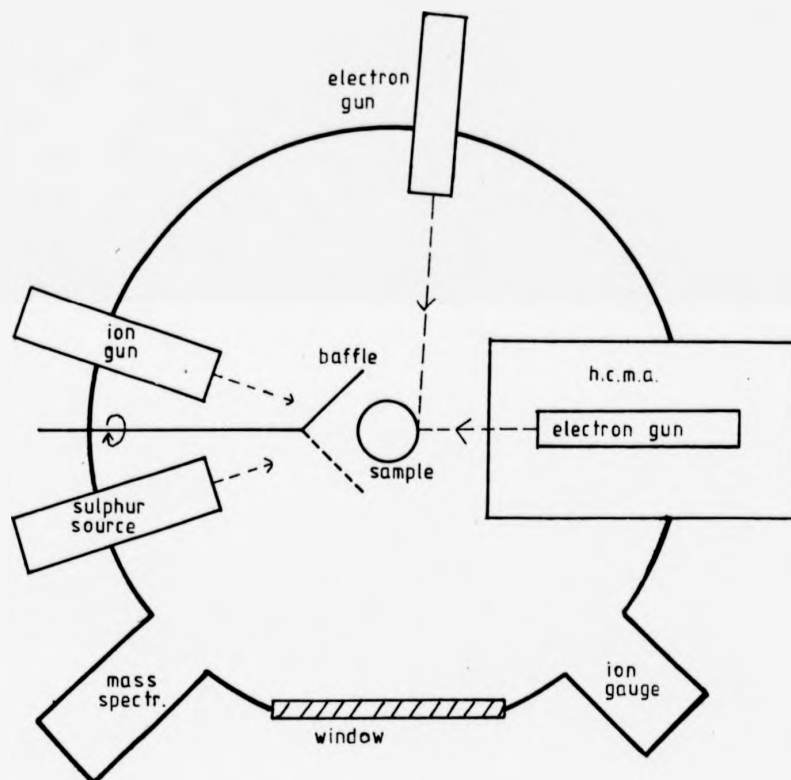


FIG 2.2  
Cross-section of u.h.v. chamber

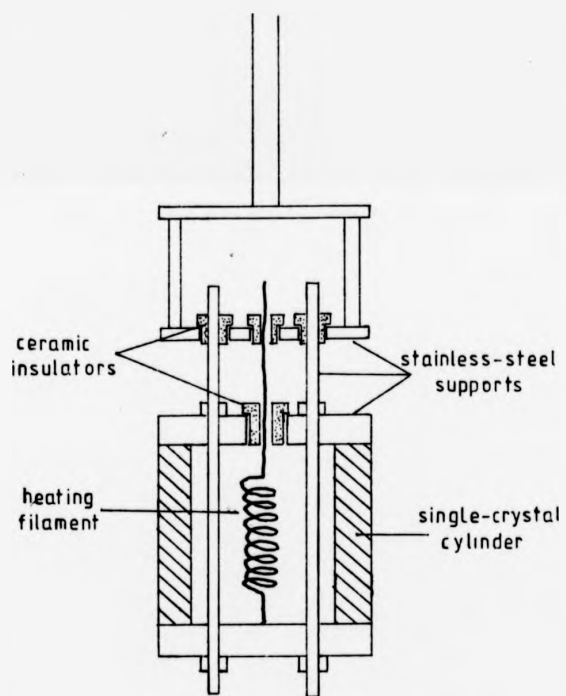


FIG. 2.3 Sample mounting assembly

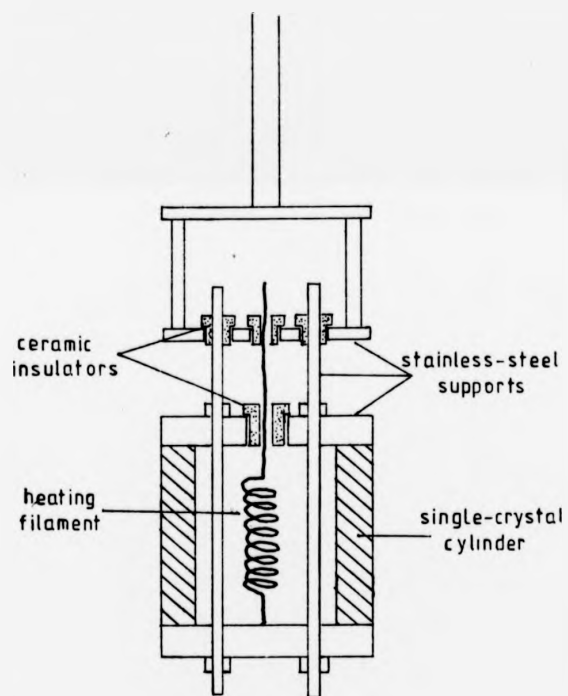


FIG. 2.3 Sample mounting assembly

carried out while the specimen was being heated by an A.C. current from a "variac " variable transformer to a temperature that could be measured by chromel-alumel thermocouples. A photograph of the copper cylinder mounted in this fashion is shown in fig 2.4. Note that the entire cylindrical surface is free from obstructing clamps and wires. Polycrystalline nickel samples were cut on the spark erosion machine to have protruding lugs which were used to bolt the sample to a support. This type of specimen mount is illustrated in fig.2.5.

### 2.3 : MANIPULATOR AND COMPUTER LINK-UP

The specimen mounting assembly was attached inside the U.H.V. chamber to a V.G. R.D.1 specimen manipulator. This allowed for movement of approx.  $\pm 1$ cm in each of the three orthogonal directions for optimum positioning of the sample in front of the analyser and electron gun. The cylindrical sample was capable of being rotated through  $360^\circ$  about its axis so that any portion of the cylinder could be brought in front of the analyser (or the argon ion gun or sulphur source).

For some experiments the rotation of the crystal was controlled by computer. This was achieved by linking an electric motor to the rotating drive of the specimen manipulator via reduction gearing (fig.2.6.) The computer (acting through a digital to analogue convertor) controlled the motor which turned the specimen and a potentiometer. The voltage output of the potentiometer was converted to a digital signal that was used by the computer to determine the orientation of the cylinder (relative to rotation about its axis). The angular position of the cylindrical sample could be controlled to better than  $1^\circ$  in  $360^\circ$ .



FIG. 2.4 Single crystal sample mount



FIG. 2.4 Single crystal sample mount



FIG. 2.4 Single crystal sample mount

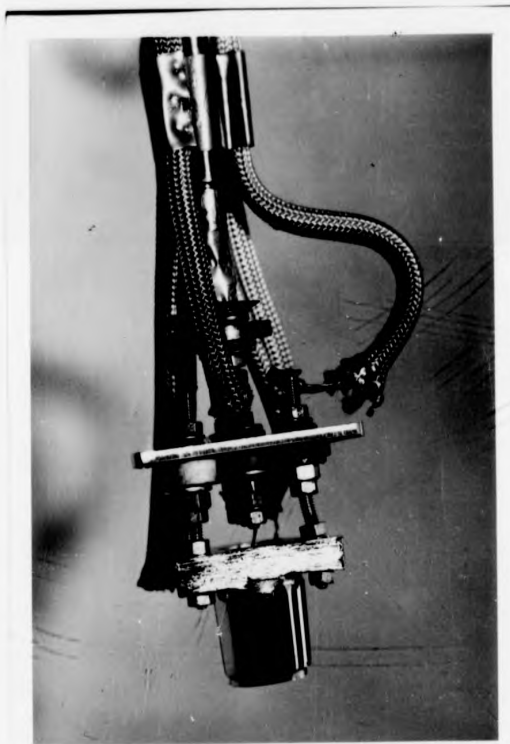


FIG 2.5 Polycrystalline nickel sample mount.



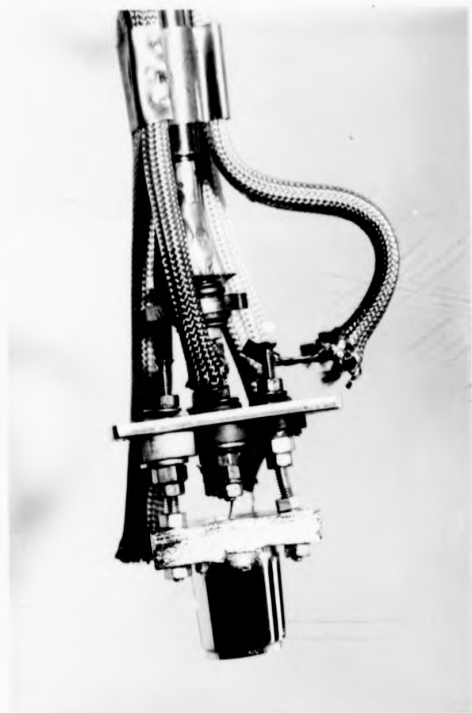


FIG 2.5 Polycrystalline nickel sample mount.

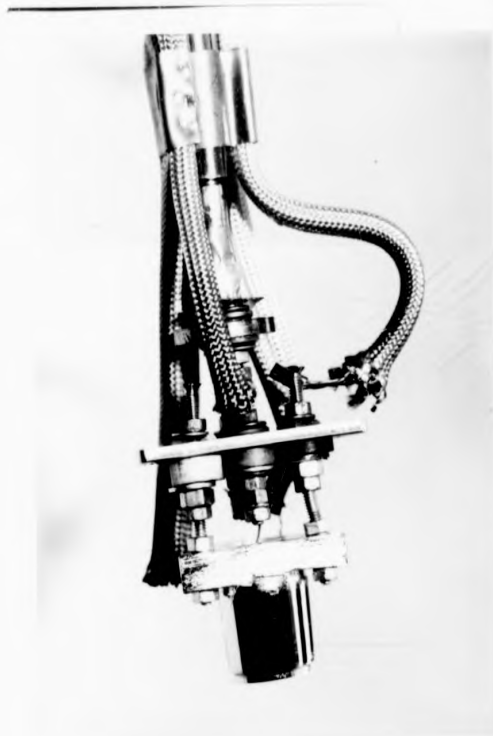


FIG 2.5 Polycrystalline nickel sample mount.

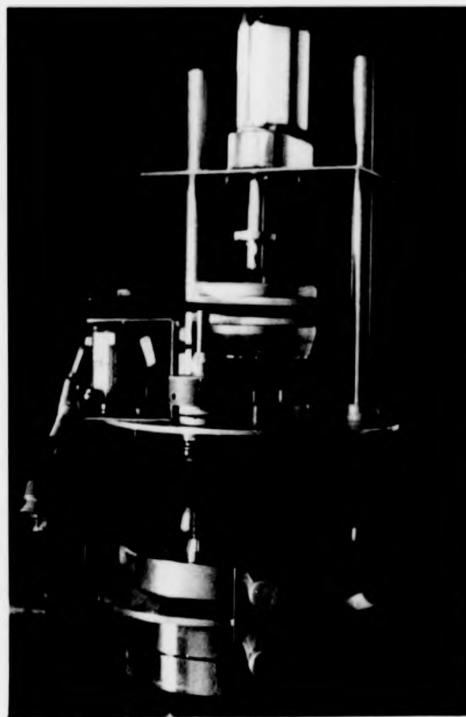


FIG 2.6 Specimen manipulator assembly (showing computer controlled motor).

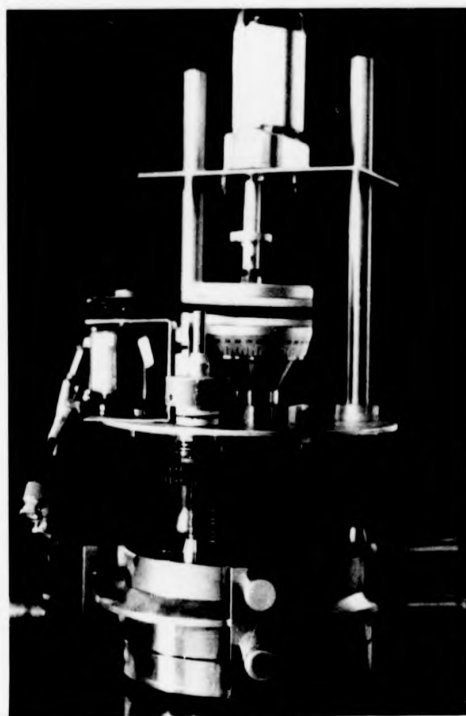


FIG 2.6 Specimen manipulator assembly (showing  
computer controlled motor).

## 2.4 : MASS SPECTROMETER

Residual gas analysis was by means of a magnetic mass spectrometer (V.G.Ltd., Micromass). Because of the large magnetic field in the vicinity of the mass spectrometer magnet, Auger electron spectra could not be obtained while the mass spectrometer magnet was in position. Despite this, several useful functions were fulfilled by the mass spectrometer such as leak detection and impurity detection. For example fig.2.7(a) shows a mass spectrum taken during an oxygen exposure experiment. It can be seen that after admission of oxygen to the U.H.V. system, the partial pressure of the other gases present is of the order of 2% of the oxygen partial pressure. For comparison fig.2.7(b) shows a typical residual gas analysis. The importance of being able to monitor the purity of gases used in adsorption experiments is obvious; monitoring of the residual gases was also necessary when the sulphur source was in use. This was because when the sulphur source was originally put into the U.H.V. chamber, it outgassed when heated to its working temperature. Mass spectrometry confirmed that the gas so produced was not primarily sulphur vapour or compounds from the cell (which could have contaminated the U.H.V. system) but consisted mainly of  $\text{CO}_2$  from the oxidation of carbon contamination of the sulphur source heating filament. Therefore, it was possible to remove the contamination by heating for a long time.

## 2.5 : SULPHUR SOURCE

### A) Solid-State Electrochemical Cell

The sulphur source was based on the solid-state galvanic cell first proposed by C.Wagner<sup>1</sup>. In the cell



silver iodide is the ionic conductor, and the ratio of Ag to S is variable<sup>2</sup>. If the left hand side of the above cell is

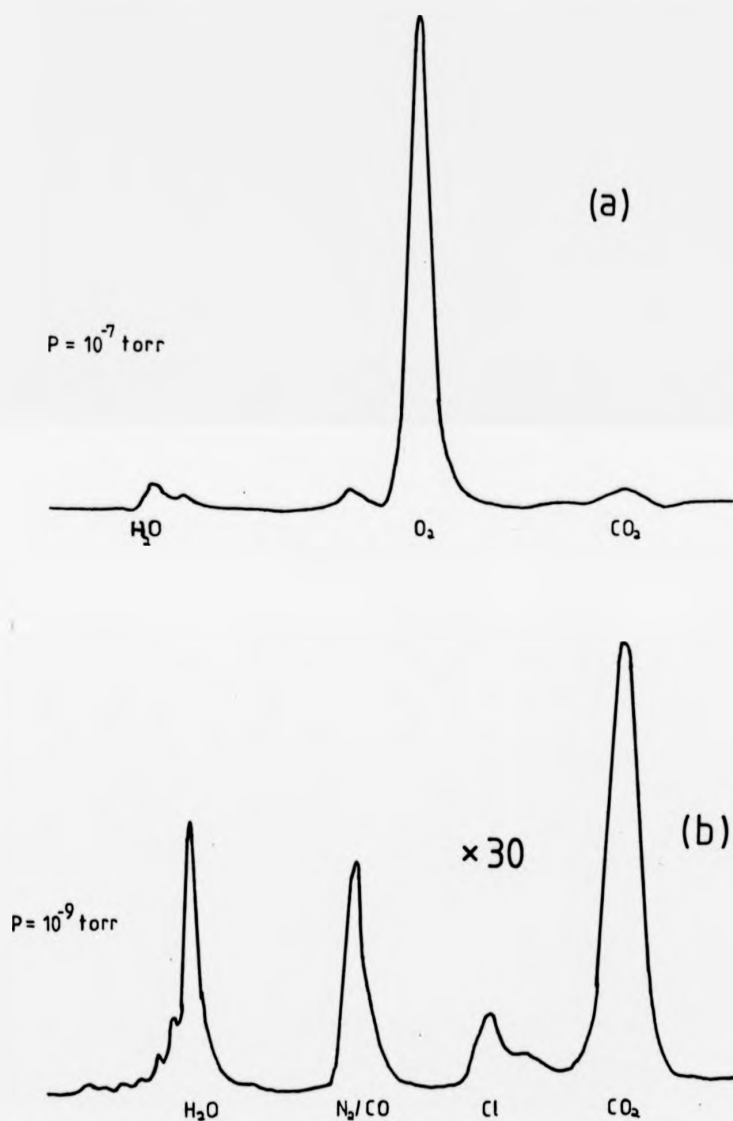


**FIG 2.7** Typical mass spectra taken (a) during an oxygen exposure, and (b) under normal u.h.v. conditions.

made negative,  $\text{Ag}^+$  ions leave the silver sulphide and move to the silver cathode via the silver iodide pellet. At the same time a flux of sulphur molecules is generated at the anode. The behaviour of the cell is discussed in detail in Refs. 1,3,4+5.

#### B) Operating Conditions

The flux of sulphur generated by the cell, and the ratio of the partial pressures of the different molecular species generated ( $\text{S}_n$ ,  $n = 2,3,4\dots 8$ ) depend on the temperature of the cell and the e.m.f. applied across the cell,  $E$ , according to the equation

$$\frac{P_{\text{sn}}}{P_{\text{sn}}^0} = \exp \left[ \frac{-2n(E^0 - E)f}{RT} \right]$$

Where  $P_{\text{sn}}$  is the partial pressure of the  $\text{S}_n$  molecules,  $P_{\text{sn}}^0$  is the partial pressure of the  $\text{S}_n$  molecules over liquid sulphur,  $f$  is Faraday's constant, and  $E^0$  is the electromotive force of the cell:  $\text{Ag} / \text{AgI} / \text{Ag}_2\text{S} / \text{Pt} + \text{S}(\text{liquid})$ . The effect of changing the e.m.f. across the cell at a fixed temperature is shown in figure 2.8; the effect of changing the temperature of the cell is shown in figure 2.9.

By keeping the cell at a temperature of approximately  $200^\circ\text{C}$ , and using an e.m.f. of 0.15 volts, a flux consisting almost entirely of  $\text{S}_2$  molecules is generated at the anode. The magnitude of the flux can be calculated by means of Faraday's law.

#### C) Cell Design

The design of the cell was based on the cell built by D.A.Andrews,<sup>6</sup> which in turn was based on a design by W.Heegeman et al.<sup>7</sup> The main requirement that had to be fulfilled when designing the cell was that all components had to be U.H.V. compatible. The cell is shown in cross-section in figure 2.10.

A small press was constructed to compress powdered  $\text{Ag}_2\text{S}$  and  $\text{AgI}$  into a pellet that fitted tightly into a ceramic tube. Electrical contact to the external circuit was by means of a platinum wire spot

made negative,  $\text{Ag}^+$  ions leave the silver sulphide and move to the silver cathode via the silver iodide pellet. At the same time a flux of sulphur molecules is generated at the anode. The behaviour of the cell is discussed in detail in Refs. 1,3,4+5.

#### B) Operating Conditions

The flux of sulphur generated by the cell, and the ratio of the partial pressures of the different molecular species generated ( $\text{S}_n$ ,  $n = 2,3,4\dots8$ ) depend on the temperature of the cell and the e.m.f. applied across the cell,  $E$ , according to the equation

$$\frac{P_{\text{sn}}}{P_{\text{sn}}^0} = \exp \left[ \frac{-2n(E^0 - E)f}{RT} \right]$$

Where  $P_{\text{sn}}$  is the partial pressure of the  $\text{S}_n$  molecules,  $P_{\text{sn}}^0$  is the partial pressure of the  $\text{S}_n$  molecules over liquid sulphur,  $f$  is Faraday's constant, and  $E^0$  is the electromotive force of the cell:  $\text{Ag} / \text{AgI} / \text{Ag}_2\text{S} / \text{Pt} + \text{S}(\text{liquid})$ . The effect of changing the e.m.f. across the cell at a fixed temperature is shown in figure 2.8; the effect of changing the temperature of the cell is shown in figure 2.9.

By keeping the cell at a temperature of approximately  $200^\circ\text{C}$ , and using an e.m.f. of 0.15 volts, a flux consisting almost entirely of  $\text{S}_2$  molecules is generated at the anode. The magnitude of the flux can be calculated by means of Faraday's law.

#### C) Cell Design

The design of the cell was based on the cell built by D.A. Andrews,<sup>6</sup> which in turn was based on a design by W. Heegeman et al.<sup>7</sup> The main requirement that had to be fulfilled when designing the cell was that all components had to be U.H.V. compatible. The cell is shown in cross-section in figure 2.10.

A small press was constructed to compress powdered  $\text{Ag}_2\text{S}$  and  $\text{AgI}$  into a pellet that fitted tightly into a ceramic tube. Electrical contact to the external circuit was by means of a platinum wire spot



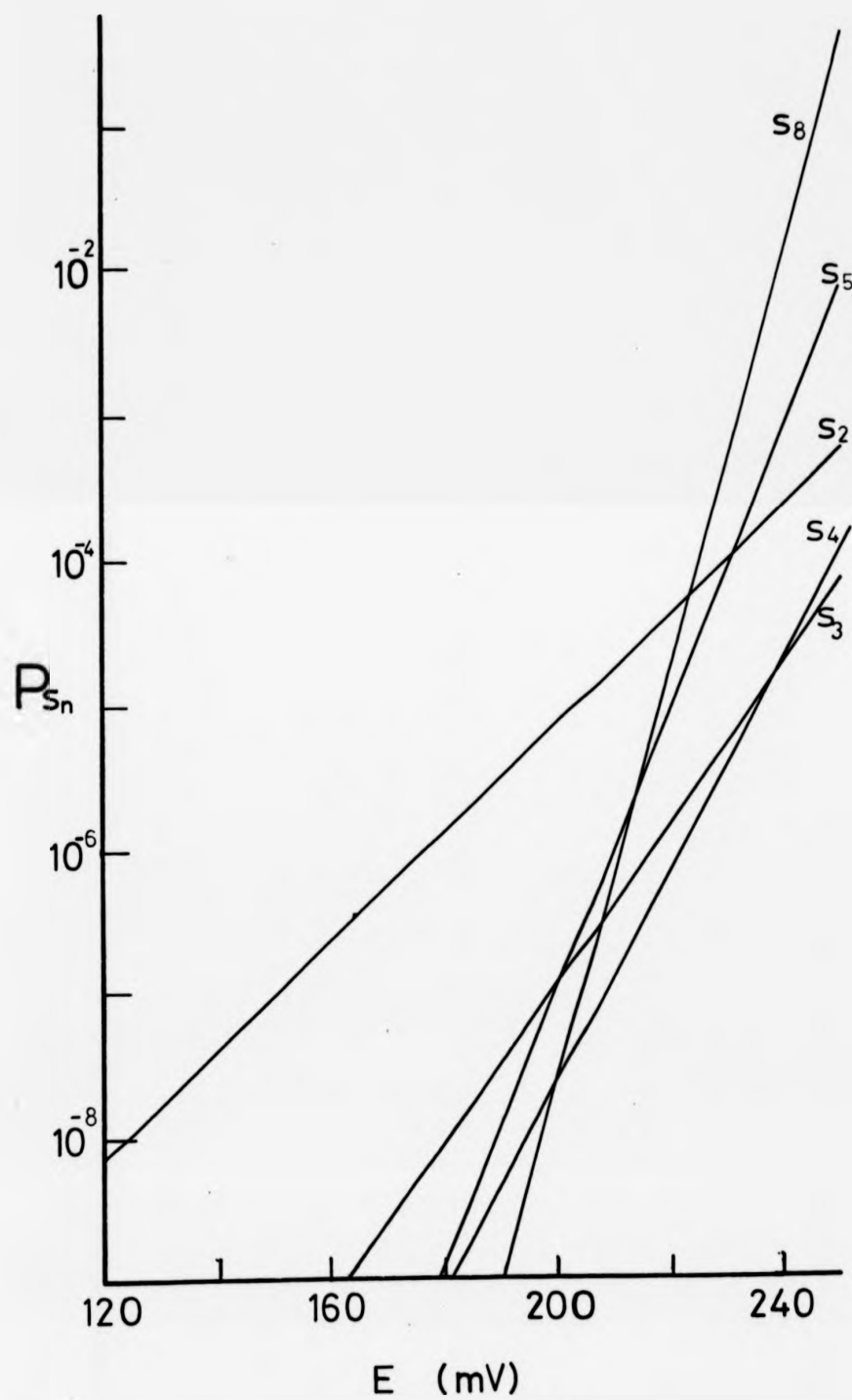


**FIG. 2.8** Flux of sulphur generated as a function of cell e.m.f.

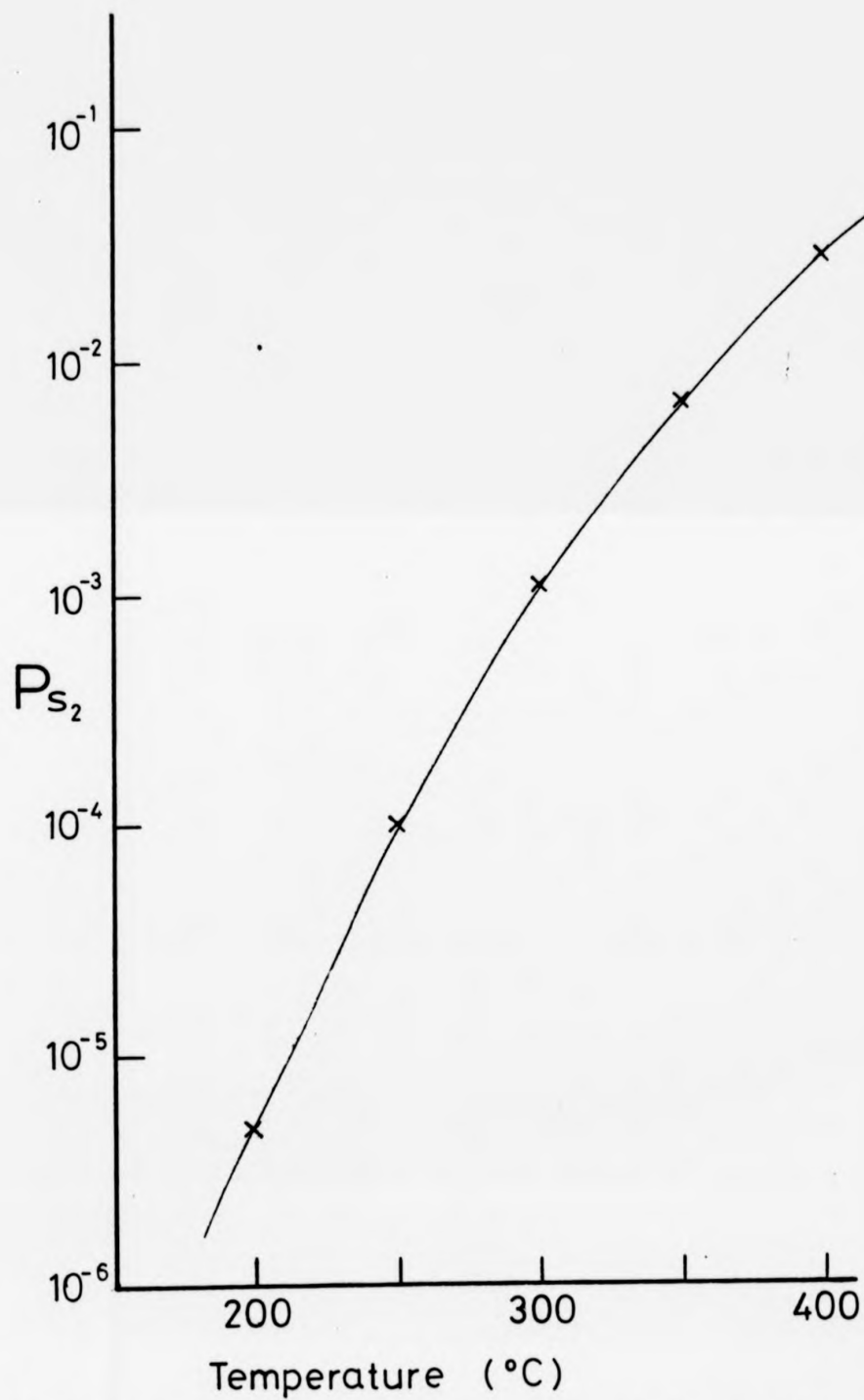


FIG 2.9 Flux of sulphur generated as a function of cell temperature.

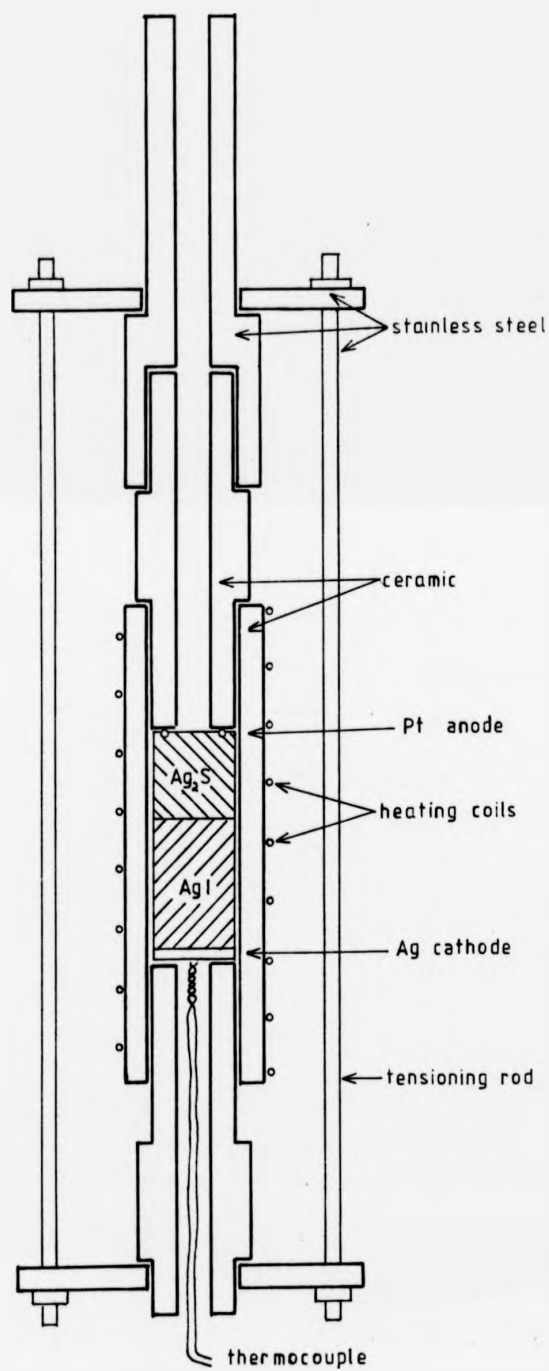


FIG 2.10

Sulphur source

welded to the back of the silver foil cathode, and by a second platinum wire pressed against the  $As_2S$  to form an anode. The whole solid state cell was kept under pressure by four adjustable tension rods bearing on stainless steel plates.

#### D) Experimental Procedure

The stainless steel capillary tube connected to the cell pointed at the specimen, the muzzle being approximately 30 mm from the specimen. The relative distribution of sulphur on the surface was monitored by A.E.S., and is plotted in figure 2.11 (a) as a function of distance parallel to the cylinder axis. The distribution round the circumference of the cylinder is plotted in figure 2.11 (b). The distribution round the cylinder is affected by the change in angle of incidence of the sulphur beam round the circumference of the crystal ( the distribution parallel to the axis is effectively the distribution on a flat plane ). The two curves can be compared by multiplying the distribution on a flat surface by  $\cos \theta$ , where  $\theta$  is the angle of incidence the beam would make with the curved surface. The result of this calculation is shown in figure 2.11 (c), and it can be seen that this curve is very similar to the distribution corresponding to the curved surface shown in (b).

The distribution is non-uniform, but near the maximum the variation of sulphur coverage with distance is small. In practice, even coverages of sulphur were obtained by rotating the cylindrical sample uniformly throughout the exposure. The electron beam was then confined in the vertical dimension to the region of maximum sulphur coverage.

Initially the sulphur source outgassed when heated. After several cycles of heating the pressure in the U.H.V. chamber could be maintained below  $5 \cdot 10^{-9}$  torr while the sulphur source was used.

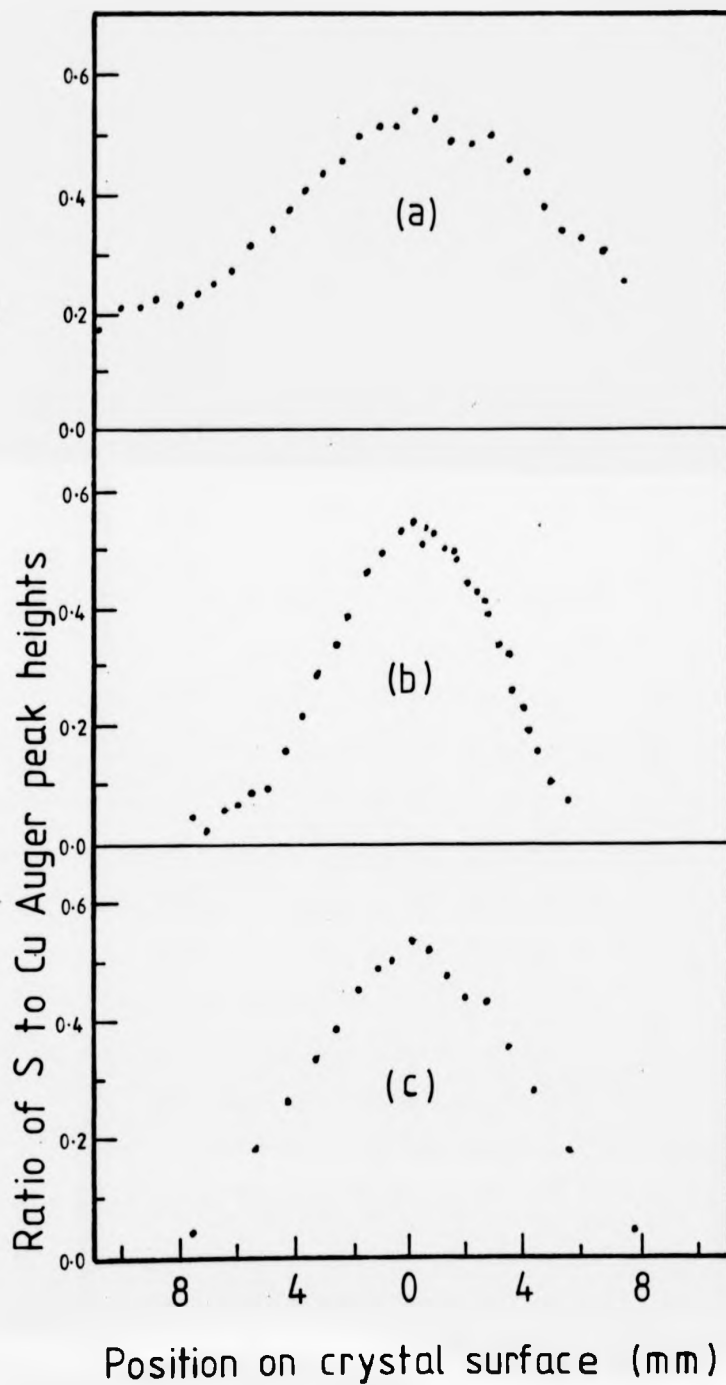


FIG 2.11 Distribution of sulphur (a) round crystal, (b) up and down crystal, and (c)  $\cos(\theta) \times (a)$ .

## 2.6) Electron Guns

Two electron guns were available for Auger Electron Spectroscopy ( figure 2.2 ). A LEG 3 electron gun ( V.G. Electronics ) was set to produce an electron beam at grazing incidence. For reasons that will be dealt with in chapter 3 this gun was rarely used; most experiments were performed using the electron gun mounted in the H.C.M.A. assembly. This gun was used to produce a beam at approximately  $15^{\circ}$  from the normal to the cylinder surface in a plane containing the cylinder axis and the H.C.M.A. axis. This electron gun was designed to produce a focussed spot at the target with a diameter of approximately 0.1 mm. The arrangement of the internal apertures and the elements of the Einzel lens is shown in the cross-section of the electron gun (figure 2.12).

The optimum beam current and voltage was influenced by several factors. The electron beam current had to be large enough to produce an easily detectable Auger electron current, and yet the electron beam current and voltage had to be as small as possible to reduce any unwanted electron stimulated desorption or adsorption effects. In practice, the small size of the tungsten cathode limited the emission current, and the maximum beam current consistent with a reasonable filament lifetime was about  $1 \mu\text{a}$ . At constant filament current, the effect on the measured Auger current of varying the electron beam voltage is shown in figure 2.13 for a clean nickel sample. Bearing in mind that a low beam voltage was desirable, a primary beam energy of 1.5 kV was chosen as this value lies approximately at the low voltage end of the plateau in the curve. Unless otherwise stated, all experiments were carried out using these values of beam current and voltage, i.e.  $1 \mu\text{a}$  and 1.5 kV.

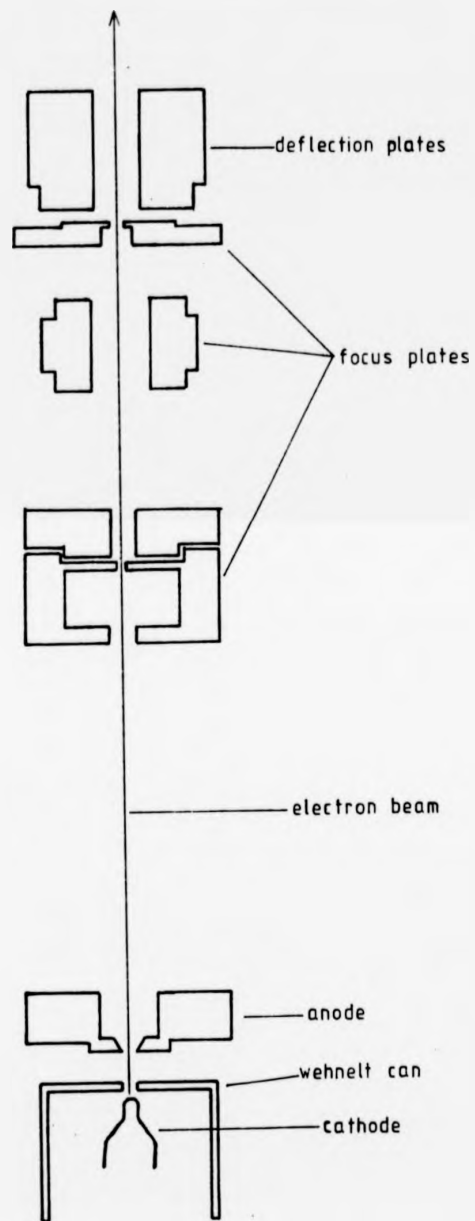


FIG 2.12 Electron gun

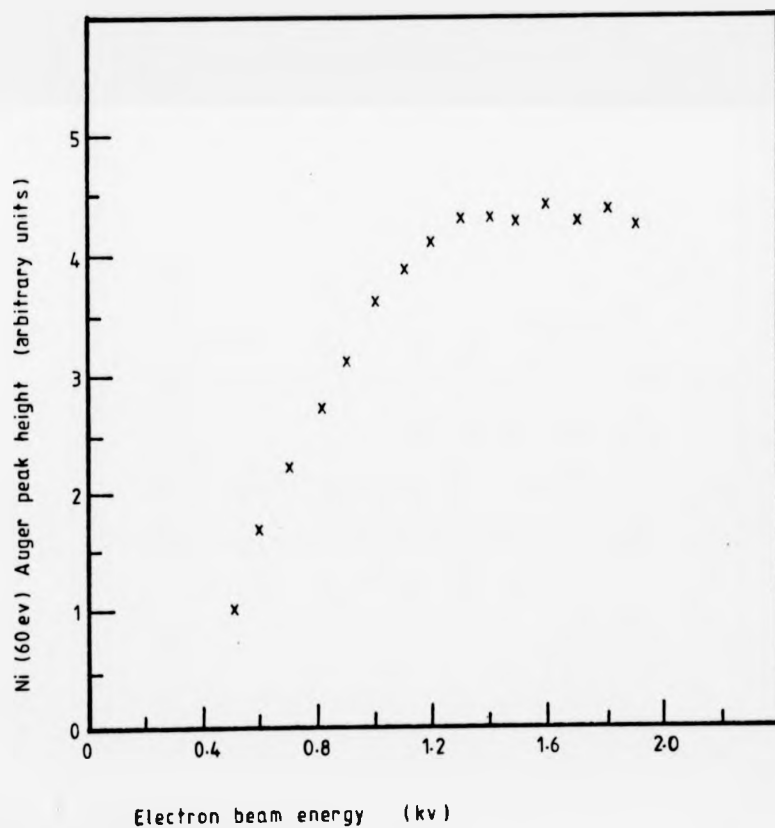


FIG 2.11 Auger electron yield as a function of electron beam energy.



## 2.7) Hemi-Cylindrical Mirror Analyser.

The analyser is a variant of the electrostatic cylindrical mirror analyser proposed by Sar-El<sup>8</sup> and Palmberg et al<sup>9</sup>. The advantage of this type of analyser is that it is a band pass filter with a high transmission. The analyser used in these experiments consisted of two hemicylindrical plates (rather than full cylindrical plates) and is shown in cross-section in figure 2.14. The azimuthal acceptance angle was  $\pm 60^\circ$  about the plane specified by the sample cylinder axis and the incident electron direction.

Electrons leaving the sample with kinetic energy  $E$  (figure 2.14) are reflected by the negative potential,  $-V$ , on the outer hemicylinder plate. Pre-focussing occurs according to the relation :

$$\frac{E}{eV} = 1.31 \ln(r_1/r_2) \quad 2.1$$

This relation only holds for an emission angle of  $42^\circ 18'$ . The high efficiency of this analyser compared with others<sup>10</sup> derives from the existence of second-order focussing for this critical emission angle. For electrons leaving at an angle  $\Delta\alpha$  from the ideal angle  $A$ , an analyser with second-order focussing creates an image of the source at a distance proportional to  $(\Delta\alpha)^3$  from the focal point (as opposed to  $(\Delta\alpha)^2$  for first-order focussing). A significant improvement in resolution can be achieved<sup>11</sup> by making the exit slit in the form of an annulus and placing it a short distance in front of the focal plane. After passing through the exit slit, the electrons are deflected by the "align trace", or "deflection" plate and pass through an earthed fine wire mesh. A potential of +7kV is used to accelerate the electrons onto a scintillator where they are detected by the photomultiplier.

The performance of the analyser is improved if the effect of external magnetic fields is reduced by enclosing the analyser in a mu-metal shield. End effects that would otherwise distort the

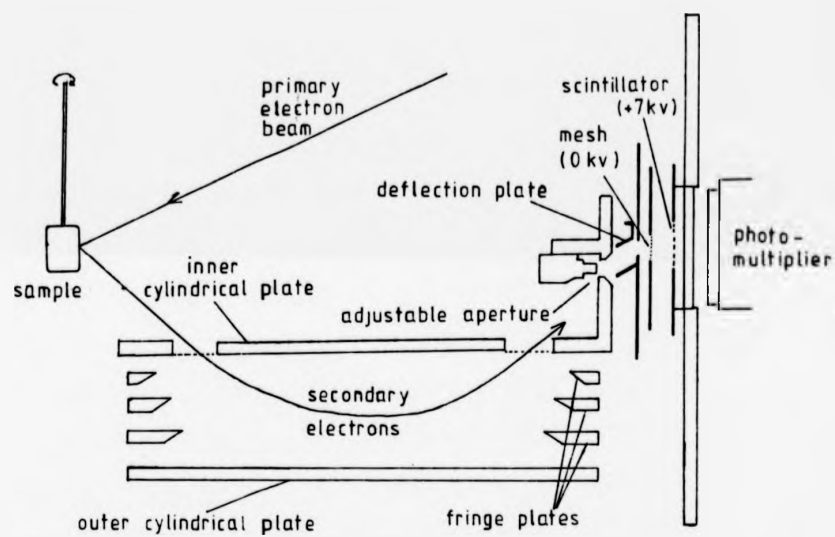


FIG 2.14 Hemi-cylindrical mirror analyser

electrostatic field within the hemicylindrical plates are reduced by the inclusion of fringe plates at each end of the hemicylindrical analyser. A resistor chain provides potentials for the fringe plates in a series between the inner hemicylindrical plate at earth potential and the outer hemocylindrical plate at  $-V$ .

## 2.8) Electronics.

The hemicylindrical mirror analyser can be operated in several modes. By setting the retarding potential to a constant value ( $V$ ), electrons of one particular energy (given by equation 2.1) are passed by the analyser. This mode was used in measuring the number of elastically reflected electrons for example. The second mode of operation was to use the output of a linear ramp generator to sweep the retarding potential ( $V$ ) through a predetermined voltage range. The output of the photomultiplier is then proportional to the energy distribution of electrons entering the analyser,  $N(E)$ . The third mode of operation was to use the analyser to measure the first derivative of the energy distribution of the electrons,  $N'(E)$ . The experimental arrangement necessary for this is shown in figure 2.15.

A small sinusoidal modulating voltage is superimposed on the ramp voltage, and a phase-sensitive detector is used to detect the first harmonic component of the output from the D.C.M.A. and photomultiplier. The first harmonic component is proportional to the differentiated electron energy distribution for small modulating voltages<sup>15</sup>. In this case, a Brookdeal lock-in amplifier (type 402) was used as the phase sensitive detector, operating at a modulation frequency of 5 kHz.

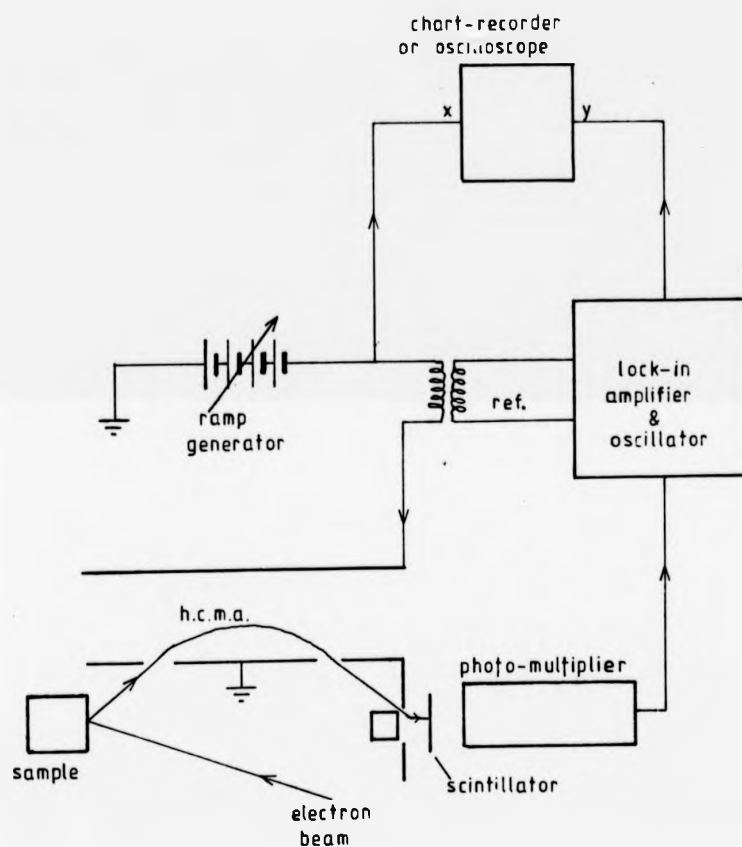


FIG 2.15 Schematic diagram of electronics

## 2.9 : SAMPLE PREPARATION

The size of samples varied slightly, but the method of preparation was the same for all specimens. A cylinder approximately 15 mm long was cut on a spark erosion machine from a single crystal rod (Metals Research Ltd, 5N). The rod was orientated with the  $[1\bar{1}0]$  direction parallel to the rod axis. The centre of the cylinder was removed by spark erosion with a copper tube. This left a hollow cylindrical crystal of outside and inside diameters approximately 12 and 8 mm respectively. The outer cylindrical surface was evened off with successively finer (6, 1, &  $\frac{1}{2}$   $\mu$ ) diamond pastes. Between each polish the cylinder was washed in acetone, rinsed in water and then air dried. The final stage of preparation was to electrolytically polish the sample in a solution<sup>12</sup> of 1 part nitric acid to 2 parts methanol at room temperature. An annular steel cathode was placed around the cylinder (at a separation of about 15 mm) and 20-30 volts was applied between the sample and the cathode for 2-5 seconds. The same method was used for polishing copper and nickel samples.

After mounting the cylinder in the mounting assembly attached to the specimen manipulator, the orientation of the crystallographic axes of the cylinder was determined in an x-ray machine by the Laue back-reflection method. As well as determining the orientation of the crystal, the x-ray photographs provide a useful check on the condition of the crystal, i.e. that it was monocrystalline and free from defects. Once the orientation of the crystallographic axes had been determined relative to the specimen manipulator rotary drive scale, the whole assembly was de-greased in a trichloroethylene vapour bath before being mounted in the vacuum chamber.

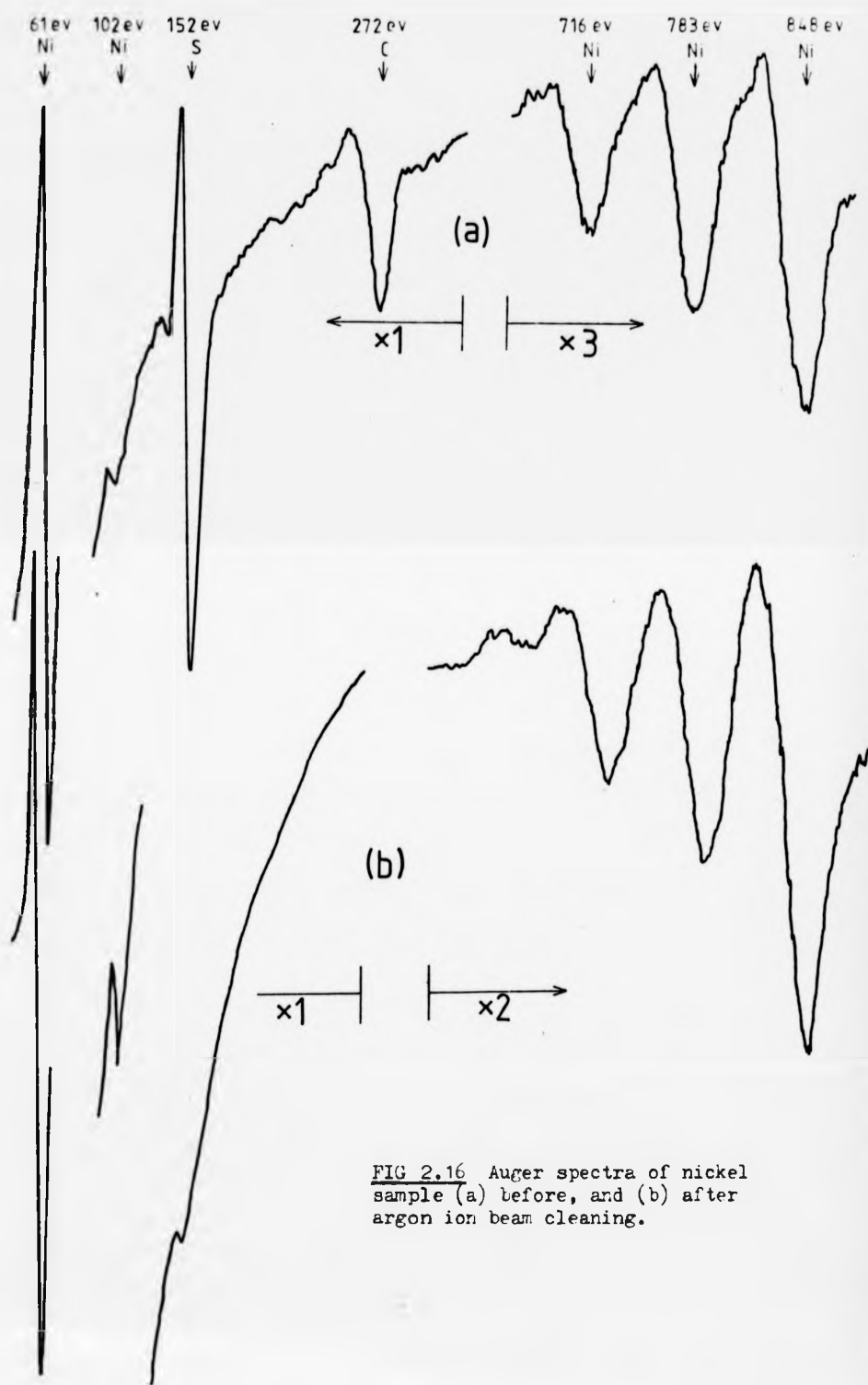


FIG 2.16 Auger spectra of nickel sample (a) before, and (b) after argon ion beam cleaning.

After the U.H.V. system had been baked out, the surface of the sample was invariably heavily contaminated. The Auger spectrum of a sample in this condition is shown in figure 2.16 (a). In situ cleaning of the sample was by repeated cycles of argon ion bombardment and annealing. In order to clean the cylinder evenly, the sample was rotated throughout the argon ion bombardment, at a rate of typically  $30^\circ$  every 5 minutes ( i.e. a total bombardment round the cylinder of 1 hour ). After each ion bombardment, the sample was annealed to reduce the damage to the crystal surface. Nickel crystals were annealed at  $700-800^\circ\text{C}$ . for twenty minutes, and copper cylinders were annealed at  $450-550^\circ\text{C}$ . for twenty minutes.

The initial cleaning of a sample from the contaminated state required typically 10 to 15 cycles of bombardment and annealing. However after this initial cleaning stage, fewer cycles were required to clean the sample. For example when the surface was being cleaned between oxygen exposures, only three or four cleaning cycles were required. The argon ion gun (V.G.Ltd) could produce a beam of energy up to 10 kV. However in order to minimise the surface damage to the crystal, it was found that it was necessary to use a less energetic beam. Initial cleaning was with an argon ion beam of  $10\mu\text{A}$  at 5 kV. On subsequent cleaning cycles, this was reduced until the bombardment immediately prior to an experiment was with an ion beam of  $1\mu\text{A}$  at 1.5 to 2 kV. After annealing this treatment produced a well ordered surface; the Auger spectrum of such a surface is shown in figure 2.16 (b).

Magnusson & Carlston <sup>13</sup> showed that the sputtering yield of copper bombarded by argon ions in the energy range 1 to 10 kV shows a large variation between the different faces, ( for example

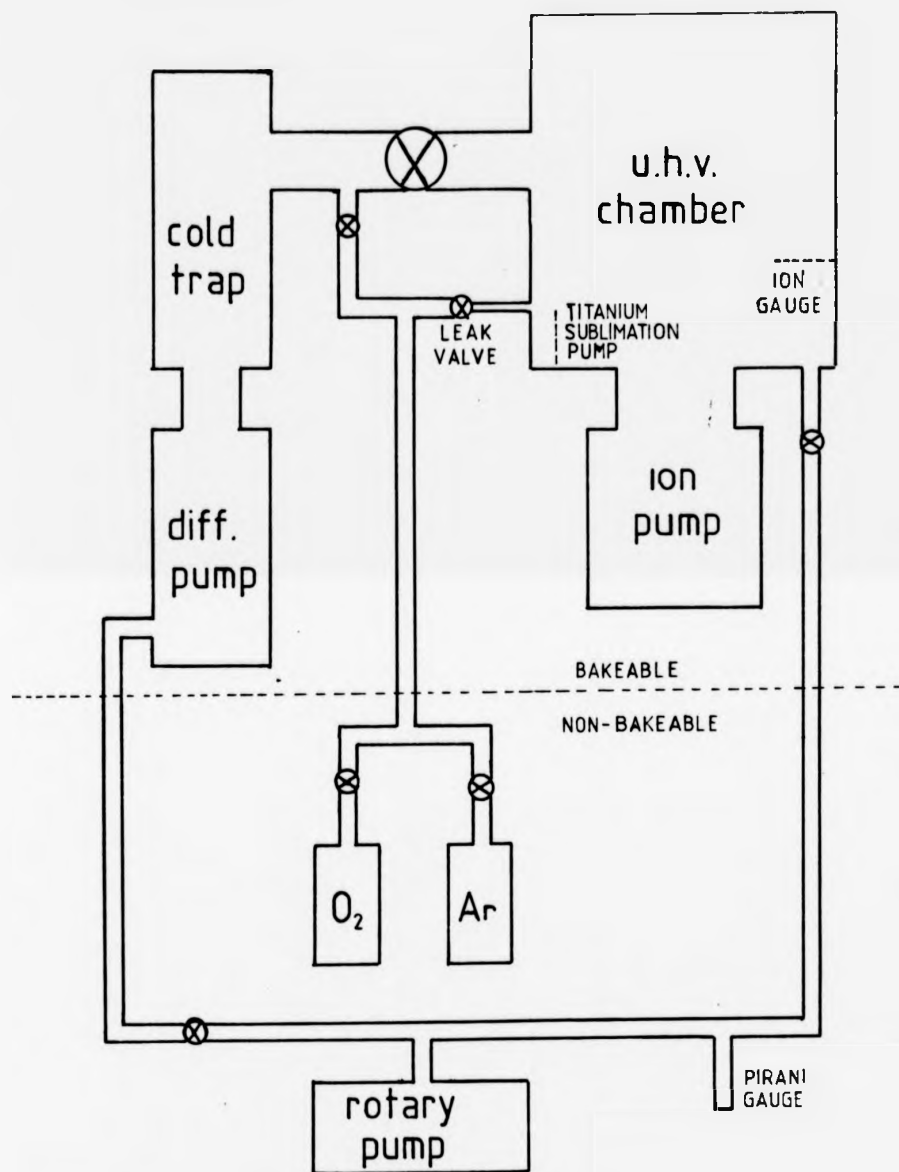


FIG 2.17

Schematic diagram of u.h.v. system



the sputtering yield of the Cu (111) face is approximately three times the yield of the Cu (110) face. It is therefore possible that some faces on the cylinder were preferentially eroded. Although this was not directly observed, there remains the possibility that the cylinder surface was not truly cylindrical on a microscopic scale.

## 2.10 BAKEOUT AND BOMBARDMENT

The following procedures were adopted to reach ultra high vacuum conditions: (see figure 2.17)

1. The rotary pump (Edwards, ED100) was used to rough out the system to approximately  $10^{-2}$  torr.
2. The oil diffusion pump (Edwards, EO4), backed by the rotary pump, reduced the pressure to about  $10^{-5}$  torr. The ion pump was then switched on.
3. After an hour of being pumped by the diffusion and ion pumps, the system was baked for 24-48 hours at  $150-200^{\circ}\text{C}$ .
4. As the temperature of the system dropped after baking, all filaments (e.g. on the ion gauge and electron gun) were outgassed, and the titanium sublimation pump was switched on. The titanium sublimation pump consisted of two titanium filaments through either of which could be passed a current of about 38 amperes. The filament was heated for about two minutes in every hour.
5. With the diffusion, ion, and sublimation pumps all functioning, the system base pressure of  $2 \times 10^{-10}$  torr was reached 3-4 hours after baking.

the sputtering yield of the Cu (111) face is approximately three times the yield of the Cu (110) face. It is therefore possible that some faces on the cylinder were preferentially eroded. Although this was not directly observed, there remains the possibility that the cylinder surface was not truly cylindrical on a microscopic scale.

## 2.10 BAKEOUT AND BOMBARDMENT

The following procedures were adopted to reach ultra high vacuum conditions: (see figure 2.17)

1. The rotary pump (Edwards, ED100) was used to rough out the system to approximately  $10^{-2}$  torr.
2. The oil diffusion pump (Edwards, EO4), backed by the rotary pump, reduced the pressure to about  $10^{-5}$  torr. The ion pump was then switched on.
3. After an hour of being pumped by the diffusion and ion pumps, the system was baked for 24-48 hours at  $150-200^{\circ}\text{C}$ .
4. As the temperature of the system dropped after baking, all filaments (e.g. on the ion gauge and electron gun) were outgassed, and the titanium sublimation pump was switched on. The titanium sublimation pump consisted of two titanium filaments through either of which could be passed a current of about 38 amperes. The filament was heated for about two minutes in every hour.
5. With the diffusion, ion, and sublimation pumps all functioning, the system base pressure of  $2 \times 10^{-10}$  torr was reached 3-4 hours after baking.

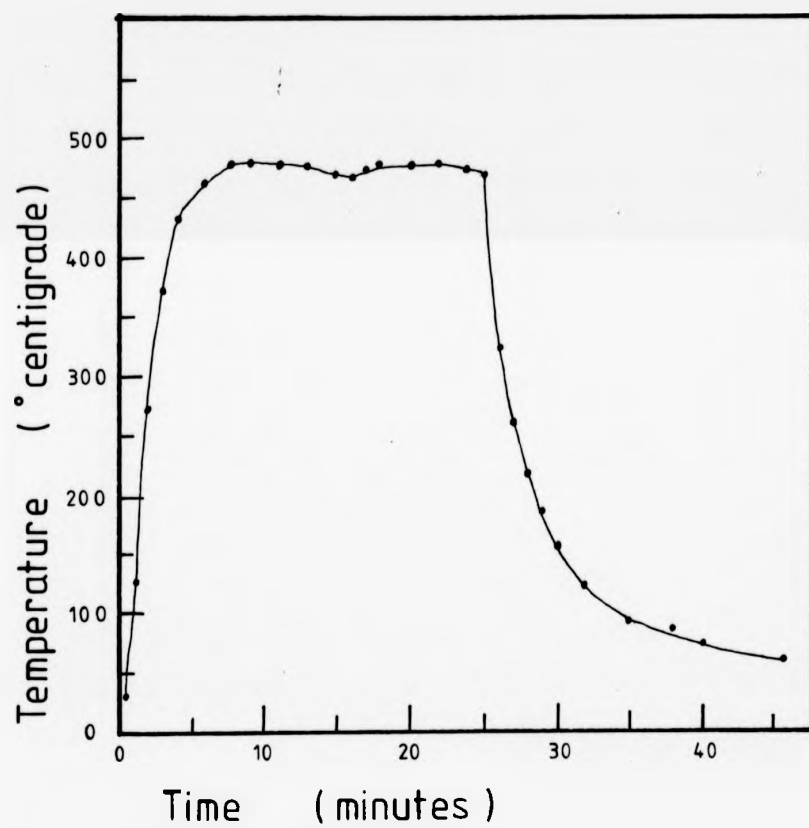


FIG 2.18 Sample temperature as a function of time.

All parts of the vacuum system were stainless steel, except for viewing ports and the glass gas handling line. This line could be used to admit argon to the argon ion gun, or oxygen to the u.h.v. system for adsorption experiments. Both gasses were B.O.C. research grade. The rate at which the gas was admitted could be finely controlled by a stainless steel leak valve. When the gas in the gas handling line was being changed (from oxygen to argon or vice versa), the line could be evacuated by the diffusion pump. The line was then purged with the new gas, evacuated again, and finally filled with the new gas. The purging of the line reduced the possibility of one gas contaminating the other. The purity of the gas was also checked by mass spectrometry.

The oil diffusion pump was fitted with a liquid nitrogen cold trap. However with the diffusion pump charged with Santovac 5 oil (an extremely low vapour pressure polyphenyl ether oil), it was not found to be necessary to fill the cold trap with liquid nitrogen. During experiments when it was desired to keep a reactive sample (such as nickel) clean for a long time, the cold trap was filled with liquid nitrogen as a precaution, but this appeared to have no measurable effect on the pressure in the vacuum system. It is probable that the chevron baffle system within the cold trap provided adequate protection against back streaming of low vapour pressure oil without having to be cooled.

After sample preparation (polishing, electropolishing, and argon ion sputter cleaning) the crystal was ready for use in experiments. Because these experiments were done at room temperature, the crystal had to be left to cool after the final anneal. Figure 2.18 shows a graph of a typical heating/cooling cycle for a cylindrical copper sample. Note that because of its large size, the

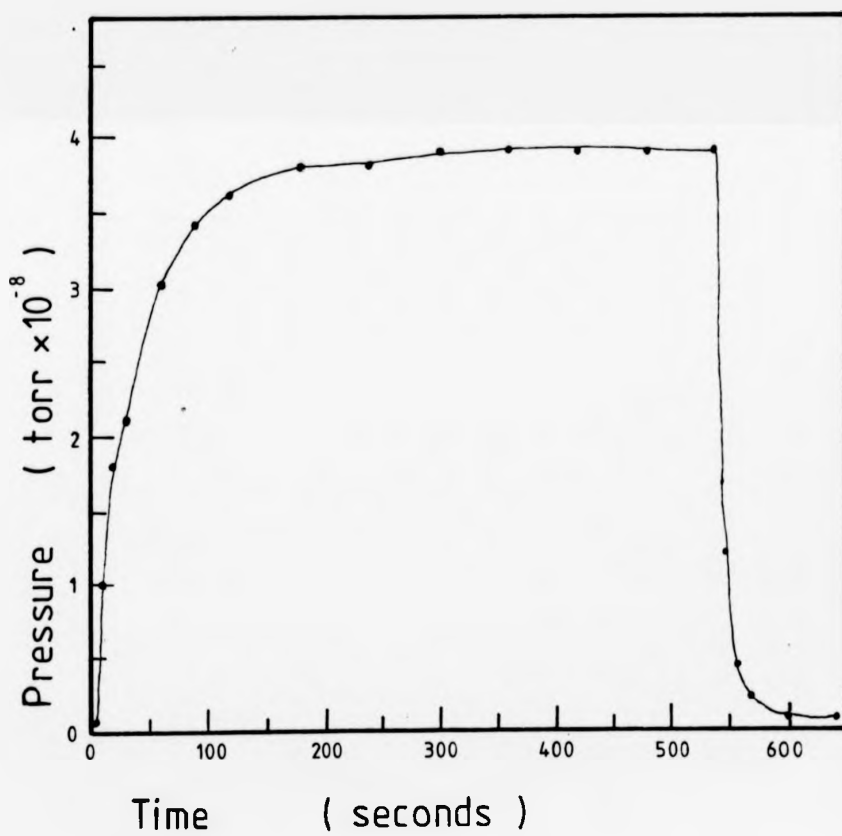


FIG 2.19 Pressure as a function of time during oxygen exposure.

sample has a high heat capacity and therefore takes some time to cool after annealing. Because of this long cooling time, most experiments were performed at temperatures slightly above room temperature (25-40°C).

In a typical experiment, A.E.S. was used to verify the cleanliness of the surface. Once the surface contaminants had been reduced to below the limits of detectability, oxygen or sulphur was adsorbed on the surface. In an oxygen adsorption experiment, the total exposure could be measured by monitoring the pressure as a function of time during the experiment (figure 2.19). The total exposure can be obtained from a graph of pressure against time by integrating graphically; in figure 2.19 for example, the total oxygen exposure was 19.7 Langmuirs. The pressure reading from the ion gauge had to be multiplied by a correction factor to allow for the difference in ion gauge sensitivity for different gasses.

It is not expected that the measurement of exposures will have been highly accurate. This is partly because of the limitations in the accuracy of the ion gauge, but also because of the experimental arrangement. The only available method of admitting oxygen to the system in controlled amounts was via the leak valve connected to the argon gun. Consequently the oxygen entered the system through the argon gun and was roughly collimated into a beam by the argon gun apertures. To reduce this beam effect, the baffle (figure 2.2) was rotated into a position between the argon gun and the sample. As a further precaution the sample was rotated evenly (at approximately 1 revolution in 4 minutes) throughout oxygen exposure to ensure even exposures around the cylinder. Despite these precautions, it is possible that the oxygen pressure at the surface of the sample was slightly different from the oxygen pressure in the vicinity of the ion gauge at a distance of about 30 cms. below

the sample. Thus the measured exposures may be slightly inaccurate, although the exposures should be the same around the cylinder.

## 2.11 QUANTITATIVE AUGER ELECTRON SPECTROSCOPY

Although the quantification of Auger electron spectroscopy has been treated by many authors<sup>14-18</sup>, difficulties and complications still remain<sup>19</sup>. Auger electron spectra, whether recorded as the energy distribution  $N(E)$ , or the differential distribution  $N'(E)$ , can be quantified by one of four methods<sup>20</sup>:-

1. Absolute calibration: for example, Perdereau<sup>21</sup> used a radioactive tracer method to obtain absolute measurements of sulphur coverages on nickel that had also been measured by A.E.S.
2. Known concentration standards: in this method binary compounds of known composition are prepared and put into the U.H.V. system so that Auger electron currents from the sample can be compared with Auger electron currents from the standards (see for example, Argile & Rhead<sup>22</sup>).
3. Pure standards: this method is similar to the previous one except that the Auger electron current from the sample is compared with the Auger electron current from a pure elemental standard. This is then related to a concentration by the use of elemental sensitivity factors<sup>23</sup>. For cases involving surface layers of different composition from the bulk, the sampling depth must be calculated from the electron inelastic mean free paths and the analysis geometry<sup>24</sup>.
4. Approximation methods: published Auger electron spectra can be used to obtain concentrations of elements by comparison of peak to peak heights.<sup>25</sup>

The accuracy of these methods is reduced by the following difficulties:-

1. Line shape changes. A number of recent studies have shown that Auger electron spectra are affected by several factors which cause shifts in the energy of Auger peaks and changes in the line shape. This is of interest in that the fine structure contains information on interatomic transition and relaxation effects<sup>30-32</sup>, but these effects reduce the accuracy of quantitative measurements, particularly if peak to peak heights in the differentiated energy spectrum are used as the measure of the concentration of an element.
2. Modulation distortion. Earlier in chapter 2 it was stated that the first harmonic in the output from the H.C.M.A. was proportional to the first derivative of the electron energy spectrum. However this relation only holds for small values of the modulation voltage. Where a large modulating voltage is used to enhance the signal to noise ratio (for instance when looking at small concentrations of a particular element), distortion will result. Furthermore, Seah has pointed out<sup>34</sup> that for a C.M.A. in which the potential for the fringe plates is provided by a chain of resistors between the outer plate and earth, the modulation voltage on the fringe plates will be out of phase with the modulation voltage on the outer plate; this will also cause distortion of the differentiated spectrum.
3. Backscattering. Secondary electrons are produced at a range of depths within the sample and backscattered electrons can cause Auger transitions, enhancing the Auger current.<sup>35</sup> The



backscattered current depends partly on the composition of the substrate (this factor can be calculated<sup>36</sup>), and partly on incident beam effects within the substrate. This second effect will be treated in greater depth in chapter 4 and so it will not be considered further here, except to note its deleterious effect on the accuracy of quantitative measurements.

4. Errors in sensitivity factors. Morabito<sup>20</sup> has pointed out that the sensitivity factors used in the three methods outlined above can vary with concentration. This can lead to errors of up to 50%.

The conclusion must be that quantitative Auger electron spectroscopy is of limited accuracy. In practice, even this theoretical accuracy was not achieved because of the necessity to complete experiments within realistic times. The most accurate measurements could theoretically be made using peaks in the undifferentiated spectrum. For example, figure 2.20 shows the nickel 61eV and sulphur 152eV Auger peaks. By integrating the area under each peak and applying elemental sensitivity factors, the relative concentrations of sulphur and nickel could be calculated. However, apart from possible errors in the elemental sensitivity factors, Seah has pointed out<sup>34</sup> that as the area under the peak depends on the method of background subtraction, errors will be introduced due to the background contribution to the peak from energy loss processes. Despite these errors, this method is potentially the most accurate because no modulation has been used, eliminating the aforementioned modulation errors.

Figure 2.21 shows examples of differentiated spectra taken during an experiment in which sulphur was adsorbed onto nickel.

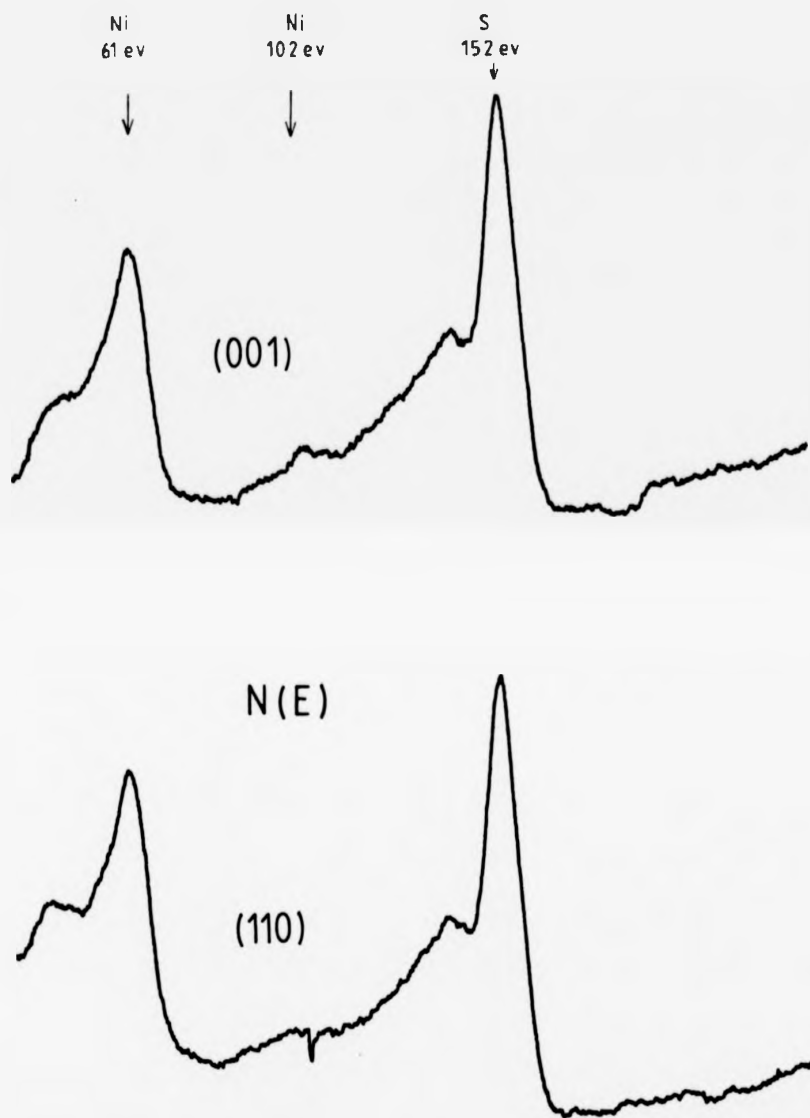


FIG. 2.20 Undifferentiated Auger spectra of a nickel crystal exposed to sulphur.

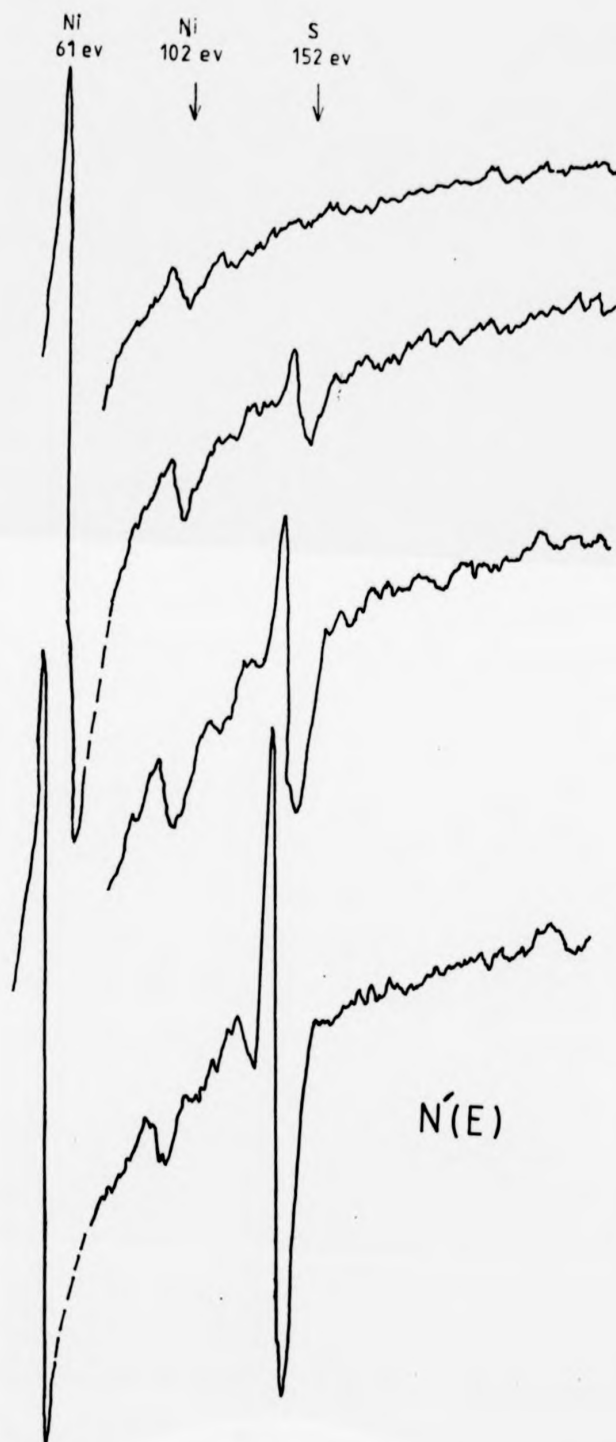


FIG 2.21 Auger spectra of a nickel sample exposed to increasing amounts of sulphur.

The advantage of this method is that the signal to noise ratio is improved by the use of modulation and a lock-in-amplifier. This type of spectrum is particularly useful for checking the initial cleanliness of the sample surface as contaminants are detectable at a concentration of 1% or less.

Both the undifferentiated and differentiated electron energy spectra suffer from one disadvantage: the long time required to obtain the spectra. Both figure 2.20 and figure 2.21 were taken at the same rate, i.e. each spectrum was recorded in 5 minutes. When concentrations of contaminants on a single face are being monitored this presents no problem. However for experiments on curved surfaces where spectra are needed from different positions around the crystal too great a time is needed to record all the spectra. For instance, a typical experiment on a cylindrical sample might involve taking readings after 5 successive oxygen exposures. After each exposure the oxygen Auger spectra are recorded at  $2^\circ$  intervals round the cylinder, a total of 900 readings. If each reading takes 5 minutes, the total time taken is 75 hours. At the base pressure of  $2 \cdot 10^{-10}$  torr it is simply not possible to avoid contamination of the surface (75 hours at  $2 \cdot 10^{-10}$  torr corresponds to an exposure of 54 Langmuirs). For comparatively reactive surfaces, such as nickel, contamination was observable over much shorter time scales. For example the adsorption of carbon from residual CO and CO<sub>2</sub> in the chamber is enhanced by the presence of the electron beam used for Auger excitation. Figure 2.22 shows the build up of carbon under such conditions. It is clear that the surface has become significantly contaminated in much less than 75 hours.

In order to avoid these problems, a different method of measuring an Auger peak in the differentiated Auger spectrum round the crystal

The advantage of this method is that the signal to noise ratio is improved by the use of modulation and a lock-in-amplifier. This type of spectrum is particularly useful for checking the initial cleanliness of the sample surface as contaminants are detectable at a concentration of 1% or less.

Both the undifferentiated and differentiated electron energy spectra suffer from one disadvantage: the long time required to obtain the spectra. Both figure 2.20 and figure 2.21 were taken at the same rate, i.e. each spectrum was recorded in 5 minutes. When concentrations of contaminants on a single face are being monitored this presents no problem. However for experiments on curved surfaces where spectra are needed from different positions around the crystal too great a time is needed to record all the spectra. For instance, a typical experiment on a cylindrical sample might involve taking readings after 5 successive oxygen exposures. After each exposure the oxygen Auger spectra are recorded at  $2^\circ$  intervals round the cylinder, a total of 900 readings. If each reading takes 5 minutes, the total time taken is 75 hours. At the base pressure of  $2 \cdot 10^{-10}$  torr it is simply not possible to avoid contamination of the surface (75 hours at  $2 \cdot 10^{-10}$  torr corresponds to an exposure of 54 Langmuirs). For comparatively reactive surfaces, such as nickel, contamination was observable over much shorter time scales. For example the adsorption of carbon from residual CO and CO<sub>2</sub> in the chamber is enhanced by the presence of the electron beam used for Auger excitation. Figure 2.22 shows the build up of carbon under such conditions. It is clear that the surface has become significantly contaminated in much less than 75 hours.

In order to avoid these problems, a different method of measuring an Auger peak in the differentiated Auger spectrum round the crystal

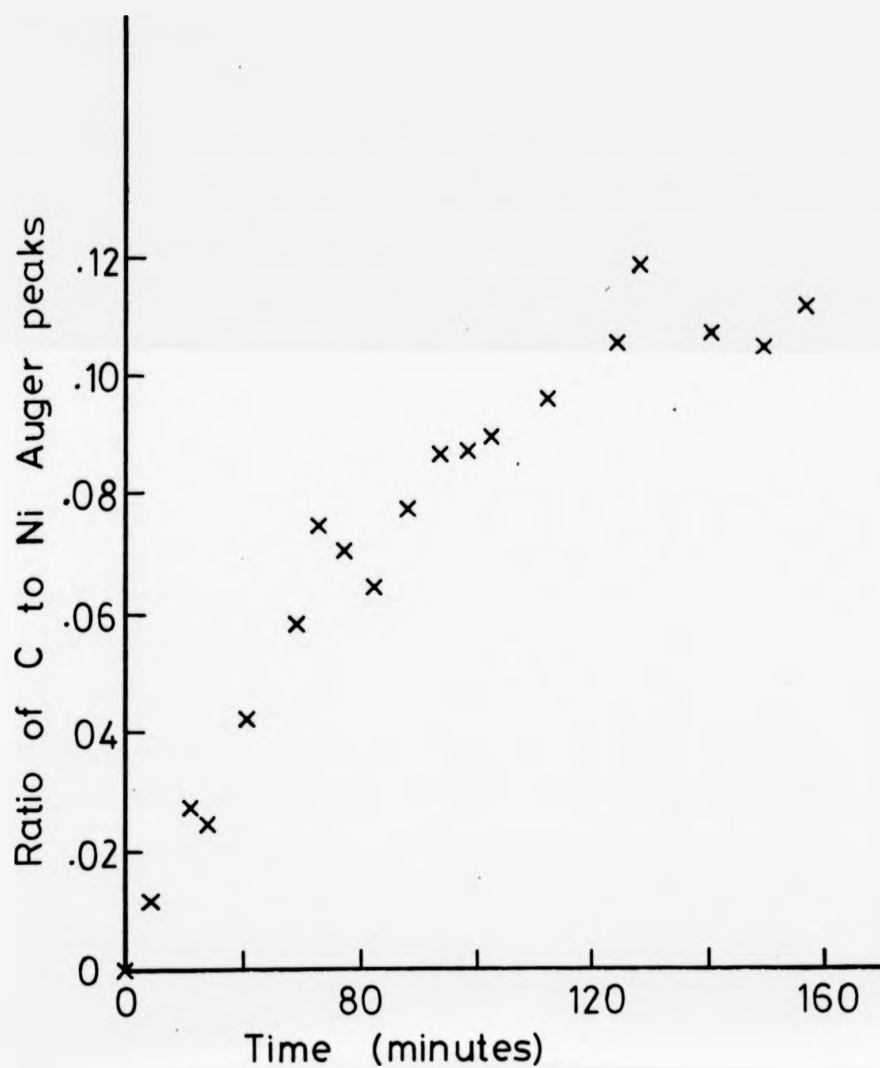
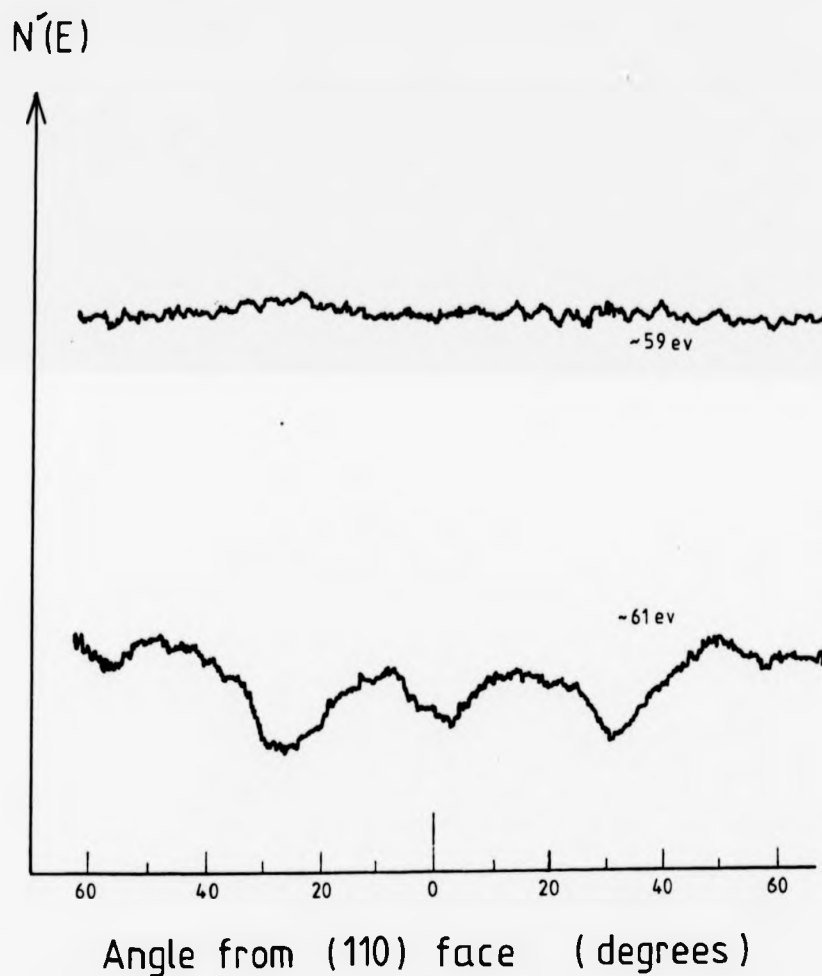


FIG. 2.22 Build-up of carbon contamination on a nickel sample in an ultra-high vacuum under the influence of a 1.5kv electron beam.

was adopted. Instead of sweeping the pass energy of the H.C.M.A., the energy was set to the energy at the top of the relevant Auger peak. The crystal was then rotated and the top of the Auger peak was recorded as a function of the position round the crystal. The pass energy of the analyser was then set to the value that would pass the negative peak, and this was also recorded as a function of the position round the crystal. An example of such a scan is shown in figure 2.23; the nickel 61 eV peak has been recorded. The top trace corresponds to the maximum positive excursion of the Auger peak (obtained when the analyser pass energy was set to approximately 59 eV). The bottom trace corresponds to the maximum negative excursion of the Auger peak (at a pass energy of approximately 61 eV). The relative Auger peak height as a function of position can then be obtained by subtracting the lower trace from the upper trace.

This method will retain all the inaccuracies of the standard differentiated spectrum (such as figure 2.21), except that now the height of an Auger peak can be recorded right round a cylinder in a time of the order of 30 minutes. The time to measure oxygen and nickel peaks for 5 experiments by this method is 5 hours, as opposed to the 75 hours of the previous method. The inaccuracies inherent in this method become an acceptable penalty for the high speed of data acquisition; most of the experiments reported in this thesis were carried out using this method.



**FIG. 2.23** An Auger spectrum taken by scanning round a nickel crystal with the h.c.m.a. pass energy set to the top then the bottom of the nickel 61eV Auger peak.



## CHAPTER 2 : REFERENCES

- 1) C.Wagner, J. Chem. Phys. 21 (1953) 1819.
- 2) C.Tubandt & H.Reinhold, Z. Elektrochem. 37 (1931) 589.
- 3) E.Bechtold, Ber. Bunsenger Physik. Chem. 70 (1966) 713.
- 4) D.Detry, J.Drowart, P.Goldfinger, H.Keller & H.Rickert,  
Z.Physik. Chem. (NF) 55 (1967) 314.
- 5) K.Schwaha, N.D.Spencer & R.M. Lambert, Surf. Sci. 81 (1979) 273.
- 6) D.Andrews, Ph.d. thesis
- 7) W.Heegeman, K.H.Meister, E.Bechtold & K.Hayek,  
Surf. Sci. 49 (1975) 161.
- 8) H.Z.Sar-El, Rev. Sci. Instr. 38 (1967) 1210.
- 9) P.W.Palmberg, G.K.Bohn & J.C.Tracy,  
Appl. Phys. Lett. 15 (1969) 254.
- 10) H.Hafner, J.Arol Simpson & C.E.Knight  
Rev. Sci. Instr. 39 (1968) 33.
- 11) J.C.Riviere, Contemp. Phys. 14(6) (1973) 513.
- 12) G.L.Kehl "Principles of metallographic laboratory practice"  
McGraw-Hill,(1949).
- 13) G.D.Magnusson & C.E.Carlston, J.Appl. Phys. 34 (1963) 3267.
- 14) F.Meyer & J.J.Vrakking, Surf. Sci. 33 (1972) 271.
- 15) J.C.Riviere, Contemp. Phys. 14(6) (1973) 513.
- 16) E.N.Sickafus, J. Vac. Sci. Technol. 11(1) (1974) 299.
- 17) J.T.Grant & M.P.Hooker, J. Colloid & Interface Sci.  
55 (1976) 370.
- 18) F.Pons, J.Le Hericy & J.P.Langeron  
Surf. Sci. 69 (1977) 547.
- 19) T.E.Gallon, N.A.T.O. Summer School, Ghent, 1977.
- 20) J.M.Morabito, Conference on Quantitative Surface Analysis,  
N.P.L., 1979.

- 21) M.Perdereau, Surf.Sci. 24 (1971) 239
- 22) C.Argile & G.E.Rhead, Surf.Sci. 53 (1975) 659
- 23) P.W.Palmberg, J.Vac.Sci.Technol. 13 (1) (1976)
- 24) M.P.Seah & W.A.Dench Surf. & Interface Analysis 1 (1) (1979) 2
- 25) L.E.Davis, N.C.Macdonald, P.W.Palmberg, G.E.Riach & R.E.Weber,  
"Handbook of Auger Electron Spectroscopy" 2nd Edn.  
Physical Electronics Industries Inc. Minnesota (1976)
- 26) M.Salmeron & A.M.Baro, Surf.Sci. 49 (1975) 356
- 27) M.Salmeron & A.M.Baro & J.M.Rojo, Phys. Rev. B 13 (1976) 4348
- 28) J.P.Coad & J.C.Riviere, Proc. Roy. Soc. A 331 (1972) 403
- 29) E.N.Sickafus & F.Steinrisser, J.Vac.Sci.Technol. 10 (1973) 43
- 30) T.W.Haas & T.J.Grant, Appl.Phys.Lett. 16 (1970) 172
- 31) A.M.Horgan & I.Dalins, Surf.Sci. 36 (1973) 526
- 32) P.M.Holloway & J.B.Hudson, J.Vac.Sci.Technol. 12 (1975) 647
- 33) M.P.Hooker, J.T.Grant & T.W.Haas, J.Vac.Sci.Technol. 13 (1976) 296
- 34) M.P.Seah, Conference on Quantitative Surface Analysis, N.P.L. 1979
- 35) J.E.Houston & R.L.Park, Appl.Phys.Lett. 14 (1967) 358
- 36) A.Jablonski, Surf.Sci. 87 (1979) 539

### CHAPTER 3 : CHOICE OF SYSTEM

#### 1) Introduction.

Let us consider two types of interface in a pure metal: solid-solid (grain boundary) , and solid-gas (free surface). The properties of these two types of interface can be investigated by observing the behaviour of foreign atoms at these interfaces. Two routes whereby an atom can migrate to an interface are possible: diffusion through the bulk to the interface, or adsorption on the interface from the gas phase. Figure 3.1 shows schematically the possible routes.

This chapter is concerned primarily with the choice of route and system. For example, a comparison is made between grain boundaries and free surfaces via the system bismuth/polycrystalline copper. The system sulphur/nickel is used to compare segregation and adsorption. Examples concerned with one route alone are the segregation of carbon to a nickel surface, and the adsorption of oxygen on copper.

A further constraint is applied if we wish to investigate the effect of crystallographic orientation at the interface, i.e. we must be able to find the crystallographic orientation of the bulk with respect to the interface. This limits consideration to single crystals or to polycrystalline material in which the grain size is large enough to allow unequivocal grain orientation by x-ray diffraction. All three routes shown in figure 3.1 are possible with a polycrystalline substrate, obviously route 1 is not feasible with a single crystal. Furthermore, the single crystals that were used in these studies were so pure that it was difficult to conduct segregation experiments because the small amounts of impurities present in the bulk were soon depleted by evaporation from the surface. Attempts at doping single crystals (for example by heating a crystal in an evacuated ampoule with a measured quantity of it's sulphide)

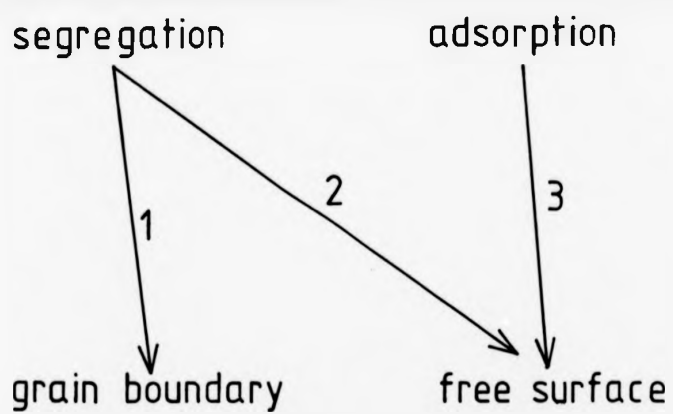


FIG. 3.1 The three possible routes for segregation and adsorption.

were not successful. Thus the experimental routes that have been followed are 1,2& 3 for polycrystalline substrates, and route 3 for single crystals.

Table 3.1 details the experiments discussed in this thesis. The term 'impurity' is used to refer to the minor constituent present. Later chapters are concerned entirely with single crystals; it will be seen that this is primarily due to the ease with which crystallographic orientations can be determined.

TABLE 3.1

IMPURITY	BULK	CRYSTAL	ROUTE	CHAPTER	KNOWLEDGE OF ORIENTATION ?
Bi	Cu	Poly-	1,2	3	No
C	Ni	Poly-	2	3	Some
S	Ni	Poly-	2,3	3	Some
O	Cu	Mono-	3	5	Yes
O	Ni	Mono-	3	6	Yes
S	Cu	Mono-	3	7	Yes
S	Ni	Mono-	3	7	Yes

The first theoretical treatment of segregation was by McLean<sup>1</sup>, who considered that the driving force for segregation to a grain-boundary (route 1) arose because the distortion energy of a solute atom in a grain interior could be reduced if the solute atom segregated to a grain boundary.

The kinetics of segregation to a surface have been considered by several authors<sup>2,3,4,5</sup>. Seah & Lea<sup>4</sup> compared segregation to grain boundaries with segregation to free surfaces for the system Fe/Sn. They concluded that at high temperatures (around 0.9 T<sub>m</sub>), surface segregation is a good guide to grain boundary segregation. Their experimental arrangement was designed to minimise the effect

of evaporation from the surface. In a later paper <sup>6</sup>, the same authors extended the treatment of McLean <sup>1</sup> to include the effect of evaporation from a free surface.

The effect of saturation (as well as evaporation) on the kinetics of segregation to surfaces and grain boundaries has been treated by Rowlands & Woodruff <sup>7</sup>. Their general treatment becomes equivalent to the more limited treatment of Lea & Seah for the particular case when saturation is not present.

For reasons that will be outlined in this chapter, the emphasis in this thesis is on the study of adsorption on single crystal surfaces. Examples of segregation that have been investigated will only be dealt with briefly, mostly with a view to establishing the reasons for concentrating on adsorption on single crystals.

## 2) Bismuth in copper

The presence of bismuth in copper at low concentrations has long been known to cause embrittlement at grain boundaries. Voce & Hallows<sup>8</sup> observed embrittlement in copper with bulk bismuth concentrations as low as 10 p.p.m. in the temperature range 450-650°C. Hondros & McLean<sup>9</sup> showed that the effect of bismuth in copper was to lower the tensile strength by reducing the grain boundary cohesion. Intergranular fracture occurred by the formation of grain boundary crack nuclei in alloys with bismuth concentrations as low as 2 p.p.m.

More recently, this system has been studied using A.E.S. (Auger Electron Spectroscopy)<sup>10,11,12</sup>. Because copper is embrittled by bismuth, the grain boundary concentrations can be studied by fracturing an embrittled sample in a U.H.V. system. Since the fracture runs along the grain boundaries, these boundaries are exposed and available for examination.

One important observation<sup>11</sup> was that the amount of bismuth that segregated to a grain boundary varied markedly between different grains. This is in contrast with the behaviour of sulphur and tin in iron<sup>13</sup> where the segregation levels of all the grain boundaries in a sample are about the same. Powell & Woodruff<sup>12</sup> studied the anisotropy in the grain boundary segregation of bismuth in copper for samples containing 60 p.p.m. of bismuth and annealed in the temperature range 400-700°C. Four samples were annealed at different temperatures and then fractured in the U.H.V. system. The amount of bismuth at the surface of fifty grains was then measured using A.E.S. Figure 3.2 shows histograms of their results in which it can be seen that there is a wide range of grain boundary concentrations at all the temperatures studied.

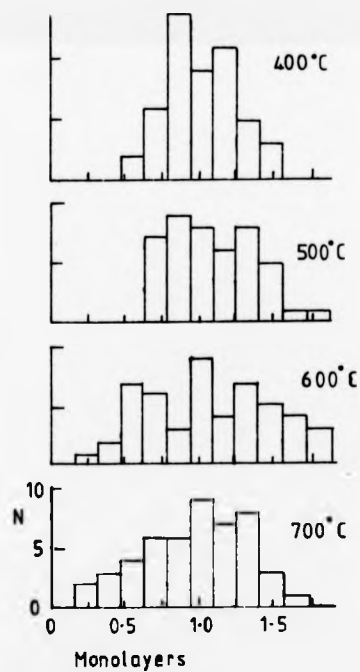


**FIG. 3.2** Population distribution of bismuth concentration for 50 grains of copper.  
(from Powell and Woodruff, Phil. Mag. 34 (1976) )



In order to compare the behaviour of a free surface with these results for grain boundaries, a small slab of copper doped with bismuth (2mm x 7mm x 9mm) was polished and placed in the U.H.V. system for examination. The sample had been prepared in the same manner as the samples used in refs 11 & 12. The ratio of the bismuth 102eV to the copper 62eV Auger peaks was monitored while the sample was held at a constant high temperature.

Figure 3.3 shows the results from such an experiment at 450°C. In figure 3.3 (a) the average ratio from 10 different grains has been plotted. In figure 3.3 (b) the ratio has been plotted for three different grains. Note that after about four hours, the ratio reaches a maximum and then declines as evaporation of bismuth begins to dominate over diffusion of bismuth from the depleted layer below the surface.

Figure 3.4 is a histogram showing the distribution of the bismuth to copper peak ratios for 34 grains. The specimen had been heated to 450°C for 110 minutes. The histogram shows the same wide distribution as those of Powell & Woodruff for grain boundaries (figure 3.2). Note that the wide distribution in figure 3.4 is not due to any inaccuracy of the method used to measure the bismuth concentrations; the graph for three different grains (figure 3.3 (b)) shows that the differences are measurable differences in the behaviour of different grains.

The conclusion is therefore that, in qualitative terms, the surface of the polycrystalline sample shows similar anisotropy of segregation to that observed for grain boundaries. However, one problem prevents further investigation in this system, and that is the difficulty of trying to orient particular grains to find out if there is a correlation between the surface orientation of a grain and the amount of bismuth that segregates to the surface of

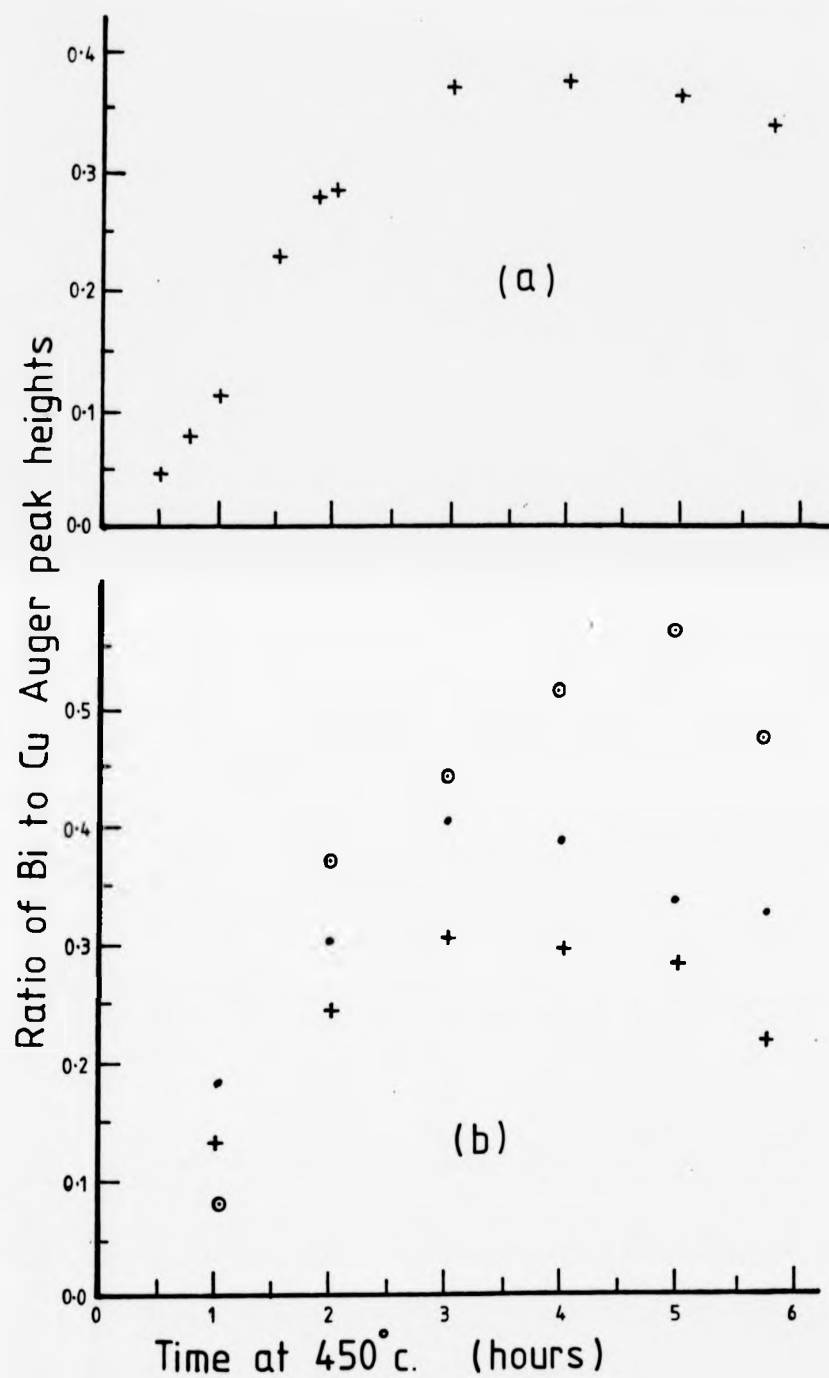


FIG. 3.3 Segregation of bismuth in copper at 450°C.  
 (a) averaged over 10 grains; (b) for three individual grains.

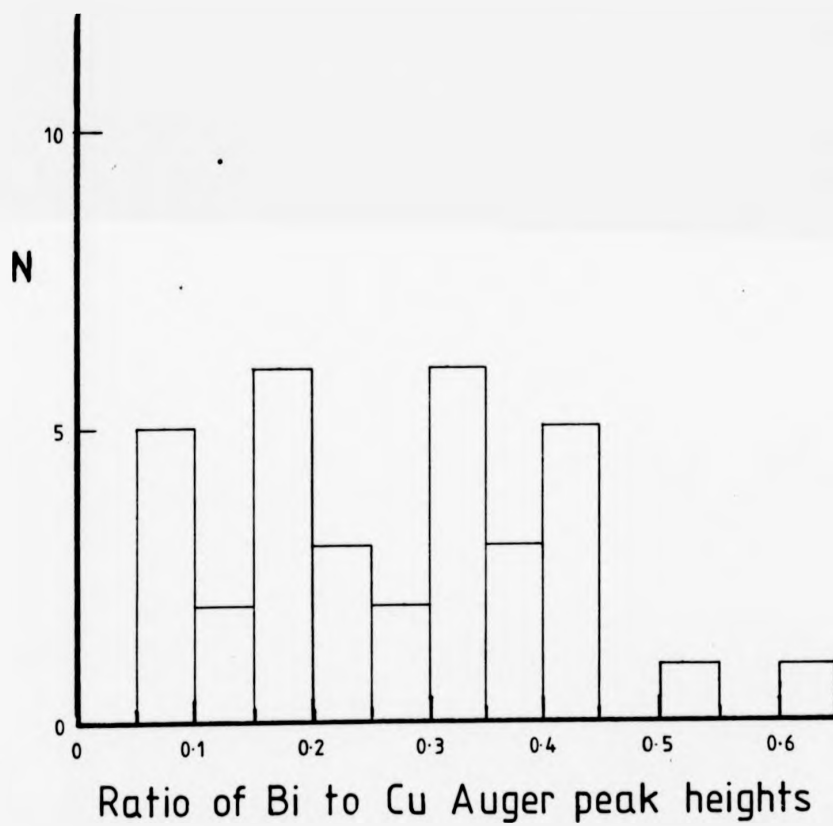


FIG. 3.4 Bismuth segregation to the surface of 34 grains of copper at 450°C.

that grain. The average grain diameter was of the order of 0.5-1.0mm, and this was too small to allow accurate orientation of individual grains by x-ray diffraction.

Of greater importance was the fact that the sample was a polycrystalline sample with a flat surface. Even if it had been possible to find the orientation of an individual grain, the resulting surface orientation would be highly unlikely to correspond to a plane with reasonably small Miller indices, i.e. the surface would most probably be a very complicated one. For example, if the 34 grains from figure 3.4 had been accurately oriented, then segregation results would have been available for 34 randomly distributed points on the stereographic triangle (randomly distributed if there were no preferred grain orientation in the sample). This approach is not satisfactory for systematically studying the variation of surface properties with surface orientation.

It is therefore desirable to study curved surfaces in which a range of orientations are presented for examination. Ideally a spherical surface could be used; this would present all possible orientations of the surface. As will be seen, there are practical problems associated with the use of a spherical sample (not the least being the difficulty of cutting such a sample ! ). One surface that presents fewer problems experimentally is that of a cylinder. The surface of a cylinder presents a smaller range of faces than a sphere, but a larger range than a flat surface. This shape of sample proves to be a workable compromise for both polycrystalline and single crystal samples.

### 3) Carbon and sulphur on polycrystalline nickel

The segregation of carbon and sulphur to single crystal nickel surfaces has been widely studied. In particular work has been reported for all three low index faces as follows:

(110) face : references 14,15,23,24,26.

(111) face : references 18,21-24,26,27.

(100) face : references 18,22,23.

Blakely and coworkers also report the result of work on several vicinal surfaces.<sup>24-26</sup> The segregation of carbon and sulphur to polycrystalline nickel surfaces has also been studied in detail<sup>16</sup>, 17,19,20.

Three possible situations can be considered: the segregation of either carbon or sulphur on their own, or the segregation of carbon and sulphur together. The segregation of carbon on it's own to the surface of nickel has been studied in greatest detail by Blakely et al.<sup>21-27</sup> They found that, on all three low index faces, carbon precipitated on the surface in the form of graphite as the solubility limit was exceeded (i.e. at low temperatures). The exact temperature at which the graphite precipitate formed depended on the bulk concentration of carbon. The relationship between the bulk concentration and the temperature at which the solubility is exceeded has been treated by Lander et al.,<sup>28</sup> and by Blakely.<sup>23</sup>

Above the precipitation temperature the three low index faces of nickel behave differently. On the (100) face Blakely et al. found<sup>a</sup> two different phases depending on the temperature.<sup>22,23</sup> The segregation behaviour could be described by a Langmuir model, suggesting that there is little interaction between the carbon adatoms on a (100) face.

In contrast to this, the behaviour of carbon on the (111) face is indicative of a strong attractive interaction among the segregated carbon atoms<sup>21,23,24</sup>. Blakely points out that a monolayer of graphite has an excellent epitaxial fit to the nickel (111) plane, and suggests that this structure forms on the nickel (111) face just above the precipitation temperature.

Preliminary results<sup>23</sup> suggest that the (110) face behaves differently from either the (111) or (100) faces in that no carbon is observed on the (110) face above the precipitation temperature.

The segregation of sulphur on its own has been less widely studied. Riwan<sup>15</sup> has studied the segregation of sulphur to a (110) nickel surface, and both Coad & Riviere<sup>16</sup> and White<sup>17</sup> have studied the segregation of sulphur to polycrystalline nickel surfaces. In impure samples (as used for segregation studies) it is often found that the sulphur segregation is accompanied by segregation of carbon<sup>14,18,25,26</sup>. A general pattern seems to emerge from systems in which sulphur segregates in competition with other species. Mroz<sup>18</sup> noted that the presence of sulphur atoms, even at concentrations of much less than a monolayer, prevents other segregants or admixtures of segregants from segregating to the surface.

Sickafus<sup>14</sup> noted that, for the (110) surface of nickel, carbon was limited to regions where there was no sulphur. There the carbon was present as randomly oriented layers of graphite between the sulphur domains. Coad & Riviere noted a similar behaviour for the co-segregation of phosphorus and sulphur in nickel.<sup>16</sup> Again the sulphur tended to suppress the segregation of the other constituent. This suppression of segregation by the presence of sulphur appears to be a comparatively common feature, with the sulphur atoms competing with other segregating species for the surface sites.

In this section results are presented for two of the cases discussed before, i.e. segregation of sulphur and the co-segregation of carbon and sulphur. These studies were performed on coarse grained polycrystalline samples supplied by I.N.C.O. Ltd. The samples had a columnar grain structure with a typical grain size of 1-2mm diameter, and 5-10mm length. These samples contained 20 and 430 w.p.m. <sup>carbon</sup> (referred to as sample 1 and sample 2 respectively).

When sample 1 was heated, it was observed that sulphur alone segregated. The kinetics of sulphur segregation are shown for a typical experiment in figure 3.5. When the sample was heated to 950°C the ratio of sulphur to nickel Auger peak heights increased until saturation was reached after about 90 minutes.

At higher temperatures diffusion to the surface is faster, and saturation is reached more rapidly. This can be seen in figure 3.6 which shows the segregation of sulphur when the sample is heated to 1100°C. At this temperature saturation is reached within about five minutes. It can also be seen that, at this high temperature, the sulphur evaporates to a significant extent. As the region below the surface becomes depleted of sulphur, the "saturation" ratio of the sulphur to nickel Auger peak heights decreases.

The next experiment involved the comparison of the kinetics of sulphur segregation at two different grains (figures 3.7 & 3.8). The sample was heated to 800°C, and the sulphur and nickel Auger peak heights were recorded as a function of time at two different positions on the sample (corresponding to two different grains). The Auger peaks were recorded alternately at the two grains throughout the experiment. After the sulphur coverage had reached saturation, the experiment was stopped. The sample was then cleaned by argon ion bombardment and the experiment was repeated. In all, three separate runs were performed with the sample being

In this section results are presented for two of the cases discussed before, i.e. segregation of sulphur and the co-segregation of carbon and sulphur. These studies were performed on coarse grained polycrystalline samples supplied by I.N.C.O. Ltd. The samples had a columnar grain structure with a typical grain size of 1-2mm diameter, and 5-10mm length. These samples contained 20 and 430 w.p.m. <sup>carbon</sup> (referred to as sample 1 and sample 2 respectively).

When sample 1 was heated, it was observed that sulphur alone segregated. The kinetics of sulphur segregation are shown for a typical experiment in figure 3.5. When the sample was heated to 950°C the ratio of sulphur to nickel Auger peak heights increased until saturation was reached after about 90 minutes.

At higher temperatures diffusion to the surface is faster, and saturation is reached more rapidly. This can be seen in figure 3.6 which shows the segregation of sulphur when the sample is heated to 1100°C. At this temperature saturation is reached within about five minutes. It can also be seen that, at this high temperature, the sulphur evaporates to a significant extent. As the region below the surface becomes depleted of sulphur, the "saturation" ratio of the sulphur to nickel Auger peak heights decreases.

The next experiment involved the comparison of the kinetics of sulphur segregation at two different grains (figures 3.7 & 3.8). The sample was heated to 800°C, and the sulphur and nickel Auger peak heights were recorded as a function of time at two different positions on the sample (corresponding to two different grains). The Auger peaks were recorded alternately at the two grains throughout the experiment. After the sulphur coverage had reached saturation, the experiment was stopped. The sample was then cleaned by argon ion bombardment and the experiment was repeated. In all, three separate runs were performed with the sample being



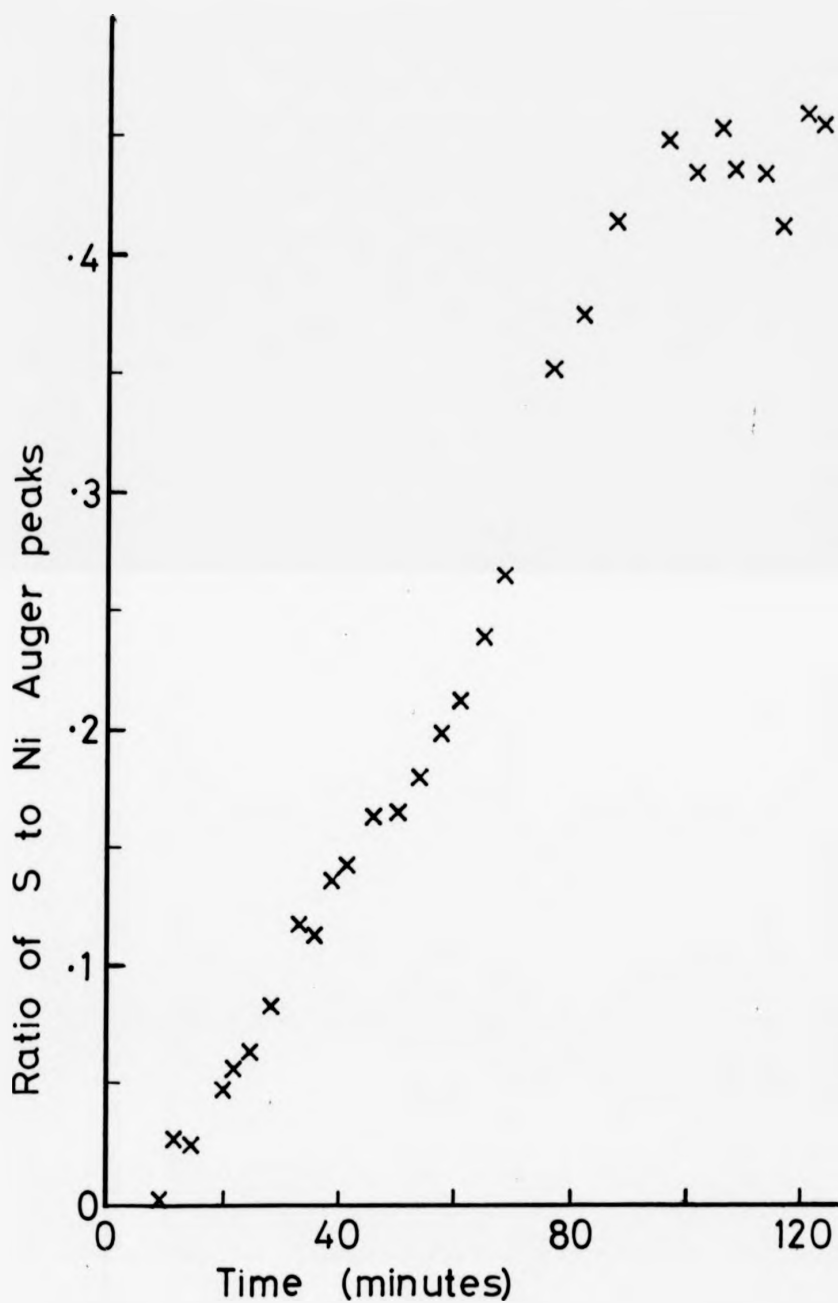


FIG. 3.5 Build-up of sulphur on the surface of a nickel grain heated to 950°C.

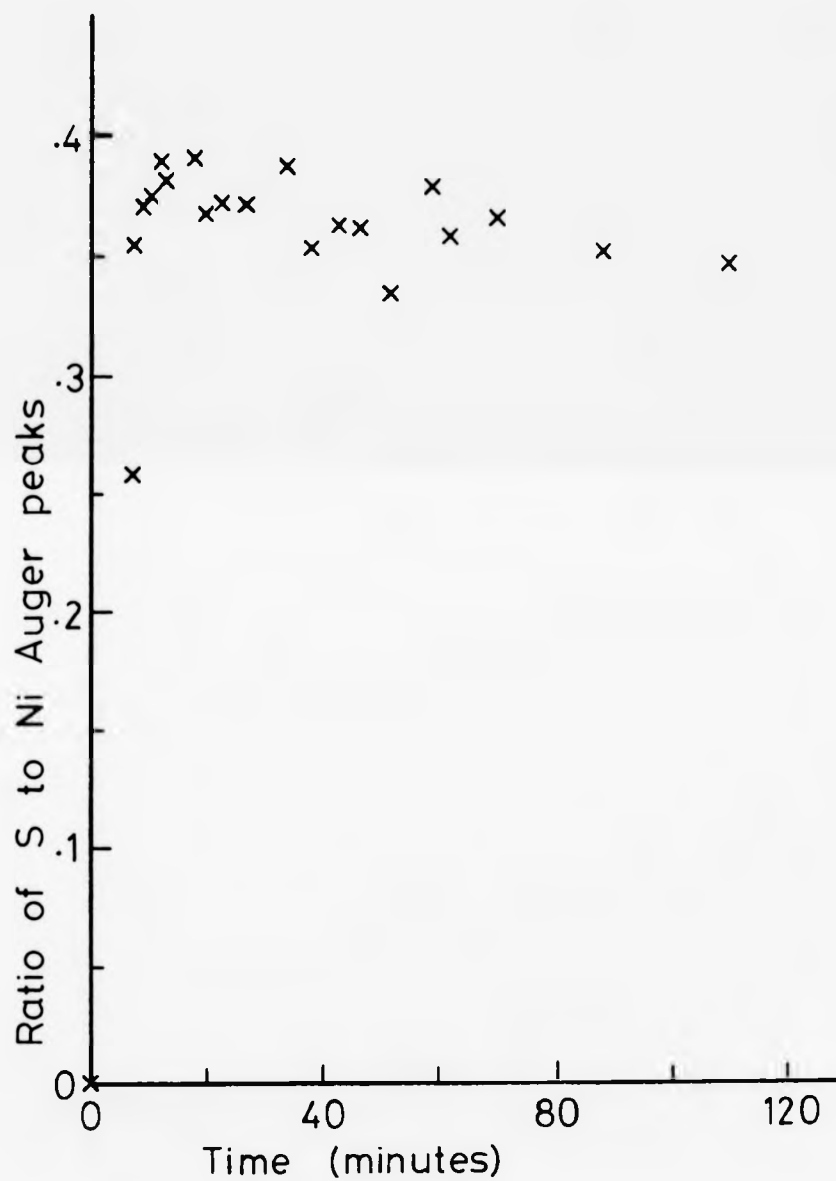


FIG. 3.6 Build-up of sulphur on the surface of a nickel grain heated to  $1100^{\circ}\text{C}$ .

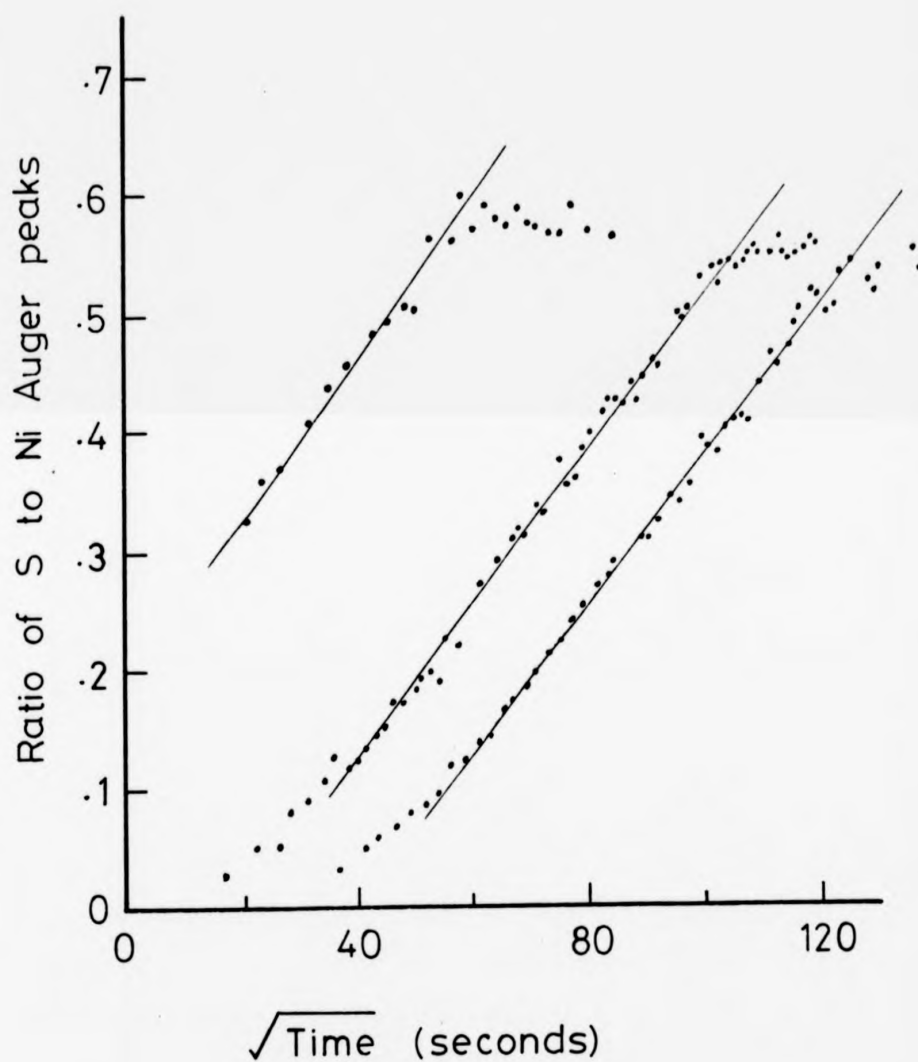


FIG. 3.7 Build-up of sulphur as a function of  $(\text{time at } 800^{\circ}\text{C})^{\frac{1}{2}}$ .  
Three successive experiments at position 1 (sample 1).

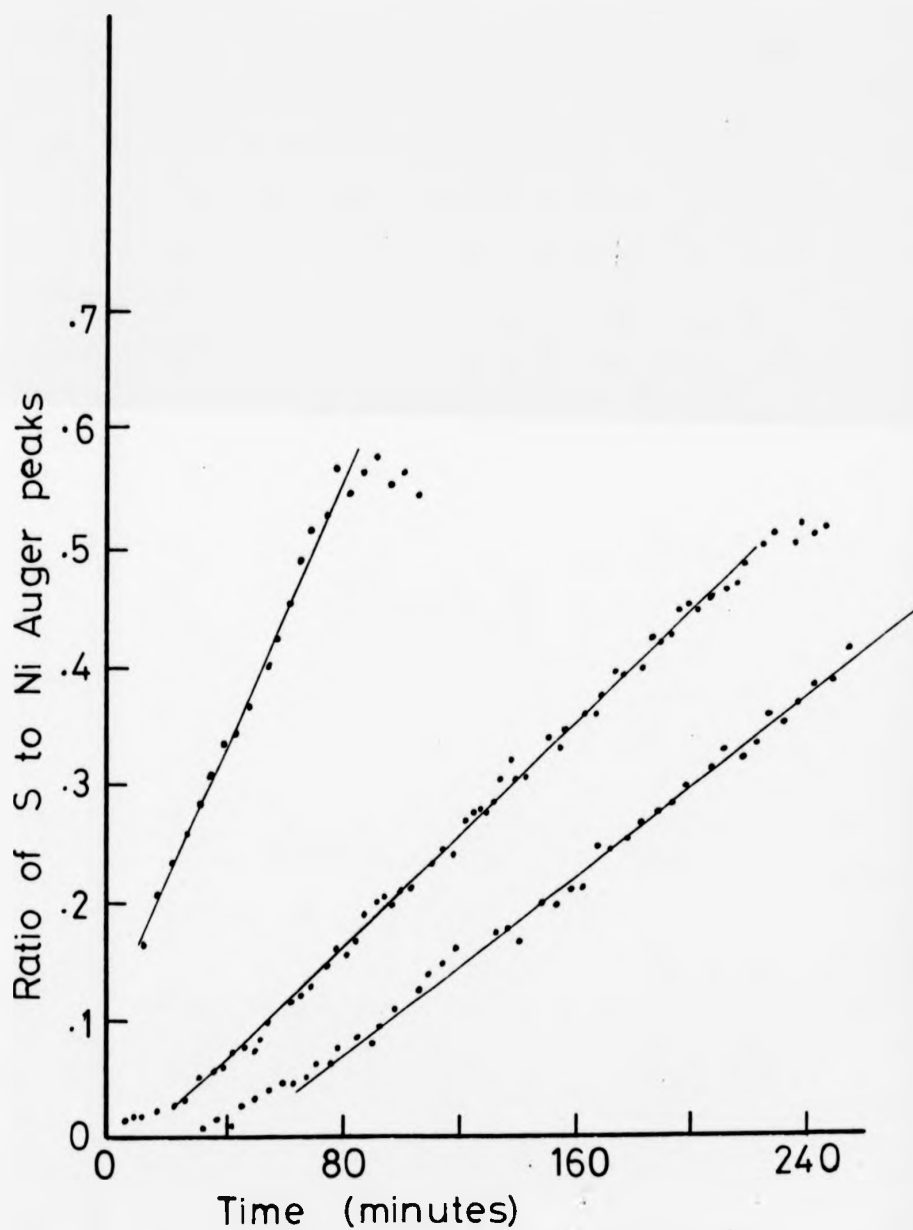


FIG. 3.8 build-up of sulphur as a function of time at 800°C.  
Three successive experiments at position 2 (sample 1).

cleaned between each run.

Figure 3.7 shows the results for the segregation of sulphur at position 1. The segregation at this grain varies with the square root of the time elapsed. Furthermore the rate of change of the sulphur to nickel Auger peak height ratio is the same for all three experimental runs. This type of segregation behaviour has been discussed for carbon segregation in nickel by Mojica & Levenson<sup>19</sup>. More generally, Rowlands & Woodruff<sup>7</sup> have considered the problem of surface segregation in which saturation is important. They found that, for systems in which saturation is important, the kinetics of segregation could be described by the following equation:

$$\frac{\phi}{\phi_{\infty}} = \frac{2C_a}{C_m\sqrt{\pi}} (Dt)^{\frac{1}{2}} \quad \dots 3.1$$

In equation 3.1  $\phi$  is the coverage at time  $t$ ,  $\phi_{\infty}$  is the coverage at infinite time,  $D$  is the bulk diffusion coefficient,  $C_m$  is the maximum concentration the surface can support, and  $C_a = C_0/d$  ( $C_0$  is the bulk concentration and  $d$  is the interplanar spacing).

This equation describes the behaviour of sulphur in nickel as demonstrated in figure 3.7 in that the concentration varies with the square root of the time elapsed, and the gradient is the same for each run (i.e. the diffusion coefficient does not vary). There is one feature that is not described by this equation, and that is the horizontal displacement between the results of successive runs, i.e. the increasing delay before segregation starts on successive runs. It is thought that this effect may be due to the build up of a sulphur depleted layer below the surface as the result of the repeated segregation of sulphur to the surface, and then the removal of this sulphur rich layer by argon ion bombardment between each run.

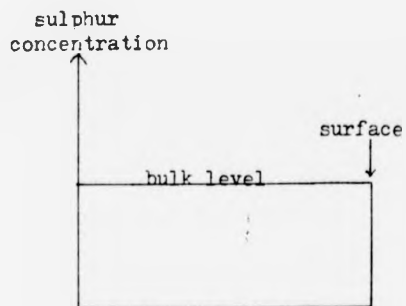
Figure 3.9 illustrates a sequence of events which might lead to such a depleted layer in the region of the surface. When the sample is first heated, the sulphur concentration profile changes from the initial level (1 in figure 3.9) to that shown in (2). Sputter cleaning of the surface layer will remove the sulphur-rich region near the surface, but may not remove all of the sulphur-depleted sub-surface layer, as in (3). Any subsequent segregation (4) then starts with a concentration profile different from the "ideal" initial concentration profile of (1).

The behaviour of the second grain is in marked contrast to the behaviour of the first grain. At position 2 the ratio of the sulphur to nickel Auger peak heights varied linearly with time (figure 3.8). Furthermore the rate of segregation of sulphur decreased with each successive run. A possible explanation for this type of behaviour is that the segregation through this particular grain is being fed by an internal source, such as a precipitate within the bulk.

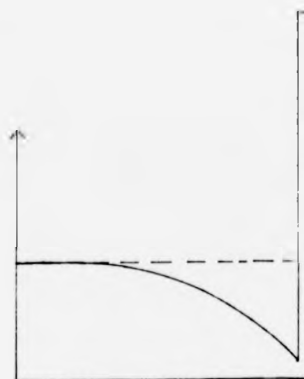
Precipitates within the bulk could form either at the grain boundary or within a grain as the solubility limit is exceeded. If a sulphide particle was present below the surface, it could act as a source of sulphur, altering the sulphur concentration profile.

K.R.Jones<sup>30</sup> showed that, for a constant source concentration at a fixed distance from the surface, the sulphur concentration at the surface would be expected to increase linearly with time.

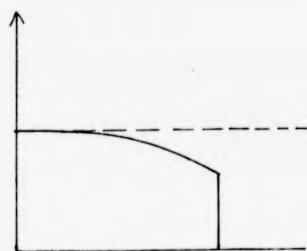
The bulk sulphur concentration of the polycrystalline samples was not known. The fact that the kinetics of segregation at some grain surfaces could be explained by the presence of sulphide precipitates, whereas the kinetics of segregation at other grain surfaces suggested that no precipitate was present, implies that the bulk sulphur concentration was near the solubility limit.



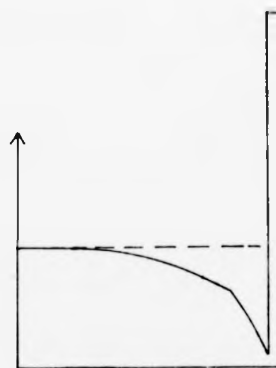
1. Initial profile.



2. After segregation.



3. After sputter cleaning.



4. After 2<sup>nd</sup> segregation.

FIG. 3.9 Sequence of events leading to a sub-surface depletion layer.

As the solubility limit of sulphur in nickel is known to be about 0.006 a.o.<sup>31</sup>, the diffusion coefficient of sulphur in nickel can be estimated. Equation 3.1 gives a value for the diffusion coefficient of approximately  $1.3 \cdot 10^{-12} \text{ cm}^2 \text{ sec}^{-1}$ .

A practical problem that limits the usefulness of these results is that it did not turn out to be easy to determine the orientation of a particular grain surface. In cases where x-ray diffraction did permit unequivocal grain orientation to be made, it was found that the surfaces corresponded to high Miller index faces with complicated surface structures. The effect of the surface structure could therefore not be easily determined.

One parameter that did not vary greatly between different grains was the saturation ratio of the sulphur to nickel Auger peak heights at a given temperature. At saturation this ratio was constant to within about 5%. In one experiment, for example, the ratio of the peaks was measured at approximately 1000K at ten positions round the cylinder (corresponding to 10 different grains). The average sulphur to nickel peak ratio was 0.808, and the standard deviation of the measurements was 0.023, less than 3% of the average.

The most accurate measurements of the equilibrium ratio of the S 152eV to Ni 61eV Auger peak heights were obtained for the two grains of figure 3.7 and 3.8. For these two grains there was a small, but significant, difference in this equilibrium ratio. Measurements of this ratio (and the standard deviation in these measurements) are given in table 3.2. On average the equilibrium ratio at grain B was 3.2% larger than the equilibrium ratio at grain A (the standard deviation being 1.9%).



TABLE 3.2

Equilibrium ratio of the S:Ni Auger peak heights for 2 grains

Temp °C	No. of readings	Average grain A	Average grain B	$\sigma_a$ (%)	$\sigma_b$ (%)	$\frac{B-A}{A}$ (%)
750	8	0.580	0.589	2.9	2.3	+1.5
800	7	0.557	0.580	2.1	1.7	+4.2
880	7	0.550	0.551	3.7	2.3	+1.8
880	5	0.502	0.509	3.8	3.1	+1.5
950	6	0.446	0.465	4.2	2.4	+4.4
1080	5	0.339	0.360	1.9	3.5	+6.0

These observed variations in the equilibrium ratio of S:Ni were smaller than expected. This may be due to the fact that the random surface orientation of the grains resulted in a set of surfaces in which there were no low index planes present. The low index planes, with a comparatively simple surface structure, would be expected to have the greatest effect on the equilibrium concentration of a segregating species.

The equilibrium ratio of the sulphur to nickel peaks has been plotted as a function of temperature in figure 3.10. Each point in this graph is the average of the ratio at several positions on the cylinder, and results are presented from both of the polycrystalline samples. At low temperatures (below about 600°C) the time taken to reach equilibrium was so great as to make experiments unreasonably long. In the low temperature region therefore the sulphur adlayer was produced by adsorbing sulphur from the vapour phase rather than by segregation from the bulk (i.e. by using the sulphur source to produce a beam of S<sub>2</sub> molecules directed at the specimen).

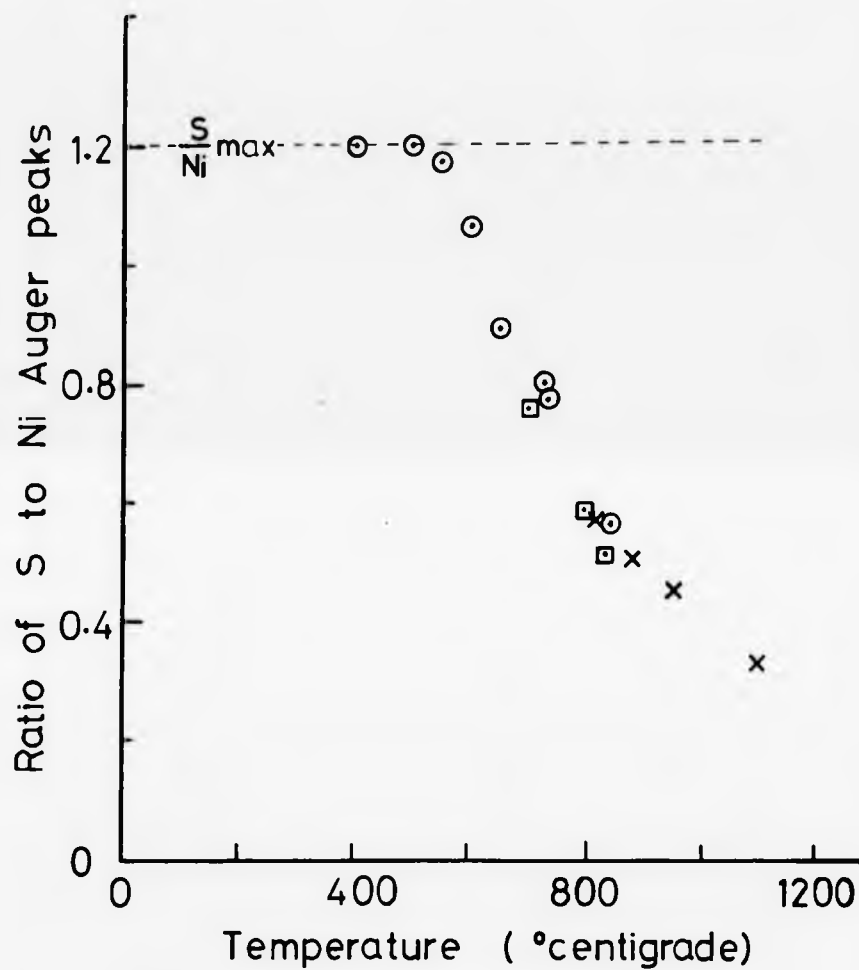


FIG. 3.10 Equilibrium ratio of S 152eV to Ni 61eV Auger peaks as a function of temperature.

- × Sample 1
- ▣ Sample 2
- Sample 2 (sulphur deposited from the sulphur source)

The form of curve in figure 3.10 resembles the form of the adsorption curve predicted by the Langmuir model (assuming that the concentration of sulphur on the nickel surface is proportional to the sulphur to nickel Auger peak ratio).

The Langmuir model is based on the assumption that the surface presents a set of equivalent adsorption sites on the topmost plane, which atoms or molecules from in solution or the vapour may occupy with binding energy different from the bulk. The Langmuir equation was first applied by McLean<sup>1</sup> to describe grain boundary segregation in metals in the form:

$$\frac{\theta}{1-\theta} = X \cdot \exp(-\Delta E_{\text{seg}}/RT) \quad \dots 3.2$$

In equation 3.2,  $\theta$  is the fractional occupancy of the surface sites,  $\Delta E_{\text{seg}}$  is the partial molar excess free energy of segregation, and  $X$  is a constant.

To check whether the results plotted in figure 3.10 fit equation 3.2, they have been replotted in the form of the standard Langmuir plot in figure 3.11. The results suggest that the Langmuir adsorption model is a good model for the sulphur/nickel system. Good agreement is also seen between the results from segregation experiments and the results from the adsorption experiments. A straight line has been fitted to the points in figure 3.11 by the method of least squares. The gradient of this line gives the heat of segregation of sulphur in nickel as  $\Delta E_{\text{seg}} = -11.6 \pm 0.9 \text{ K cal mole}^{-1}$ .

The behaviour of sample 2 (with a higher carbon content than sample 1) was quite different at low temperatures. Below about 650-700°C the sample was covered in a thick layer of carbon, probably in the form of a graphitic precipitate. As the sample was heated to above 700°C, the carbon Auger signal suddenly dropped

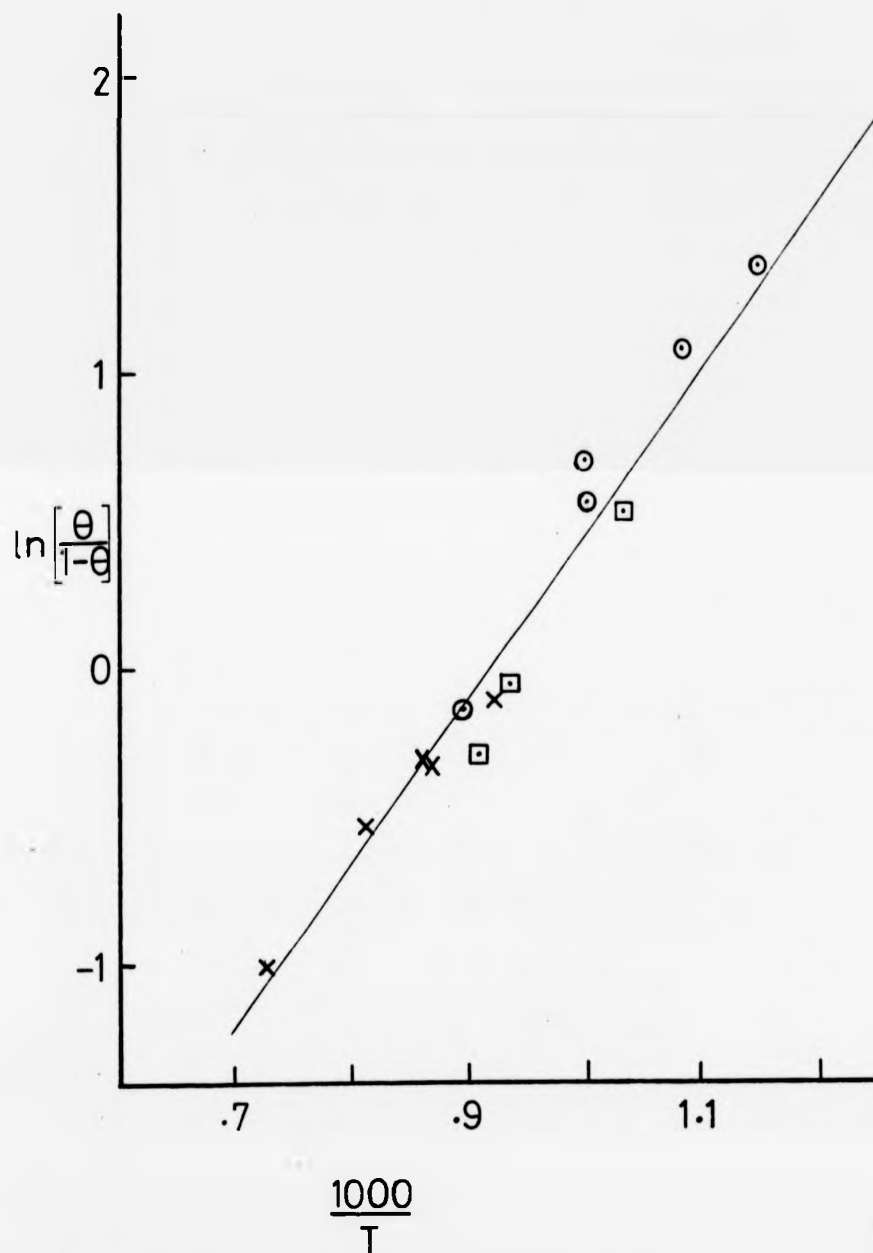


FIG. 3.11

Langmuir plot for Sulphur on Nickel.  $\theta$ , the fractional coverage, is the Sulphur to Nickel ratio divided by the maximum Sulphur to Nickel ratio.

- X Sample 1
- Sample 2
- ⊙ Sample 2 with Sulphur deposited from a Sulphur source

by an order of magnitude. At the same time, the nickel Auger signal increased by about 70-80%.

Isett & Blakely<sup>23</sup> have plotted solubility data for carbon in nickel as a function of temperature. According to their data the solubility limit for carbon in sample 2 (containing 430 w.p.p.m. carbon) should be exceeded when the temperature drops below 625°C. The uncertainty in this estimate is of the order of 80°C. In fact the sudden change in the carbon Auger peak was seen at temperatures in the range 640-700°C and so does probably correspond to the precipitation temperature.

The Auger spectrum of the 272 eV carbon peak at low temperatures was typical of graphitic carbon rather than a carbide. This can be seen from figure 3.12 in which the carbon peak from sample 2 is compared with carbide and graphitic carbon peaks from the "Handbook of Auger Electron Spectroscopy!"<sup>29</sup>

Whenever the nickel surface was covered with a carbon layer the amount of sulphur on the surface was so low as to be almost undetectable. When the sample temperature was raised so that the carbon redissolved in the bulk, sulphur (and on some grains phosphorus) began to segregate to the surface. This sort of behaviour is exemplified by the results plotted in figure 3.13. The carbon surface layer at 600°C and 650°C must be inhibiting the segregation of sulphur because, even if the sulphur was on the nickel surface under the carbon layer, an attenuated sulphur Auger peak would have been visible in the same way that the substrate nickel Auger peak was visible. Furthermore, if sulphur had been present on the surface immediately under the graphite, it would have become "visible" as soon as the graphite redissolved; this was not the case.

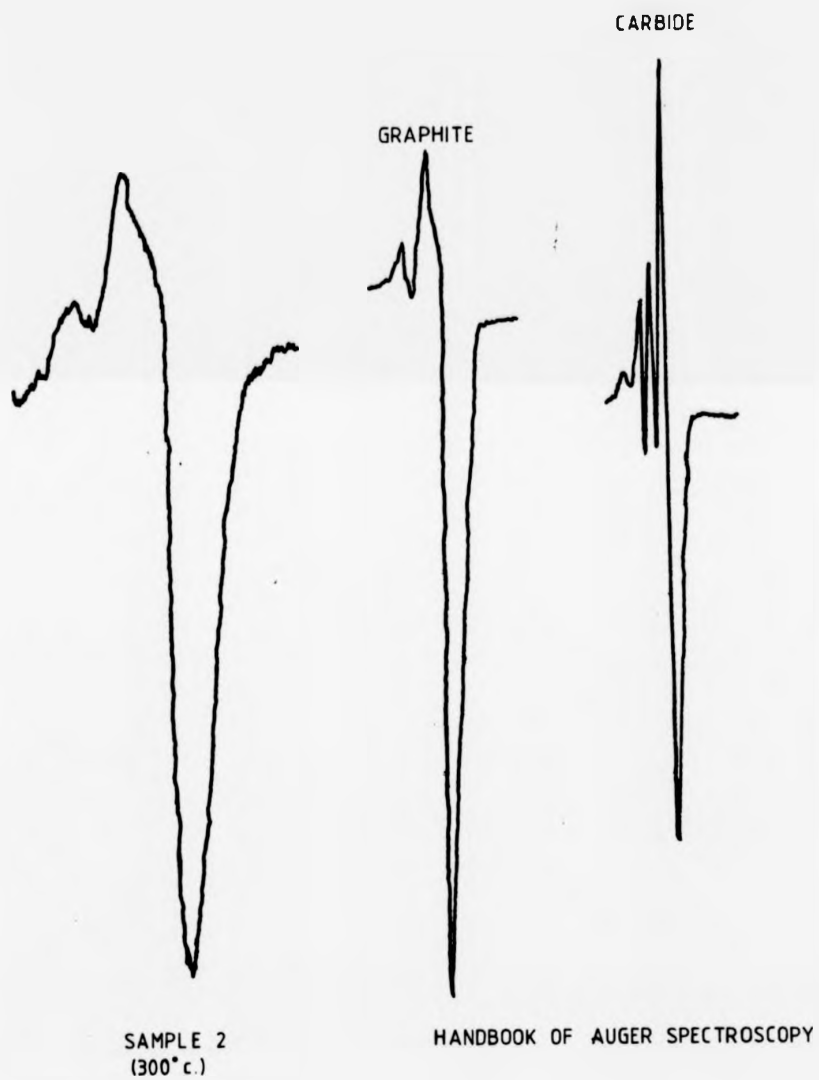


**FIG. 3.12** Carbon Auger peak from a poly-crystalline sample compared with "standard" carbon Auger spectra.

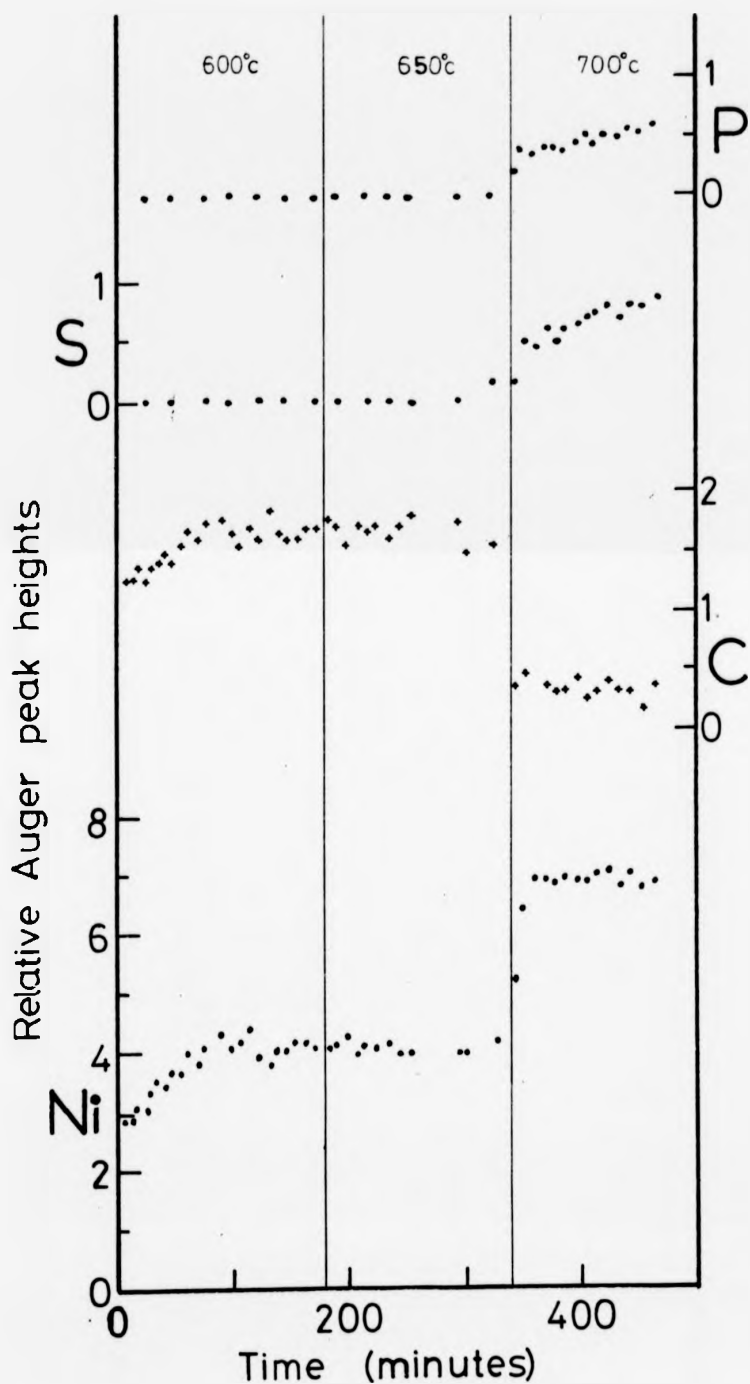


**FIG. 3.13** Relative Auger peak heights of nickel, carbon, sulphur, and phosphorus as a function of time at different temperatures in the range 600-700°C. Position 1, sample 2.

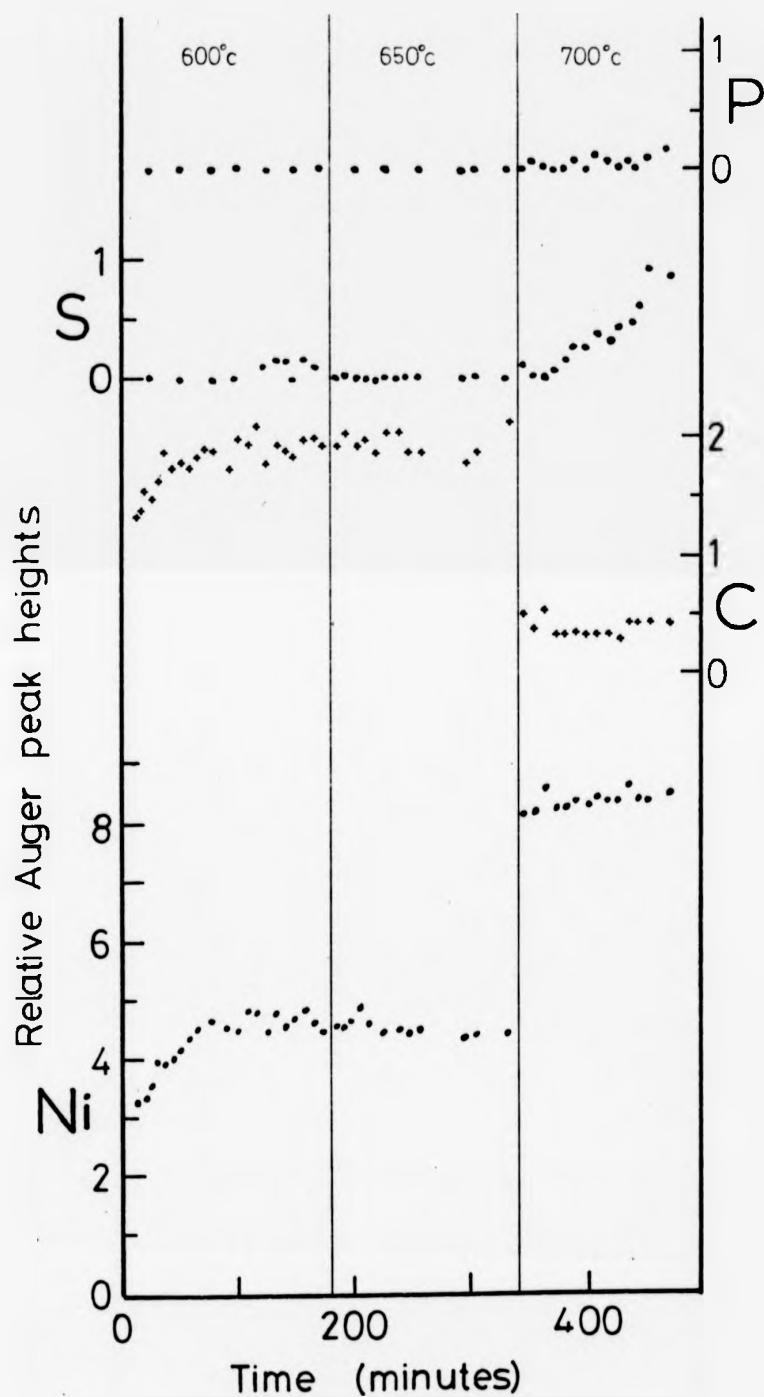


**FIG.3.14** Relative Auger peak heights of nickel, carbon, sulphur, and phosphorus as a function of time at different temperatures in the range 600-700°C. Position 2, sample 2.



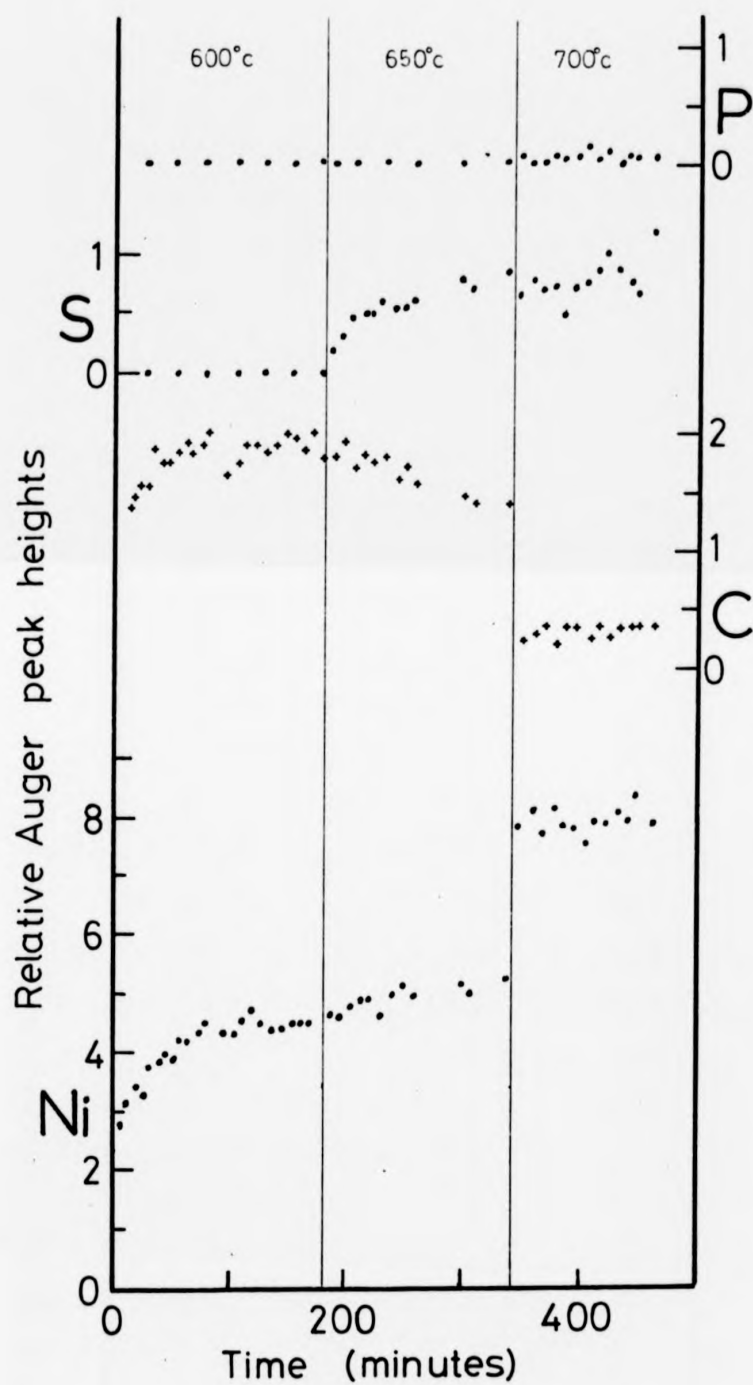


FIG.3.15

Relative Auger peak heights of nickel, carbon, sulphur, and phosphorus as a function of time at different temperatures in the range 600-700°C Position 3, sample 2.

Measurements from different grains at the same time yield slightly different results. In figure 3.14 there is almost no phosphorus detectable at 700°C. A third grain (figure 3.15) behaves in a different manner from either of the other two grains. On the surface of this grain sulphur begins to appear at 650°C while there is still a carbon layer present. As the sulphur segregates to the surface the carbon Auger peak height drops slightly. This must be due to a slight reduction in the carbon concentration at the surface, and not to the sulphur simply masking the carbon, because at the same time as the carbon Auger signal decreases, the signal from the nickel substrate increases. On the other two grains (figures 3.13 & 3.14) the carbon and nickel Auger peaks remained constant all the time the sample was at 650°C.

Sickafus<sup>14</sup> noted that, on the (110) surface of nickel, carbon was limited to regions where sulphur was not present. Carbon existed as patches of randomly oriented graphite between the sulphur domains. It is likely that this sort of behaviour was occurring on the grain surface of figure 3.15, with the sulphur domains growing at the expense of the graphite domains. Unfortunately there was no way of telling whether the Auger signals were coming from an intimate mixture of sulphur and carbon, or from quite separate sulphur and carbon domains.

The last experiment was done to see if there was any variation between grains in the temperature at which the solubility limit was exceeded. The carbon and nickel Auger peak heights were measured at seven different positions round the sample, and then the sample was heated up in steps of about 12°C. Results from each step of the experiment are shown in figures 3.16 to 3.20.

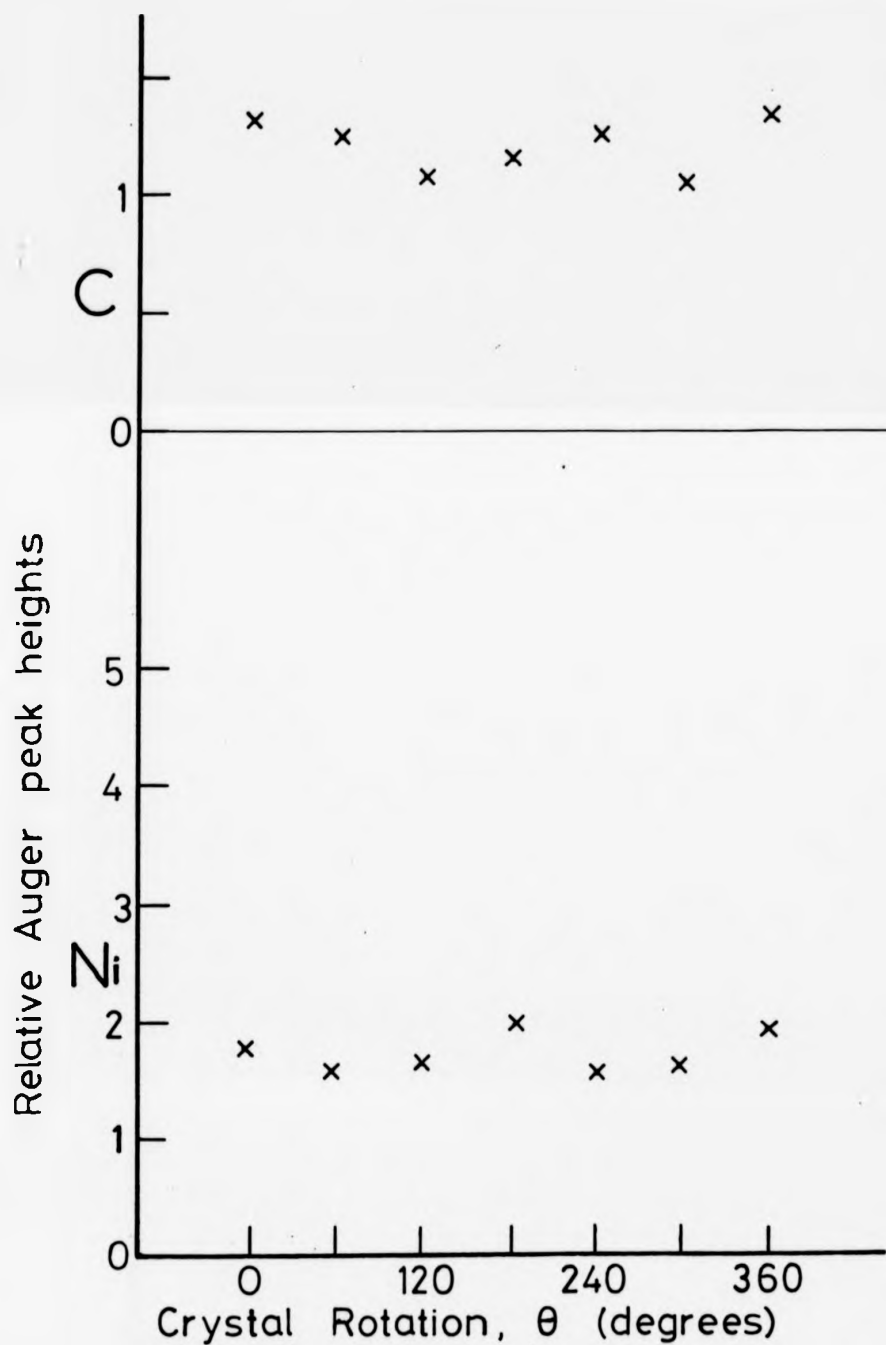


FIG.3.16

Nickel 61eV and carbon 272eV Auger peak heights at 672°C.

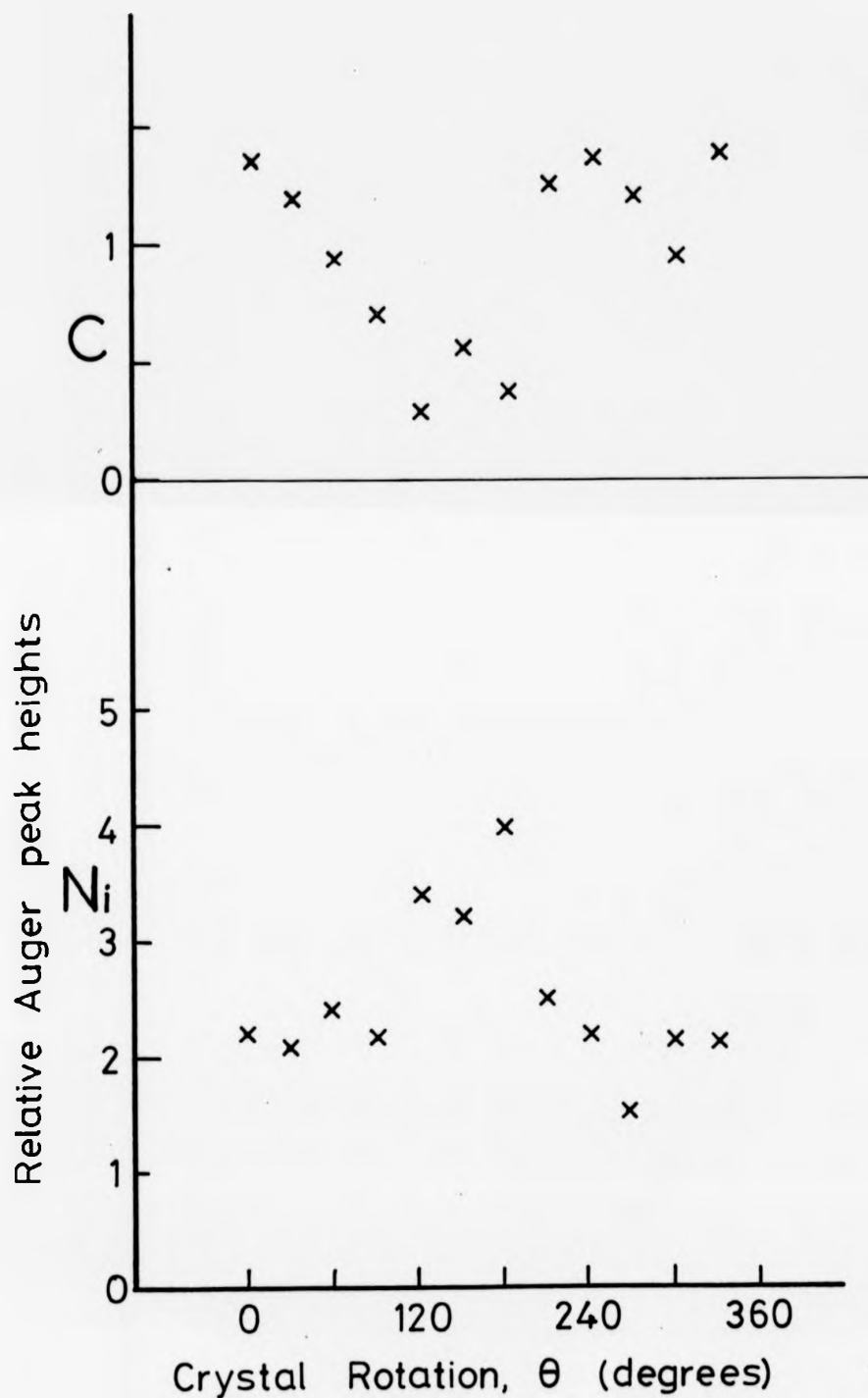


FIG. 3.17 Nickel 61eV and carbon 272eV Auger peak heights at 684°C.

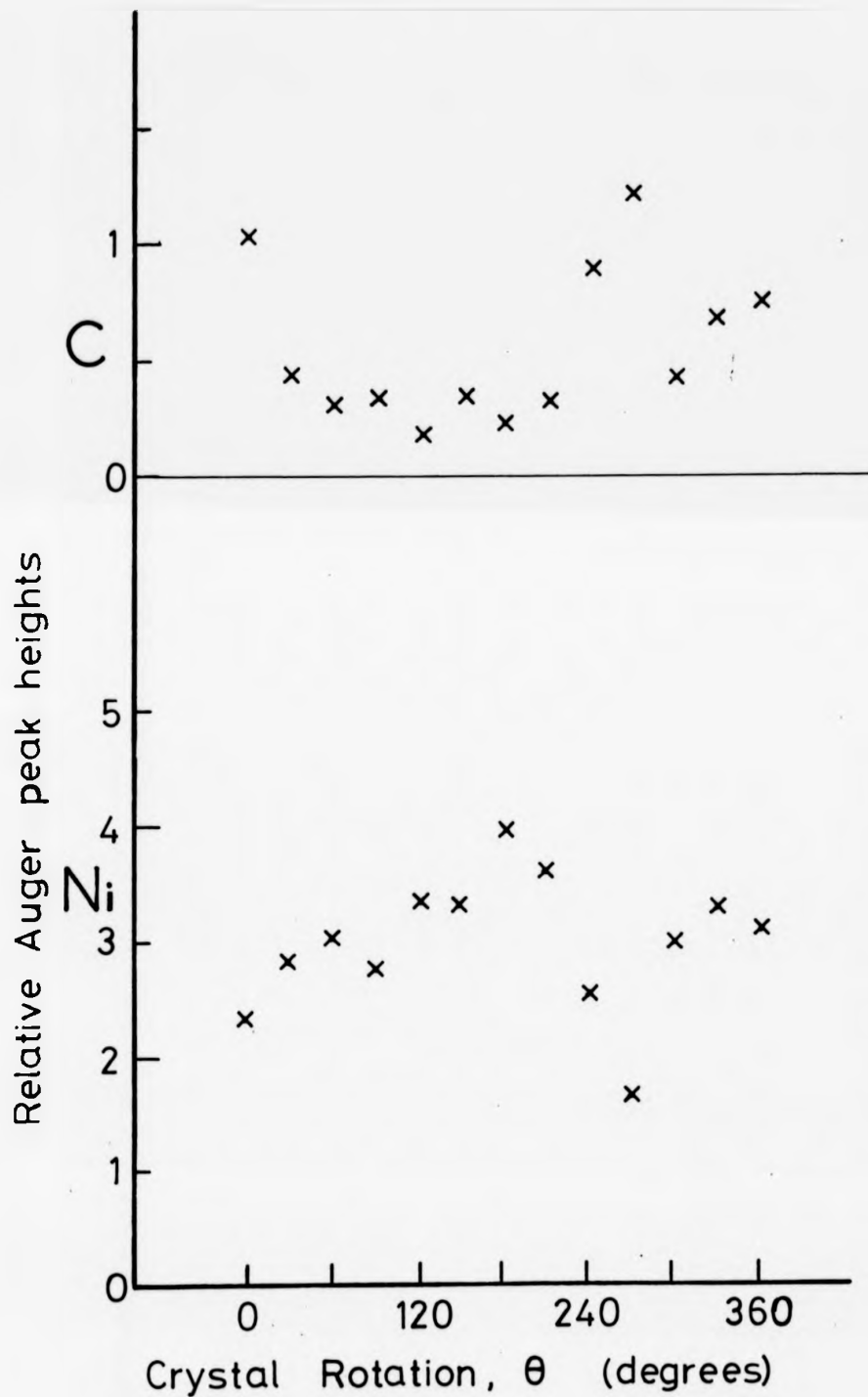


FIG. 3.18

Nickel 61eV and carbon 272eV Auger peak heights at 697°C.

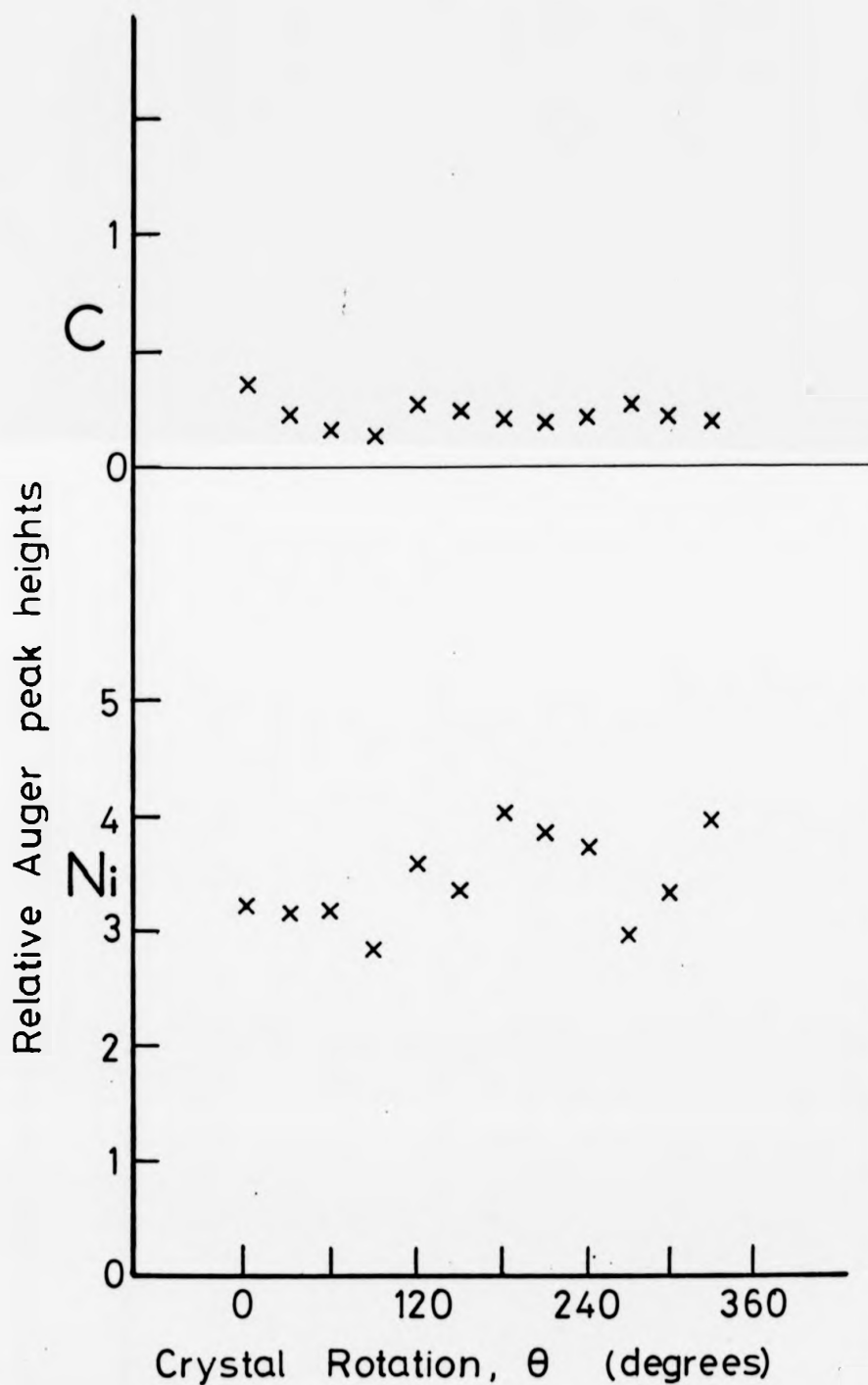


FIG. 3.19

Nickel 61eV and carbon 272eV Auger  
peak heights at 709°C

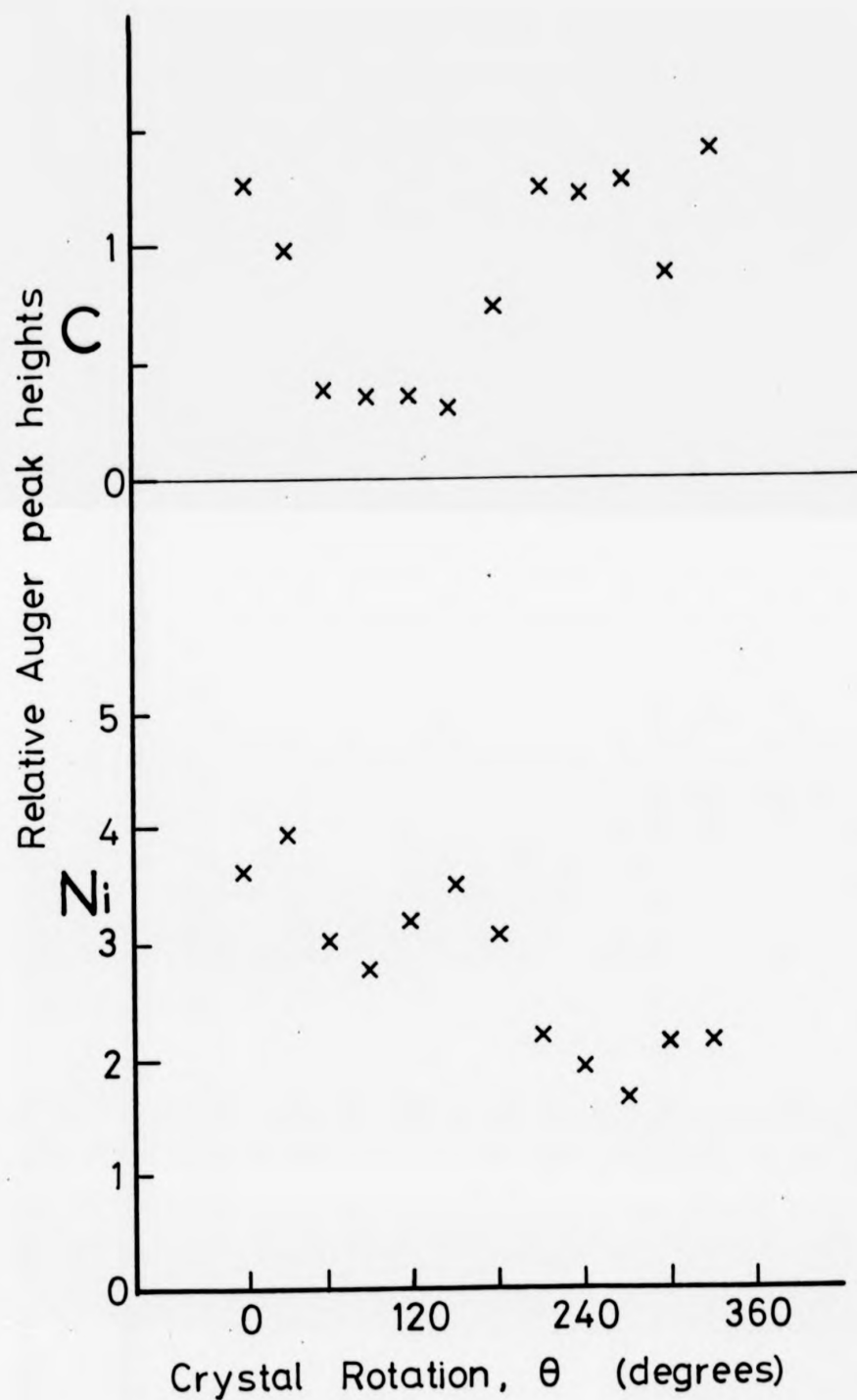


FIG. 3.20 Nickel 61eV and carbon 272eV Auger peak heights at 647°C

At 672°C (figure 3.16) all the grains were covered with carbon. At 684°C (figure 3.17) the carbon level has dropped considerably on several grains and the nickel Auger peak has increased on these grains.

At 697°C (figure 3.18) more of the grains are showing low levels of carbon; a few grains still have a high carbon level. It is not until the temperature has reached 709°C (figure 3.19) that the carbon level has dropped on all the grains.

In the final part of the experiment, the sample was cooled again until the carbon reappeared on the surface. The precipitation displayed some hysteresis; in figure 3.20 it can be seen that even when the sample had been cooled to 647°C some of the grains were still not showing the full carbon surface layer again.

The variation in the observed precipitation temperature between different grains is most probably due to variations of the concentration of carbon within these grains. It is more interesting to note the variation in the interaction between carbon and sulphur, as this may be related to the surface structure. For example, on only one out of the three grains examined (figure 3.15) did sulphur appear at the surface while there was still a high amount of carbon present on the surface.

The inability to identify precisely the surfaces involved severely limits the use to which these results can be put. Because of this, the next stage of the investigation was to use a single crystal of nickel whose surface orientation was known. Moreover the crystal that was used was hemispherical, thereby presenting surfaces of all possible orientation for examination. The advantages and disadvantages of using such a sample will become apparent in the next section of this chapter.



#### 4) Nickel hemisphere

A single crystal of nickel had been cut by J. Onuferko so that it had a hemispherical face. This had been mechanically polished and briefly electropolished. A side view of the crystal is shown in figure 3.21. A slit was spark eroded in the rear portion of the crystal so that a tungsten filament could be passed through the slit in order to heat the crystal radiatively. The crystal

was then mounted on a sample holder so that the vertical axis of rotation passed approximately through the point that was the centre to the spherical surface. By rotating the sample in front of the H.C.M.A., any part of the crystal on the circumference of the hemisphere along the line marked in figure 3.21 could be examined. Theoretically by raising or lowering the sample with respect to the analyser, any part of the hemisphere could be made available for analysis. In practice this changed the distance between the point being probed by the electron beam and the analyser; this affected the gain of the analyser. The angle of incidence of the electron beam on the crystal surface was also changed by this process.

In fact slightly less than  $180^\circ$  around the circumference of the hemisphere was available for examination because the ceramic mount holding the sample intruded between the sample and the H.C.M.A. if the sample was rotated too far off centre. This is illustrated in figure 3.22 which shows the nickel 61eV Auger peak round the crystal; note that the signal drops off sharply at the edges. A useful range of about  $120^\circ$  was available for Auger spectroscopy.

Figure 3.23 shows the result of heating the sample to  $500^\circ\text{C}$  for 15 minutes. Sulphur and carbon segregated to the surface. The sulphur peak varies slightly round the crystal. However this small

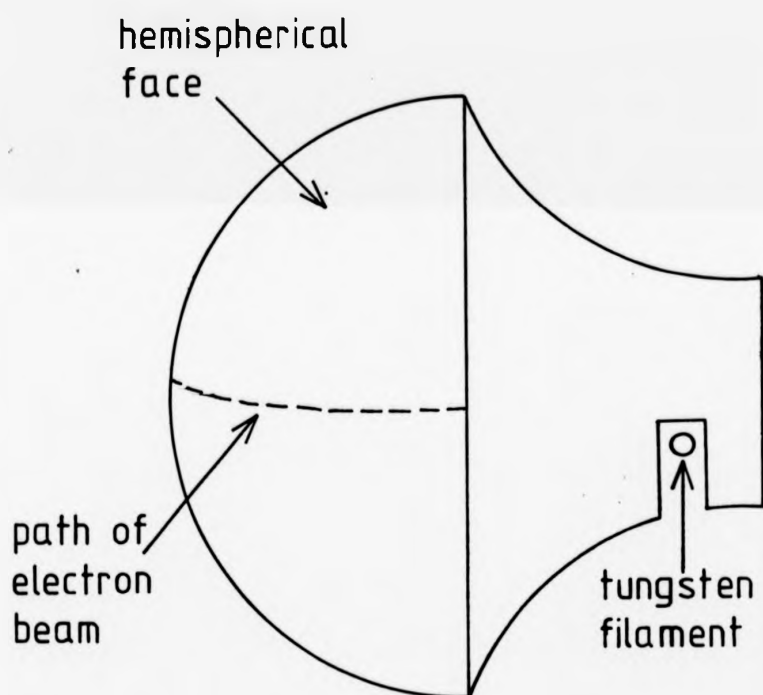


FIG. 3.21 NICKEL CRYSTAL

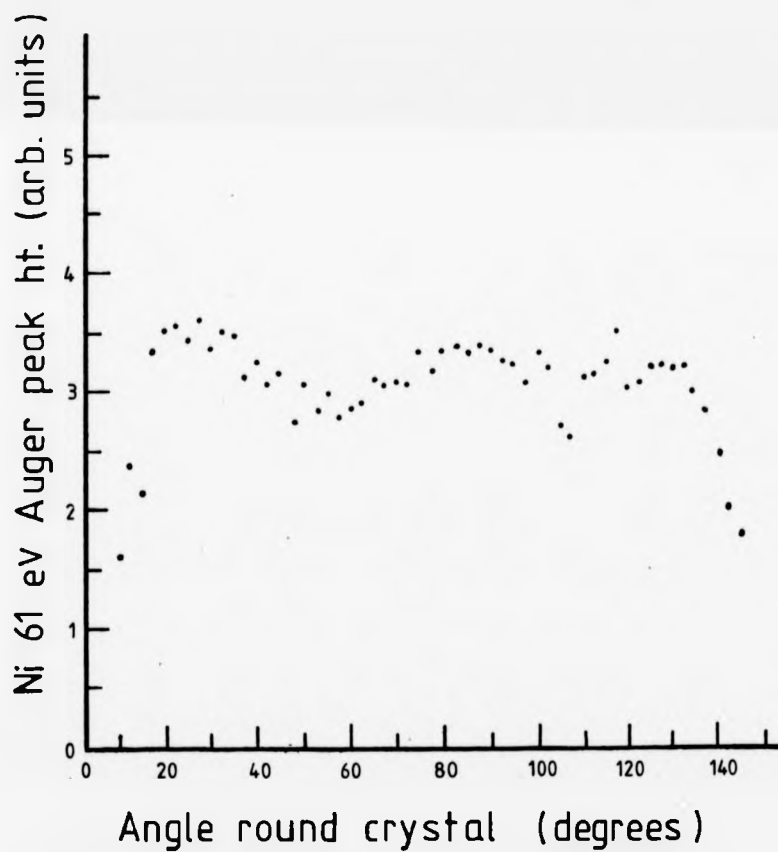


FIG.3.22 Ni 61eV Auger peak round the circumference  
of a hemispherical nickel crystal.

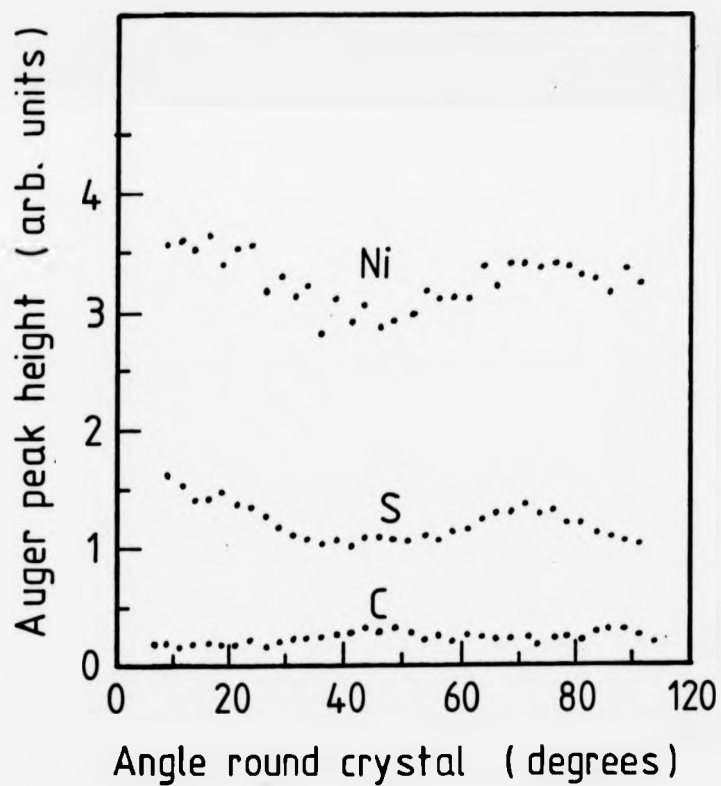


FIG. 3.23 Carbon and sulphur on the surface of the hemispherical crystal after heating to 500°C.

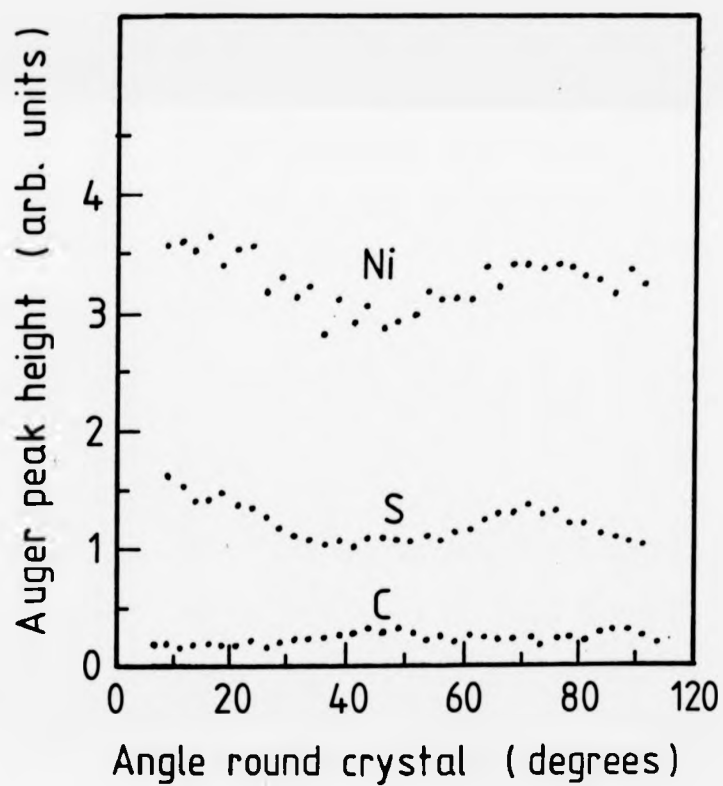


FIG. 3.23 Carbon and sulphur on the surface of the hemispherical crystal after heating to 500°C.

variation may be due to small misalignments of the axis of rotation with respect to the hemispherical face, or to incident beam diffraction effects (these will be dealt with more fully in the next chapter). This conclusion is born out by examining the ratio of the sulphur to nickel Auger peaks. Figure 3.24 is the same set of results as in figure 3.23, but now the ratio of the peaks has been plotted rather than the absolute values. There does not appear to be any large variation in the ratio of the sulphur to nickel Auger peaks around the crystal. Small fluctuations ( of the order of  $\pm 15\%$ ) are present, but may largely be due to noise.

Apart from the apparent uniformity of segregation, there is one major problem in the interpretation of the results from the hemispherical crystal. The major crystallographic axes of the crystal could be located by x-ray diffraction so that in principle the positions of the major faces on the hemispherical surface were known. But it proved to be practically impossible to locate the position of electron beam on the surface with sufficient accuracy to be able to determine the precise location in the stereographic triangle of the point being examined.

The major difficulty was with the vertical position of the beam. The hemisphere had a radius of about 6mm; so if the beam was displaced in a vertical direction by only 1mm the angle of the surface with respect to the beam changed by about  $10^\circ$ . Consequently to locate the beam on a particular face to within  $\pm 1^\circ$  required the electron beam to be positioned to within  $\pm 100\mu$ . For a fine polycrystalline sample (such as the bismuth/copper sample studied earlier) a secondary electron picture could be obtained by scanning the electron beam in a raster pattern. This produced a picture of sufficient contrast and detail to allow accurate location of the

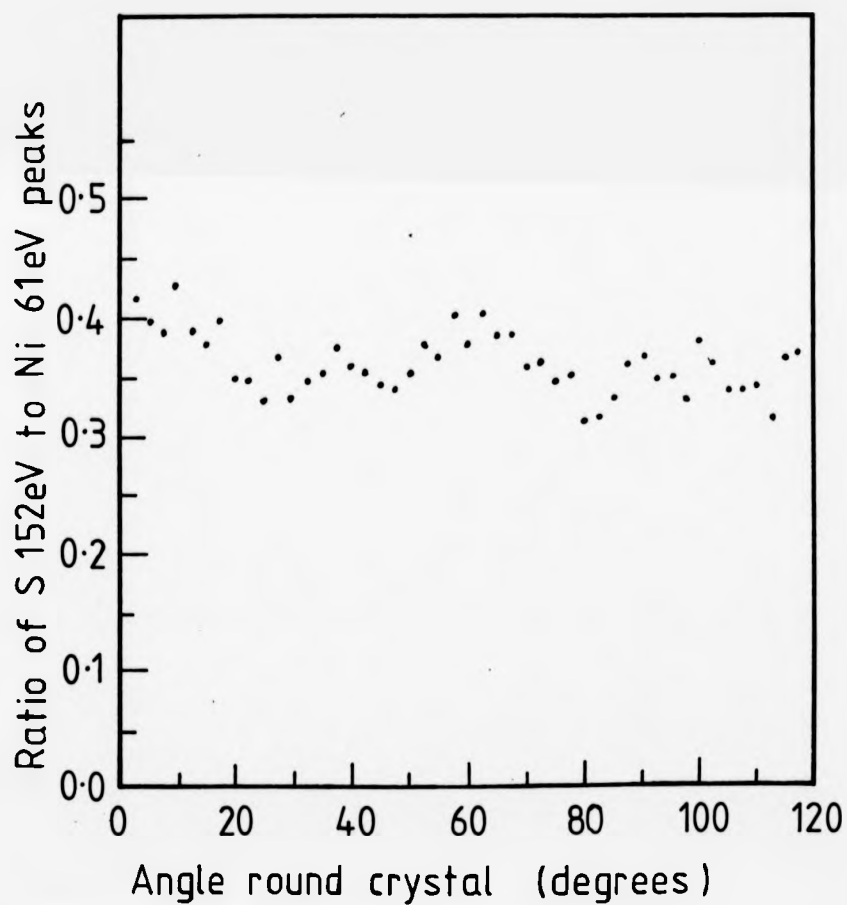


FIG.3.24 Ratio of S 152eV to Ni 61eV auger peaks  
round the hemispherical crystal.

beam with respect to, say, a particular grain. With the hemispherical crystal there was insufficient detail in the secondary electron picture to allow for such precise location of the beam.

The main advantage of using a spherical crystal, that all possible faces were available, was thus nullified by the lack of information on the precise surface orientation being studied. For the simpler system of a cylindrical crystal, positioning is only required accurately in one direction, and this can be achieved by the use of the symmetry properties of the cylinder as will be seen in the next section.



### 5) The cylinder

Two things are required of the sample. Firstly it must present a range of surface orientations for examination under identical conditions. Secondly it must be possible to determine the orientation of the surface at the point being sampled by the electron beam. All the systems described so far fail to meet one or other of these requirements.

The flat polycrystalline sample provides only a few dozen points, randomly positioned in the stereographic triangle. The cylindrical polycrystalline samples provide a larger range of orientations to study (a few dozen randomly positioned short lines on the stereographic triangle). However this is still not a large enough range of orientations to ensure that a face of relatively low Miller index is present. The hemispherical crystal provided all possible orientations (i.e. the whole of the stereographic triangle was available), but experimental limitations in the accurate positioning of the electron beam meant that precise location of the point being sampled on the stereographic triangle was not possible.

The approach adopted to overcome these problems was to use a cylindrical crystal. This limits the number of surfaces available for examination, but does have several advantages over a spherical crystal. Firstly the complete range of surfaces can be brought into the same position in front of the H.C.M.A. by a simple rotation around the cylinder axis (moving the electron beam is not necessary). Secondly the electron beam does not need to be accurately positioned in the plane parallel to the axis of rotation of the cylinder.

If a cylindrical crystal is used the location of the point being sampled at any one time is obvious from the symmetry of the results. X-ray crystallographic orientation of the cylinder is only necessary to ensure that the orientation of the rotational axis of the cylinder is known (and should preferably lie along a low index direction for simplicity). The limitation compared with a spherical crystal that only a small number of orientations are available (one zone in the stereographic triangle) can be overcome to a large extent by careful choice of the axis of the cylinder.

The cylindrical samples in this study had a  $\langle 110 \rangle$  type axis as the rotational axis of the cylinder. This type of sample has been used by Kramer et al.<sup>32</sup> for the study of oxygen adsorption on tungsten. Such a cylinder has 2mm symmetry (one mirror plane lying in the  $\langle 001 \rangle$  direction, and one lying in the  $\langle 110 \rangle$  direction). If the rotational axis is labelled  $\langle \bar{1}10 \rangle$ , then all hkl planes are present in which  $h=k$ . The three low index planes (001), (110), and (111) are all present, as are such planes as (221), (112), (113) etc.

An important property of this type of cylinder is that (provided the cylinder has no defects in it) all stepped planes consist of steps with straight edges only (i.e. they have no kinks). As a consequence the "roughness" around the cylinder depends only on the step density (and on the presence of any defects). Moreover the step density varies linearly round the cylinder, with maxima at the (110) and (113) planes and minima at the (001) and (111) planes. This system therefore provides an excellent way of studying the influence of surface structure on the reactivity of the surface.

### CHAPTER 3: REFERENCES

1. D. McLean, "Grain boundaries in Metals", Oxford, Clarendon Press (1957).
2. H. P. Stuwe & I. Jager, Acta Met. **24** (1975) 605.
3. M. Lagues & J. L. Donange, Surf. Sci. **47** (1975) 77.
4. M. P. Seah & C. Lea, Phil. Mag. **31** (1975) 627.
5. S. Hofmann & J. Erlewein, Surf. Sci. **77** (1978) 591.
6. C. Lea & M. P. Seah, Phil. Mag. **35** (1977) 213.
7. G. Rowlands & D. P. Woodruff, Phil. Mag. **40** (1979) 459.
8. E. Voce & A. P. C. Hallows, J. Inst. Metals **73** (1947) 323.
9. E. D. Hondros & D. McLean, Phil. Mag. **29** (1974) 771.
10. A. Joshi & D. F. Stein, J. Inst. Metals **99** (1971) 178.
11. B. D. Powell & H. Lykura, Acta Met. **21** (1973) 1151.
12. B. D. Powell & D. P. Woodruff, Phil. Mag. **34** (1976) 169.
13. M. P. Seah & E. D. Hondros, Proc. Roy. Soc. A **335** (1973) 191.
14. E. N. Sickafus, Surf. Sci. **19** (1970) 181.
15. R. Riwan, Surf. Sci. **27** (1971) 267.
16. J. P. Coad & J. C. Riviere, Proc. Roy. Soc. Lond. A **331** (1972) 403.
17. C. L. White, Ph.D. Thesis, Michigan Technological University (1974).
18. S. Broz, C. Koziol & J. Kolczkiewicz, Vacuum **26** (2) (1976) 61.
19. J. F. Mojica & L. L. Levenson, Surf. Sci. **59** (1976) 447.
20. O. L. J. Gijzeman, F. C. Schouten & G. A. Bootsma, Surf. Sci. **71** (1978) 174.
21. J. C. Shelton, H. R. Patil & J. M. Blakely, Surf. Sci. **43** (1974) 493.
22. L. C. Isett & J. M. Blakely, Surf. Sci. **47** (1975) 645.
23. L. C. Isett & J. M. Blakely, Surf. Sci. **58** (1976) 397.
24. J. M. Blakely. Paper presented at 3rd Internat. Summer Inst. in Surf. Sci., University of Wisconsin, Milwaukee, August (1977).
25. H. V. Thapliyal & J. M. Blakely, J. Vac. Sci. Technol **15**(2) (1978), 600

26. J. I. Blakely & H. V. Thapliyal. Paper presented at A.S.I. symposium on Interfacial Segregation, Chicago, October (1977).
27. M. Eizenberg & J. I. Blakely, Surf. Sci. **82** (1979) 228.
28. J. J. Lander, H. E. Kern & A. L. Beach, J. Appl. Phys. **23** (1952) 1305.
29. "Handbook of Auger Electron Spectroscopy", 2nd Edn., Physical Electronics Industries Inc., Minnesota (1976).
30. K. R. Jones, Ph.D Thesis, University of Warwick (1982).
31. I. Pfeiffer, Z. Metallk. **46** (1955) 516.
32. H. M. Kramer, E. Langer & E. Bauer, Proc. 4th Internat. Conf. Solid Surfaces and 3rd ECOSS, Cannes (1980), "Le Vide, Les Couches Minces", 1, 217.

## CHAPTER 4 : X-RAY SCATTERING AND CRYSTAL MOUNTING

### 4.1 Cylindrical system

The segregation studies (chapter 3) have highlighted the problems involved in using polycrystalline samples and the suitability of using single crystals cut to include a range of faces. However the experimental difficulties of using a hemi-spherical crystal outweigh the advantage of using a crystal with all possible surface orientations. The compromise adopted, i.e. using a cylindrical crystal, has many practical advantages that make up for the smaller range of faces compared with a hemisphere.

The first advantage is that mounting the crystal is comparatively simple. If the cylinder is mounted so that it can rotate about its major axis, then all the faces present on the cylinder can be brought in front of the H.C.M.A. by a simple rotation. The second advantage is that because the surface orientation of the crystal is the same along a line on the cylinder surface parallel to the major cylinder axis, there is no need to align the electron beam accurately in this direction. In fact it is a useful experimental check to be able to duplicate readings simply by taking measurements from different heights up and down the cylinder. This was done, not by moving the electron beam up and down the crystal, but by raising or lowering the crystal in front of the beam. This ensured that the point of analysis never shifted with respect to the H.C.M.A. Using this method, reproducible readings could be obtained over a range of typically 5 to 8mm up and down the 12mm long cylinder.

The structural and symmetry properties of the samples used are relevant and will now be discussed. All the cylinders were cut so that the cylindrical axis was parallel to a  $\langle 110 \rangle$  type axis. The cylinder is shown in cross-section in fig.4.1 with the labeling

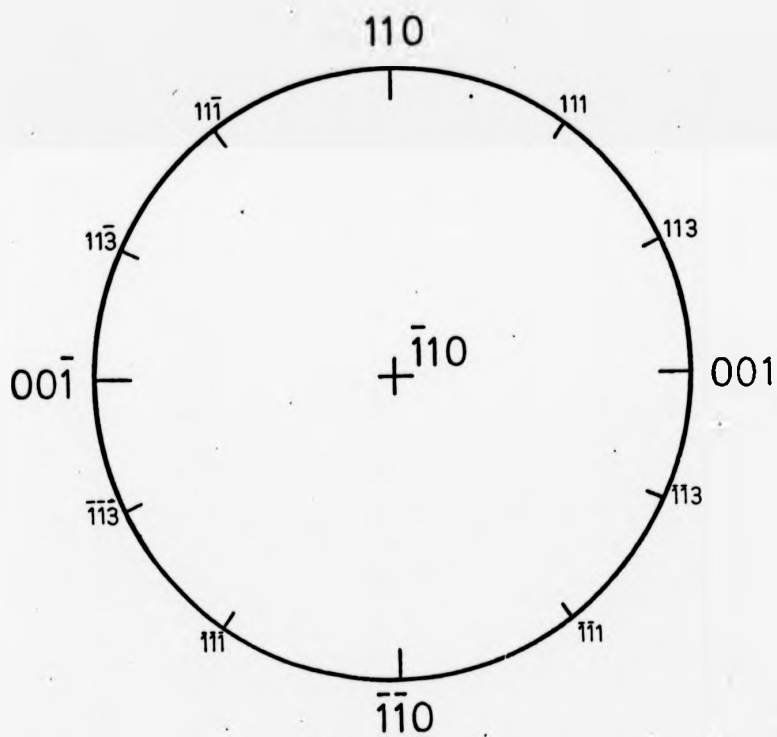


FIG.4.1 The faces present on the cylindrical crystals.

of axis chosen such that the cylinder axis is in the  $[110]$  direction. It can be seen that all the  $hkl$  planes for which  $h=k$  are present. In particular  $(001)$ ,  $(110)$ ,  $(111)$  and  $(11\bar{3})$  planes are present. The cylinder has  $2mm$  symmetry so that there are two of each of the faces forming mirror planes (that is there are two  $(001)$  and two  $(110)$  type planes) whereas there are four each of the other types of planes.

A perfect cylinder cut in this fashion has unique structural properties at the surfaces. Firstly, if there are no defects, there are only a limited number of types of surface site exposed. In particular there are no sites exposed where an adsorbate atom can possess six or more nearest neighbour substrate atoms. There are only 6 possible sites, apart from those involving 1 or 2 nearest neighbour atoms, and these are illustrated in fig.4.2. Note that these sites are represented on four key faces  $((111), (100), (110)$  and  $(311))$ . The importance of these four faces will soon become apparent.

The next property of this type of cylinder is that all the steps are straight, i.e. with no kinks. Furthermore the edges of these steps are aligned parallel with the cylinder axis (that is in the  $[110]$  direction using the notation of fig.4.1.). An example of a typical face on the surface of this cylinder is the  $(221)$  face shown in plan and cross-section in fig.4.3. This face has steps with large flat areas of a  $\{11\}$  type of arrangement of atoms. The atoms at the edge of each step (shown in a bold line in fig.4.3) are coordinated to 7 other substrate atoms and we refer to these as  $C_7$  atoms. They have five nearest neighbour bonds broken and have the lowest coordination of any atoms in faces in the  $\langle 110 \rangle$  zone. An important point is that any step in a face in this zone has  $C_7$  atoms at the edge of each step. Therefore the  $C_7$  atom density around this zone is equivalent to the step density. Fig.4.4 is a plot of the  $C_7$  atom density around the symmetrically inequivalent  $90^\circ$  of this zone. The points correspond to the following faces:-

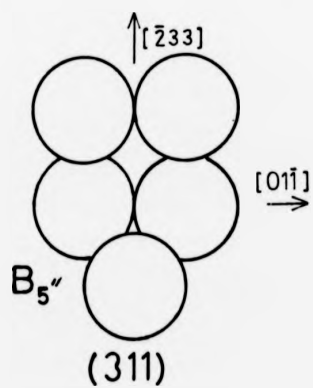
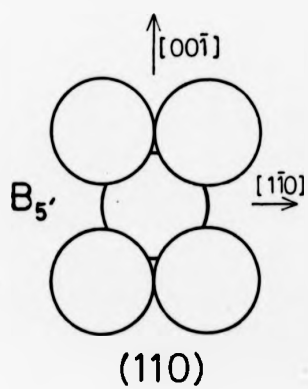
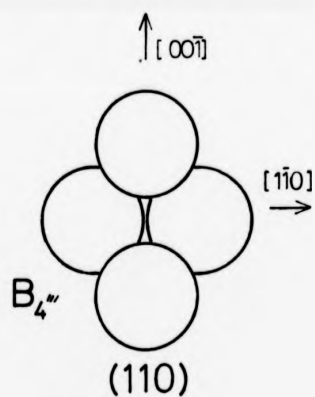
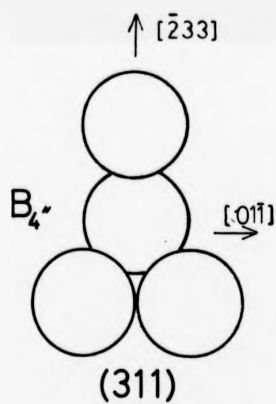
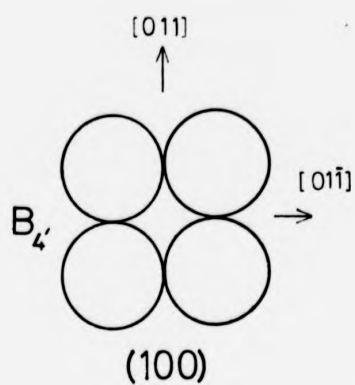
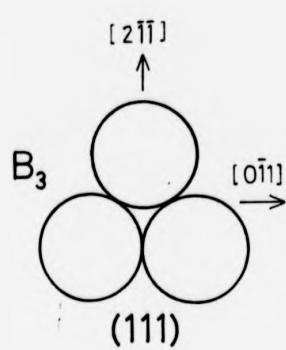


FIG. 4.2 The six possible sites of coordination 3 or higher.



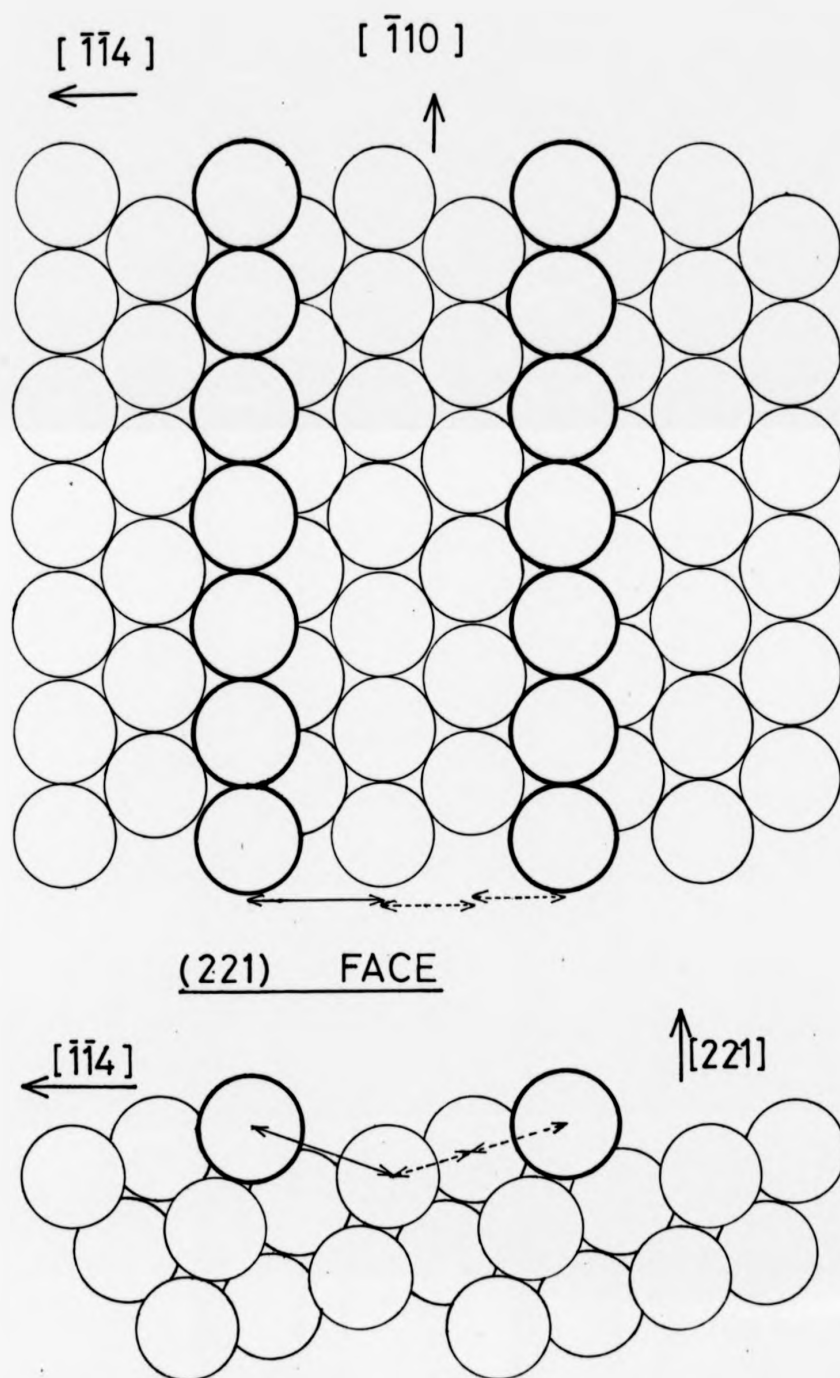


FIG. 4.3 A typical face in the  $\langle 110 \rangle$  zone

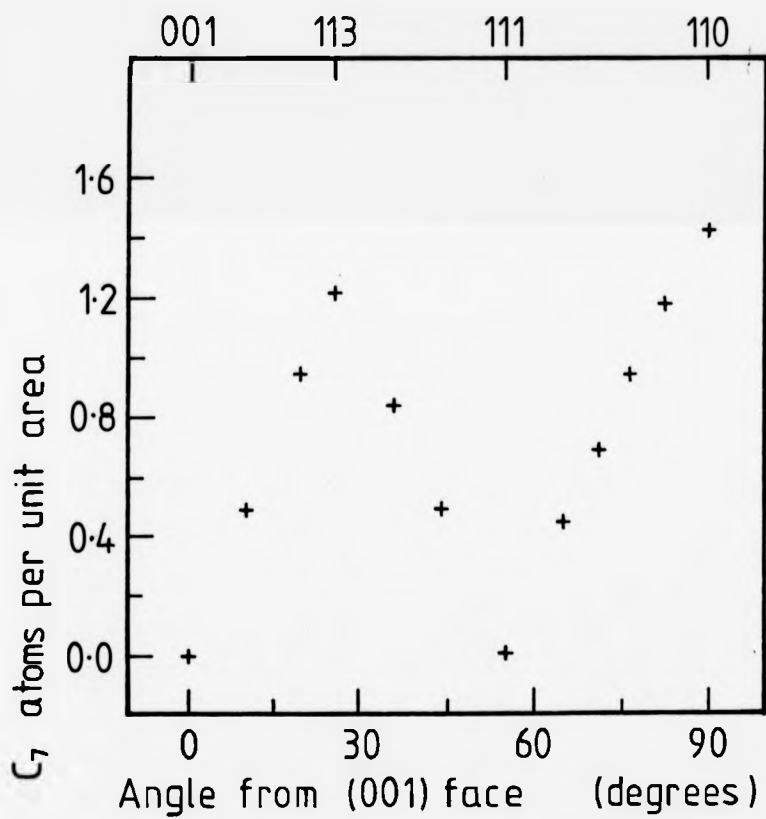


FIG.4.4 Plot of the  $C_7$  site density in the  $\langle 110 \rangle$  zone

(001)(118)(114)(113)(112)(223)(111)(332)(221)(331)(661)(110).

There are maxima at (110) and (113), and minima at (001) and (111). This leads to the idea of classifying the surfaces as smooth ((001) and (111)) or rough ((110) and (113)). Intermediate faces can then be thought of as consisting of flat (001) or (111) terraces with rough (110) or (113) steps. These four key faces are shown in fig.4.5.

This can be put on a quantitative basis as follows. Because any face in this zone consists of rows of neighbouring atoms parallel to the  $[110]$  direction (see fig.4.5 for example), an arbitrary face can be split into sections parallel to the  $[110]$  direction. For example, the unit mesh of the (221) face in fig.4.3 contains one unit of a stepped  $\{110\}$  type (shown by the solid arrows) and two units of a flat  $\{111\}$  type (shown by the broken arrows). The repeat distance between the rows of atoms in the (110) sections and the (111) sections can be calculated, and for any arbitrary face the proportion of "flat" and "rough" face present has been taken as being the ratio of  $N_f D_f : N_r D_r$ , where  $N_f$  is the number of flat type repeat units and  $D_f$  is the distance between the centres of the atoms in the flat type plane. Similarly  $N_r$  is the number of rough type repeat units and  $D_r$  is the distance between the centres of the atoms in the rough type plane. The proportion of these faces has been plotted in fig.4.6 for 17 faces round the zone.

This idea of splitting an arbitrary face into a proportion of smooth and rough surface will be used repeatedly. The usefulness of the model as a basis for explaining the adsorption of oxygen on copper (chapter 5) depends on the fact that most adsorption occurs at sites with 3 or more nearest neighbour atoms. Therefore an arbitrary boundary down a line of the centres of the atoms on top of a ridge on a rough plane does not split any sites of 3 or higher coordin-

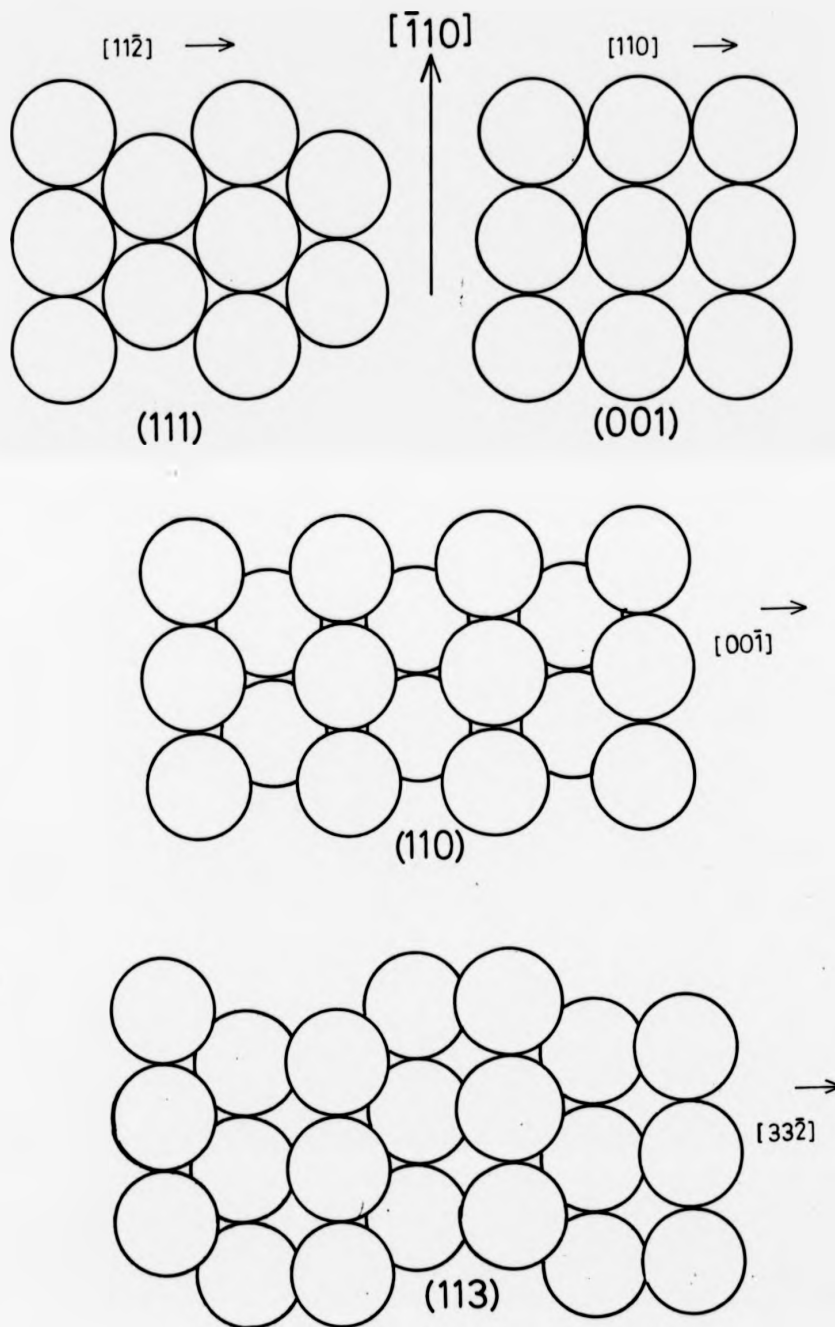


**FIG.4.5** The four key faces in the  $\langle 110 \rangle$  zone.

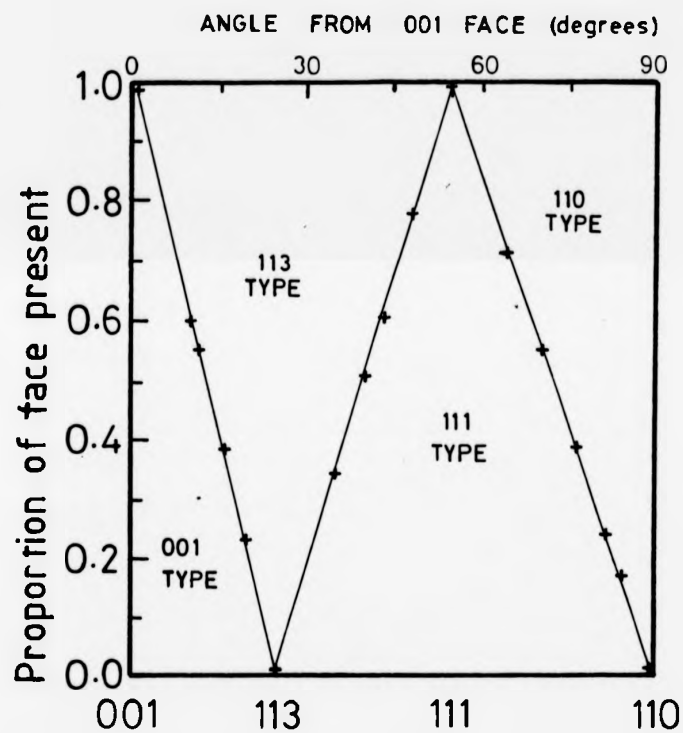


FIG. 4.6 The proportion of the four key faces present.

ation. This would not be true if any of the sites were kinked. Thus the advantage of using a cylinder with faces in the  $\langle 110 \rangle$  zone containing only simple straight steps becomes apparent.

The mounting of the cylinder in the U.H.V. system was simpler than for the hemispherical crystals, however some problems remain. Distortions were introduced by inaccuracies in the mounting, and, as well as this, there were strong effects caused by diffraction of the incident electron beam. These problems will be considered in the rest of this chapter.

#### 4.2 : ELECTRON CHANNELLING EFFECTS

One problem encountered in the quantification of A.E.S. is that of angular effects in the stimulation of emission, or in the collection of electrons. The acceptance angle of the H.C.M.A. used in this study was large enough to average out most of the fine angular structure that is known to occur in the emitted Auger electron spectrum<sup>1-9</sup>. However crystallographic effects associated with the incident beam<sup>10-14</sup>, played a large part in this study and their influence in the determination of adsorbate concentration from A.E.S. requires consideration.

The majority of experiments in this study were carried out by rotating the crystal in front of the electron beam and analyser assembly. This led to the diffraction of the incident electron beam, which in turn affected the emitted electron spectrum, as can be seen in figure 4.7.

Diffraction of the incident electron beam showed up in many ways (e.g. variations in the Auger signal and in the elastically reflected electron peak). As expected these variations clearly show the 2mm point group symmetry about the  $\langle 110 \rangle$  type axis of the cylindrical crystals. Because of this, results usually are presented only for an angular range slightly larger than the

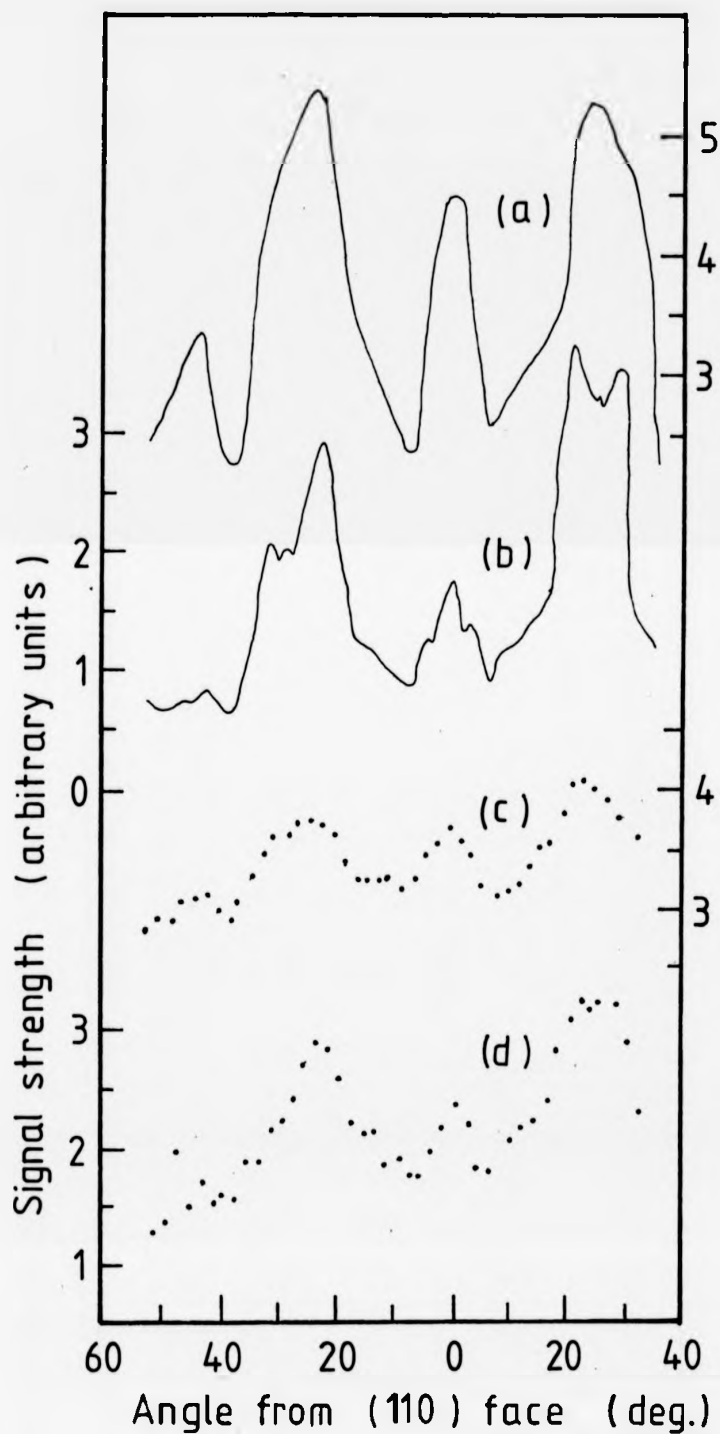


**FIG. 4.7** Variation round the crystal of: (a) the crystal current, (b) the elastic peak, (c) Cu 60eV Auger peak, (d) 920eV Auger peak.

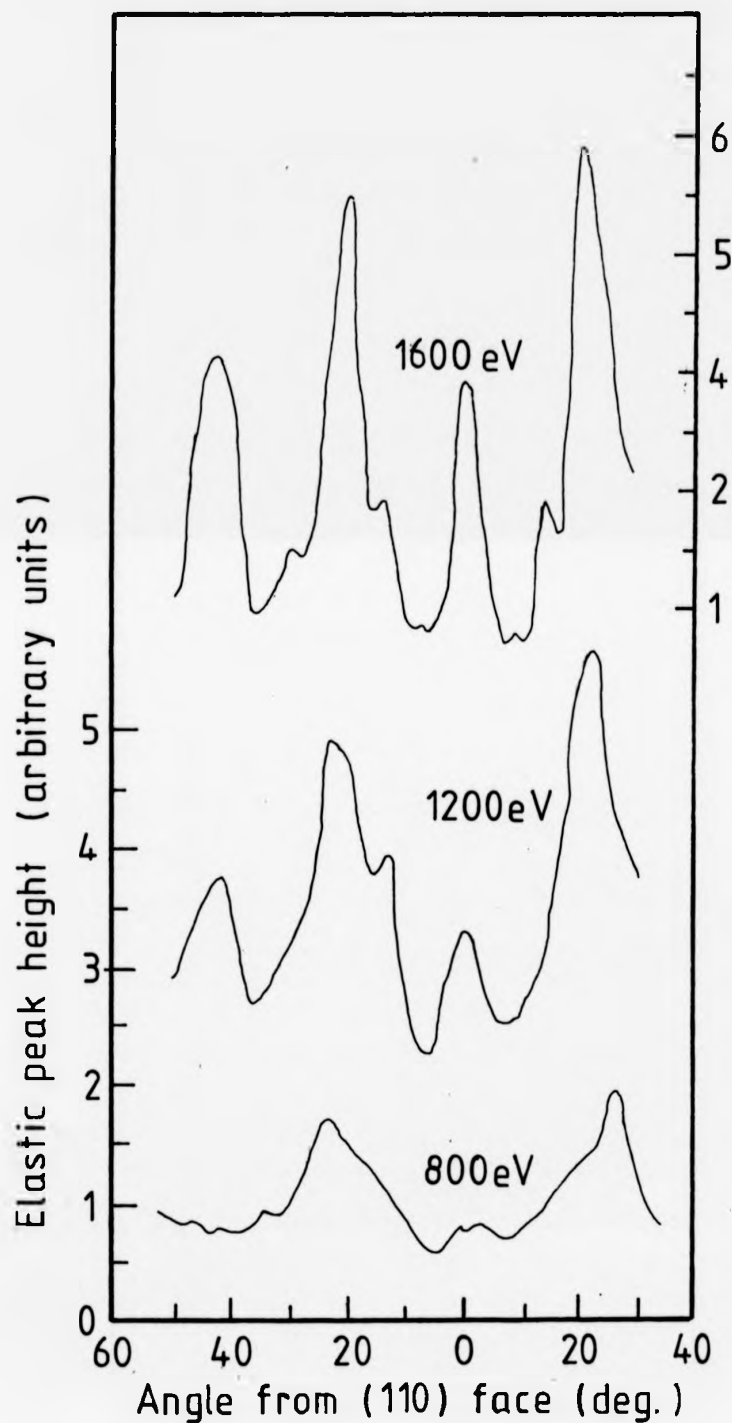
90° of symmetrically inequivalent rotation.

Figure 4.7 shows results from the clean crystal for the peak-to-peak differentiated Auger electron signal from the two principle Cu emissions at 60eV ( $M_{2,3}VV$ ) and at 920eV ( $L_{VV}$ ). These spectra were taken using an incident electron energy of 1500eV. They also show the elastically scattered signal and the total crystal current (i.e. the total secondary electron yield less the incident current).

All signals vary strongly with crystal orientation. They display essentially the same angular structure, but there are some differences in the fine structure (especially for the elastically scattered flux). The fact that these structures are essentially independent of the emitted electron energy suggests that this effect stems from the direction of the incident electron beam and is associated with channelling or "inverse Kikuchi" effects leading to variations in the electron flux seen by surface atoms. Other studies on flat crystal faces in which the incidence (azimuthal) angle was varied<sup>10,11,13</sup> support this conclusion. This is further supported by the weak but definite influence the energy of the incident electrons has on these patterns for the elastically scattered flux (fig.4.8).

The relationship of the (quasi-elastic) Kikuchi pattern<sup>15</sup> with the observed intensity variations of the entire secondary electron pattern (remembering that the H.C.M.A. will have "averaged" out angular emission effects) can be understood on the basis of the reciprocity theorem by the following argument<sup>16</sup>: If an electron from a hypothetical internal source diffracts to give a relative minimum (or maximum) field intensity for a particular direction out of the crystal, then, using this orientation for the incident beam direction will result in diffraction of the incident electrons within the crystal to give a minimum (or maximum) field intensity at the internal source. If this hypothetical source





**FIG. 4.8** Variation in the elastic peak height round the crystal for three different incident beam energies.

is actually an atom, then the probability of  $\epsilon_A$  excitation of the source will vary with the field intensity i.e. the  $\epsilon_A$  excitation of the internal source depends on the incident beam geometry as determined by the Brillouin zone diagram. Once excited, the source will emit elastic and inelastic secondary electrons. Thus the variation of the total secondary electron emission is determined by the intensity variation of the Kikuchi pattern. Effects caused by variation of the incident beam direction were first seen with an electron microscope by D.G.Coates<sup>17</sup> and are so often referred to as Coates-Kikuchi patterns (or electron beam channelling patterns),

Where the Kikuchi features are closely spaced the total secondary electron emission is found to be sharply attenuated<sup>18</sup>. This is because the intersection of several Kikuchi lines corresponds to the  $\epsilon_A$  excitation of simultaneous diffracted beams which at moderately high energies (several hundred eV or above) are in the forward direction resulting in a greater penetration of the beam into the bulk. This results in a reduced escape probability for the secondary electrons.

Above several hundred eV poles appear in the Brillouin zone diagram<sup>16</sup> corresponding to directions in which no Brillouin zone boundary exists. The position of the poles is independent of the electron energy and corresponds to some low-index direction in the crystal. This can be observed in fig.4.8 where there is a maximum corresponding at all energies to the (110) face. It can be seen that although the position of the (110) maximum remains constant, the maxima on either side change their angular position as the beam energy changes. (the maxima are at approximately  $20^\circ$ ,  $22^\circ$ , and  $25^\circ$  from the (110) direction at 1600, 1200 and 1800 eV respectively).

We have already seen that the Auger signal varies in approximately the same manner as the secondary electron current (fig.4.7).

Evidently these large variations in Auger electron emission as a function of electron incidence direction are potentially disturbing to attempts to quantify surface compositions by A.E.S.; on the other hand the clean surface of an element is not a relevant test of this problem for in the absence of other species the composition is not in doubt and quantitative studies in A.E.S. do not rely on absolute yields. Moreover, as the effects have been shown to be associated with the relatively high incident electron energies and the features correlate with bulk crystal directions, we might suppose that these angular effects would be much less important for the Auger electron yield from a species localised in, or on, the surface, because elastic backscattering is low at these energies. Evidence providing some support for this view has been provided by Chang<sup>14</sup> who noted that while strong angular effects of the type we show here were seen for Auger electron emission from a Si (111) substrate, the Auger peaks from a 10Å amorphous oxide on this surface showed no observable angular dependence. However, in figure 4.9 the orientation dependence of the oxygen KVV Auger electron emission at 520eV from the copper surface after high oxygen exposure (10,000L) is compared with the Cu substrate low energy  $M_{2,3}$  VV emission from both clean and oxygen saturated surfaces. At lower exposures of oxygen very much larger variations in the oxygen Auger electron yield were seen which are clearly attributable to real coverage variations with surface orientation; these coverage variations are the information that is sought in this investigation, the diffraction effects constituting an unwanted signal. At saturation coverage the remaining angular variations appear to show the same structure as the substrate Auger electron emission indicating that the actual oxygen coverage at these exposures is essentially independent of orientation. Nevertheless, the data of fig.4.9 do show angular variations

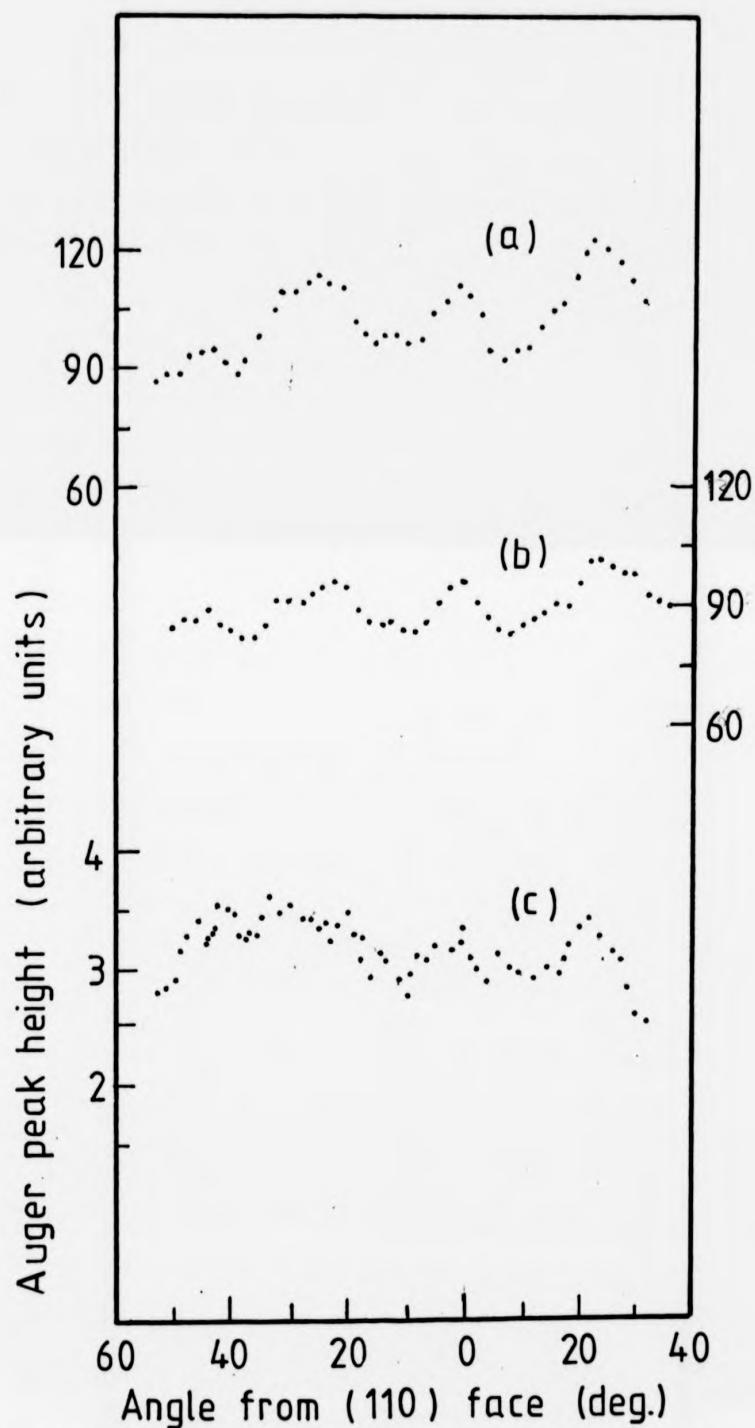
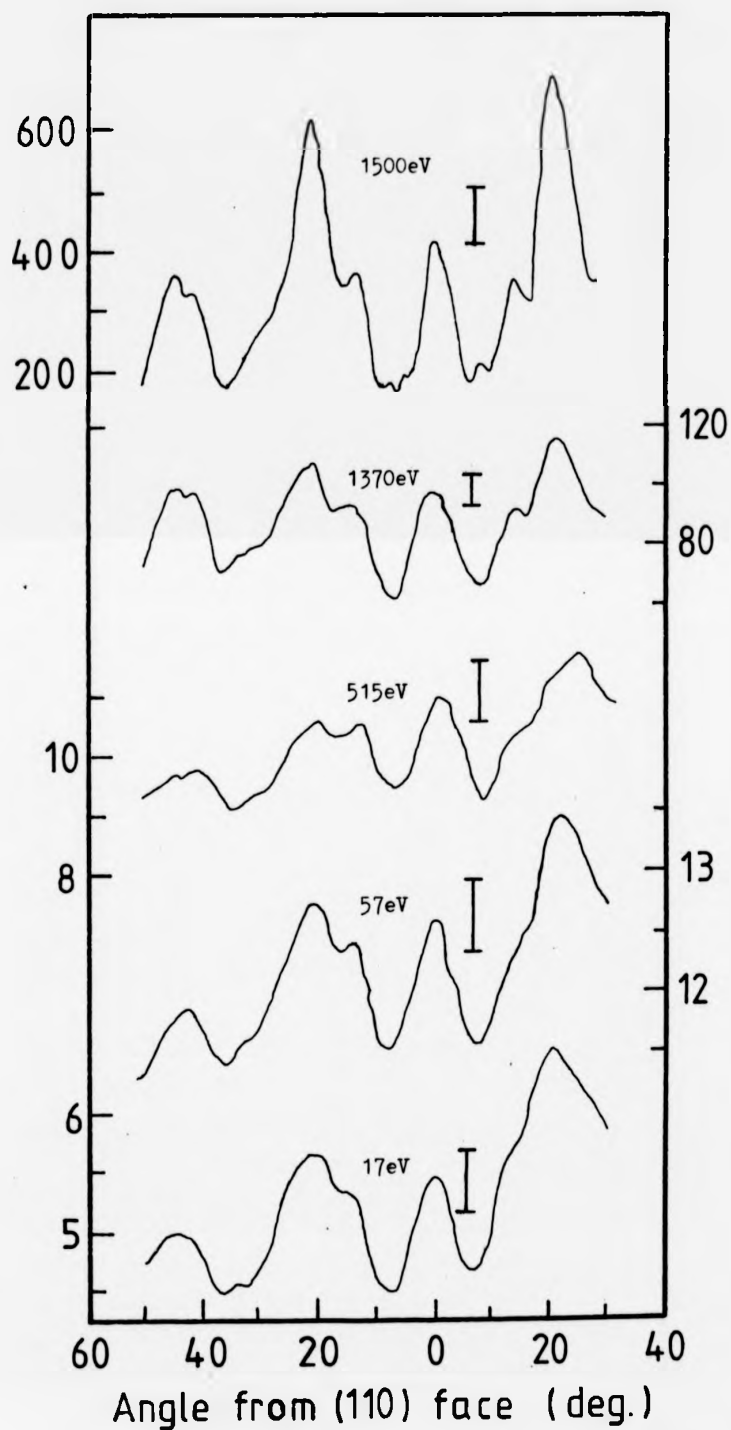


FIG. 4.9 Variations in the Cu Auger peaks round the crystal:  
 (a) 60eV, clean surface, (b) 60eV after  $10^4$  L of  $O_2$ , (c) 520eV  
 after  $10^4$  L of  $O_2$ .

somewhat larger than the low energy copper Auger emission for this oxygen-covered surface. We see, therefore, that the anisotropy is not restricted to subsurface or "bulk" effects. Of course, at very high oxygen exposures we cannot exclude the possibility that not all the oxygen is absorbed above or within the top copper atom layer of the surface; indeed for the (100) surface there is evidence that at saturation coverage some oxygen incorporation does occur<sup>19,20</sup> but this seems to be a marginal effect at room temperature and low oxygen pressures. X-ray photoelectron spectroscopy studies indicate the need for high partial pressures of several torr to produce true CuO oxide formation.<sup>21</sup>

While a large anisotropy of an adsorbate emission seems surprising, it appears to be in keeping with the systematic behaviour of all aspects of the secondary emission spectrum if we remember that the adsorbate species Auger emission in this case occurs at a higher energy than that of the substrate we have chosen for comparison. Fig.4.7 shows that when comparing the two Cu Auger emission peaks and the elastically scattered peak the anisotropy decreases with decreasing energy. Moreover, this trend is seen in the overall background secondary electron emission itself as seen in fig.4.10 which shows selected energies of emission from the clean surface using 1500eV incident electrons. The vertical bars in each graph correspond to a 10% variation and thus aid comparisons of the different scales. This trend for the secondary electrons is not unexpected as the anisotropy appears to result from elastic scattering effects in the primary beam, and the lower the emitted energy, the greater the energy losses and directional scrambling that can be expected. This is consistent with the observation<sup>22</sup> that Kikuchi-Coates patterns are most easily observed (have the greatest contrast) when only high-energy back-scattered electrons are collected. note that the Auger emissions ( fig 4.7) show stronger anisotropy than the background



**FIG. 4.10** Secondary electron signal as a function of crystal rotation for different kinetic energies of emission.

at a similar energy, presumably because these emissions are stimulated by ionisation involving more energetic (and thus more anisotropic) electrons. In this respect, despite the fact that the oxygen is likely to be situated predominantly in the top atomic layer of the surface, the Auger emissions (fig.4.9) for oxygen show a similarly enhanced anisotropy relative to that of the adjacent background (fig.4.10).

Evidently these substantial variations in adsorbate or impurity species Auger electron yield could lead to significant errors in the determination of surface composition.. While absolute coverages in A.E.S. are rarely claimed to be substantially more precise than the size of the variations (approx. 30%) observed in the data of fig.4.9, these effects could be important in the comparisons of adsorption or segregation behaviour on different crystal surfaces either through independent studies of separate crystals, through studies of curved surfaces or in scanning Auger electron microscopy of polycrystalline samples. In the latter case, at least, attempts have been made to take some account of the effects of variations of incident angle on a rough surface (e.g. a fractured surface) by normalising to a substrate Auger electron emission<sup>23</sup> or to the background secondary electron emission at an adjacent energy<sup>24</sup>. These procedures are designed to cope primarily with the  $\sec \theta$  type of dependence on incidence angle  $\theta$  which is unrelated to crystallographic effects. However, both methods will evidently take some account of the observed crystallographic effects in that the form, but not the magnitude, of these effects is largely independent of the energy of character of the emission. These results indicate that normalisation using substrate Auger emissions may under-, or over-correct for the problem depending on whether the chosen substrate emission lies at a substantially lower or higher kinetic energy than that from the adsorbate.

In this work attempts were made to reduce these diffraction effects by using an electron beam incident on the surface at a grazing angle. This should have the effect of increasing the number of atoms near the surface that are excited by the incident beam, reducing the relative effect of the back-scattered electrons. This approach proved to be impracticable for reasons that will be dealt with in the third section of this chapter.

The problem therefore remains that diffraction effects will cause a variation of up to 30% or so on all measurements. For typical experiments involving adsorption of  $O_2$  or  $S_2$  onto Ni or Cu surfaces this variation has not been corrected for. There are several reasons for this : firstly the necessity to take a large number of readings in a reasonably short time results in a large amount of scatter (typically of the same order as the diffraction effects; see for example figure 4.9 (c) where the oxygen signal has a large scatter, even after the results of two runs have been averaged). Secondly, and more importantly, the variations in the adsorption rates are generally very much larger than the diffraction effects. For example, the oxygen coverage on Cu varies with orientation by a factor of up to 50 in the low coverage region.

Despite the disadvantages that are introduced by the diffraction effects when measuring coverages, these effects can in fact be the source of useful information. The diffraction pattern can be easily monitored via the crystal current, and this provides an easy check of the state of the crystal. Polishing defects and polycrystallinity show up readily using this technique, although the sampling depth of typically several hundred Å means that the state of the surface layers is not resolved. Furthermore the diffraction effects provide an easy method of determining the orientation of the symmetry planes and therefore the angular position of the crystallographic faces.



One further use of the diffraction pattern is in the detection of amorphous surface layers. Wolf et al.<sup>22</sup> measured the pseudo-Kikuchi pattern from an amorphous adlayer of varying thickness of silicon on a single crystal of silicon. They reported that an amorphous adlayer of several tens of Å produced a notable degradation of the back-scattered electron patterns. In chapter 7 the adsorption of sulphur on Ni and Cu from a molecular beam of S<sub>2</sub> is described. It is found that an amorphous adlayer, probably of copper or nickel sulphide, builds up with increasing exposure, and this growth can be followed by monitoring the decrease in the pseudo-Kikuchi pattern contrast. Although no direct attempt was made to obtain an absolute depth calibration for this method it did prove to be a useful guide to the course of the reaction.

#### 4.3 : DIFFRACTION IN COPPER AND NICKEL

The results in the previous section are all for a single crystal copper substrate; most of the work on diffraction effects was carried out on copper crystals. At first sight the diffraction effects in nickel might be expected to be similar, as nickel has the same face-centred cubic structure as copper, and a very similar lattice parameter. If the diffraction effects are governed only by the arrangement of the atoms in a lattice, the effects should be the same for the two metals.

This turns out to be the case as can be seen from fig.4.11 which shows the variation of the elastic peak with crystal rotation and from fig.4.12 which shows the variation of the crystal current. There are small differences between the copper and nickel diffraction patterns, but it is known that there are several factors which distort the results (see next section), and it is thought that these experimental errors are the major cause of the small variations. For example in fig.4.11 the differences between the elastic peak variations for copper and nickel crystals is no greater than

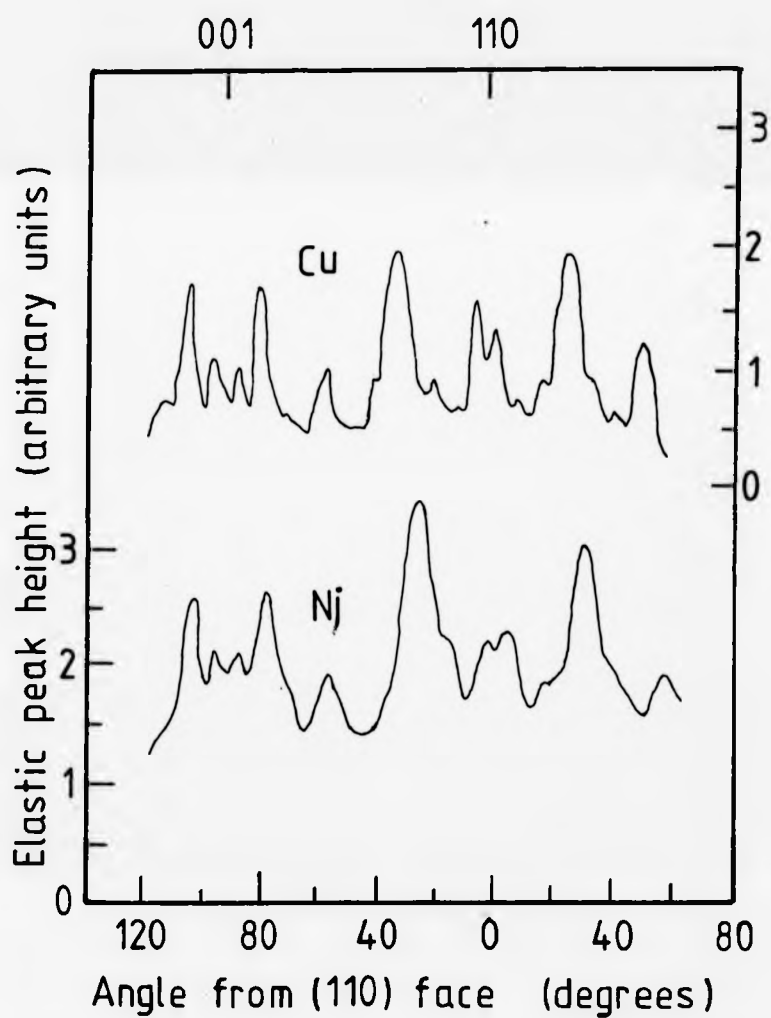


FIG. 4.11 Comparison of the elastic peak height variation in copper and nickel.

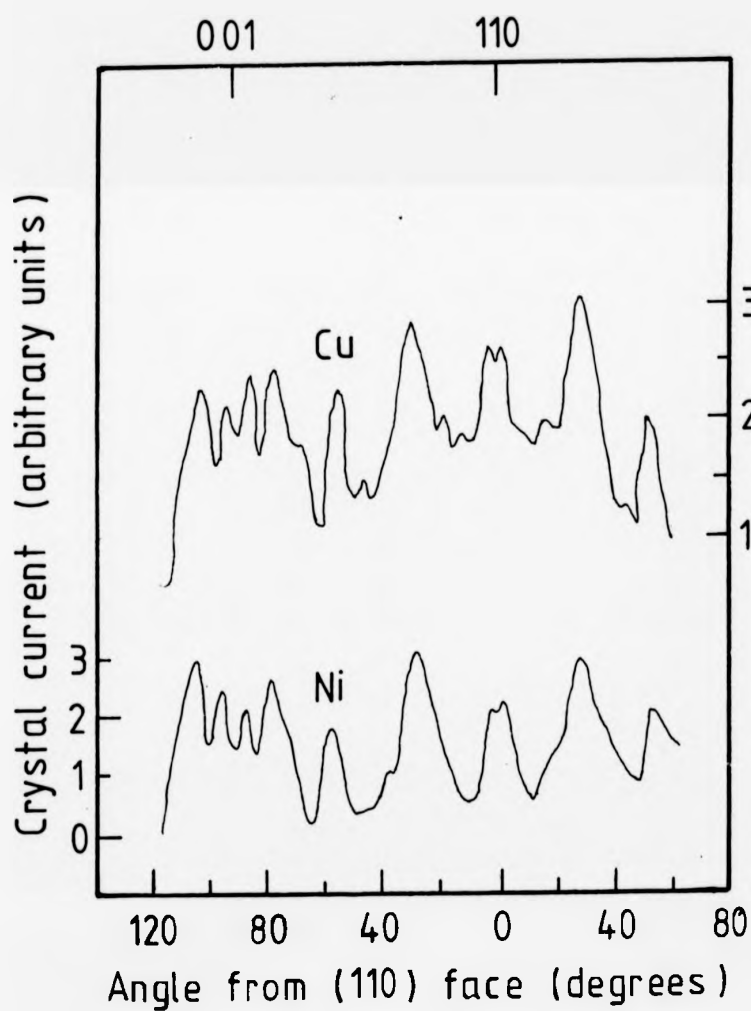


FIG. 4.12 Comparison of the crystal current variation with crystal rotation for copper and nickel.

the differences resulting from two different copper crystals.

These effects were not limited to the secondary electrons. Fig.4.13 shows the crystal current measured when the sample was being bombarded with 6kV argon ions (at a current of approx. 12ua). Again there is a variation round the crystal that is symmetric about the mirror planes. The fractional variation in the crystal current is not as large as for the case of electron channelling, but is still quite marked. This variation is related to the variation in the sputter yield between different faces.<sup>25,26</sup> Southern et al.<sup>25</sup> quote sputter yields for 5keV argon ions normally incident on copper single crystals as follows:-

face	yield (atoms removed per incident ion)
(110)	2.7
(221)	6.8
(111)	9.3
(113)	7.5
(001)	4.2

In this system the argon beam is unfocussed and so at any time is incident on a range of faces at a range of incidence angles. However it can be seen that the rough trend of fig.4.13 follows the values quoted in the table, i.e. low yields at (110) and (001), high yields at (113) and (111).

#### 4.4 : DISTORTIONS

In the previous section it was mentioned that there are small distortions to the pseudo-Kikuchi diffraction patterns. There are in fact two distinct types of distortion which are observable under different conditions.

An example of the first type of distortion is given in fig.4.14 which is a polar plot of the crystal current from a copper cylinder. Broadly speaking the 2mm symmetry is apparent; however there are

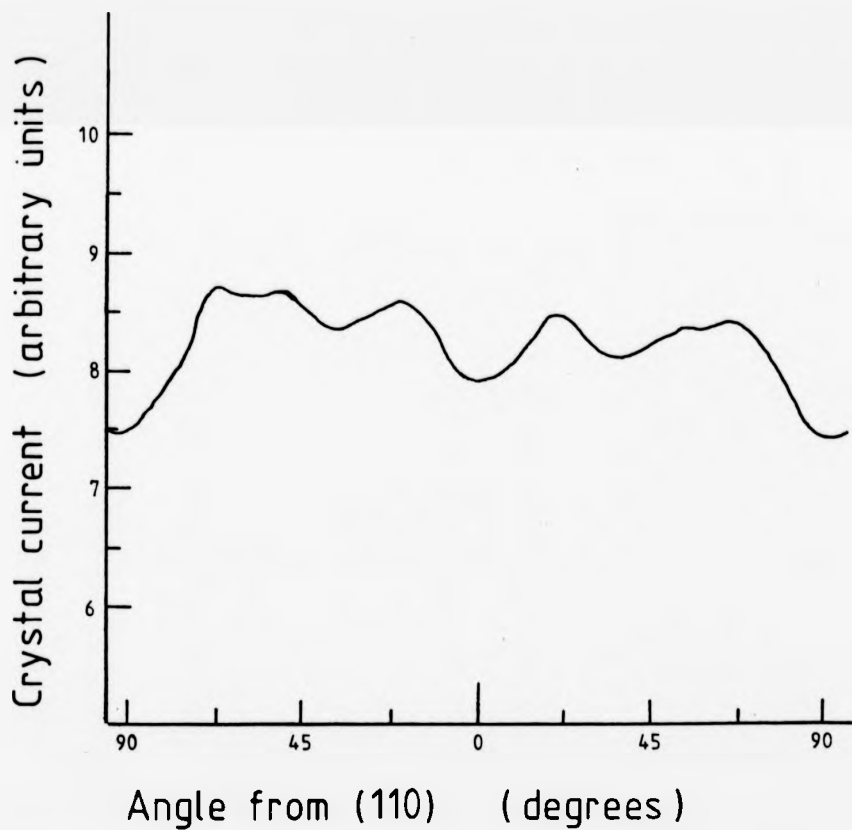


FIG. 4.13 Variation of crystal current during argon ion bombardment as a function of crystal rotation.

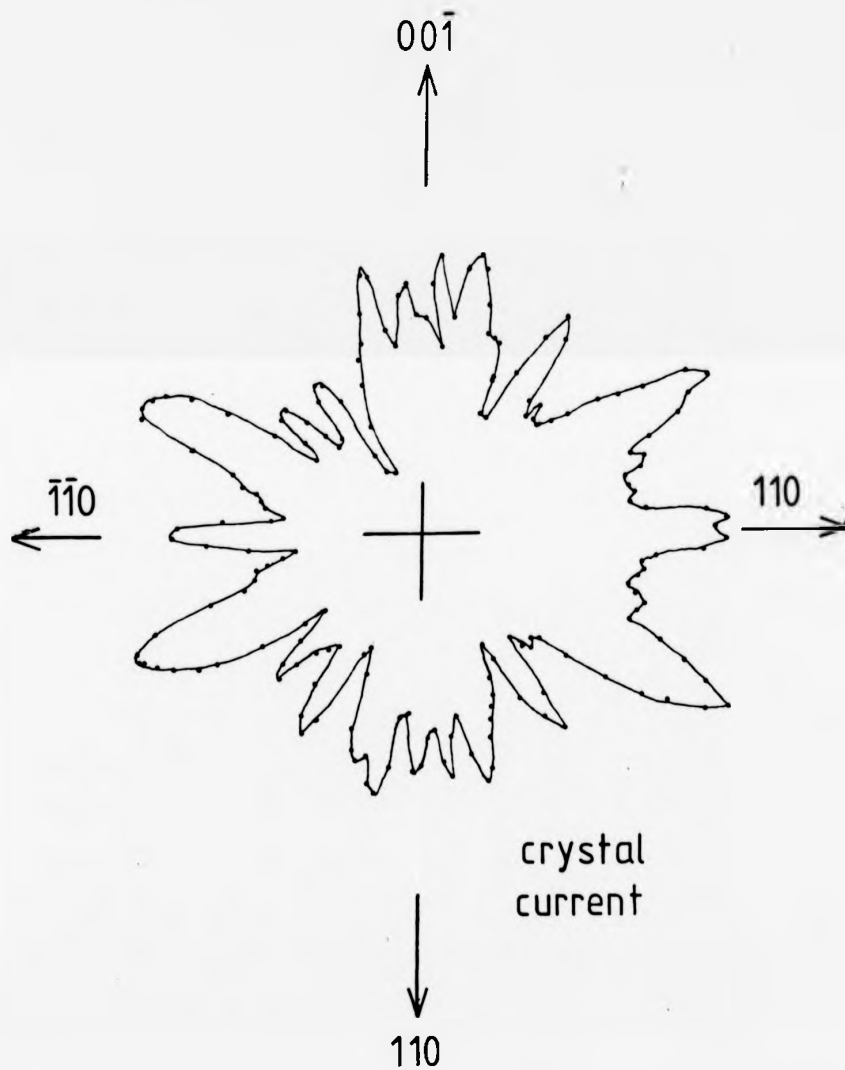


FIG. 4.14 Polar plot of the crystal current from a clean copper cylinder.

small irregularities. The symmetry about the  $\langle 110 \rangle$  type axis (the horizontal axis in fig.4.14) is excellent. The symmetry about the  $\langle 001 \rangle$  axis is not as good; For example, on the right hand side of the figure there is one large and one small lobe near the midpoint between the  $\langle 001 \rangle$  and  $\langle 110 \rangle$  directions. On the left hand side of the polar plot there are two approximately equal lobes in the equivalent position.

This distortion is due to the  $[\bar{1}10]$  axis of the cylinder being inclined at a slight angle to the axis of rotation. If the axis of rotation of the crystal coincided exactly with the  $[\bar{1}10]$  axis, then the 2mm symmetry about this axis should be clearly reflected in the plot of the crystal current. However, if the crystal rotated about a slightly different axis, then the crystal current plot would not necessarily show the 2mm symmetry, but would show the symmetry of the axis that the crystal was rotating about.

If, in fig.4.14, the axis of rotation of the cylinder was displaced from the  $(\bar{1}10)$  direction in the plane containing the  $(\bar{1}10)$  and  $(110)$  directions, then the symmetry about the  $(110)$  direction would be preserved, while the symmetry about the  $(001)$  direction would be weakened (as is in fact observed). In practise it was never found to be possible to mount the crystal so accurately that this distortion could be removed. However the effect was small, and certainly not large enough to have a noticeable effect on the measurement of adsorbed gases by AES.

A more important effect (in that it did influence measurements of adsorbed species) was the distortion introduced by the displacement of the centre of the cylinder and the axis of rotation (shown in schematic form in fig.4.15). The first effect of this is that as the crystal rotated, the distance between the H.C.M.A. and the front surface of the cylinder changed. Two factors were influenced by this: the position of Auger peaks in the energy

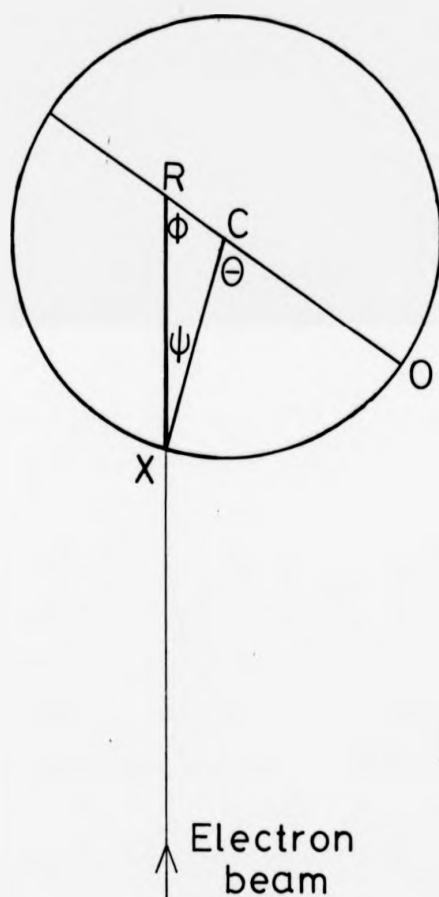


FIG. 4.15 Schematic diagram of the eccentric rotation of the cylindrical samples.



14  
spectrum, and the gain of the H.C.M.A. This last effect is shown clearly in fig.4.16, which is a polar plot of the elastic peak from the same crystal as in fig.4.14. Again, broadly speaking, the 2mm symmetry is apparent. However there is now a variation in gain round the crystal, for instance the lobes directly to either side of the (001) face are over twice as big as the corresponding lobes near the (001) direction. This obviously should not affect the crystal current, which is not measured by means of the H.C.M.A., and it can be seen from fig.4.14 that this is the case.

Again this distortion could be avoided by accurately mounting the crystal so that the axis of rotation and the centre of the cylinder were coincident. In practice this proved impossible as the cylinder had been cut using a tube cutter on a spark erosion machine (rather than by turning) and so <sup>the</sup> inner and outer surfaces were not concentric, leading to mounting difficulties. Fig.4.16 has been chosen because it demonstrates this effect clearly; later crystals were mounted more accurately so that this effect was reduced, although it was never eliminated. The variation in the gain of the H.C.M.A. also affected the measurement of Auger peaks. Where the effect was pronounced (for instance in measurements of the saturation coverage of oxygen on the same crystal as in fig.4.16) normalisation had to be used (for example by measuring the ratio of oxygen to copper Auger peak heights).

A further consequence of this displacement of the cylinder surface on rotation was that grazing incidence electron beams could not be used. In extreme cases a beam that was grazing the surface at one orientation would miss the surface altogether when the crystal was rotated through  $180^\circ$ . Even when this extreme effect did not occur, the position of the beam on the cylinder surface (with respect to a fixed point, such as the H.C.M.A.) would vary as the cylinder rotated. Consequently all results

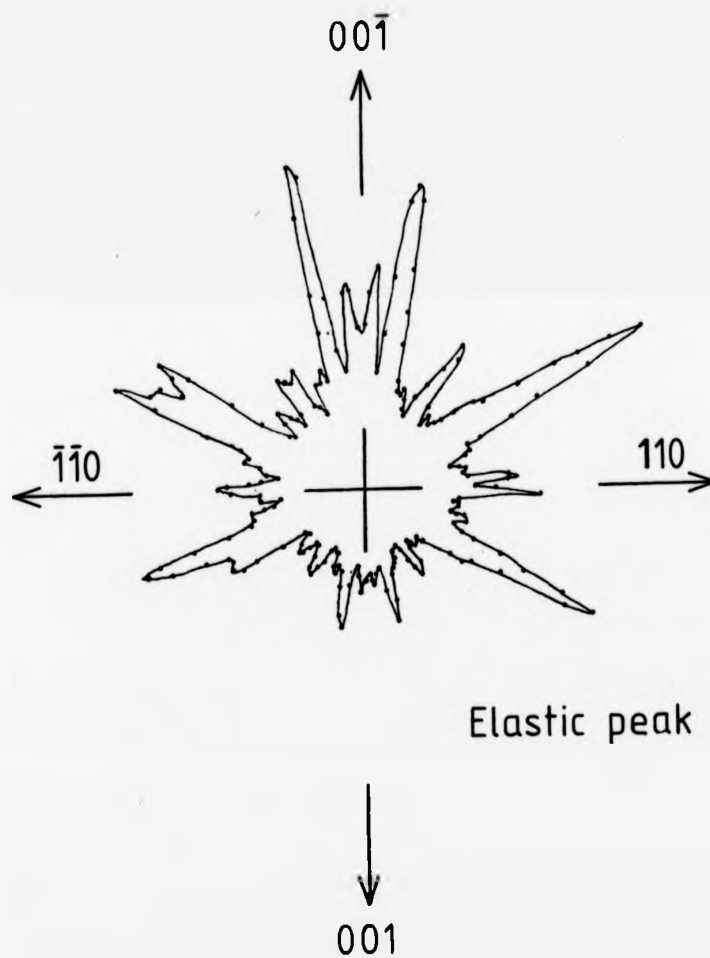


FIG. 4.16 Polar plot of the elastically scattered electron peak from a clean copper cylinder.

were taken with an electron beam as near normal incidence as possible.

Fig.4.15 highlights another problem generated by the displacement between the centre of rotation and the centre of the cylinder; A shift in the apparent position of the electron beam on the surface with respect to the crystallographic axis. However this problem is readily understood, and can be allowed for as follows:-

The centre of rotation (K in fig.4.15), and the centre of the cylinder C, are not coincident. The line RC extended provides an origin on the surface of the cylinder at the point O. Suppose that initially the electron beam is incident on the point O, with the beam and the line OR colinear. When the crystal has been rotated through an angle  $\phi$ , the position of the beam on the surface moves from O to X. The surface at the point X is at an angle  $\theta$  with respect to the surface at O. The relation between  $\theta$  and  $\phi$  can be determined as follows:-

$$\begin{aligned} \frac{CX}{\sin\phi} &= \frac{RC}{\sin\psi} \\ \text{Therefore } \sin\psi &= \frac{RC}{CX} \sin\phi \\ \text{or } \psi &= \sin^{-1} \left( \frac{RC}{CX} \sin\phi \right) \\ \text{but } \theta &= \phi + \psi \\ \text{so } \theta &= \phi + \sin^{-1} \left( \frac{RC}{CX} \sin\phi \right) \end{aligned}$$

In this equation CX is the radius of the cylinder so if RC is known  $\phi$  can be obtained as a function of  $\theta$ .

Unfortunately RC could not be measured accurately when the sample was in situ. However on the second sample, the displacement RC was observed to be approximately towards the (110) face. Taking this face as the origin, O, the position of the maxima and minima could be fitted to the symmetry of the crystal by a trial and error choice of the distance RC. A distance of 1.9mm gave the results shown in fig.4.17, where the uncorrected oxygen Auger peak height is shown at the top (after an exposure of approx. 90L). The same plot, corrected for angular position, is shown

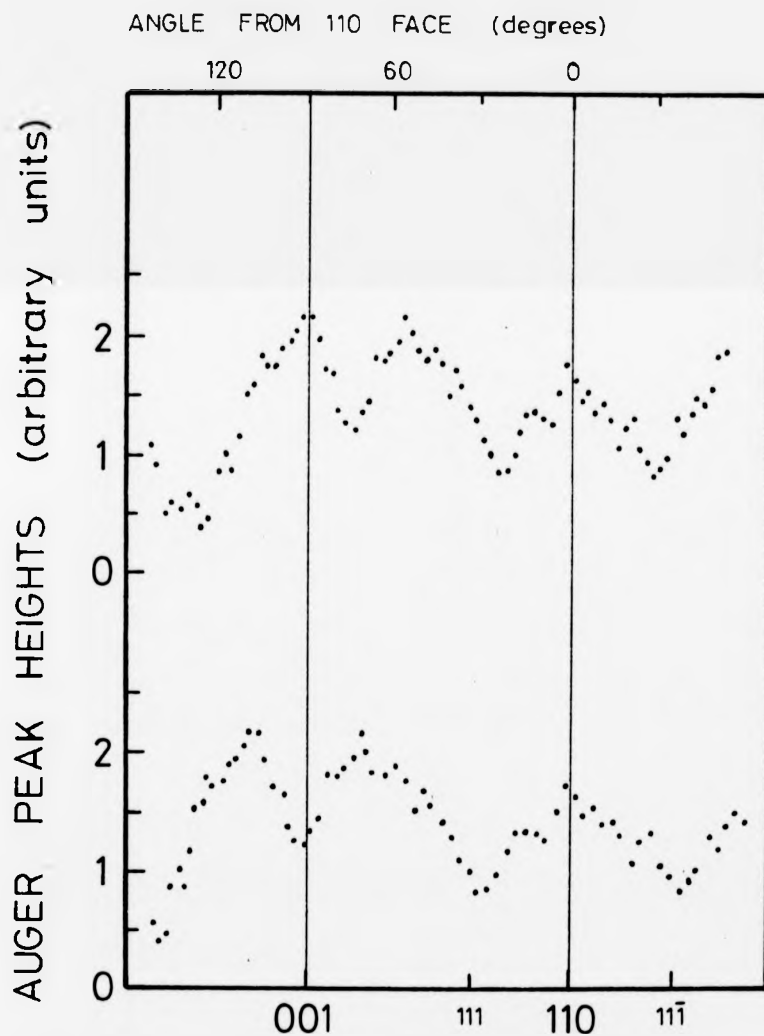


**FIG. 4.17** Oxygen Auger peak from a copper crystal. The top set of results is as measured, the bottom set has been corrected to allow for the eccentric rotation of the cylinder.

16  
at the bottom. In general the variation of the oxygen coverage showed definite maxima and minima such that there was only one possible alignment of the oxygen coverage with the 2mm symmetry of the crystal. For example it can be seen that the correction in fig.4.17 changes the coverage at the (001) face from an apparent maximum to a minimum. When the coverage around the whole crystal is considered, it is apparent that the only possible symmetric position is when the (001) is a minimum.

Although the above correction adequately resolves the distortion for this particular case, the fact that the distance RC was not accurately known for each crystal meant that this correction could not always be applied. However for the other crystals used the distortion was less than the extreme example of fig.4.17, and the position of the maxima and minima corresponding to the three low-index faces could always be easily identified. Consequently no correction was needed for results taken from the (001), (110) and (111) faces. If it was desired to take measurements from a particular face intermediate between the low-index faces difficulty was found in exactly locating the face with respect to the measured angle of rotation of the crystal. However as the three low-index faces (plus the (113) face) were all identifiable, there were always plenty of reference points (12 round the crystal). Consequently no intermediate plane was more than about  $20^\circ$  from a reference plane, and so could be located to within one degree.

#### 4.5 Oxide layer on nickel.

Having looked at some of the complications that can arise through electron channelling effects, let us finish the chapter by looking at an example of the information that can be gained from these effects. Consider the case of the epitaxial growth of an oxide film on nickel ( this topic will be considered in greater detail in Chapter-6 ). Figure 4. 18 shows that the clean

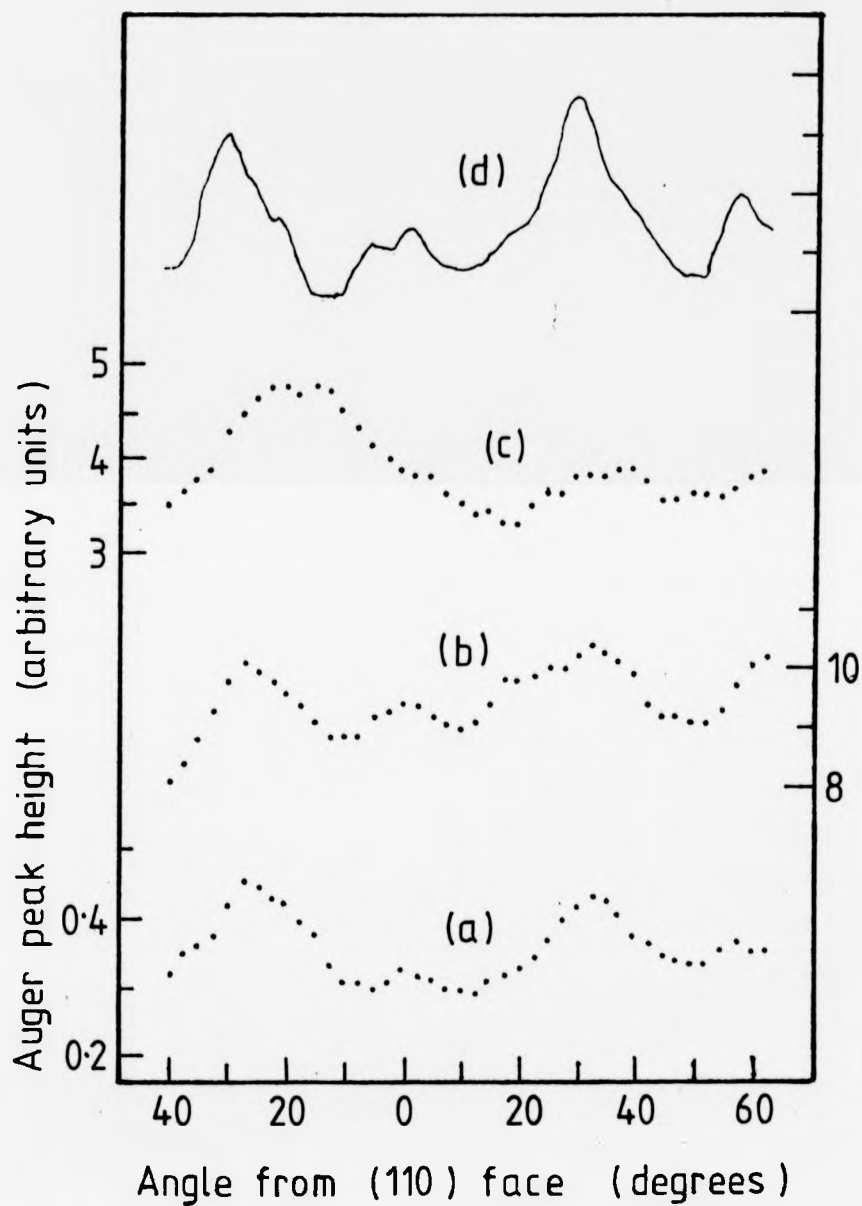


FIG. 4.18 Variation round the crystal of the Auger peaks:  
 (a) clean 848eV peak, (b) clean 61eV peak, (c) 61eV peak after  
 an oxygen exposure of 158L; (d) elastic peak from clean crystal.

17

848 and 61eV Ni Auger peaks ((a) and (b)) vary in a similar way to the elastic peak (d). The 61eV Ni Auger peak is also shown after an exposure of 158L of oxygen (c). There are two effects on the Auger peak. Firstly, the intensity of the Auger peak is attenuated (approx.  $\frac{1}{2}$  the intensity from the clean surface). Secondly, an additional feature appears : a peak in the intensity at about  $15^\circ$  to the left of (110) direction in fig.4.18. This is in fact caused by the slight dip in the Oxygen coverage on the (110) surface. (see fig.6.6) As noted before, the eccentricity of rotation of the cylinder causes a slight angular displacement between the (110) surface (which depends on the position of the beam on the cylinder surface), and the position of the (110) direction in the diffraction pattern (which depends on the angle between the incident beam and the crystallographic axis). Thus in fig.4.18 the peak at about  $15^\circ$  from the (110) direction corresponds to the (110) surface where there is less oxygen. Consequently the Ni 61eV peak is not attenuated as much as in surrounding areas and a peak appears in the plot of the Ni Auger peak height.

The fact that the 61 eV Auger peak still shows some variation in step with the elastic peak from the clean crystal (d) shows that the oxide is present as a surface film only. If true bulk oxide was forming we would expect a different electron channelling pattern altogether. The information from the electron channelling pattern complements the information from the Auger spectra because the former is sampling the crystal to a greater depth than the latter. Taken together, the two techniques tell us about the surface composition and the depth of the oxide film.

#### CHAPTER 4: REFERENCES

1. B. W. Holland, L. M. Donnell & D. P. Woodruff, Solid State Commun. **11** (1972) 991.
2. L. McDonnell & D. P. Woodruff, Vacuum **22** (1972) 477.
3. T. Matsudaira, I. Watanabe & I. Onchi, Japan. J. Appl. Phys., Suppl. **2**, Pt. 2 (1974) 181.
4. L. McDonnell, D. P. Woodruff & B. W. Holland, Surf. Sci. **51** (1975) 249.
5. J. R. Noonan, D. M. Zehner & L. H. Jenkins, J. vac. Sci. Technol. **13** (1976) 183.
6. D. M. Zehner, J. R. Noonan & L. H. Jenkins, Solid State Commun. **18** (1976) 483.
7. G. Allie, E. Blanc & D. Dufayard, Surf. Sci. **57** (1976) 293.
8. S. P. Weeks & A. Leibsch, Surf. Sci. **62** (1977) 197.
9. S. J. White, D. P. Woodruff & L. McDonnell, Surf. Sci. **72** (1978) 77.
10. T. W. Rusch, J. P. Bertino & W. P. Ellis, Appl. Phys. Letters **23** (1973) 359.
11. T. W. Rusch & W. P. Ellis, Appl. Phys. Letters **23** (1975) 44.
12. S. K. Anderson & A. Howie, Surf. Sci. **50** (1975) 197.
13. M. Baines, A. Howie & S. K. Anderson, Surf. Sci. **53** (1975) 546.
14. C. C. Chang, Appl. Phys. Letters **31** (1977) 304.
15. S. Kikuchi, J. Phys. Japan. **5** (1978) 83.
16. R. M. Stern & H. Taub, C.R.C. Crit. Rev. in Solid State Sci. (1970) 221.
17. D. G. Coates, Phil. Mag. **16** (1967) 1179.
18. R. M. Stern & H. Taub, Phys. Rev. Letters **20** (1968) 1340.
19. P. Hofmann, R. Unwin, W. Wyrbisch & A. E. Bradshaw, Surf. Sci. **72** (1978) 635.
20. J. H. Onuferko & D. P. Woodruff, Surf. Sci. **20** (1980) 30.
21. M. J. Braithwaite, R. W. Joyner & M. W. Roberts, J.C.S. Faraday Disc. **60** (1975) 89.
22. E. D. Wolf, M. Braunstein & A. I. Braunstein, Appl. Phys. Letters **15** (1969) 389.



23. B. D. Powell, D. P. Woodruff & B. W. Griffiths, J. Phys. E. Sci. Inst. 8 (1975) 548.
24. A. P. Janssen, C. J. Harland & J. A. Venables, Surf. Sci. 62 (1977) 277.
25. A. L. Southern, W. R. Willis & M. T. Robinson, J. Appl. Phys. 34 (1963) 153.
26. G. D. Magnusson & C. E. Curlston, J. Appl. Phys. 34 (1963) 3267.

## CHAPTER 5 : OXYGEN ON COPPER

### 5.1 PREVIOUS WORK.

The first evidence of anisotropic oxidation of copper was obtained by Tammann<sup>1</sup>, who noted that the different grains in a polycrystalline sample showed different interference colours when they were oxidised. The classic study on anisotropic oxidation of copper was performed by Gwathmey and co-workers.<sup>2-4</sup> Limited by the techniques available at the time they used elliptically polarised light to monitor the growth of oxide films on a spherical copper crystal, and a spherical copper crystal cut to have flat (100), (110), (111), and (311) faces. They found that the (100) face oxidised most quickly, followed by (111) then (110) and (311) (the (110) and (311) faces behaved almost identically). These experiments suffered from several limitations. Firstly the oxide film thickness could only be measured to limited accuracy (typically  $\pm 5\text{\AA}$ ). Secondly, working under moderately high vacuum with no truly surface sensitive method of elemental analysis, the presence and effect of impurities could not be ruled out.

Despite the limitations of the experimental techniques, Gwathmey and co-workers were aware of the advantages of using a curved single crystal.<sup>4</sup> In essence the work in this chapter is a repeat of their experiments with the improvements afforded by the availability of modern U.H.V. technology and a surface sensitive analytical technique (A.E.S.). This has made it possible to prepare, maintain and characterise clean crystal surfaces with surface impurity levels of the order of 1% or less so adsorption in the monolayer regime can be studied (where one monolayer is defined as a layer of adatoms in a ratio of 1:1 to the surface atoms of the substrate).

## CHAPTER 5 : OXYGEN ON COPPER

### 5.1 PREVIOUS WORK.

The first evidence of anisotropic oxidation of copper was obtained by Tammann<sup>1</sup>, who noted that the different grains in a polycrystalline sample showed different interference colours when they were oxidised. The classic study on anisotropic oxidation of copper was performed by Gwathmey and co-workers.<sup>2-4</sup> Limited by the techniques available at the time they used elliptically polarised light to monitor the growth of oxide films on a spherical copper crystal, and a spherical copper crystal cut to have flat (100), (110), (111), and (311) faces. They found that the (100) face oxidised most quickly, followed by (111) then (110) and (311) (the (110) and (311) faces behaved almost identically). These experiments suffered from several limitations. Firstly the oxide film thickness could only be measured to limited accuracy (typically  $\pm 5\%$ ). Secondly, working under moderately high vacuum with no truly surface sensitive method of elemental analysis, the presence and effect of impurities could not be ruled out.

Despite the limitations of the experimental techniques, Gwathmey and co-workers were aware of the advantages of using a curved single crystal.<sup>4</sup> In essence the work in this chapter is a repeat of their experiments with the improvements afforded by the availability of modern U.H.V. technology and a surface sensitive analytical technique (A.E.S.). This has made it possible to prepare, maintain and characterise clean crystal surfaces with surface impurity levels of the order of 1% or less so adsorption in the monolayer regime can be studied (where one monolayer is defined as a layer of adatoms in a ratio of 1:1 to the surface atoms of the substrate).

With the advent of modern bakable U.H.V. systems, the possibility of true surface analysis has arisen in the last 20 years. The first surface characterisation technique to be developed was Low Energy Electron Diffraction (L.E.E.D.). The interpretation of surface structure information from L.E.E.D. is complicated and so from early on the use of this technique became confined largely to the study of the comparatively simple low-index faces. Generally these studies were done on crystals cut to present one flat low-index face, for example early L.E.E.D. work on oxygen adsorption deals mostly with the low-index (100), (110) and (111) faces.<sup>5-11</sup>

As new surface analytical techniques have arisen, the interaction of oxygen with copper has been studied by a variety of techniques: A.E.S.<sup>12-15</sup>, Work function measurements<sup>12,14,16,17</sup>, U.P.S.<sup>17,18</sup>, X.P.S.<sup>18,19,20</sup>, electron energy loss spectroscopy<sup>21</sup>, low energy ion scattering<sup>22</sup> and S.I.M.S.<sup>23,24</sup>. However these studies have in general been limited to a few low-index faces. One group in particular has done a thorough study of all three low-index faces using ellipsometry, A.E.S., L.E.E.D. and work function measurements.<sup>25-30</sup> This work of Habraken and co-workers provides such a good reference base for this work, and consequently will be referred to so often, that in future Habraken et al. will be referred to simply as H.

Some work has been reported on curved or vicinal surfaces<sup>31-33</sup>, but in general these studies have been restricted to small ranges of surface orientation near a low-index face. Recently Kramer et al.<sup>34</sup> have reported studies of cylindrical crystals using retarding potential work function measurements that are similar in approach, and complementary to, the studies reported in this chapter.

A brief summary of the results of previous studies on the three major low-index faces will demonstrate the differences ( and similarities ) in the behaviour of these faces.

#### A) 100

For increasing oxygen exposures, the following sequence of L.E.E.D. patterns has been reported: low exposures ( less than 100L) result in a weak "4 spot" pattern<sup>5,7,14,21,H</sup> which is converted into a  $(\sqrt{2} \times \sqrt{2})R 45^\circ$  pattern<sup>7,9,11,14,21,H</sup> at exposures of the order of  $10^3 L$ . At higher exposures a  $(\sqrt{2} \times 2/2)R 45^\circ$  pattern appears.<sup>5-7,9,14,H</sup>

Comparison of LEED diffracted beam intensities with dynamical theory calculation<sup>37</sup> suggests that the oxygen is initially adsorbed into 2-fold bridge sites, but may be subsequently incorporated into almost coplanar 4-fold sites. The  $(\sqrt{2} \times \sqrt{2})R 45^\circ$  structure seems to be less well defined and stable than the comparable structure on nickel. It appears to evolve easily into the  $(\sqrt{2} \times 2/2)R 45^\circ$  structure with which it may partially coexist. According to H the adsorption of oxygen in the chemisorption regime (i.e. up to the formation of the  $(\sqrt{2} \times \sqrt{2})R 45^\circ$  pattern at approx.  $10^3 L$  corresponding to 0.5 monolayers) can be described by simple second order kinetics with the sticking factor varying proportionally to  $(1-\theta)^2$  and with an initial value of between  $0.01^H$  to  $0.03^{14}$ .

#### B) 110

At low exposures L.E.E.D. patterns show streaks parallel to the (110) direction which change into a  $(2 \times 1)$  pattern at intermediate exposures (approx 100L)<sup>6-7,H</sup>. The  $(2 \times 1)$  pattern is assumed to correspond to 0.5 monolayers. At higher exposures weak spots of a  $c(6 \times 2)$  structure have been reported<sup>6,7,H</sup>.

The work function increases on oxygen adsorption<sup>12</sup>, reaching a maximum at  $2 \times 10^3 L^{16}$ . Low energy ion scattering experiments indicate that at approx. 60L no surface reconstruction has occurred, and the adsorbed oxygen atoms are located  $0.6 \pm 0.1\text{\AA}$  below the midpoint between two neighbouring Cu atoms in a (001) direction<sup>22</sup>.

The initial sticking factor has been estimated to lie in the range 0.05 - 0.1<sup>6,7</sup>. H obtains a value of 0.17 for the initial sticking factor, and finds that the adsorption process can be described by Langmuir kinetics if dissociative adsorption on empty n n site pairs and an attractive interaction in the adsorbed layer are taken into account.

### C) 111

L.E.E.D. experiments show no superstructures on this face below about  $5 \times 10^4 L$ . The sticking factor lies between  $10^{-3}$  and  $10^{-2}$ <sup>6,7,9</sup> and is constant up to exposures of about  $10^3 L$ . H finds that the kinetics can be described by the equation of Kohrt and Gomer<sup>35</sup> for dissociative adsorption via a precursor state requiring a pair of adjacent sites. The chemisorption stage saturates at approx.  $\frac{1}{2}$  a monolayer<sup>H</sup>.

## 5.2 CALIBRATION OF AUGER PEAK HEIGHTS

In the chemisorption region (coverages less than 0.5 monolayers of oxygen), H found that the ratio  $h_o/h_{cu}$  varied linearly with the ellipsometric parameter  $\Delta$  ( $h_o$  and  $h_{cu}$  are the peak to peak heights in the differentiated spectrum of the oxygen 510eV and copper 920eV peaks). This suggests that the Auger peak height in the differentiated spectrum is a good linear measure of the oxygen coverage (for coverage of 0.5 monolayers or less).

Absolute calibration, however, is not easy. Calibration against well-known L.E.E.D. structures are possible for some, but not all, faces. For example, H measured the absolute Auger signal for the (110) face when showing the (2 x 1) superstructure i.e. 0.5 monolayers. H then uses this calibration for the (111) face, assuming that the Cu 920eV Auger signal is equal for the (110) and (111) faces. However, this last assumption is not justified because it makes no allowance for the variation in Auger current

arising from the Kikuchi-like variations discussed in chapter 4. This can be seen from fig. 4.7 (d) in which the Cu 920eV Auger peak is plotted as a function of angle round the crystal. The Auger signal for the (111) and (110) faces is <sup>in</sup> the approximate ratio of 3:5. It can be seen that care must be taken when comparing Auger spectra from different crystallographic faces.

No attempt has been made to convert Auger peak heights directly to coverages because it is not possible to correct simply for these incident beam diffraction effects. Despite this it is believed that the Auger peak height is a reasonably good measure of relative oxygen coverages. It will be seen in the next chapter that line shape changes further complicate the use of Auger peak heights as a measure of oxygen coverages on nickel.

### 5.3 RESULTS

As discussed earlier in this chapter, previous measurements of the initial sticking factor vary between different faces. The sticking factors for the (111), (100) and (110) faces are (very approximately)  $10^{-3}$ ,  $10^{-2}$  and  $10^{-1}$  respectively. This implies that a cylindrical crystal containing these three faces would show a highly anisotropic adsorption of oxygen at low coverages.

This is in fact the case, as can be seen from fig. 5.1, which shows the 510eV oxygen peak height round the crystal after an exposure of 2 Langmuirs. Note that, although absolute values of oxygen coverage can not be derived directly from the peak heights, the oxygen peak height varies by a factor of more than 15 round the crystal. This variation is far greater than the variations of typically 20-30% caused by both the Kikuchi effects and the distortion due to the off-centre rotation of the cylinder. Thus the variation in the oxygen peak height is far greater than the variation in, say, the copper Auger peak heights from the clean cylinder (fig. 4.7).

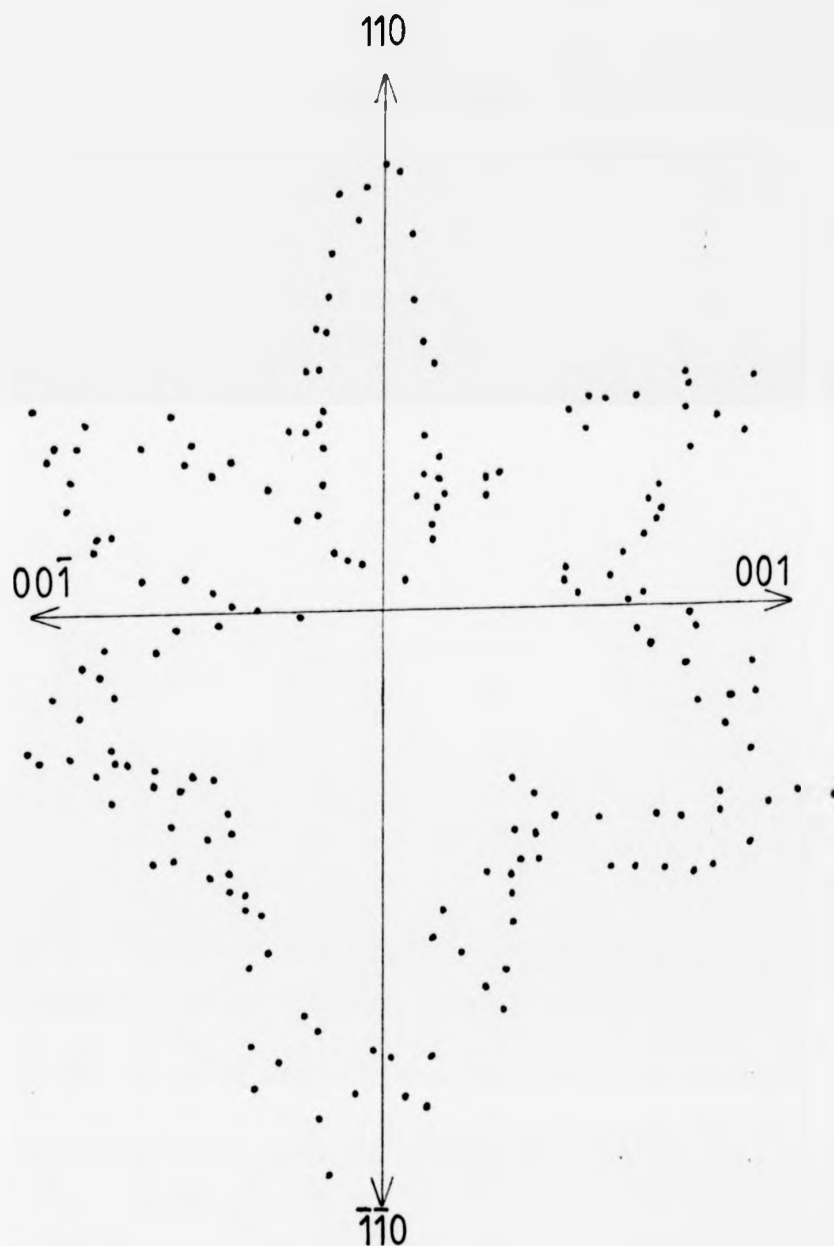


FIG. 5.1 Polar plot of the 510eV Auger peak of adsorbed oxygen after an oxygen exposure of 2 Langmuirs.



This means that the variation in the oxygen Auger peak height in fig. 5.1 is in fact due to a variation in the oxygen coverage.

The 2mm symmetry of the crystal is clearly reflected in the adsorption of oxygen as measured in fig. 5.1. However, these results also demonstrate that the symmetry is not perfect. This is because of the distortion discussed earlier, resulting from the off-centre rotation of the crystal. In fig. 5.1 this can be seen in the proportionately large signal from the portion of the crystal in the region of the (110) plane.

The accuracy of this technique, and its limitations, can be deduced from the comparison of the results from two different samples. Fig. 5.2 shows the 510eV oxygen Auger peak height round two different cylindrical crystals after each crystal had been exposed to 90L of oxygen. The lower set of results is the average of several runs and therefore appears less noisy than the upper set of results. The broad features of the two sets of results are the same, i.e. there are peaks in the exposures at (110) and (113) surfaces, and troughs at (001) and (111). The fine detail however, does differ markedly between the two sets of results. The off-centre rotation of the cylinders has two effects. Firstly the variation in gain round the cylinder is slightly different for each crystal. This accounts for the fact that for the upper trace the (110) peak is larger than the (111) peaks trace, but the opposite is true for the lower trace. Secondly, the apparent distortion to the angular position of the faces is different for the two cylinders. For example the (111) "troughs" appear to be nearer to the (110) face in the upper trace than in the lower.

For the reasons given in Chap. 4, it was not possible to correct exactly for the distortion to the apparent angular positions of all faces. However, the four key faces (001), (110), (111), and (113) always correspond to extremes at low coverages and therefore were

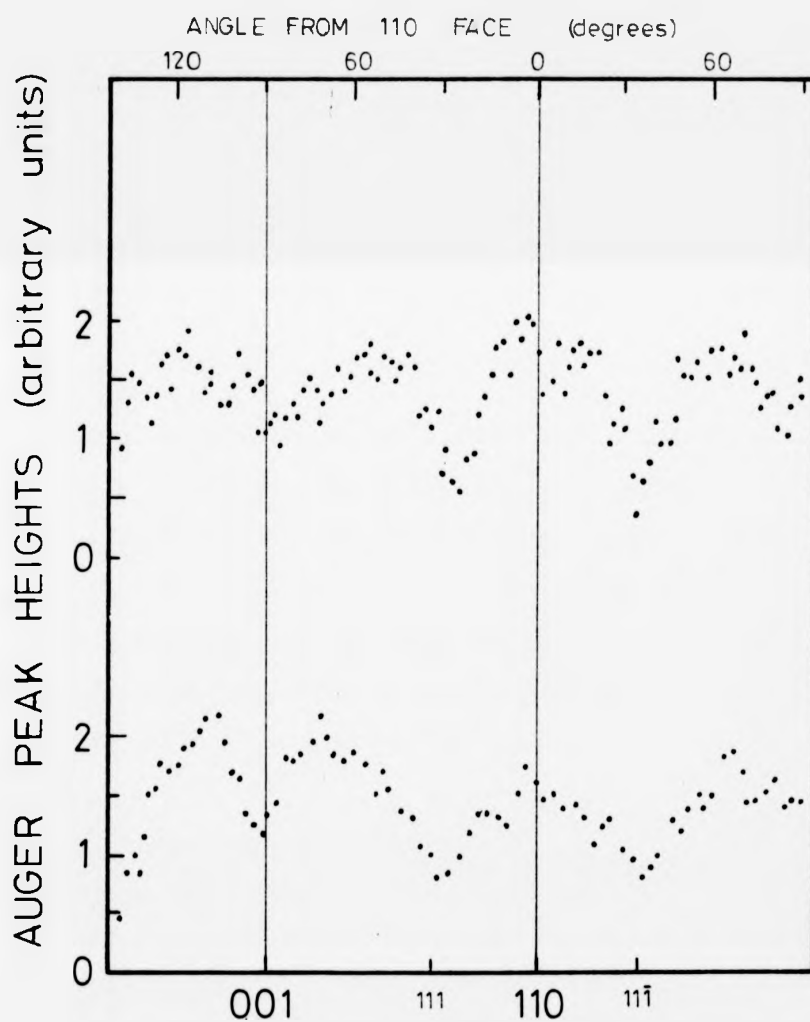


FIG. 5.2 510eV Oxygen Auger peak around two different copper cylinders exposed to 100 Langmuirs of oxygen.

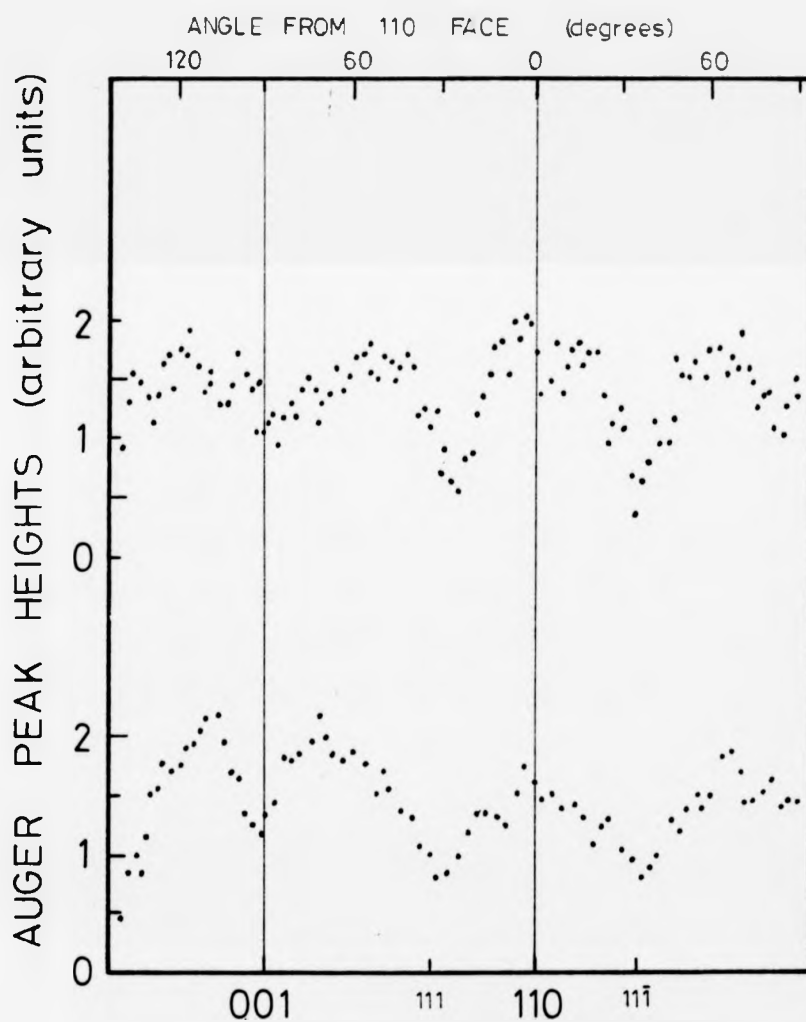


FIG. 5.2 510eV Oxygen Auger peak around two different copper cylinders exposed to 100 Langmuirs of oxygen.

easily located. Once the key faces were found, intermediate faces could be located to an accuracy of  $\pm 1$  degree.

The differences in the two sets of results in fig. 5.2 lead us to expect a rather limited accuracy from this method. However, one helpful guide was the symmetry of the results. For instance, in early experiments results were obtained which were highly asymmetric and so these results were rejected. It was thought that the argon ion sputter cleaning using 5keV ions was leaving a badly disordered surface ( even after annealing ). A lower energy argon ion beam (1.5keV) was therefore used for the sputter cleaning before an oxygen adsorption experiment. This was found to result in the more symmetric data, such as that of fig. 5.1 , and so all experiments after this were preceded by the comparatively low energy ion bombardment.

Complete results from two experiments are shown in fig. 5.3 and fig. 5.4 . In each case the peak heights of the 510eV oxygen Auger peak are related to the peak heights at saturation coverage. The saturation coverage is the essentially isotropic coverage seen at high exposures (approx. equal to  $10^4$ L), which was measured in each of these experiments but is not shown in figs. 5.3 and 5.4 . Note that by 300L (fig. 5.4 ) the oxygen coverage is nearly isotropic.

The three main low-index faces have been studied in detail; therefore to aid comparison with earlier work the coverage on these faces from this study is shown as a function of exposure in fig. 5.5 . The numbers refer to four different experiments like those shown in figs. 5.3 and 5.4 . Note that, in principle, similar graphs could be constructed for any intermediate face. The results of H have been chosen for comparison, as H has studied all three low-index faces. Fig. 5.6 shows his results taken from ref. 30. The two sets of results are compared in fig. 5.7 . Agreement is reasonable,

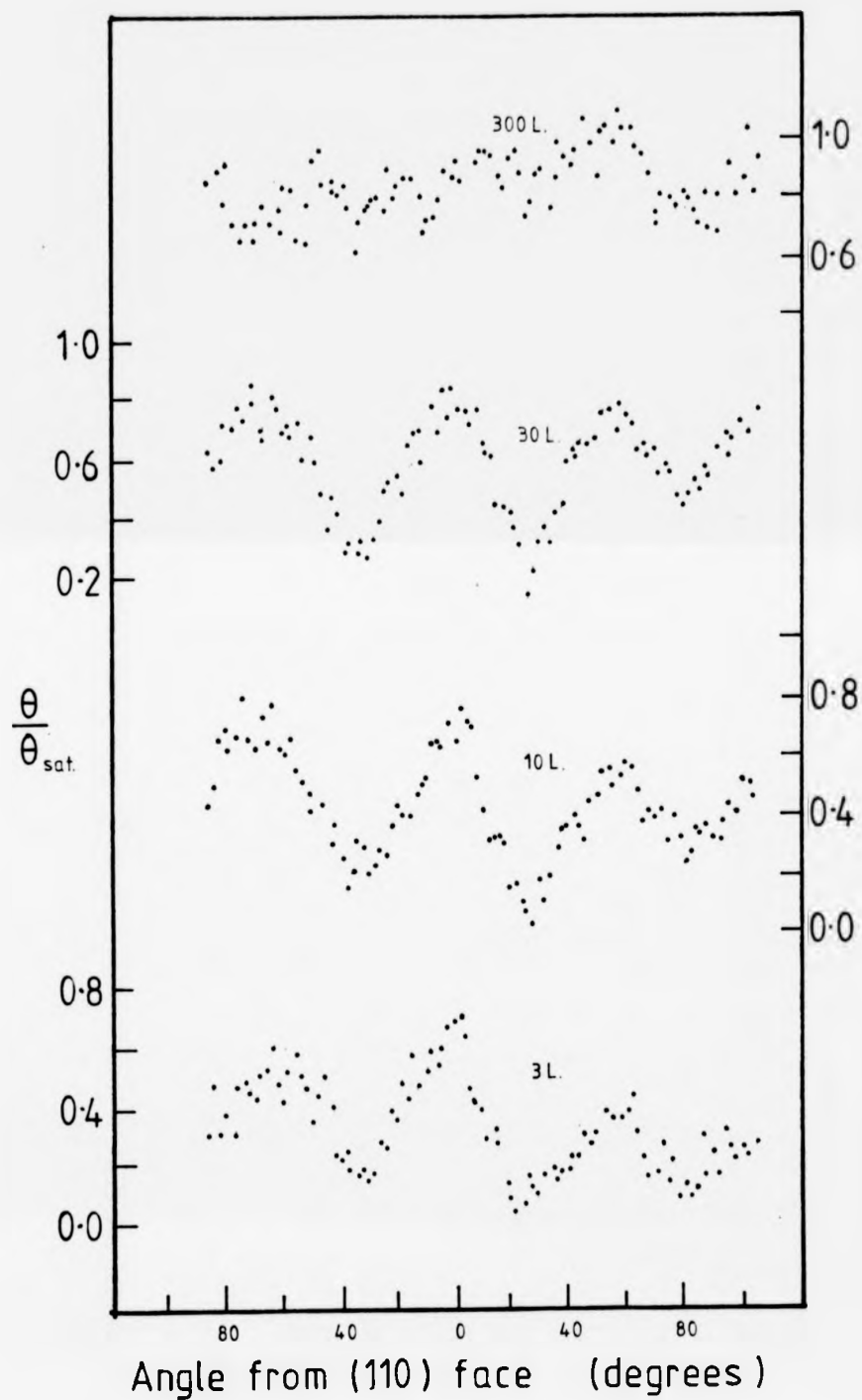


**FIG. 5.3** Normalised oxygen coverage around a copper cylinder exposed to increasing amounts of oxygen.

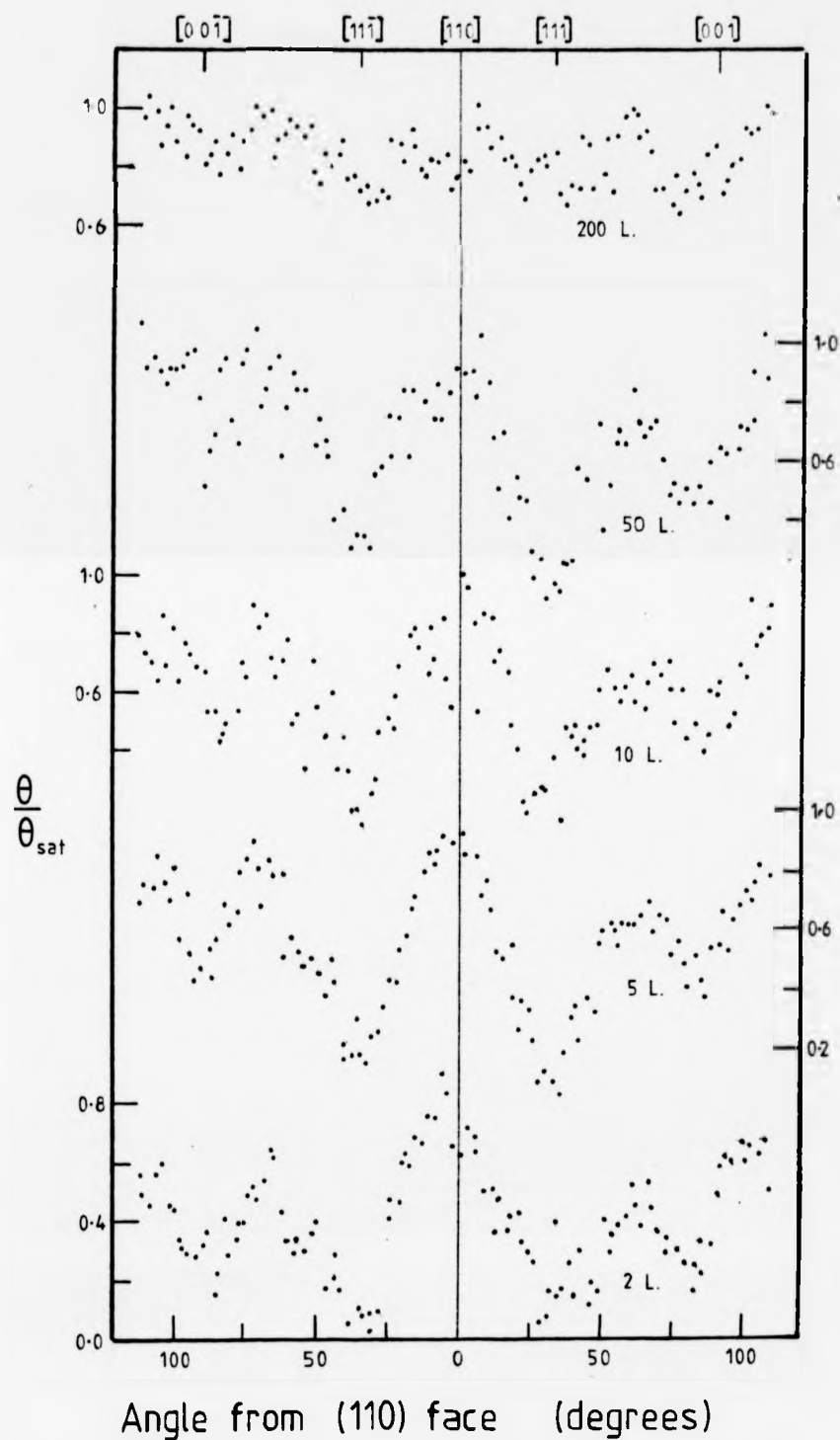


**FIG. 5.4** Normalised oxygen coverage around a copper cylinder exposed to increasing amounts of oxygen.

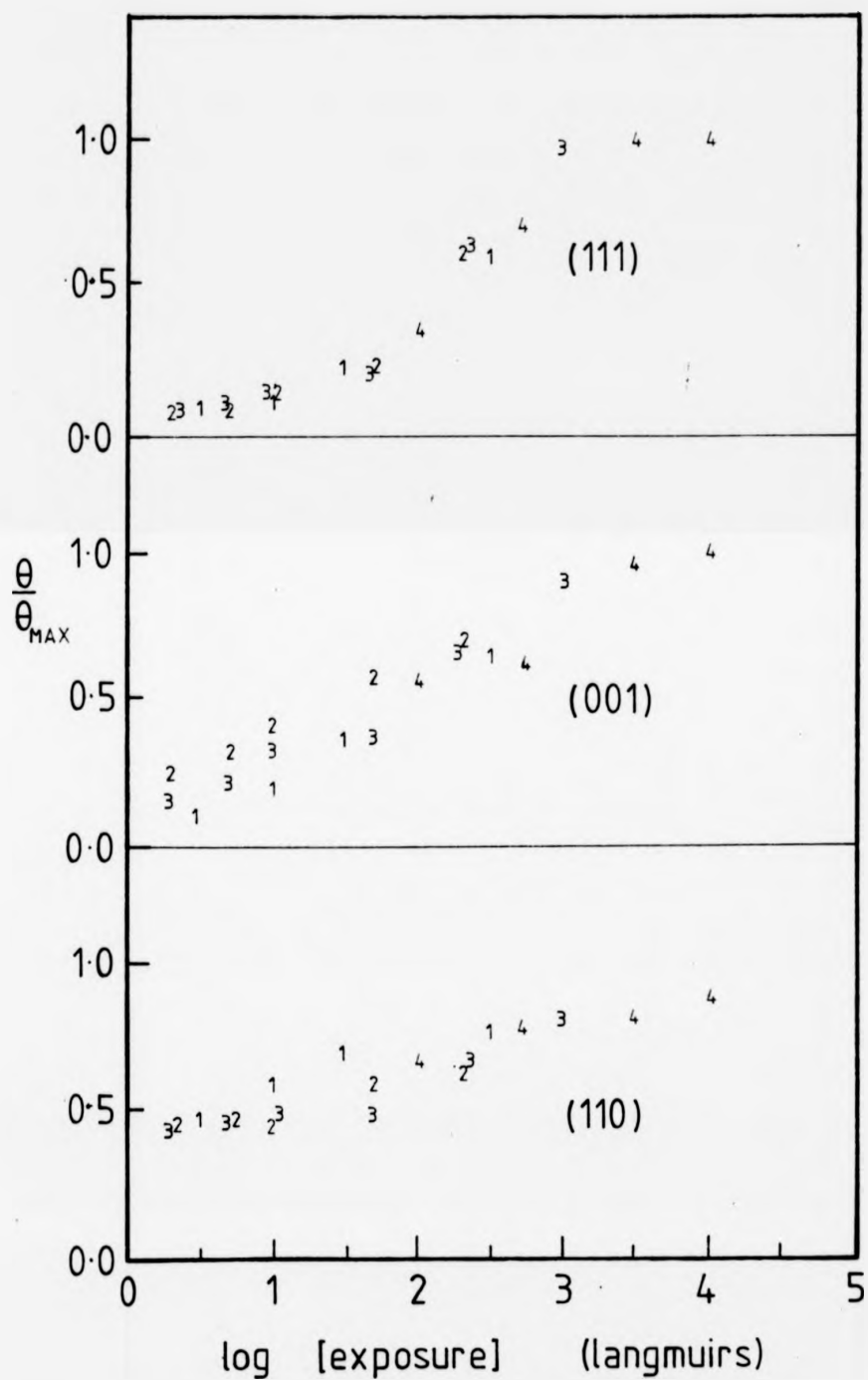


FIG. 5.5 Normalised oxygen coverage as a function of exposure for the three low index faces. Results are shown for four experiments on a copper cylinder.

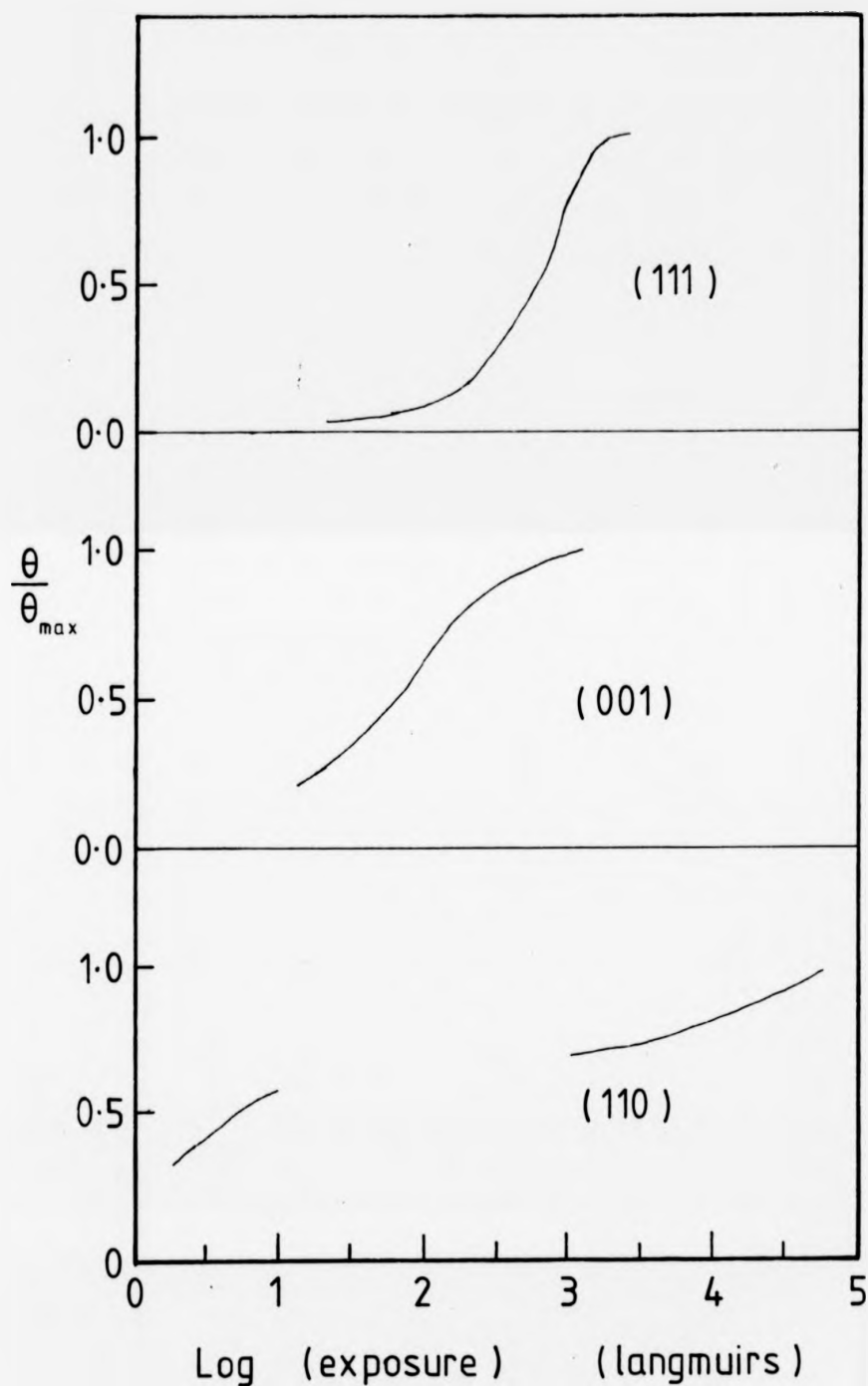


FIG. 5.6 Oxygen coverage as a function of exposure, taken from F.H.P.M.Habraken (ref. 30).



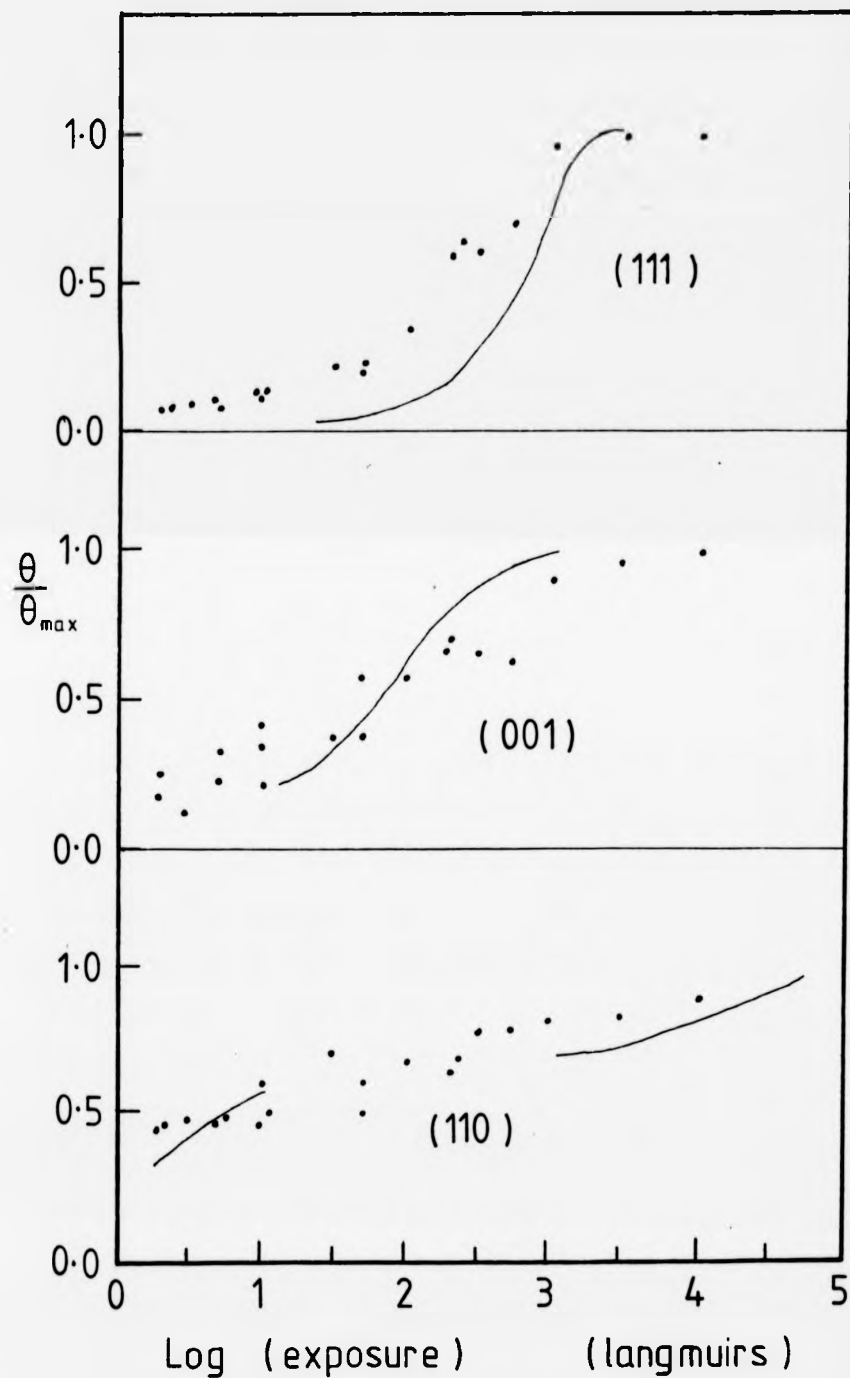


FIG. 5.7 Comparison of results from a copper cylinder (dots) with Habraken's results (solid lines).

Except for low coverages on the (111) face. Not surprisingly the results from this work show more scatter.

One problem with comparing adsorption kinetics studied by adsorption from an ambient gas pressure is the variation of exposure calibration between different vacuum systems. Differences of chamber geometry, ion gauge calibration and so on can lead to differences of a factor of two or more in exposure calibration. This would correspond to a linear shift in the logarithmic scale of fig. 5.5 relative to fig. 5.6 of about 0.3. This does not appear to be necessary, as the fit in fig. 5.7 would not be improved by shifting one set of data with respect to the other. Because of this good fit, the adsorption kinetics results of H will be used to model the results found for the cylindrical crystals.

#### 5.4 DISCUSSION

In order to understand the anisotropy of adsorption around the cylindrical surfaces (e.g. figs. 5.3 and 5.4), we need to develop a model that will describe the experimental results. Perdereau and Rhead<sup>33</sup> studied surfaces vicinal to a (100) plane, and they concluded; "adsorption takes place preferentially at steps and that the rate of adsorption increases with step density." This then provides the basis of a simple model. Ideally the initial sticking factor round the cylinder should be compared with the step density. Unfortunately the difficulty of performing experiments at very low exposures means that it has not been possible to obtain accurately the initial sticking factor as a function of position round the crystal. However, the oxygen coverage at low exposures should vary approximately with the initial sticking factor so that the oxygen coverage (at low exposures) should vary with the step density.

As was seen in Chap. 4, in the (110) zone the step density

varies with the  $C_7$  site density. Fig. 5.8 compares the 510eV oxygen Auger peak heights round the crystal (after an exposure of 2L of oxygen) with the  $C_7$  site density. The two agree remarkably well, but not perfectly. For example, the (001) faces have adsorbed more oxygen than the (111) type faces, although both types of face have zero step density.

This model of adsorption is simple, but limited. There is no obvious way in which it could be extended to predict adsorption kinetics. This is because we know from the work discussed earlier, that the kinetics of adsorption are different on different low-index faces. The success of the simple model of step density does suggest one way in which a model of the adsorption kinetics can be developed for the cylinder, and that is by considering an arbitrary surface as being composed of a mixture of flat and rough type surfaces.

Before developing models for the cylindrical surface, the kinetics on the low-index faces will be considered in detail.

#### 5.5 ADSORPTION KINETICS OF LOW-INDEX FACES.

We saw in Chap. 4 that an arbitrary face in the  $\{110\}$  zone contains only straight steps, with the step edge being parallel to the  $\{110\}$  direction. The face can therefore be split into stripes of a flat type ((001), (111)) or a rough type ((110), (113)) (fig. 5.9). Thus the surface roughness is highest where there is a greater proportion of the rough (110) or (113) type faces present. Thus the plot of surface roughness in fig. 5.8 is closely related to the plot of the proportions of (113) or (110) type face (fig. 5.9). If we know the adsorption kinetics for the four key faces shown in fig. 5.9, then some prediction for kinetics on intermediate faces can be made by combining the key face behaviour in suitable proportions.

The basis for this model must be a set of equations governing

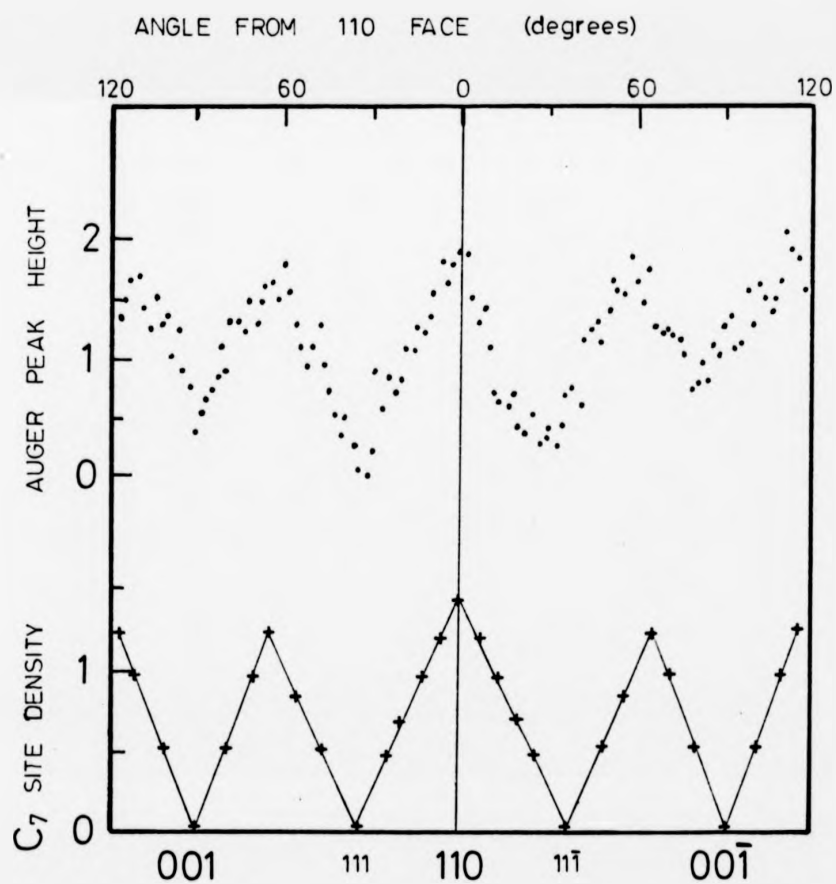


**FIG. 5.6** Comparison of oxygen Auger peak heights after a 2L exposure with the C<sub>7</sub> site density.

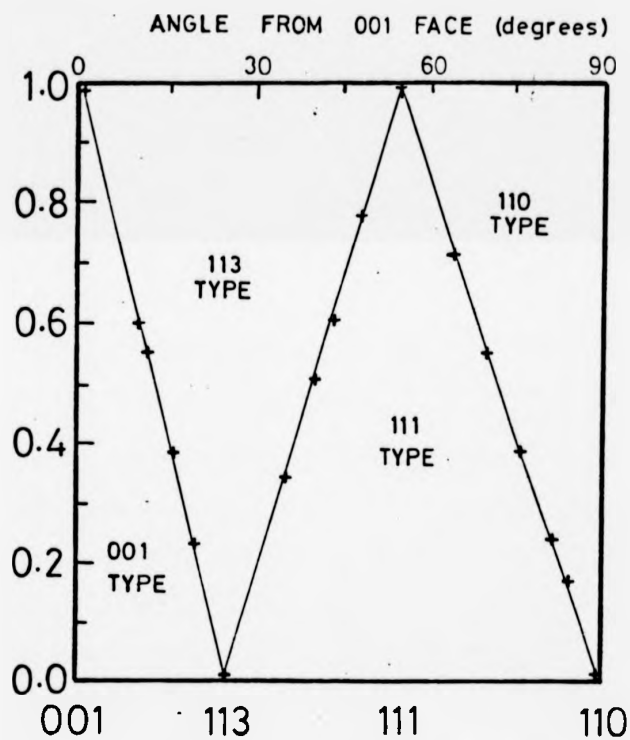


FIG. 5.9 Proportion of the four key faces present around the cylindrical sample.

the kinetics of adsorption on these four key faces. The most comprehensive work on kinetics, by H, covers the three low-index faces. Unfortunately data is not available for the (113) face. This face was studied by Gwathmey et al.<sup>2-4</sup>, but only for the formation of an oxide film. To the authors knowledge, data for the (113) in the chemisorption region does not exist.

To provide some sort of estimate of the adsorption kinetics, the assumption has been made that the (113) face behaves like the (110) face. The justification for this is two-fold. Firstly, the structure of the two faces is similar, that is both surfaces are ridged surfaces containing  $B_4$  and  $B_5$  adsorption sites. Secondly, Young, Cathcart and Gwathmey<sup>4</sup> found that the (113) face and the (110) face behaved almost identically, whereas the (111) and (001) faces each behaved differently. Admittedly this was for an experiment in the oxidation rather than chemisorption regime, but it does lend support to the hypothesis that the (113) and (110) faces behave similarly.

Although the ridged structure of the (113) and (110) faces are similar, the spacing between the ridges is different. This will be allowed for explicitly in the models for adsorption that will be developed.

If H's results are to be used as the basis of a model of adsorption on the cylinder, then the next step is to look at H's results in some detail. For the purpose of describing chemisorption resulting from exposures of less than  $10^3 L$  some simplification can be made to the equations that H derives for the low-index faces. For example, for the (111) face H found that the kinetics can be described by the equation of Kohrt and Gomer<sup>35</sup> for dissociative adsorption via a precursor state requiring a pair of adjacent sites. However, for exposures of less than  $10^3 L$  at room temperature the sticking factor is essentially constant, i.e. the coverage varies linearly

the kinetics of adsorption on these four key faces. The most comprehensive work on kinetics, by H, covers the three low-index faces. Unfortunately data is not available for the (113) face. This face was studied by Gwathmey et al.<sup>2-4</sup>, but only for the formation of an oxide film. To the authors knowledge, data for the (113) in the chemisorption region does not exist.

To provide some sort of estimate of the adsorption kinetics, the assumption has been made that the (113) face behaves like the (110) face. The justification for this is two-fold. Firstly, the structure of the two faces is similar, that is both surfaces are ridged surfaces containing  $B_4$  and  $B_5$  adsorption sites. Secondly, Young, Cathcart and Gwathmey<sup>4</sup> found that the (113) face and the (110) face behaved almost identically, whereas the (111) and (001) faces each behaved differently. Admittedly this was for an experiment in the oxidation rather than chemisorption regime, but it does lend support to the hypothesis that the (113) and (110) faces behave similarly.

Although the ridged structure of the (113) and (110) faces are similar, the spacing between the ridges is different. This will be allowed for explicitly in the models for adsorption that will be developed.

If H's results are to be used as the basis of a model of adsorption on the cylinder, then the next step is to look at H's results in some detail. For the purpose of describing chemisorption resulting from exposures of less than  $10^3 L$  some simplification can be made to the equations that H derives for the low-index faces. For example, for the (111) face H found that the kinetics can be described by the equation of Kohrt and Gomer<sup>35</sup> for dissociative adsorption via a precursor state requiring a pair of adjacent sites. However, for exposures of less than  $10^3 L$  at room temperature the sticking factor is essentially constant, i.e. the coverage varies linearly

with the exposure. For the (100) face, H finds that his results can be described by simple second order kinetics with the sticking factor  $S$  being described by :

$$S = (1 - \theta)^2 \quad 5.1$$

where  $\theta$  is the coverage in monolayers. The behaviour of the (110) face, according to H, can be described by Langmuir kinetics if dissociative adsorption on empty nn site pairs and an attractive interaction in the adsorbed layer are taken into account. However for the purpose of developing a model to describe the kinetics on intermediate faces, a simpler, but adequate, description for the (110) face is possible using the second order kinetics equation (5.1).

H.'s data for the variation in the room temperature coverage on the (110) face as a function of the exposure is shown in fig. 5.10. The solid line represents the integral of H.'s equation, while the broken line is the integral of eqn. 5.1 i.e.:

$$cS_0 E = \frac{\theta}{0.5 - \theta} \quad 5.2$$

where  $E$  is the exposure in Langmuirs,  $S_0$  is the initial sticking factor, and  $c$  is a constant ( the integration of eqn. 5.1 is given in appendix A ).

Note that the limited amount of experimental data presented by H is described as well by the simple equation, 5.2. One major difference that results from the two different equations is the difference in the gradients at zero coverage (i.e. the initial sticking factors). H's equation yields a value for the sticking factor,  $S_0$ , of 0.17. The simple second order kinetics equation yields a value of 0.86.

To test these simple equations for the low index faces, they have been used to plot H's data in the form shown in fig. 5.11. For the (111) face, if  $\theta$  is proportional to  $E$ , then  $\theta/E$  should be constant; this is in fact the case. For the (110) face eqn. 5.2



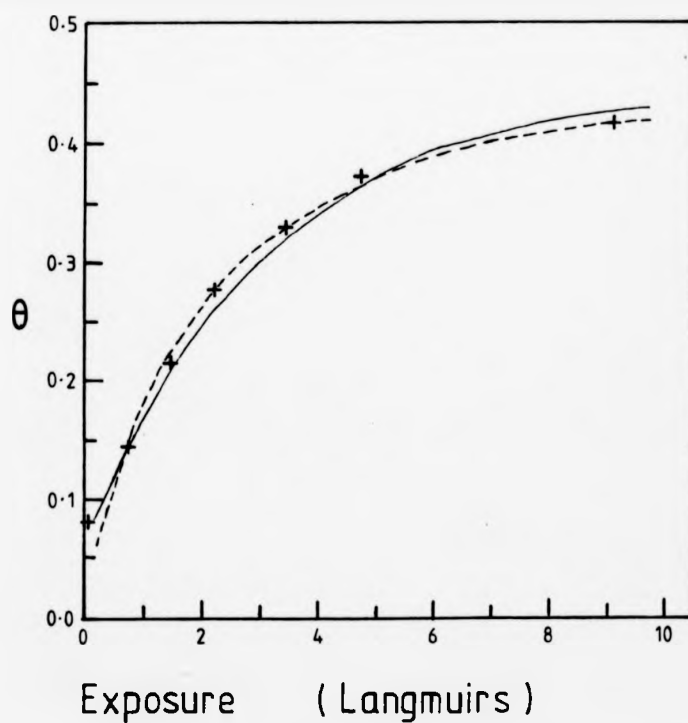


**FIG. 5.10** Possible curves that could be fitted to Habraken's data:  
 + = Habraken's experimental results (ref.30) for (110),  
 solid line = Habraken's equation,  
 broken line = simple (001) type equation.

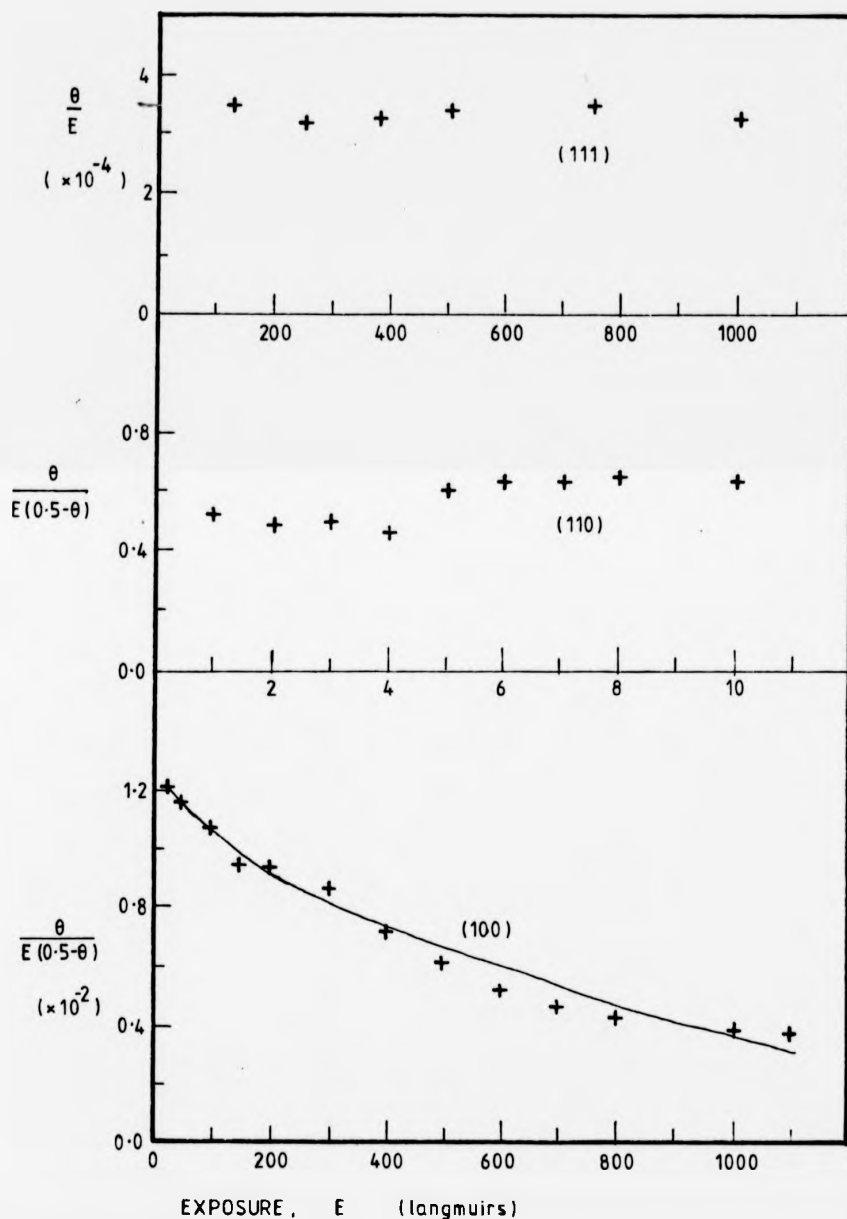


**FIG. 5.11** Test of the simple equations describing oxygen adsorption on the three low index faces. The solid line on the graph for the (100) face is the result of a least squares fit.

can be re-arranged to give :

$$\frac{\theta}{E(0.5-\theta)} = C S_0 \quad 5.3$$

Consequently the left hand side of equation 5.3 should be constant. This is in fact the case as can be seen from fig. 5.11. According to H, equation 5.3 should also be true for the (100) face. Fig. 5.11 shows that  $E(\frac{\theta}{.5-\theta})$  varies quite markedly. So we find that the equation derived by H for the (100) plane fits his results for the (110) plane better than his results for the (100) plane! It would be possible to describe the variation in the value of  $\frac{\theta}{E(0.5-\theta)}$  by the empirical equation :

$$\frac{\theta}{E(0.5-\theta)} = 1.37 \times 10^{-2} - 3.17 \times 10^{-4} \sqrt{E} \quad 5.4$$

This equation is shown as a solid line in fig. 5.11 and was obtained by the method of the least squares approximation. Note that this empirical alteration of equation 5.3 has no physical basis. Furthermore it only has a minor effect in the region of interest, but does allow H's results to be described accurately. However, it must be borne in mind that equation 5.4 breaks down for exposures of about 1,800L or greater.

The three equations are plotted in fig. 5.12 in a form in which they can be compared with H's experimental results (fig. 5.6).

In calculations, however, it will be assumed for simplicity that

equation 5.3 without the empirical alteration of 5.4 is an adequate description of the behaviour of the (001) face. For the (001) and (111) faces the coverage saturates at about 0.5 monolayers at the end of the chemisorption stage. However on the (110) saturation does not occur at 0.5 monolayer and reconstruction of the surface layers takes place at high coverages. Therefore in fig. 5.6  $\theta_{max}$  corresponds to the end of the chemisorption regime for the (100) and (111) faces but not for the (110) face. This has been allowed for in the plot for the (110) face in fig. 5.12.

Comparing figs. 5.6 and 5.12, it can be seen that the three equations plotted in fig. 5.12 describe H's experimental results

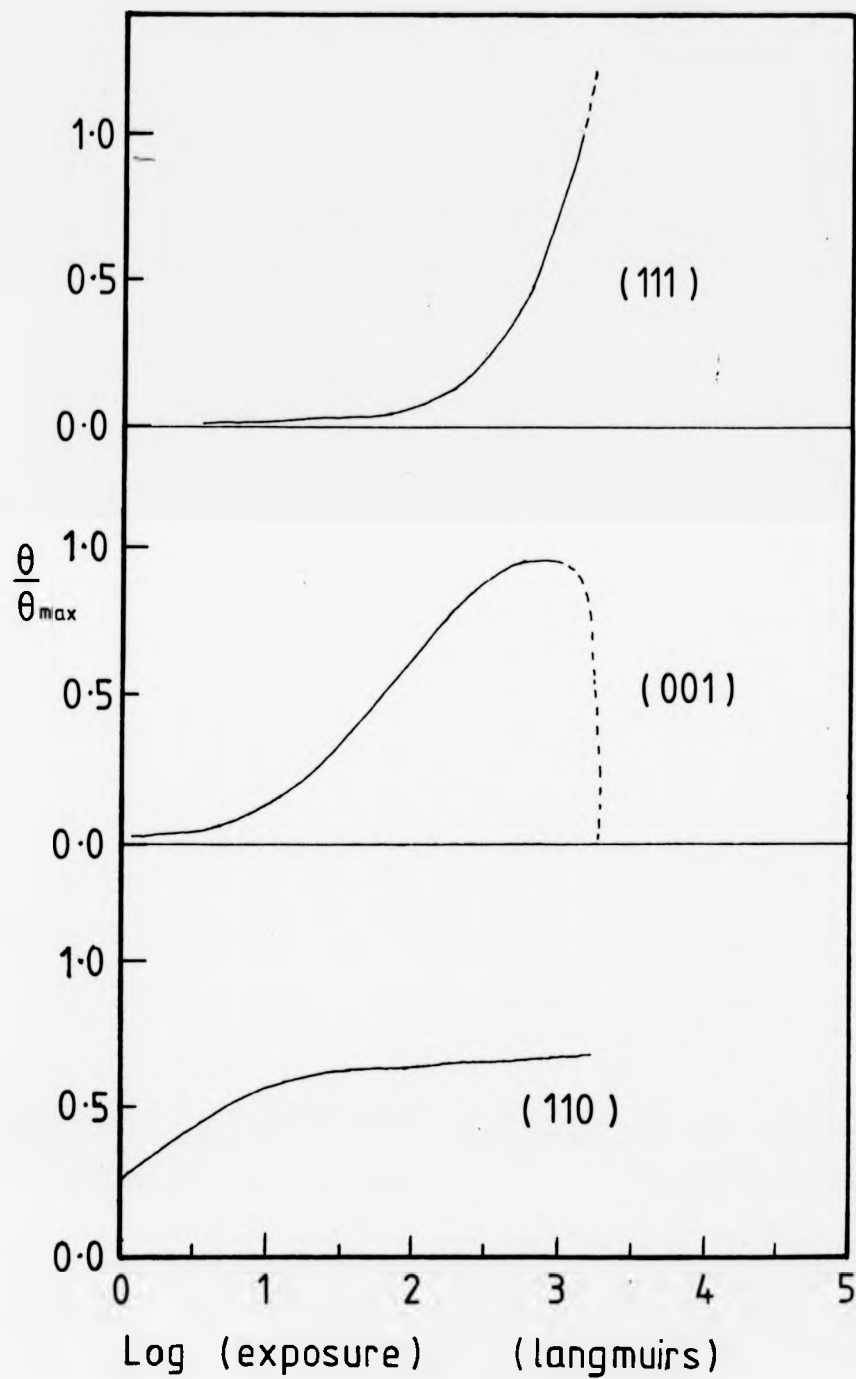


FIG. 5.12 The three equations of fig. 5.11 plotted in a form in which they can be directly compared with H's results (fig 5.6)

in fig. 5.6 very accurately up to approx.  $10^3$ L, but break down at higher exposures. These equations should provide a firm basis for modelling the kinetics of adsorption, as we have already seen that the anisotropic adsorption occurs only up to about 300L (further adsorption being essentially isotropic). Thus the region of interest (the chemisorption region) occurs well within the region where these equations are valid.

## 5.6 ADSORPTION KINETICS MODELS

### MODEL 1

The rate of change of oxygen coverage on a crystal surface is given by the following equation :

$$\frac{d\theta}{dt} = c'ps \quad \text{5.5}$$

where  $c'$  is a constant,  $p$  is the oxygen pressure and  $s$  is the sticking factor.

The constant  $c'$  can be derived from standard gas kinetic theory; it relates the number of gas atoms arriving at unit area of the surface in unit time with the number of atoms per unit surface area necessary to form one monolayer of adsorbed gas atoms.  $S$  is generally some function of  $\theta$  itself; for a low-index surface  $s$  is often a simple function of  $\theta$ . For example we saw in section 5.5 that the adsorption of oxygen on the three low-index copper faces can be described by :

$$\left. \begin{array}{l} 001 : S_1 = S_{o1} (1-\theta)^2 \\ 111 : S_3 = S_{o3} \\ 110 : S_4 = S_{o4} (1-\theta)^2 \end{array} \right\} \quad \text{5.6}$$

where  $S_{oi}$  is the initial sticking factor of the  $i^{\text{th}}$  face using the notation that  $i = 1, 2, 3, 4$  for the (001), (113), (111) and (110) faces respectively.

The above equations describe only three of the four key faces; no previous work on the (113) face has been reported. As discussed earlier, the assumption will be made that the (113) face behaves like the (110) face. However the spacing of the ridges on the (113) plane is greater than on the (110) plane, i.e. the site density is less on the (113) plane (by about 15%). Thus, for want of a better description of the behaviour of the (113) plane, we postulate that the (113) plane behaves exactly like the (110) plane, except that the initial sticking factor is correspondingly smaller. Therefore, to the above equations can be added :

$$113 : S_2 = S_{02} (1-2\theta)^2 \quad \underline{5.6}$$

where  $S_{02} = 0.853 \times S_{04}$

These equations can be integrated so that equations for these four faces can be obtained that relate the coverage in monolayers ( $\theta$ ) to the oxygen exposure in Langmuirs ( $E$ ). The integration of the equation common to the other three faces is given in appendix A. The resulting equations are :

$$\left. \begin{aligned} 001 : \theta_1 &= 0.5 / \left(1 + \frac{1}{EC_1 S_{01}}\right) \\ 113 : \theta_2 &= 0.5 / \left(1 + \frac{1}{EC_2 S_{02}}\right) \\ 111 : \theta_3 &= C_3 S_{03} E \\ 110 : \theta_4 &= 0.5 / \left(1 + \frac{1}{EC_4 S_{04}}\right) \end{aligned} \right\} \quad \underline{5.7}$$

The values of the constants  $C_i$   $S_i$  can be derived from H's work as plotted in fig. 5.11. For example, for the (110) face, the left hand side of equation 5.3 (which has been plotted in fig. 5.11) is equal to  $C_4 S_{04}$ .

As we have already seen, the left hand side of equation 5.3 is not exactly constant for the (001) face. For this face therefore  $C_3 S_{03}$  has been taken to be the average value of the left hand side of equation 5.3 in the region of interest (i.e. up to 500L). The value of  $C_i S_{0i}$  for the four key faces is given in table 5.6.1.

TABLE 5. 1.

i	Face	$C_i S_{0i}$
1	001	$9.41 \pm 1.8 \times 10^{-3}$
2	113	$4.87 \pm 0.5 \times 10^{-1}$
3	111	$3.38 \pm 0.1 \times 10^{-4}$
4	110	$5.71 \pm 0.6 \times 10^{-1}$

In developing a model to describe the kinetics on intermediate faces, an assumption must be made about the way in which the behaviour of the intermediate faces is related to the behaviour of the low-index faces. The first model is based on the assumption that the "rough" and "smooth" portions of an arbitrary intermediate face behave independently. That is to say, that the coverage,  $\theta$ , on the intermediate face will simply be a linear combination of the coverage on the key face areas that are present, i.e.

$$\theta = \sum_i \alpha_i \theta_i \quad \text{5.8}$$

where  $\theta_i$  is the coverage on the  $i^{\text{th}}$  key face, and  $\alpha_i$  is the proportion of that key face that is present in the face under consideration.

One simplifying factor is that although there are 4 possible key faces present (i.e.  $i$  can take any value from 1 to 4), any arbitrary face consists of a combination of only two key faces. Thus there is always one "smooth" ((001) or (111)) and one "rough" ((113) or (110)) type face.

In equation 5.8  $\alpha_i$ , the proportion of a key face that is present, is a linear function of the angular position round the crystal, and has already been plotted in fig. 5.9.  $\alpha_i$  is equal to the angle between the intermediate face and the  $i^{\text{th}}$  key face, divided by the total angle between the two key faces that the intermediate face is situated between. As an example, let us consider the (221) face. This face lies between the (111) and (110) faces so that using the above notation, equation 5.8 becomes :

$$\theta(221) = \alpha_3 \theta_3 + \alpha_4 \theta_4$$

On substituting for  $\theta_3$  and  $\theta_4$  from equation 5.7, we obtain :

$$\theta_{(221)} = \alpha_3 C_3 S_{O_3} E + \alpha_4 \left( \frac{0.5}{1 + \frac{1}{E \cdot A \cdot S_{O_4}}} \right)$$

where the constants  $C_3 S_{O_3}$  and  $C_4 S_{O_4}$  are given in table 5.6.1.

Now the (221) face is approximately  $15.8^\circ$  from the (111) face, and  $19.5^\circ$  from the (110) face so that :

$$\alpha_3 \approx \frac{15.8}{15.8 + 19.5} \approx 0.448$$

and

$$\alpha_4 = 1 - \alpha_3 = \frac{19.5}{15.8 + 19.5} \approx 0.552$$

Thus, for the (221) plane we obtain :

$$\theta_{(221)} \approx 1.51 \times 10^{-4} E + 0.552 \left( \frac{0.5}{1 + \frac{1}{0.571 \times E}} \right)$$

In this manner the coverage round the crystal can be calculated for any arbitrary face, and this model has been used to calculate the coverages shown in fig. 5.13 and fig. 5.14. These figures have been plotted in such a manner as to make them readily comparable with the experimental results plotted in figs. 5.3 and 5.4.

#### MODEL 2

For the second model, we make the assumption that the rough and smooth areas of an intermediate face can interact by the instantaneous diffusion of adatoms. We will assume that on any particular face the oxygen adatoms are distributed evenly over that face. Instead of the coverage being the weighted average of the coverage on the rough and smooth sections of that face as in the first model, it is now the sticking factor that is the weighted average of the sticking factors on the component sections of the face.

This second assumption is not realistic in that if there was infinitely fast diffusion over a face we would still expect the adatoms to accumulate in areas of higher binding energies (i.e. the rough section). However, by assuming an even covering over a face, it does allow us to develop a simple model that includes some interaction between the rough and smooth sections of a face.



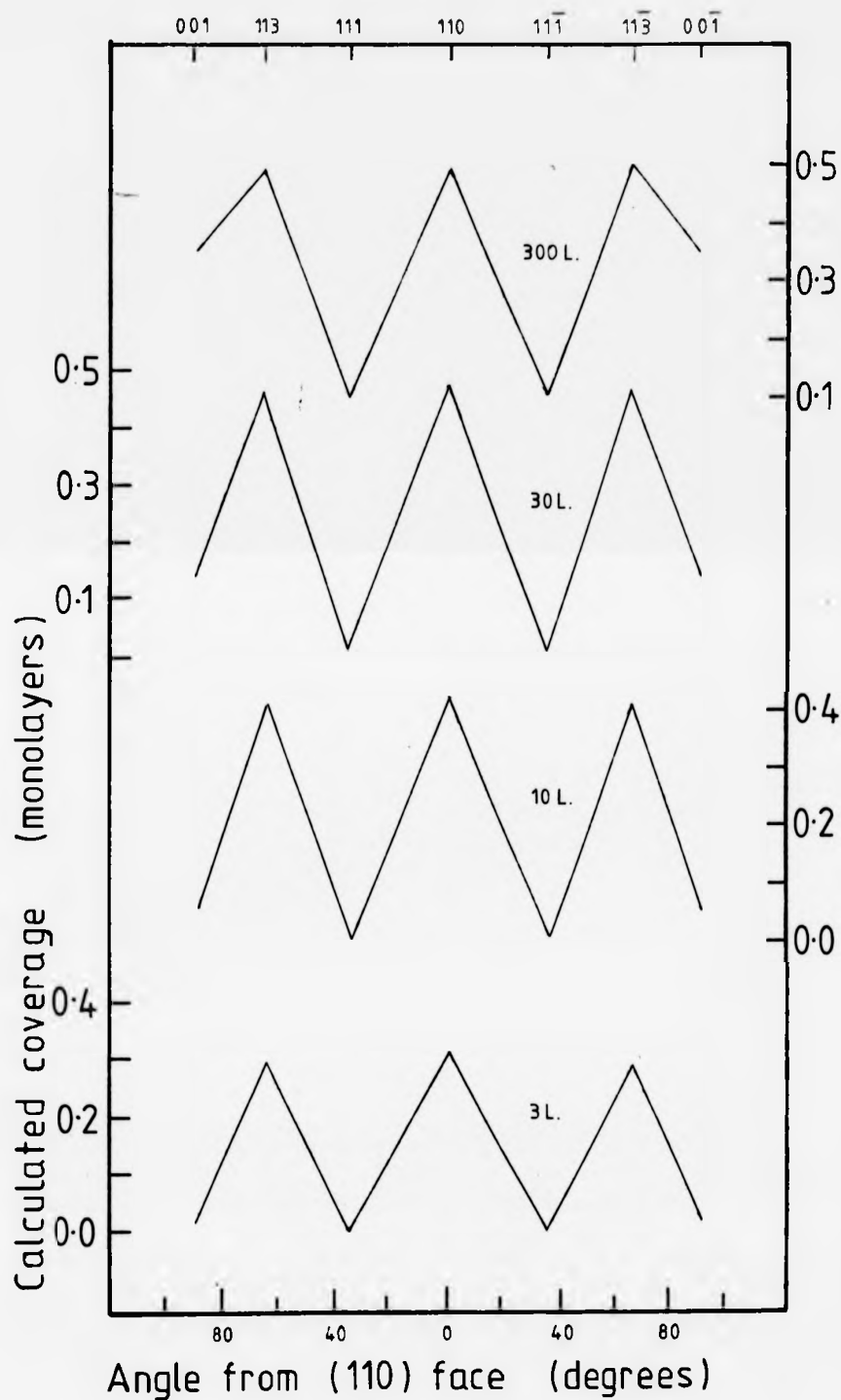


**FIG. 5.13** Calculated oxygen coverages at increasing exposures, (model 1).

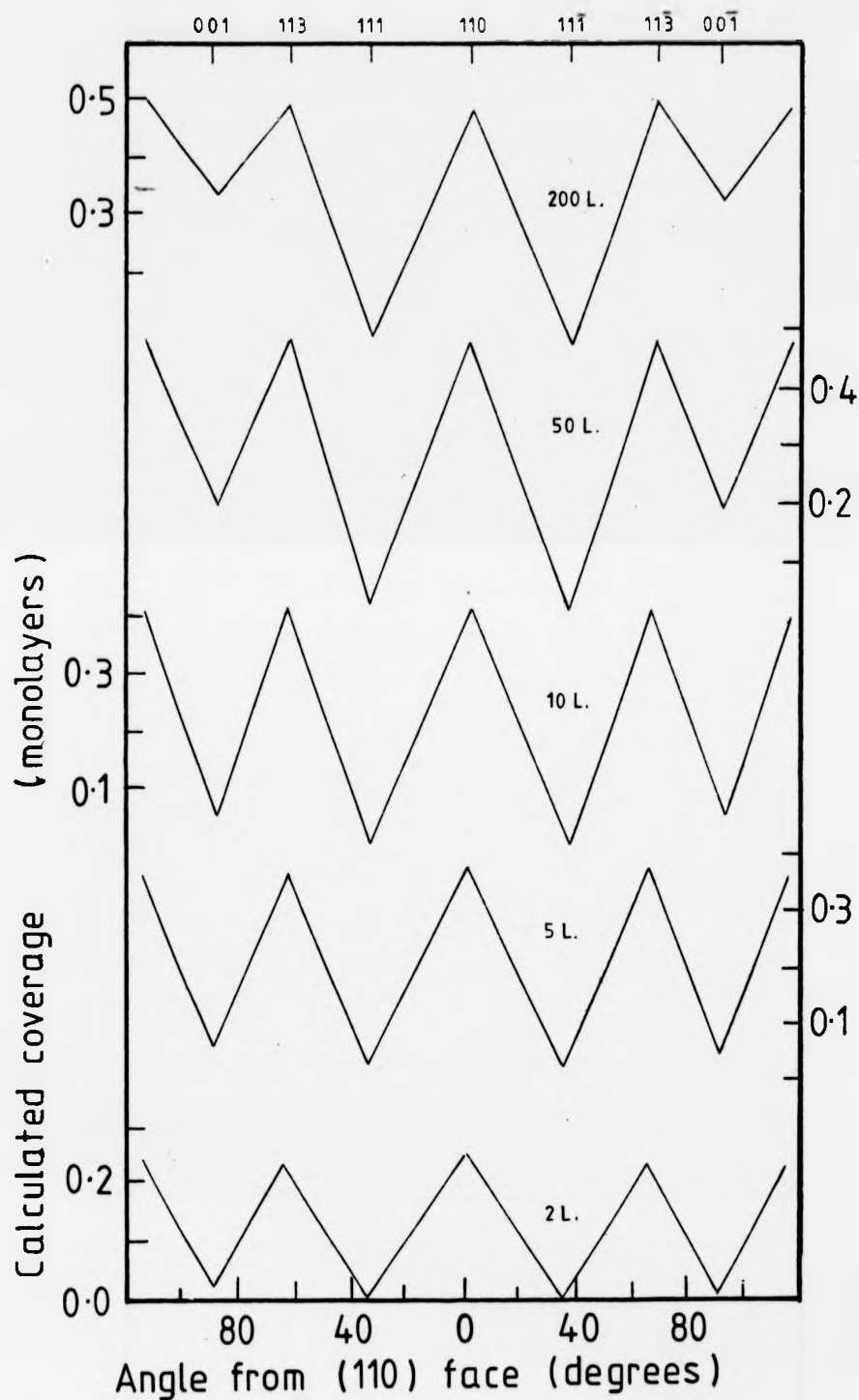


FIG. 5.14 Calculated oxygen coverages for increasing exposures, (model 1).

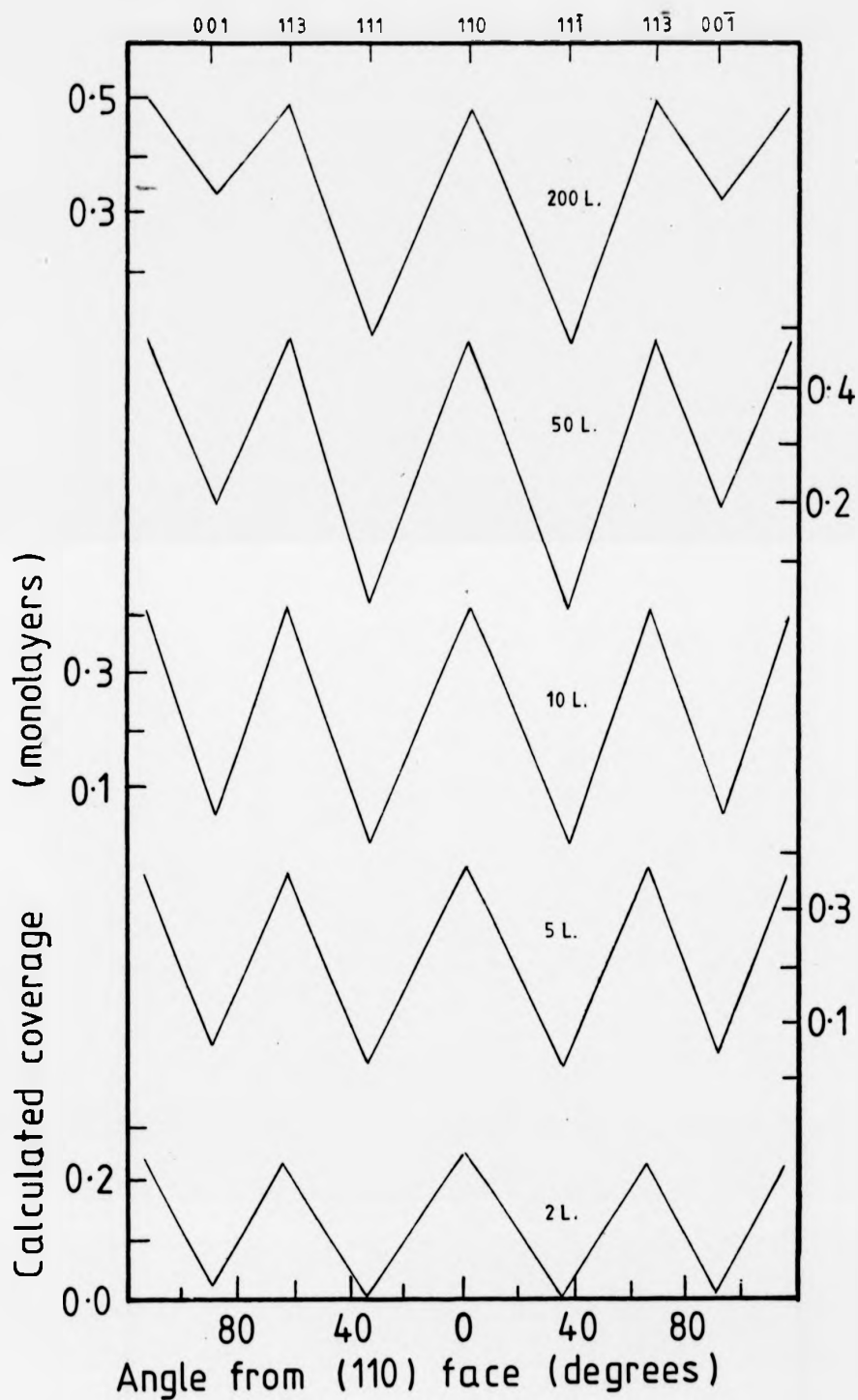


FIG. 5.14 Calculated oxygen coverages for increasing exposures, (model 1).

Equation 5.5 will become :

$$\frac{d\theta}{dt} = \sum_i P_i \alpha_i C_i S_{oi} \quad 5.9$$

where the factors  $C_i S_{oi}$  are given in equation 5.6.

Again let us consider the example of the (221) face. Substituting equation 5.6 into 5.9, we obtain :

$$\frac{d\theta}{dt} = P \alpha_3 C_3 S_{o3} + \alpha_4 C_4 S_{o4} (1-2\theta)^2$$

This can be rearranged to give :

$$\frac{d\theta}{dt} = P \alpha_4 C_4 S_{o4} \left[ \frac{\alpha_3 C_3 S_{o3}}{\alpha_4 C_4 S_{o4}} + (1-2\theta)^2 \right]$$

$$\text{let } \delta = \frac{\alpha_3 C_3 S_{o3}}{\alpha_4 C_4 S_{o4}}$$

then

$$\frac{d\theta}{dt} = P \alpha_4 C_4 S_{o4} \left[ (1-2\theta)^2 + \delta \right] \quad 5.10$$

Equation 5.10 cannot be integrated analytically. Because  $S_{o3}$  (the sticking factor on the (111) plane) is much smaller than  $S_{o4}$  (the sticking factor on the (110) plane),  $\delta$  is very small. Because of this, a Taylor expansion for equation 5.10 can be obtained which may be integrated (see appendix B).

#### GENERAL RESULT

The equations for the coverage on an intermediate surface (as derived in appendix B) are as follows :

for surfaces between the (001) ( $i=1$ ) and (113) ( $i=2$ ) faces:

$$\theta = \frac{0.5}{1 + \left[ \frac{1}{E C_1 S_{o1} \alpha_1 + \alpha_2 C_2 S_{o2}} \right]} \quad 5.11$$

This equation is of the same form as equation 5.7; the values of  $C_i S_{oi}$  have been given in table 5.6.1.

For surfaces between the (113) and (111) ( $i=3$ ) faces:

$$E(\alpha_2 C_2 S_{o2}) = \frac{1}{1-2\theta} - \frac{\delta/3}{(1-2\theta)^3} + \frac{\delta}{3} - 1$$

$$\text{where } \delta = \frac{\alpha_3 C_3 S_{o3}}{\alpha_2 C_2 S_{o2}} \quad 5.12$$

Similarly for surfaces between the (111) and (110) ( $i=4$ ) faces :

$$E(\alpha_4 C_4 S_{04}) = \frac{1}{(1-2\theta)} - \frac{\delta'/3}{(1-2\theta)^2} + \frac{\delta'}{3} - 1$$

$$\text{where } \delta' = \frac{\alpha_3 C_3 S_{03}}{\alpha_4 C_4 S_{03}} \quad \underline{5.13}$$

In equations 5.12 and 5.13,  $\delta$  is small and is only significant near the (111) plane. For example for an intermediate face  $6^\circ$  from the (111) face in the direction of the (110) face,  $\delta/3$  in equation 5.13 is  $2.73 \times 10^{-3}$ .

One problem arises at comparatively high coverages, and that is that the model we have chosen for the (111) plane is no longer valid. H showed that above a coverage of about 0.3 monolayers, the coverage on the (111) plane ceases to vary linearly with the exposure. In model 1 this presented no problem because for an independent (111) plane this did not occur until approximately  $10^3 L$ , i.e. at a coverage higher than we are interested in. But, for model 2, the coverage on the (111) portions of an intermediate plane is increased by diffusion from the rough (110) or (113) areas. This means that a coverage of 0.3 monolayers is attained at comparatively low exposure. H found that for the (111) face the sticking factor dropped sharply above 0.3 monolayers and was zero at approx. 0.4 monolayers. For the purpose of model 2, therefore, the assumption has been made that on the (111) type face the sticking factor is constant up to a factor of 0.35 monolayers, and zero above this figure. This comparatively crude approximation can be made because the contribution to the total sticking factor of the (111) plane is so small. For example, for the surface  $6^\circ$  from the (111) plane (i.e.  $29.3^\circ$  from the (110) plane) the (111) type area (which covers 83% of this surface) contributes at most 5% towards total coverage.

The coverages predicted by this model have been plotted in figs. 5.15 and 5.16 in a form which is directly comparable with the predictions of model 1 (figs. 5.13 and 5.14) and the experimental results (figs. 5.3 and 5.4)

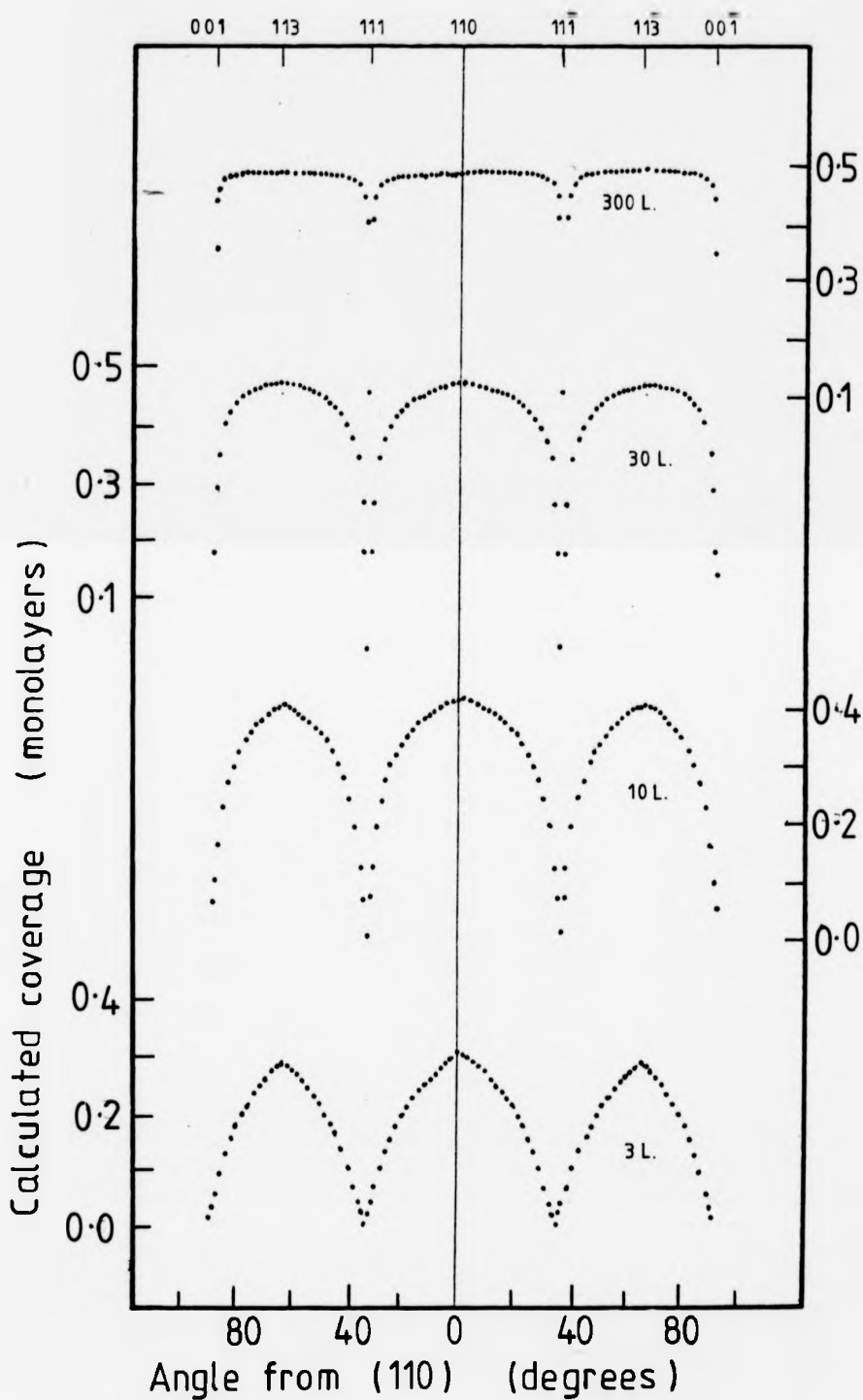


FIG. 5.15 Oxygen coverages calculated using model 2.

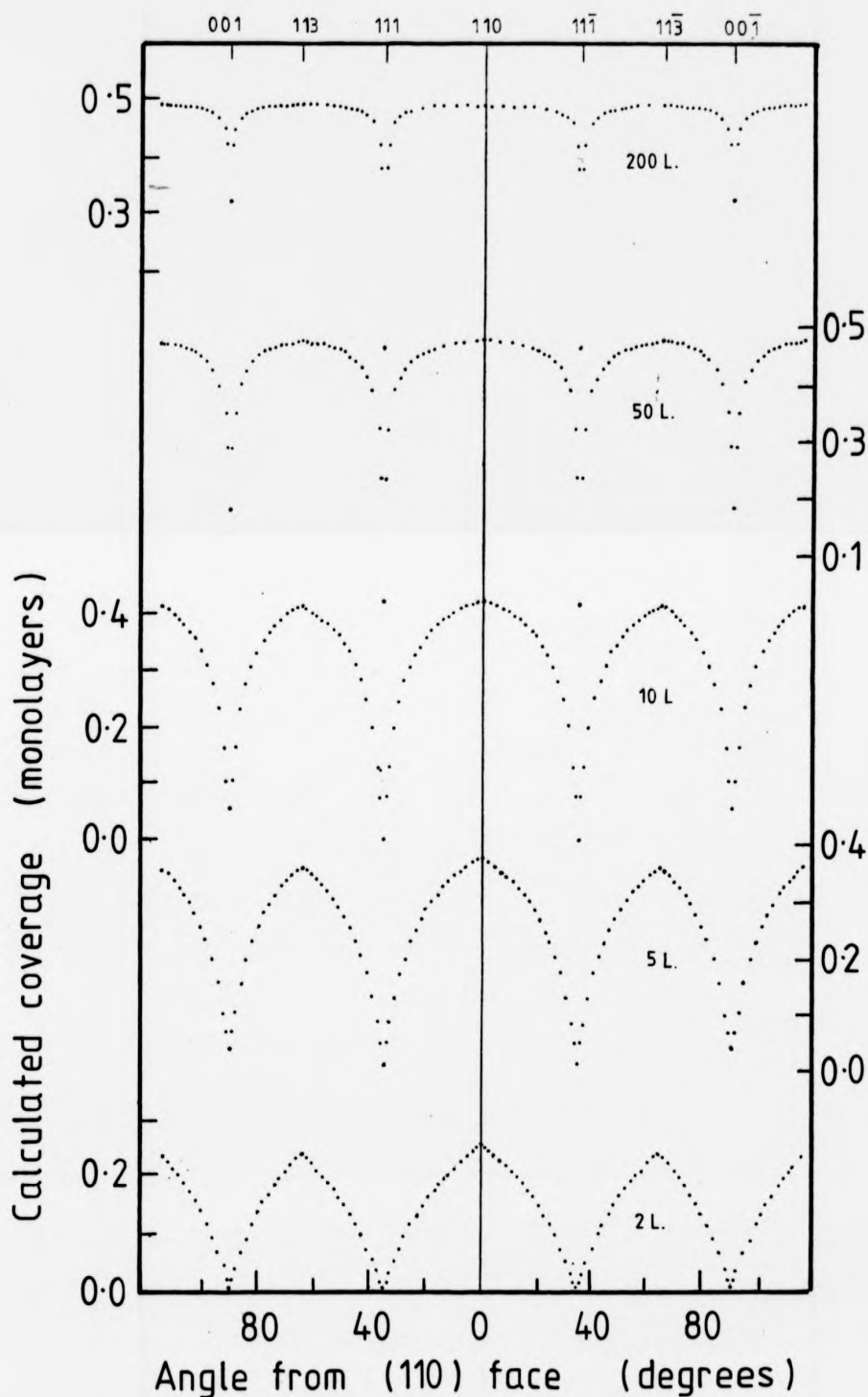


FIG. 5.16 Oxygen coverages calculated using model 2.

## 5.7 CONCLUSIONS

The coverages predicted by models 1 and 2 have been plotted with the results of two experiments in figs.5.17 and 5.18. It can be seen that, as is to be expected, the greatest difference in the coverage predicted by the two models is in the vicinity of the flat (001) and (111) surfaces. Particularly at high coverages the second model leads to sharp cusps at these atomically smooth surfaces. These cusps are so sharp that they would not be fully resolved using an electron probe beam in which the spot size covers an area of the cylinder where the surface orientation varies by  $1^\circ$  or  $2^\circ$ .

An experiment was done after an oxygen exposure of 2L over a small area of the cylinder in which more detailed measurements were taken than in the previous experiments. The results are shown in fig.5.19. The coverage calculated from model 1 is also shown normalised to the experimental result at the (110) surface. At this low exposure the agreement between the experimental and calculated coverage is very good.

The predicted coverage (particularly from model 1) describes the experimental results well at low exposures, but poorly at exposures of approx. 200L and above. This is not surprising because the model is based on kinetics equations that have been derived from Habraken's work, and we know that in comparing the low-index areas of the cylinder with Habraken's results, the poorest agreement was found in the sets of readings for the (111) plane.

The two models proposed to account for the adsorption of oxygen on copper have been extremes i.e. Model 1, no surface diffusion; Model 2, infinitely fast diffusion. In practice the actual behaviour may be intermediate between these extremes. There is evidence



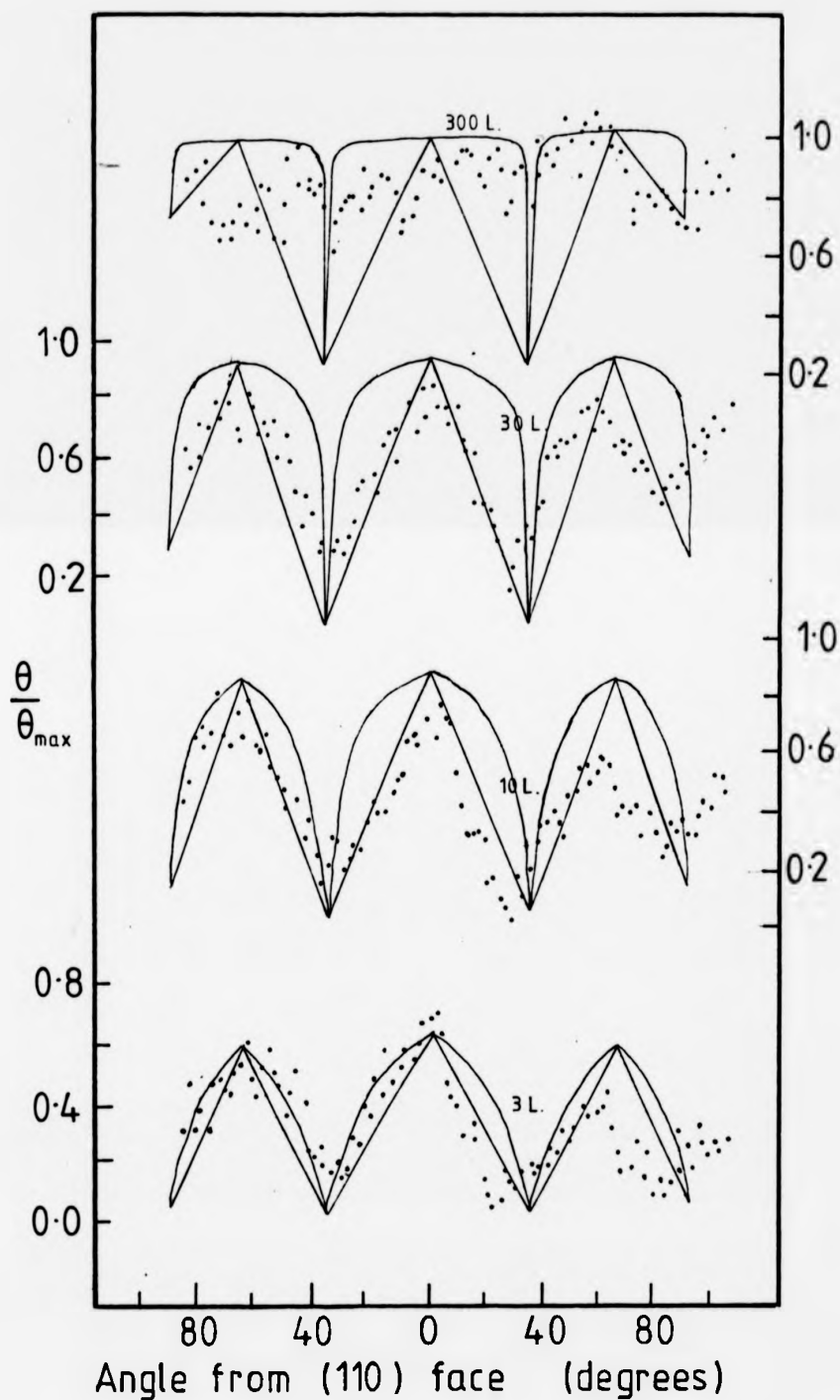


FIG. 5.17 Comparison of figs. 5.3, 5.13, 5.15.

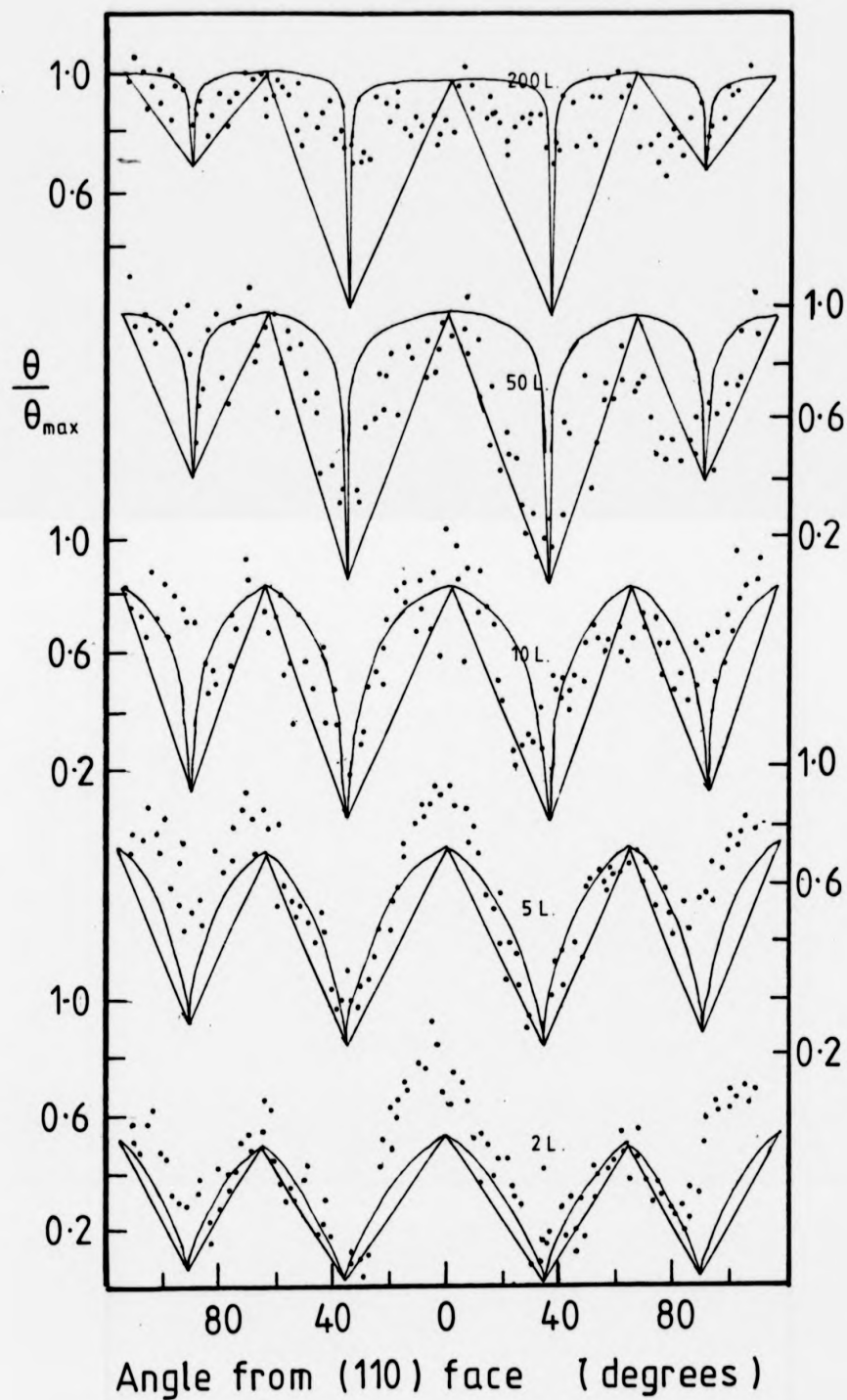


FIG. 5.18 Comparison of figs. 5.4, 5.14, and 5.16.

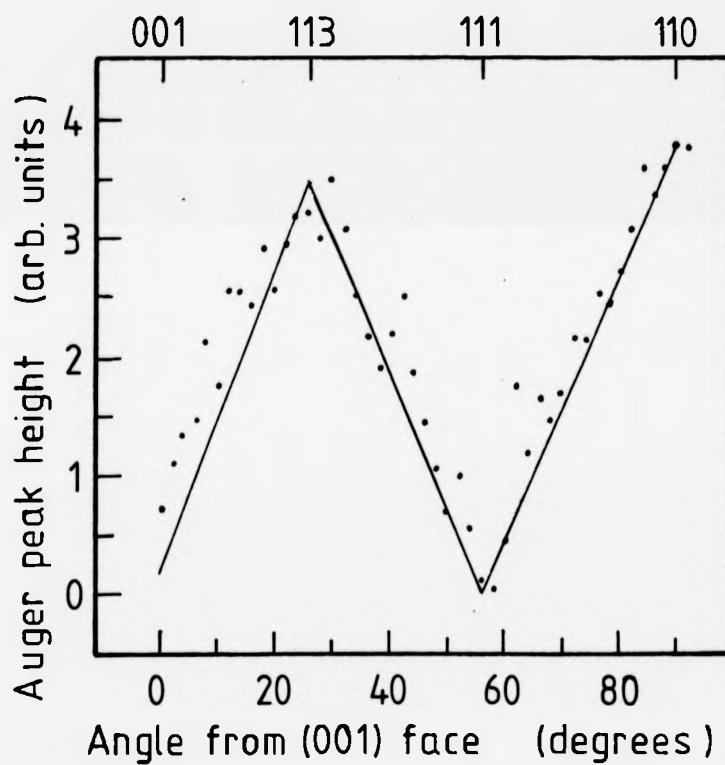


FIG. 5.19 Coverage predicted by model 1 compared with the 510eV Auger peak after an exposure of 2 Langmuirs.

of mobile precursor states on the (100) and (111) surfaces. An ordered superstructure forms on the (100) surface <sup>7,9,11,H</sup>, but not on the (111) surface below about  $5 \times 10^4$  L. <sup>6,11</sup>. This suggests that the formation of a superstructure is not controlled by the rate of surface diffusion of a precursor state (which ought to be fastest on the smooth (111) surface). The lack of an ordered superstructure on the (111) surface is therefore more likely to be due to the low binding energy of the (111) surface allowing the precursor states to diffuse away from the (111) surface rather than to bind on to it. It is therefore likely that the slow diffusion model (1) is appropriate in the region of the (100) surface, and the fast diffusion model (2) is the best description on the region of the (111) surface where diffusion allows some feeding of oxygen atoms from steps to (111) terraces.

In summary, it is found that the oxygen coverage round the cylinder can be predicted by a model in which the rough and the smooth areas of any face behave independently, except for faces vicinal to the (111) face where diffusional feeding between the terraces and steps may be occurring. This leads to higher coverages near the (111) face than would be expected from a diffusionless model.

#### CHAPTER 5: REFERENCES

1. G. Tammann, J. Inst. Metals, 44 (1930) 29.
2. A. T. Gwathmey & A. F. Benton, J. Chem. Phys. 8 (1940) 431.
3. A. T. Gwathmey & A. F. Benton, J. Phys. Chem. 46 (1942) 969.
4. F. W. Young Jr., J. V. Cathcart & A. T. Gwathmey, Acta Met. 4 (1956) 145.
5. R. N. Lee & H. E. Farnsworth, Surf. Sci. 3 (1965) 461.
6. G. Ertl, Surf. Sci. 6 (1967) 208.
7. G. W. Simmons, D. F. Mitchell & K. R. Lawless, Surf. Sci. 8 (1967) 130.
8. N. Takahoshi, H. Tomita & S. Motoo, Compt. Rend. (Paris) 269 (1969) 618.
9. A. Oustry, L. Lafourcade & A. Escaut, Surf. Sci. 40 (1973) 545.
10. L. McDonnell, D. P. Woodruff & K. A. R. Mitchell, Surf. Sci. 45 (1974) 1.
11. L. McDonnell & D. P. Woodruff, Surf. Sci. 46 (1974) 505.
12. G. Ertl & J. Koppers, Surf. Sci. 24 (1971) 104.
13. J. R. Noonan, D. K. Zehner and L. H. Jenkins, Surf. Sci. 69 (1977) 731.
14. P. Hofmann, R. Unwin, W. Wyrobisch & A. E. Bradshaw, Surf. Sci. 72 (1978) 635.
15. I. E. Wachs & R. J. Madix, Appl. Surf. Sci. 1 (1978) 303.
16. T. A. Delchar, Surf. Sci. 27 (1971) 11.
17. L. F. Wagner & W. E. Spicer, Surf. Sci. 46 (1974) 301.
18. S. Evans, D. E. Parry & J. M. Thomas, Faraday Disc. Chem. Soc. 60 (1975) 102.
19. S. Kono, C. S. Fadley, N. F. T. Hall & Z. Hussain, Phys. Rev. Letters 41 (1978) 117.
20. S. Kono, S. A. Goldberg, N. F. T. Hall & C. S. Fadley, Phys. Rev. Letters 41 (1978) 1831.
21. C. Benndorf, B. Egert, G. Keller & F. Thieme, Surf. Sci. 74 (1978) 216.
22. A. G. J. de Wit, R. P. N. Bronckers & J. M. Fluit, Surf. Sci. 82 (1979) 177.
23. A. Kuller & A. Henninghoven, Surf. Sci. 41 (1974) 493.

24. S. P. Holland, B. J. Garrison & M. Winograd, Phys. Rev. Letters 42 (1979) 220.
25. F. H. P. M. Habraken, E. Ph. Kieffer & G. A. Bootsma, Proc. 7th Internat. Vac. Congr. and 3rd Internat. Conf. Solid Surfaces, Vienna (1977), vol. 2, p. 877.
26. F. H. P. M. Habraken, E. Ph. Kieffer & G. A. Bootsma, Surf. Sci. 83 (1979) 45.
27. F. H. P. M. Habraken & G. A. Bootsma, Surf. Sci. 87 (1979) 333.
28. F. H. P. M. Habraken, G. A. Bootsma, P. Hofmann, S. Hachicha & A. K. Bradshaw, Surf. Sci. 88 (1979) 285.
29. F. H. P. M. Habraken, C. M. A. M. Mesters & G. A. Bootsma, Surf. Sci. 97 (1980) 264.
30. F. H. P. M. Habraken, Doctoral Thesis, Rijksuniversiteit, Utrecht (1980).
31. U. Gerhardt & G. Franz-Moller, Proc. 7th Internat. Vac. Cong., 3rd Internat. Conf. Solid Surfaces, Vienna (1977).
32. H. Hopster, H. Ibach & G. Comsa, J. Catalysis 46 (1977) 37.
33. J. Perdureau & G. E. Rhead, Surf. Sci. 24 (1971) 555.
34. H. L. Kramer, E. Langer & E. Bauer, Proc. 4th Internat. Conf. Solid Surfaces and 3rd ECOSS, Cannes (1980), Suppl. Rev. "Le Vide, Les Couches Minces", 201 1 217.
35. C. Kohrt & R. Gomer, J. Chem. Phys. 52 (1970) 3283.
36. D. R. Lloyd, C. L. Quinn & M. V. Richardson, Surf. Sci. 68 (1977) 419.
37. J. H. Onuferko & D. P. Woodruff, Surf. Sci. 95 (1980) 555.

## CHAPTER 6 : OXYGEN ON NICKEL

### 6.1 : PREVIOUS WORK

The adsorption of oxygen on the low-index faces of nickel has been studied many times. Agreement between different studies has not always been evident, particularly on the (111) face. As with the copper cylinder, the results of previous studies on low-index faces will be used for comparison with the results from the low-index areas of the nickel cylinder in this study. It is therefore worth discussing briefly the major findings of the other authors.

#### A) (100) FACE

The adsorption of oxygen on the (100) face of nickel has been studied extensively using L.F.P.D.<sup>1-5</sup> The observed sequence of L.E.E.D. structures is  $p(2 \times 2)$  at low exposures then  $(\sqrt{2} \times \sqrt{2})R 45^\circ$ <sup>1-6</sup> At higher exposures a pattern characteristic of NiO is observed<sup>1,2,5</sup> The sequence  $(p(2 \times 2), (\sqrt{2} \times \sqrt{2})R 45^\circ, NiO)$  has also been observed using R.H.E.E.D.<sup>6</sup> This system has also been studied by photoemission<sup>8</sup>.

The kinetics of the reaction of oxygen with nickel (100) have been reported for an A.E.S./ Work function study<sup>5</sup> and for a study using x-ray emission<sup>7</sup>. The broad features of both kinetics studies were the same. After an initial chemisorption region (complete after only a few langmuirs exposure), the sticking factor drops to a minimum. At higher exposures (50-200L) an oxide film two or three planes thick grows epitaxially. The epitaxial relations of the oxide layer to the substrate will be discussed later.

#### B) (110)FACE

L.E.E.D. studies of oxygen adsorption on the (110) face of nickel give a  $(2 \times 1)$  structure followed by a  $(3 \times 1)$  structure<sup>4,7,9,10</sup>. The formation of a preliminary  $(3 \times 1)$  structure before the  $(2 \times 1)$

structure has been reported<sup>7</sup> but was found not to occur by some authors<sup>4,9</sup>. A similar sequence ((2x1) then (3x1)) was reported from a study using R.H.E.D.<sup>13</sup> In that study a (9x4) structure was also observed at high coverages.

The kinetics of the reaction have been studied using A.E.C.<sup>11,12,15</sup>, Work function measurements<sup>11,15</sup>, X.P.S.<sup>12</sup>, x-ray emission<sup>13</sup>, I.E.I.S.<sup>14</sup> and E.L.S.<sup>15</sup>. As with the (100) plane the broad features of the kinetics are similar in these studies. Rapid chemisorption occurs up to an exposure of 1 or 2 langmuirs. There is then a plateau in the adsorption kinetics (i.e. the sticking factor decreases). At higher coverages (more than 10L) an oxide film grows by a nucleation and island growth mechanism. Finally the oxide film thickens as bulk oxide is formed.

#### C) (111) Face

The adsorption of oxygen on the (111) face of nickel has been extensively studied using L.E.E.D.<sup>4,7,16-19,26</sup>. Roelofs et al. have published an experimental phase diagram for oxygen chemisorbed on a nickel (111) surface<sup>26</sup>. At low coverages and temperatures a (2x2) pattern is observed. As the coverage is increased, a complex pattern is observed in a transition region; this is followed by a  $(\sqrt{3} \times \sqrt{3})R30^\circ$  pattern. At higher coverages still, nickel oxide begins to form<sup>5</sup>.

The kinetics of the reaction have been studied using A.E.S.<sup>19,20</sup> and work function measurements<sup>19</sup>. The low coverage chemisorption region (up to several Langmuirs exposure) is quickly followed by growth of an oxide film. This film is essentially complete after an exposure of about 30L (at a much lower exposure than for the corresponding films on the (100) and (110) faces).

Despite the amount of work that has been done on the adsorption of oxygen on low-index nickel faces, there has been no comprehensive study of the kinetics on all three low-index faces by the same authors.



For the oxygen/copper system the work of Habraken as discussed in the previous chapter, provides a valuable basis. It allows the kinetics of the reaction of oxygen with the three low-index faces to be compared without the problems of exposure calibrations that can arise when results from different U.H.V. systems are compared. For nickel no such set of results for all three faces is available. However several authors have studied two out of the three low-index faces. Holloway and Hudson have studied the (100) face<sup>5</sup> and the (111) face<sup>19</sup>. Mitchell et al. have reported results for both the (100) face<sup>6</sup> and the (110) face<sup>13</sup>. The results of these studies will therefore be used most for comparison with results obtained from this study of cylindrical crystals.

## 6.2 CALIBRATION OF AUGER PEAK HEIGHTS

The accuracy of using oxygen KLL Auger peak heights as a measure of the amount of oxygen on the nickel surface is open to question. Hooker et al.<sup>12</sup> studied oxygen on nickel (110) using XPS. They observed chemical shifts in the XPS spectra associated with oxide formation. These chemical shifts will also show up as peak shape changes in the Auger spectra. Consequently the use of peak-to-peak heights from the first derivative of the energy spectra may not be accurate.

On the other hand, Benndorf et al.<sup>15</sup> compared the peak-to-peak heights in the  $N'(E)$  spectra with the integrated intensities of the O(KLL) Auger peaks. They found an almost linear relationship between the two except at high coverages when the slight increase in the  $O(K_{23}^{L_{23}})$  line width resulted in an undervaluation of the coverage as measured by the peak-to-peak height. However this effect was less than the variations between experimental runs ( $\pm 10\%$ ).

Roll and Palmer, when studying NiO on Nickel<sup>21</sup>, found that the oxygen "peak shape remains constant throughout. Therefore the p-p height of the oxygen signal is still a good measure of the

oxygen concentration".

Holloway and Hudson<sup>5,19</sup> assumed that for low coverages a linear coefficient of proportionality between the oxygen Auger signal and the oxygen concentration applied. However they point out that the Auger signal from material more than one layer thick must be corrected for inelastic scattering of Auger electrons. They found that the correction to the apparent Auger signal was of the order of 20%.

As with the copper cylinder it was not possible to get readings all round the cylinder in an experimentally reasonable time and maintain a high degree of accuracy. This fact, coupled with the possible errors due to the Kikuchi effect, leads us to believe that the accuracy of this method will not be great. It was certainly not possible to take measurements all around the crystal in sufficient detail to be able to do double integrals in the search for greater accuracy.

However, a kinetics experiment was done in which readings were taken only from the mirror planes (i.e. the two (001) and two (110) type planes). These planes can be easily located with high accuracy on the cylinder because they were mirror planes (unfortunately the (111) planes could not be located as accurately as they are not mirror planes on the cylinder). It will be seen that by performing an experiment on a limited area, the accuracy could be improved to such an extent that the error introduced by using Auger peak-to-peak heights becomes significant.

For the majority of experiments (i.e. experiments on the whole of the cylinder) the inaccuracy caused by using peak-to-peak heights will be assumed not to be significant in a study in which we will be mostly concerned with relative coverages on different planes, rather than in absolute coverages.

### 6.3 RESULTS

The results of the experiments in which readings were taken for the (110) and (100) planes only are shown in fig.6.1. The points in this diagram are averages of the readings from the two equivalent diametrically opposite faces (i.e. the average of (110) and ( $\bar{1}\bar{1}0$ ) and the average of (001) and ( $00\bar{1}$ )). In both cases the initial reaction rate is high, falls off after an exposure of several langmuirs, and then increases again. This behaviour has been widely recognised.<sup>5,6,11-15,19,20,21</sup> The three stages correspond to an initial rapid chemisorption stage, a plateau of low sticking factor, and a true oxidation phase in which an oxide film several layers thick builds up on the surface.

In order to compare the results from the cylindrical crystal with results from previous studies on flat crystals, it is worthwhile examining the amount of agreement that there is between different studies on flat crystals. The kinetics of the reaction of oxygen with Ni(110) have been widely studied.<sup>11-15</sup> In fig.6.2 some of these results are compared. Hooker et al.<sup>12</sup> present results for both the peak-to-peak height and the double integral of the spectrum for the oxygen KLL Auger peak. The difference in these two curves demonstrates the error introduced by using the peak-to-peak height due to the change in peak shape.

Benndorf et al.<sup>15</sup> also present results for the KLL Auger peak-to-peak heights as a function of exposure. As would be expected their results are close to the peak-to-peak heights of Hooker et al.

Mitchell et al.<sup>13</sup> used x-ray emission as a measure of the oxygen coverage. It can be seen from fig. 6.2. that the x-ray emission results show the same general trend as the other results, but they are not exactly the same. A reasonably good fit is obtained between the x-ray emission results of Mitchell and doubly integrated Auger peak results of Hooker if a correction factor is applied to the exposure calibrations.

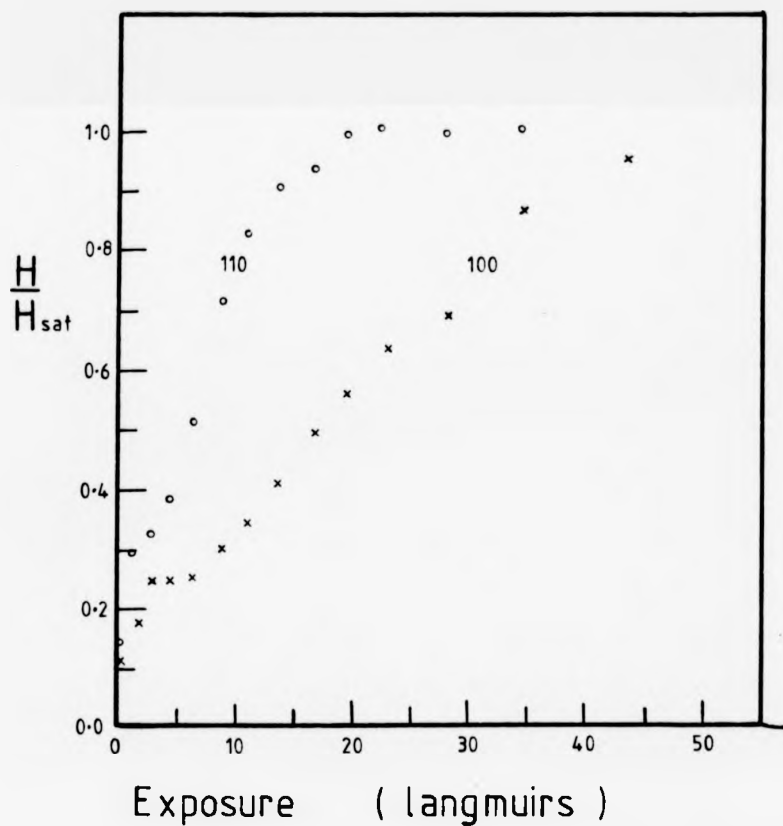


FIG. 6.1 Uptake of oxygen on the (100) and (110) planes of nickel.  $H$  is the ratio of the 510ev oxygen Auger peak to the 61ev nickel Auger peak.  $H_{sat}$  is the same ratio at saturation oxygen coverage.

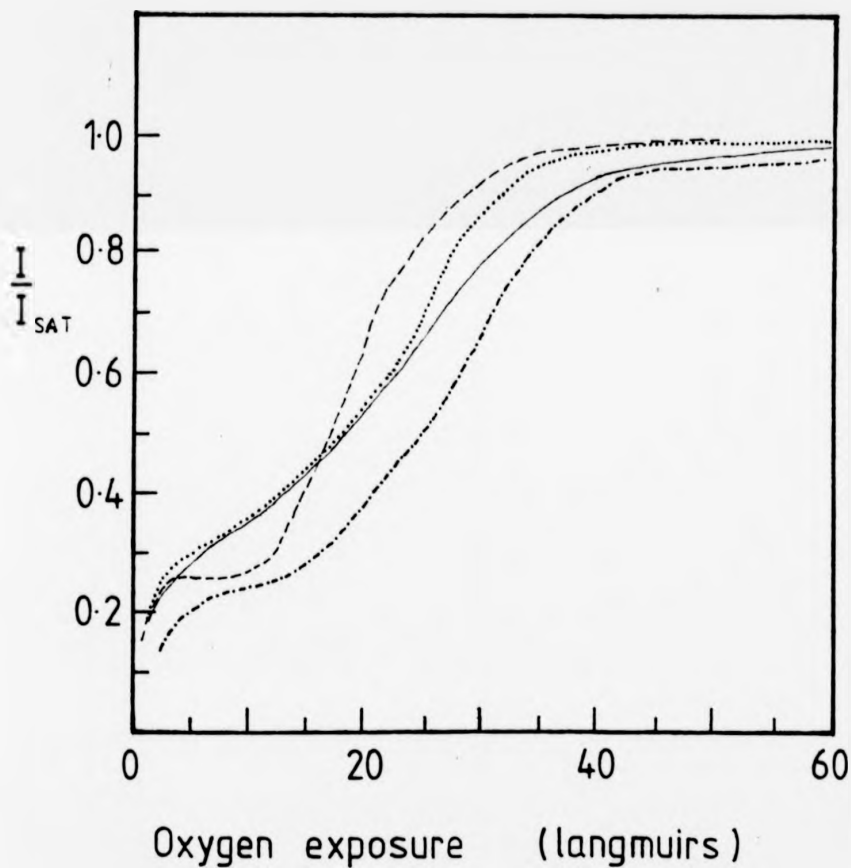


FIG. 6.2 Oxygen coverages on the (110) face of nickel. Results taken from references 12, 13, and 15:

- ..... ref. 12, A.E.S. (peak-to-peak height measurements),
- ref. 12, A.E.S. (integrated peak measurements),
- ref. 13, X-ray emission measurements.
- ref. 15, A.E.S. (pk-pk height measurements).

In summary, it can be seen from fig.6.2 that the agreement between different flat crystal studies is reasonable, but by no means perfect. These results will be compared with the measurement of the oxygen Auger peak heights round the cylindrical crystal. We would expect the best fit to occur if we consider the flat crystal experiments in which the oxygen coverage is measured by the Auger peak-to-peak heights. Therefore the results from fig.6.1 will be compared with the results of Holloway and Hudson<sup>5</sup> for the (100) face, and with the peak-to-peak heights of Hooker et al. for the (110)<sup>12</sup> face.

This comparison is made in fig.6.3 in which the solid lines represent results from flat crystal studies, and the points are the results from this study of the cylinder (the points are in fact the same points that are plotted in fig.6.1).

The exposure axis in fig.6.3 is logarithmic because a correction factor had to be applied to the exposures in this study to optimise the fit. On the logarithmic scale the results for the cylindrical crystal were shifted to the right by 0.37. This corresponds to multiplying the apparent exposure by 2.37. Although this seems to be a rather large factor, absolute exposure calibration is not easy and it is thought that the pressure readings in either study could well have been out by a factor of 2 or more.

Having established that the kinetics of the reaction of oxygen with the (100) and (110) type areas of the cylinder are similar to the kinetics as reported for flat (100) and (110) crystal faces, the next step is to look at the oxygen coverage as a function of exposure right round the crystal. Fig.6.4 shows the results of an experiment in the chemisorption regime. Figs.6.5 and 6.6 show the results of a second set of experiments, this time for coverages in the oxidation region. Note that the exposures in these diagrams are as measured and have not been corrected.

The results plotted in figs.6.5 and 6.6 are from different

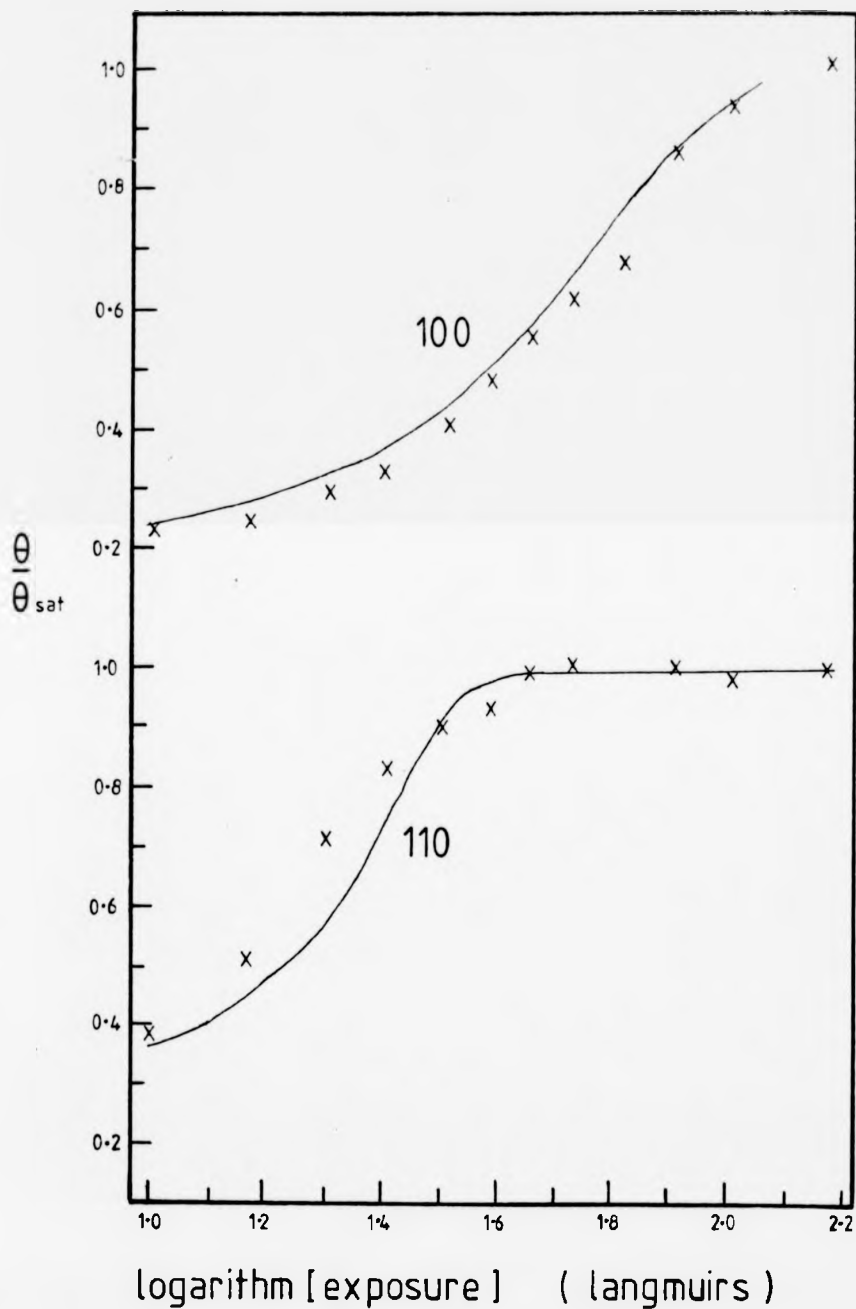


FIG. 6.3 Results of oxygen coverage measurements from the cylinder (crosses) compared with results from flat crystal studies (solid lines). (100) face results from ref. 5, (110) face results from ref. 12. A correction factor has been applied to the exposure scale.

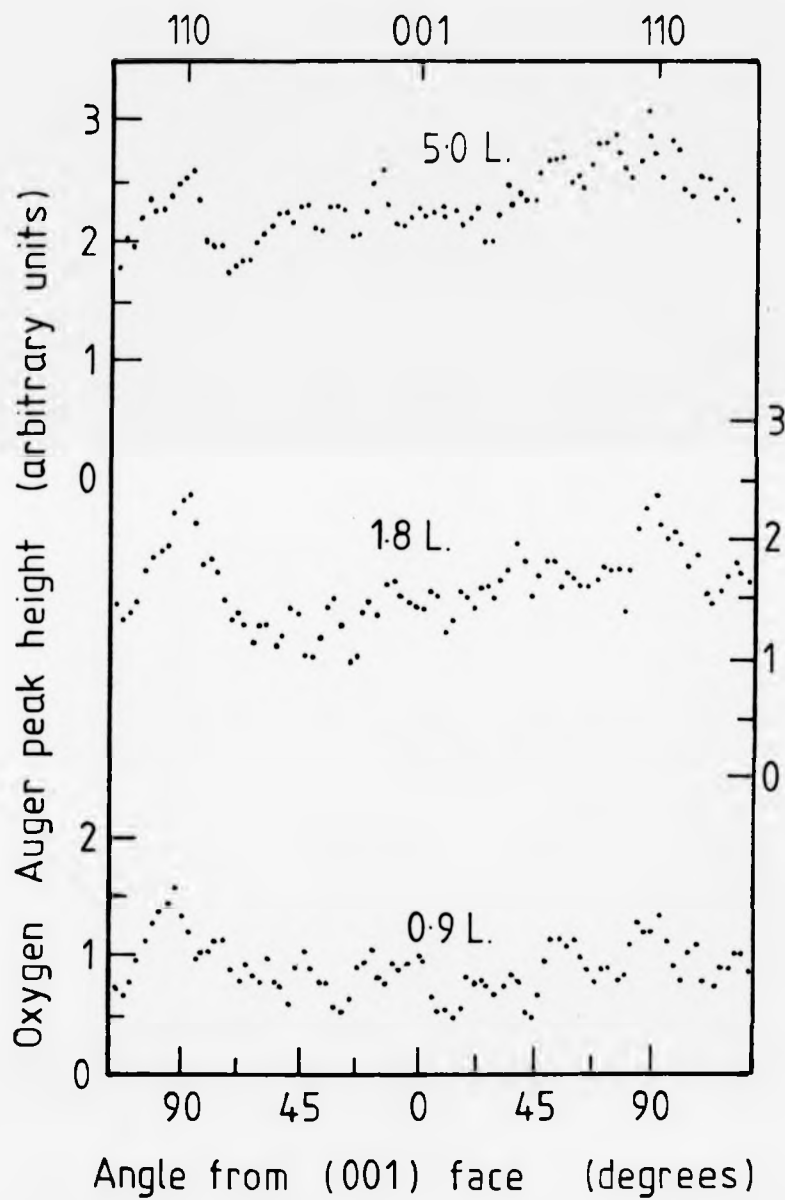


FIG. 6.4 Oxygen coverages on a nickel cylinder exposed to small amounts of oxygen.



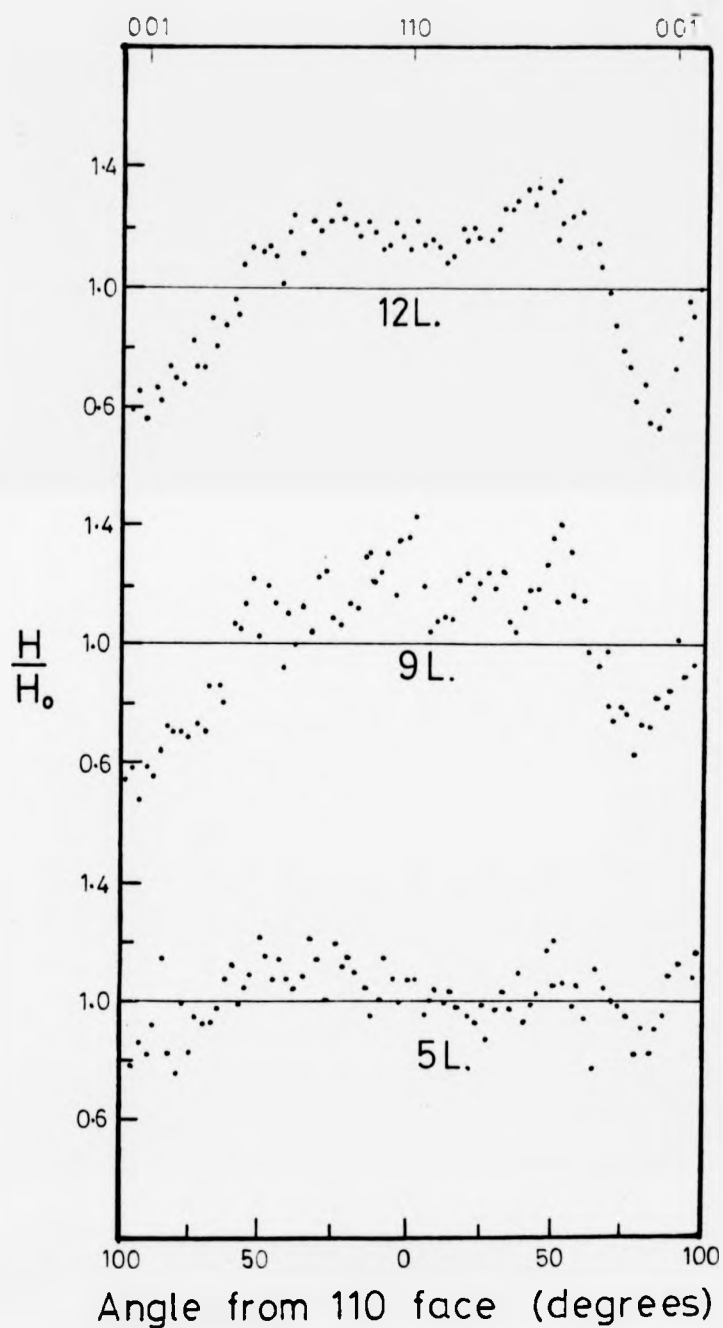
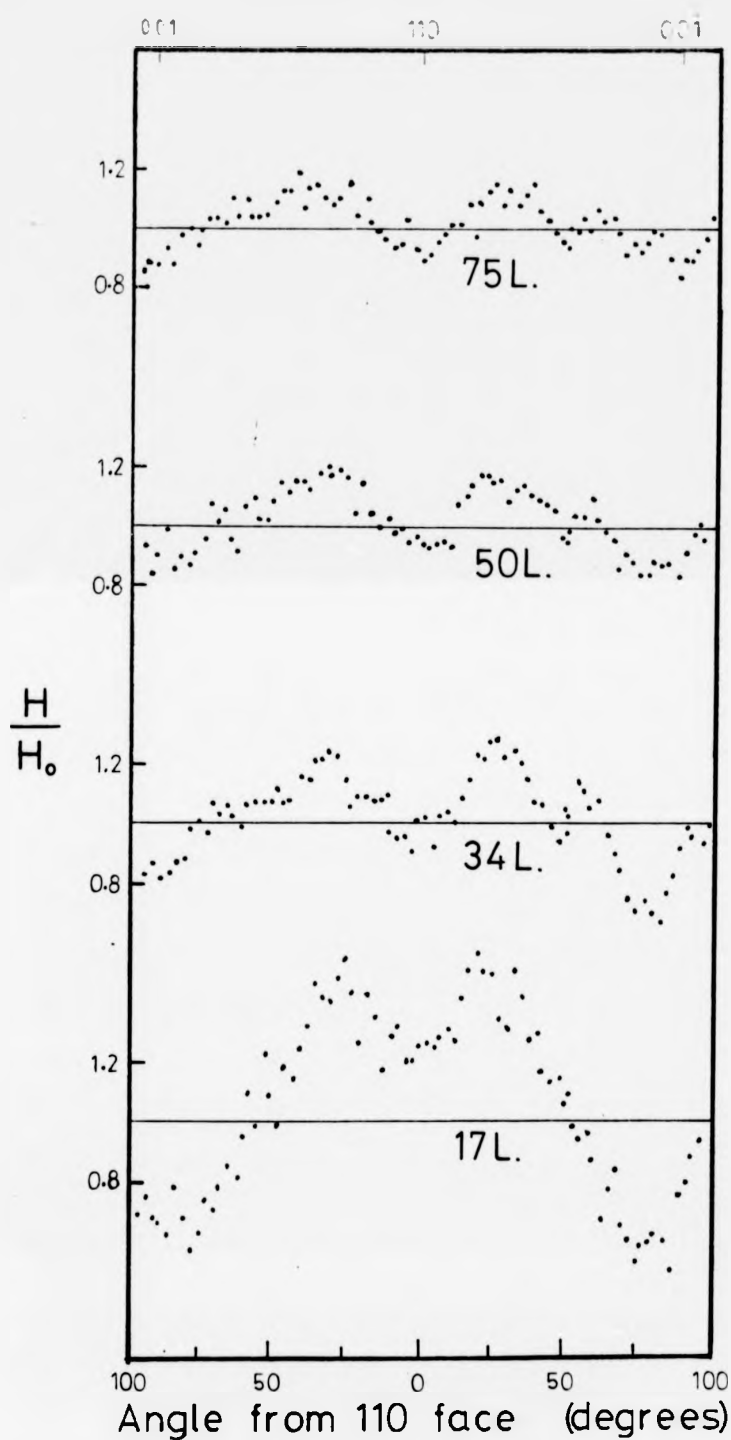


FIG. 6.5 Normalised oxygen coverages as a function of exposure.  $H_0$  is the average oxygen Auger peak height at any given exposure.



**FIG. 6.6** Normalised oxygen coverages as a function of exposure.  
 $H_0$  is the average oxygen Auger peak height at any given exposure.

experimental runs, on different days. Because the response of the electronics of the Auger spectrometer varied from day to day, the results had to be normalised. This was done by dividing all the Auger peak heights at a given exposure by the average Auger peak height at that exposure. Note that it was not necessary to do this for the results plotted in fig.6.1. This was because by limiting the measurements to a few selected points, the experiment could be done in one comparatively brief run (without switching the electronics off and on).

The following points can be seen from the results :

- 1) In the chemisorption region the coverage around the cylinder is very even, except at the (110) faces where the oxygen Auger signal is about 50% greater.
- 2) In the oxidation region the coverage increases most quickly on the (111) face such that minima in the Auger signals develop at the (001) and (110) faces. When this variation is at its most extreme the oxygen Auger signal from the (001), (110) and (111) faces is in the approximate ratio 1:2:2.5 respectively.
- 3) At saturation when the oxide film is complete the Auger signal from the (111) face is still greater than from the (001) or (110) faces. The variation between the low-index faces is not as large as before, the ratio of the signal from the (001), (110) and (111) faces being of the order of 1:1:1.3.

#### 6.4 DISCUSSION

##### 1) Chemisorption

Estimates of the oxygen coverage at the end of the chemisorption stage for the three low-index faces are given in table 6.1 with the references that they were taken from:

TABLE 6.1

COVERAGE,  $\theta$ , IN MONOLAYERS AT THE END OF CHEMISORPTION

<u>100</u>	<u>110</u>	<u>111</u>
0.4 (5)	0.67 (15)	0.34 (19)
0.33 (7)	0.5 (13)	0.25 (20)
0.25 (23)		0.25 (23)

The initial chemisorption phase on the (100) has recently been discussed by Brundle<sup>24</sup>. X.F.S. detects the formation of NiO at about 0.33 monolayers so that Holloway & Hudson's estimate<sup>5</sup> for the end of the chemisorption region as 0.4 monolayers is probably too high. The dissociative kinetics in this stage are pseudo-first order with the sticking factor  $s = (1-4\theta)$  controlled by the formation of an ordered (2x2) phase with coverage  $\theta = 0.25$ . This implies that there is a strong repulsion between adsorbed oxygen atoms in nearest neighbour sites. The kinetics (with the sticking factor dropping as  $\theta$  approaches 0.25) are thus correlated with the difficulty of finding nearest neighbour sites for incoming oxygen molecules to dissociate at.

The drop in sticking factor as the (2x2) phase nears completion causes an adsorption plateau. This plateau can be suppressed by preventing the formation of this long range structure either by damaging the surface with ion bombardment or by performing the experiments at low temperature<sup>24</sup>.

The situation is similar on the (111) face in that a (2x2) structure ( $\theta=0.25$ ) forms at first. The (110) face is markedly different, however, for the end of the chemisorption phase may be associated with a  $\frac{1}{2}$  monolayer (2x1) structure. Mitchell et al. found that the kinetics of the chemisorption stage could be represented by a non-activated dissociative Langmuir equation in which the

coverage exponentially approaches the limiting value of  $\theta=0.5$ .

This equation has the form:

$$Q = Q_a [1 - \exp(-kpt)] \quad 6.1$$

In this equation  $Q$  is the oxygen uptake,  $Q_a$  is the limiting value of the exponential uptake, and  $k$  is a constant relating gas impingement rate and number of adsorption sites.

In comparing the behaviour of the three faces in the chemisorption region, it has been found that equation 6.1 describes the behaviour of the (100) face<sup>5-7</sup>, the (110) face<sup>13</sup>, and the (111) face<sup>19</sup>. For each face the constant  $k$  will be slightly different so that the term in the square brackets in equation 6.1 will be slightly different for each face. However the main difference is in the term  $Q_a$ , the limiting value of the exponential uptake in the chemisorption regime.

If these limiting values for the exponential uptake on the (110), (111), and (100) faces are indeed  $\frac{1}{2}$ ,  $\frac{1}{4}$ , and  $\frac{1}{2}$  monolayers respectively, then the limiting amounts of oxygen on each face will be in the ratio 1.43 : 1.15 : 1.00, in good agreement with the measured ratio (fig 6.4) of 1.5 : 1.0 : 1.0.

It can be seen from fig. 6.4 that the (311) face does not behave in the same way as the (110) face, rather it appears to saturate at a similar level to the (001) or (111) faces. This is in contrast with the behaviour of oxygen on copper, where the (311) and (110) faces behave almost identically.

## 2) Oxide film growth.

The oxide film that is observed on all three low-index faces grows epitaxially. Table 6.2 gives values of the number of oxide layers measured at completion of the oxide film, and the observed NiO plane epitaxial to the Ni plane.

TABLE 6.2

COVERAGE, IN MONOLAYERS, AT COMPLETION OF OXIDE FILM.

<u>100</u>	<u>110</u>	<u>111</u>
$2.0^5 \text{NiO}(001)$	$2.0^{13} \text{NiO}(001)$	$1.8^{19} \text{NiO}(111)$
$3.0^6 \text{NiO}(001)$		
or $\text{NiO}(111)$ (two orientations)		

In the same way that the results for the (100) and (111) areas of the cylinder were compared with the results of previous studies on flat crystals (fig.6.3), the results for the complete cylinder can be compared with a simple model based on previously published data.

This model uses the assumption that the nickel cylinder behaves similarly to the observed behaviour of the copper cylinder, i.e. that the coverage on intermediate faces is a linear combination of the coverage on the adjacent key faces.

The results of Holloway and Hudson<sup>5,19</sup> and Mitchell, Sewell and Cohen<sup>6,13</sup> will be used and the assumption made that, as for copper, the (311) face behaves like the (110) face. The relative coverage  $\theta'$  can be tabulated (the relative coverage  $\theta'$  is the coverage divided by the coverage at the completion of the oxide film). Normalising in the same way as the results for the cylinder produces plots such as those of figs.6.7 and 6.8. These have been plotted in a form in which they can be directly compared with the results from the cylinder, figs.6.5 and 6.6. In plotting figs.6.7 and 6.8 the exposure calibration factor deduced in the previous section has been applied.

This model agrees reasonably well with the observed experimental results considering that two assumptions have been made that may not be justified.

Firstly the assumption that the (311) face behaves identically to the (110) face seems to be doubtful because we have already

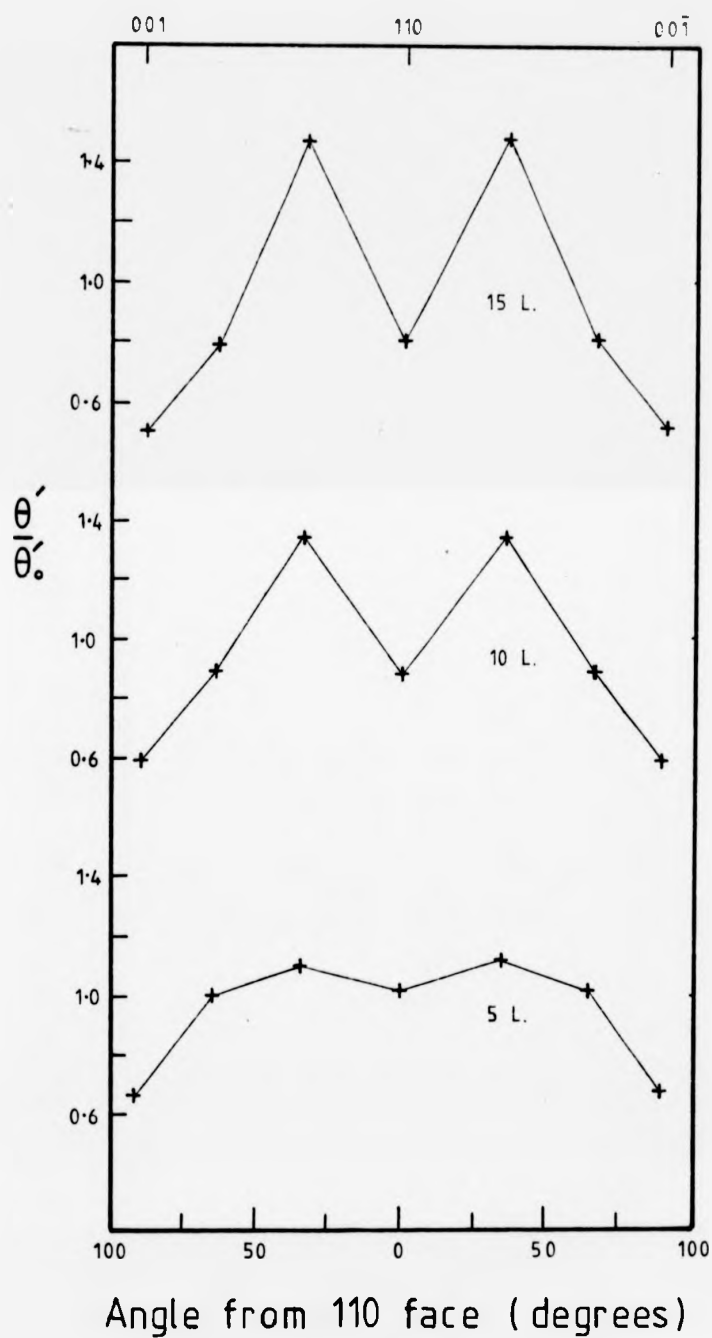


FIG. 6.7 Predicted oxygen coverages on a nickel cylinder.

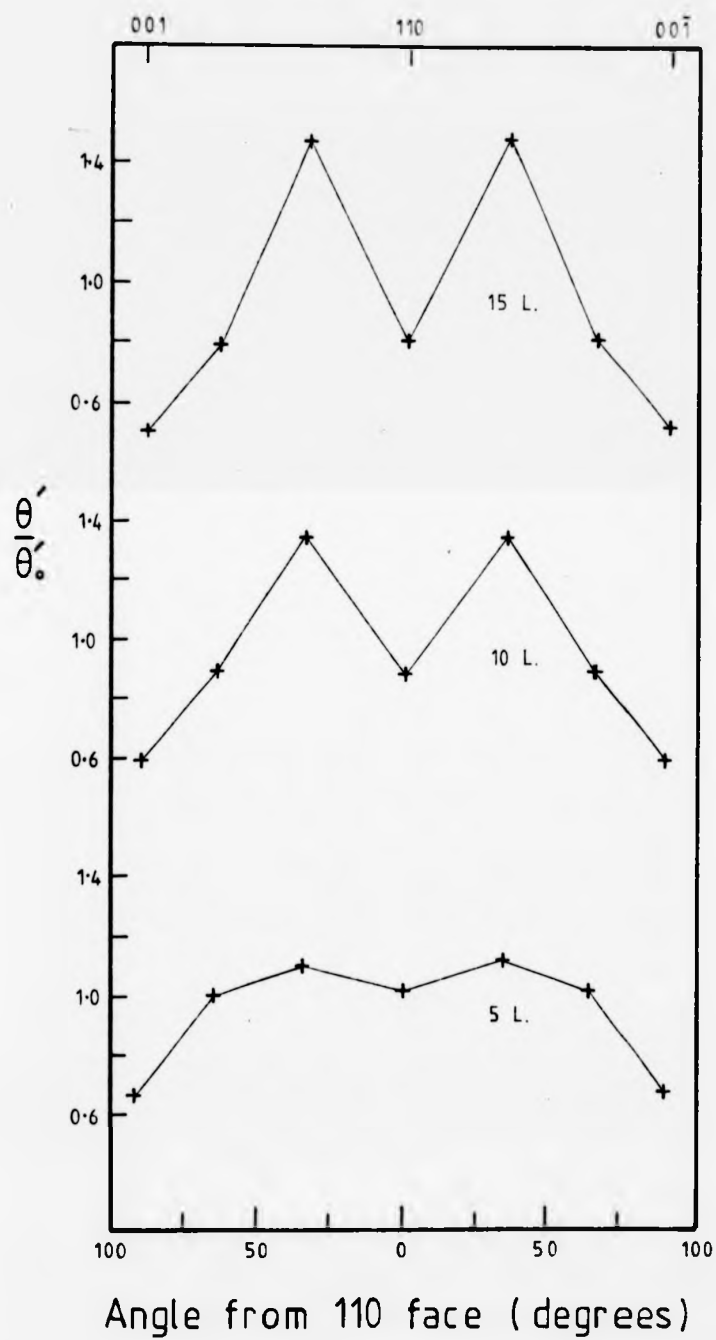


FIG. 6.7 Predicted oxygen coverages on a nickel cylinder.



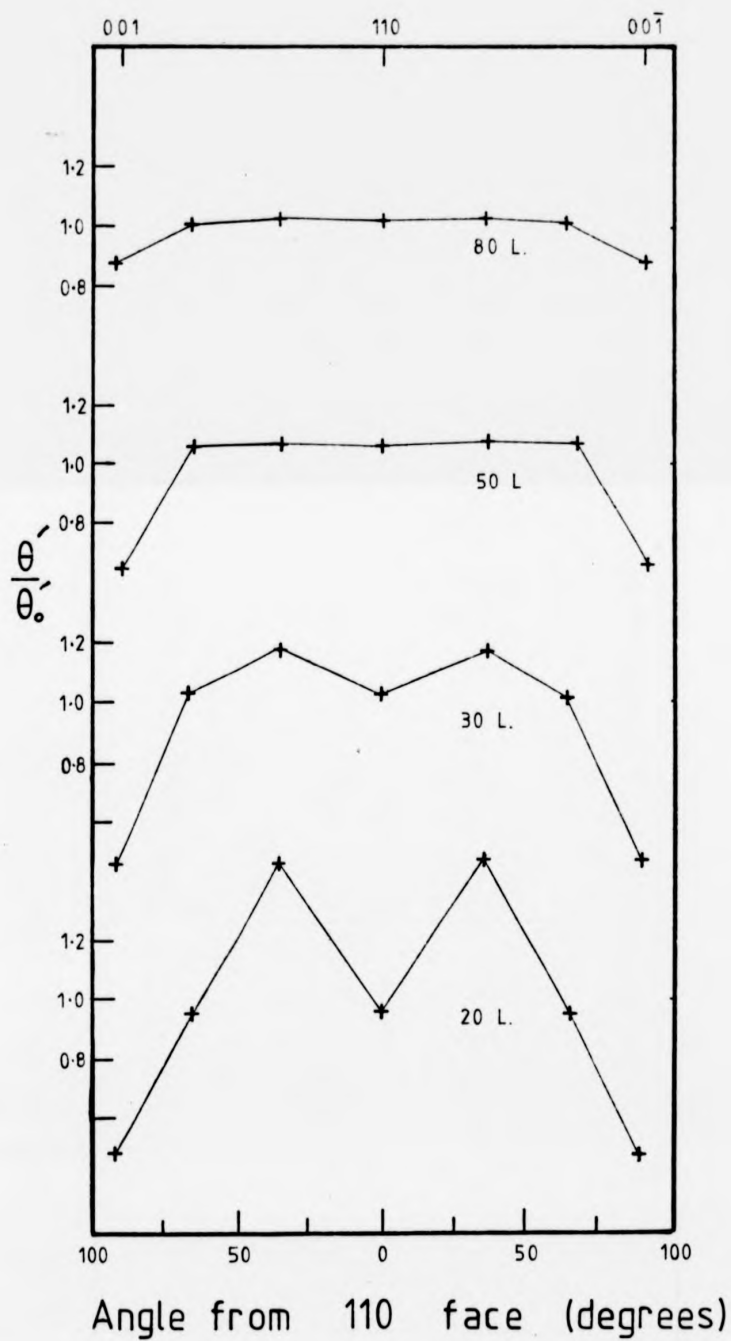


FIG. 6.8 Predicted oxygen coverages on a nickel cylinder.

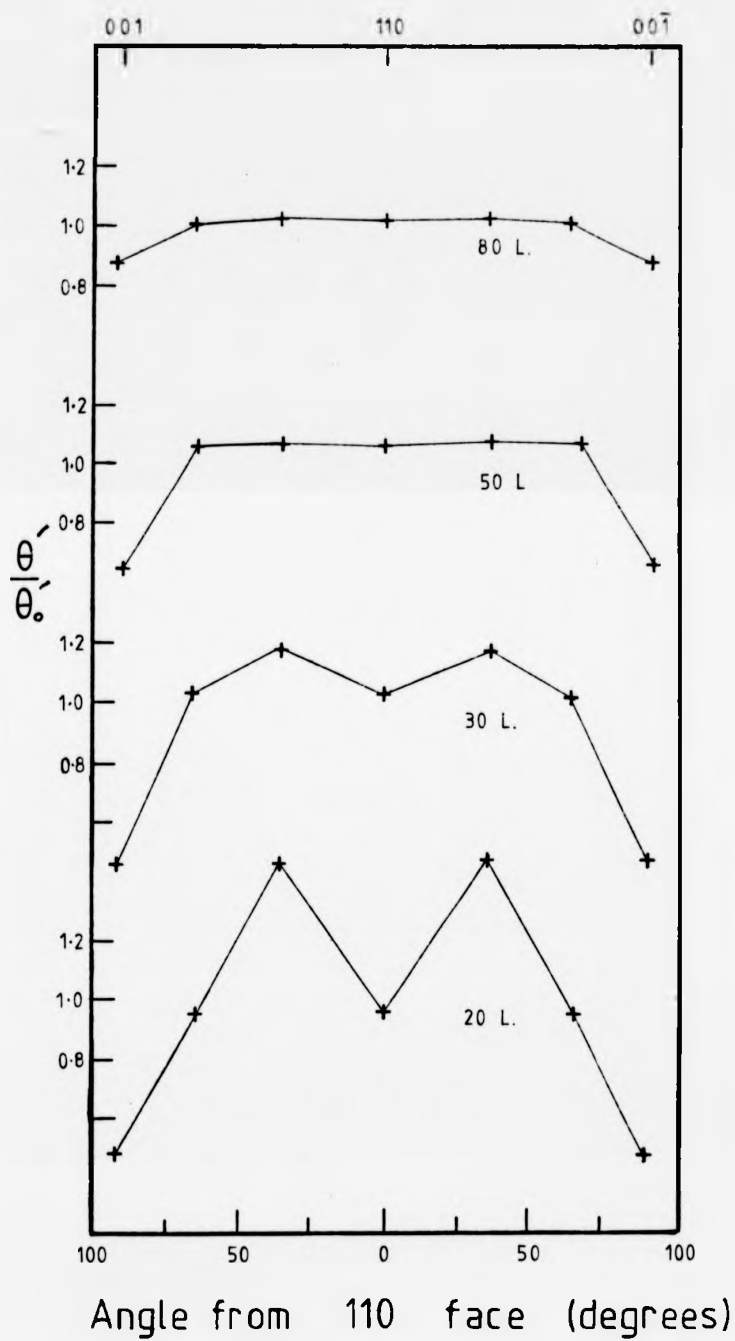


FIG. 6.8 Predicted oxygen coverages on a nickel cylinder.

seen that in the chemisorption stage the two behave differently.

Secondly, the model deals only in terms of coverages relative to the saturation coverage at completion of the oxide film. It therefore takes no account of the fact that at completion of the film the density of oxygen atoms on different surfaces will be different. This is <sup>partly</sup> because of the difference in the number of atoms per unit area in the epitaxial film of differing orientation and partly because the number of layers of oxide film at saturation may be different at different faces.

An experiment was done with a greater angular frequency of measurements at an exposure of 20L where the anisotropy is at its greatest. Fig.6.9 compares the results from the cylinder with the results from flat single crystal faces in the same manner as for figs.6.7 and 6.8. It can be seen that, as before, the agreement between results from the cylinder and published results is good.

### 3) Nucleation of Oxidation

Holloway and Hudson<sup>5</sup> showed that the growth of the oxide film, after the adsorption plateau, was governed by the rate of incorporation of oxygen at the edges of oxide islands. They developed a formula to describe the oxidation kinetics based on an island growth model containing a parameter  $K_i N_0$ .  $N_0$  is the number of NiO nuclei and  $K_i$  is a parameter involving the rate controlling process. They related the temperature dependence of this parameter to a Boltzmann factor in  $K_i$  which contains an activation energy.

Mitchell et al.<sup>6</sup> subsequently found that the parameter  $K_i N_0$  is governed by the temperature in the initial phase of oxidation as the adsorption leaves the plateau. They attributed this to a temperature dependence in  $N_0$  not  $K_i$ . This suggests that it is variations in the number of oxide nuclei between different

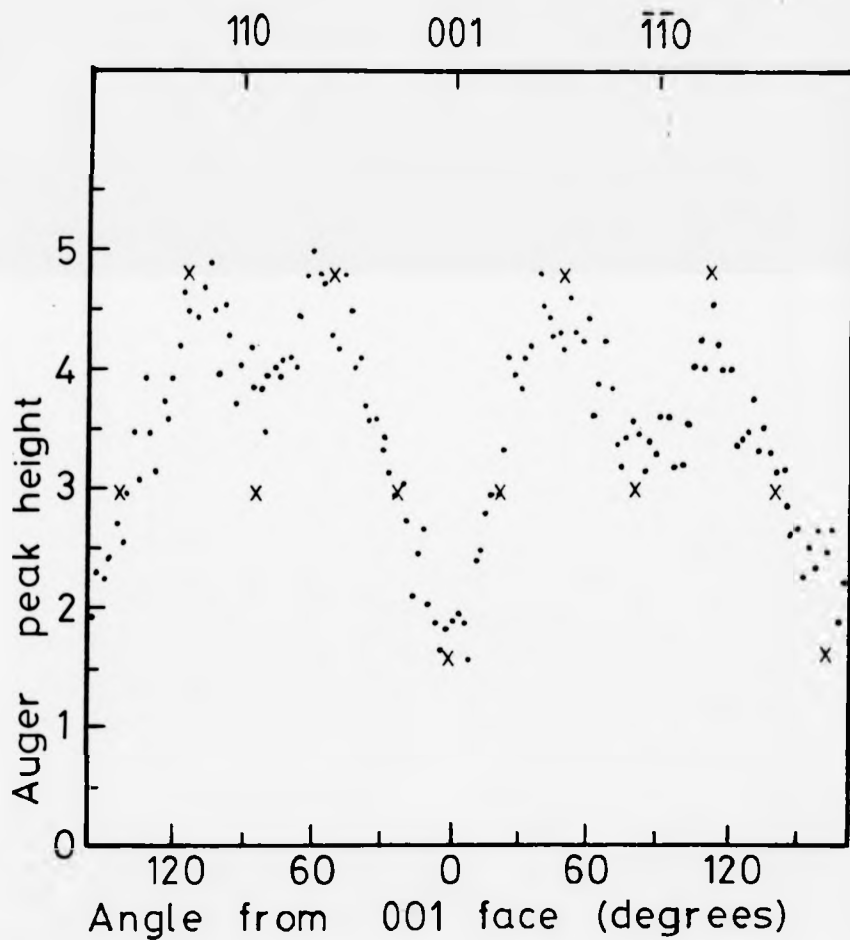


**FIG 6.9** Comparison of oxygen coverage at 20L measured from the cylinder (dots), and from flat crystal surfaces (crosses), (refs 5,6,13,&19).

faces that cause the variations in the oxidation kinetics.

There is also indirect evidence that the kinetics are related to the density of oxide nuclei on each face. Diffraction features for the second phase on Ni(100) (i.e. the two orientations of NiO(111) epitaxial to Ni(100)) are very sharp, much sharper than for the NiO film on Ni(111). This suggests a larger grain size for the NiO on Ni(100) which in turn implies that for similar final coverages the particle density is lower on Ni(100) than on Ni(111). The high oxidation rate on Ni(111) could thus be due to a high initial nuclei density compared with Ni(001).

For the mechanism of oxide nucleation, Mitchell et al.<sup>7</sup> propose the existence of proto-nuclei, based on 'latent sites' which can grow into useful nuclei under suitable conditions. They and Brundle<sup>24</sup> suggest that these latent sites are associated with surface defects. However, it can be seen from the results from the cylinder (e.g. fig.6.9) that there is a peak in the oxygen coverage at the (111) face. The surfaces vicinal to (111) have a lower oxygen coverage than the smooth (111) face itself. This suggests that the presence of steps, which might act like defects, decreases the rate of oxidation. This is in contradiction to what Mitchell et al. and Brundle propose for the (100) face.

An alternative view of the rate limiting process is that the control arises from the need for a certain threshold coverage to be obtained in the chemisorbed layer before nucleation can occur. This is analogous to supersaturation in the case of nucleation from the bulk. The variation in the oxidation kinetics between faces would then arise as a result of the ease with which adequate 'supersaturation' can occur on different faces.

Consider the (100) and (111) faces, which are smooth surfaces yet which represent the extremes of the data. The initial chemisorption kinetics of both faces appear to be controlled by the formation of a (2x2) structure with atomic coverage  $\theta = 0.25$  monolayers.

For the (100) surface the (2x2) structure corresponds to a situation in which every Ni atom has an oxygen nearest neighbour atom.

There are thus no available sites (or pairs of sites) at which dissociative adsorption can take place. On (100) the (2x2) structure would tend to inhibit further adsorption towards the threshold coverage for nucleation.

On the other hand, on the (111) surface the (2x2) structure corresponds to a situation in which only  $\frac{2}{3}$  of the Ni atoms have an oxygen nearest neighbour atom. Furthermore the subsequent  $(\sqrt{3} \times \sqrt{3})R 30^\circ$  <sup>4,16</sup> structure (only seen in some studies) must involve substantial rearrangement of the oxygen atoms. This indicates that the adsorbate is significantly mobile. This in turn, coupled with the fact that  $\frac{1}{3}$  of the nickel surface atoms have no oxygen nearest neighbour, suggests that on the (111) face the (2x2) structure is not such a barrier to further adsorption towards the nucleation threshold.

The mechanism for nucleation must be consistent with the fact that in going from a chemisorbed structure to the start of the oxide film formation, oxygen must be incorporated into the metal. One process which might trigger this incorporation of oxygen is the surface dipole layer set up by the transfer of charge to the adsorbate atoms. Because the surface site density is greatest on the (111) plane, it might be expected that the dipole would be greatest on this surface. This is supported by the fact that the work function is greater on the (111) plane (approx. 0.7 eV) than on the (100) or (110) planes (approx. 0.4 and 0.45 respectively)<sup>19</sup>. It thus seems quite feasible that the surface dipole moment drives the nucleations.

#### CHAPTER 6: REFERENCES

1. R. E. Schlier & H. E. Farnsworth, Adv. in Catalysis **9** (1957) 434.
2. H. E. Farnsworth & J. Tuul, J. Phys. Chem. Solids **9** (1959) 48.
3. L. H. Germer, Adv. in Catalysis **13** (1962) 191.
4. A. U. MacRae, Surf. Sci. **1** (1964) 319.
5. P. H. Holloway & J. B. Hudson, Surf. Sci. **43** (1974) 123.
6. D. F. Mitchell, P. B. Sewell & M. Cohen, Surf. Sci. **61** (1976) 355.
7. J. E. Demuth & T. N. Rhodin, Surf. Sci. **45** (1974) 249.
8. P. M. Norton, R. L. Tapping & J. W. Goodale, Surf. Sci. **65** (1977) 13.
9. L. H. Germer & A. U. MacRae, J. Appl. Phys. **33** (1962) 2923.
10. R. L. Park & H. E. Farnsworth, J. Appl. Phys. **35** (1964) 220.
11. G. Ertl & J. Koppers, Surf. Sci. **24** (1971)
12. K. P. Hooker, J. T. Grant & T. W. Haas, J. Vac. Sci. & Technol. **13** (1976) 296.
13. D. F. Mitchell, P. B. Sewell & M. Cohen, Surf. Sci. **69** (1977) 310.
14. J. A. Van den Berg, L. K. Verheij & D. G. Armour, Surf. Sci. **91** (1980) 218.
15. C. Benndorf, M. Egert, C. Noble, H. Seidel & F. Thieme, Surf. Sci. **92** (1980) 636.
16. G. E. Becker & H. G. Hagstrum, Surf. Sci. **30** (1972) 505.
17. R. L. Park & H. E. Farnsworth, Appl. Phys. Lett. **3** (1963) 167.
18. L. H. Germer, E. J. Scheibner & C. D. Hartman, Phil. Mag. **5** (1960) 222.
19. P. H. Holloway & J. B. Hudson, Surf. Sci. **33** (1972) 56.
20. A. A. Morgan & I. Dalins, Surf. Sci. **36** (1973) 526.
21. K. Holl & W. Palmer, Surf. and Interface analysis **2** (1980) 140.
22. H. Hopster & C. R. Brundle, Proc. 4th Intern. Conf. Solid Surfaces and 3rd ECOSS, Cannes 1980, Le Vide, Les Couches minces. 1, 275.
23. P. M. Marcus, J. E. Demuth & D. W. Jepsen, Surf. Sci. **53** (1975) 501.
24. C. R. Brundle, Amer. Inst. Phys. Conf. Proc. No. 61 (ed. U. Landman, Amer. Inst. Phys., New York) 1980, p. 57.
25. J. E. Demuth & T. N. Rhodin, Surf. Sci. **42** (1974) 261.
26. L. D. Roelofs, T. L. Einstein, P. E. Hunter, A. R. Kortan, R. L. Park & R. L. Roberts, J. Vac. Sci. Technol. **17** (1980) 231.

## CHAPTER 7 : SULPHUR ADSORPTION

### 1) Sulphur on copper

The first observations of surface structure related variations in the adsorption of sulphur on copper were made by Trehan & Goswani <sup>1</sup>. After exposing copper surfaces to sulphur vapour (carried by nitrogen), they noticed that the rate of reaction was greater on polycrystalline surfaces than on a (110) surface.

Domange & Oudar have studied the structural characteristics of adsorbed layers on several low index surfaces <sup>2,3,4</sup>. In their studies, the crystals were exposed to mixtures of  $H_2$  and  $H_2S$ . They describe three stages in the growth mechanism:

1. Initially  $H_2S$  molecules dissociate on the surface, and the sulphur ions adsorb on sites of maximum coordination.
2. Islands of a well-ordered phase begin to form. This corresponds to nucleation of a two-dimensional sulphide.
3. The islands grow until the entire surface is covered in the two-dimensional sulphide.

More recently, Moison & Domange <sup>5</sup> have investigated the interaction between mono-atomic steps on a vicinal (111) copper surface and the adsorbed sulphur monolayer. There are two possible equivalent epitaxial relations for a sulphur monolayer on a copper (111) surface. However, the presence of steps has a strong influence on the epitaxy such that one equivalent epitaxy is favoured over the other.

Bonzel <sup>6</sup> used A.E.S. to monitor the adsorption of sulphur on a Cu (110) face exposed to  $H_2S$ . He concluded that  $H_2S$  adsorbs rapidly on the (110) face of copper up to a coverage of half a monolayer. Thereafter, adsorption is slow.



Cain & Vook <sup>7</sup> exposed a (111) copper face to sulphur vapour carried in high purity  $H_2/N_2$ . Of the wide variety of possible copper/sulphur compound compositions that have been found <sup>8</sup>, Cain & Vook found only cuprous sulphide ( $Cu_2S$ ). The sulphide growth formed epitaxially at room temperature, developing into islands of up to 100 nm thickness.

## 2) Segregation

The segregation of sulphur to the surface of copper was first reported by Harris <sup>9</sup>, while Jenkins & Chung <sup>10</sup> have reported the formation of an ordered sulphur superstructure on the (111) face of copper. This superstructure was composed of sulphur that had segregated from the bulk of the crystal. Singh et al. <sup>11</sup> have studied polycrystalline samples of copper of various degrees of purity. In almost all cases they found that the sulphur concentration increased as the square root of the time elapsed. RHEED data from an OFHC copper sample indicated that an orthorhombic  $Cu_2S$  surface structure was formed. Moya & Moya <sup>12,13</sup> used a radio-tracer method to study the segregation of sulphur to an artificial grain boundary between two single crystals of copper. They demonstrated equilibrium segregation for the Cu/S system, with the coefficient of segregation,  $\alpha$ , given by the equation:

$$\alpha = 1.56 \cdot \exp(15500/RT)$$

This equation is a simplification of the equation derived by McLean <sup>14</sup>.

Clough & Stein <sup>15</sup> examined commercial oxygen free coppers with a bulk sulphur content of the order of 12 ppm. They observed grain boundary embrittlement with sulphur concentrations at the grain boundaries enriched by a factor of  $10^4$  compared with the bulk.

### 3) Results and discussion . S on Cu

Early experiments in measuring the segregation of sulphur to the surface of the copper cylinder were unsuccessful because of the depletion of sulphur from the bulk. As the subsequent attempts to dope cylinders with sulphur were also unsuccessful, the segregation studies for the copper cylinder were not pursued any further.

Oudar <sup>16</sup> found that the solubility of sulphur in copper is less than 1 ppm for temperatures below  $600^{\circ}\text{C}$ . It therefore seems likely that, under near equilibrium conditions, a single crystal of copper can not be doped with enough sulphur for reasonable segregation studies. In polycrystalline samples, a precipitate of sulphide at the grain boundaries could act as a reservoir of sulphur. This would provide sufficient sulphur within the bulk of the sample to enable segregation studies to be performed ( as for example in the experiments of Clough & Stein <sup>15</sup> , in which commercial polycrystalline copper containing 12 ppm sulphur was used ).

For cylindrical single crystals this is not possible, and adsorption of sulphur from an external source must be studied in preference to segregation from the bulk. However the decision to use a solid state electro-chemical cell as a source of sulphur had two important consequences. Firstly, most previous work has been on the adsorption (and dissociation) of  $\text{H}_2\text{S}$ , not sulphur molecules. Secondly, the electrochemical cell proved not to be reliable in operation. In particular, a reliable measure of the flux of sulphur

could not be obtained because of trouble with electrical contacts within the cell. It was thus not possible to determine the amount of sulphur adsorbed as a function of the exposure.

Figure 7.1 shows the results of a typical experiment in which the copper crystal was given three successive exposures to the sulphur beam from the sulphur source. The S 152eV Auger peak increases during each sulphur exposure, but without knowing the actual sulphur exposures, it is not possible to calculate a sticking factor for sulphur on copper. One thing that is obvious from figure 7.1 is the lack of variation in the height of the sulphur Auger peak round the crystal. Any variation that is present is too small to be detected above the background noise.

Figure 7.2 shows the effect on the 60eV copper Auger peak of successive exposures of the crystal to the sulphur beam. The large Kikuchi type variations in the clean copper Auger signal are reduced after one exposure, and almost disappear after the second exposure. A similar effect can be seen in the behaviour of the crystal current as the crystal is given successive exposures to the sulphur beam (figure 7.3). Again the Kikuchi type variations (i.e. the electron channelling patterns) become progressively weaker. Eventually the only variation left is the slow sinusoidal variation caused by the eccentric rotation of the cylinder.

It is thus apparent that an amorphous layer is forming on the crystal during sulphur exposures. This situation is different from the situation in which copper is exposed to oxygen. In that case clear electron channelling variations were still visible after very high exposures of oxygen. For example, figure 7.4 shows these variations from a copper cylinder that has been exposed to  $10^4$  Langmuirs of oxygen.

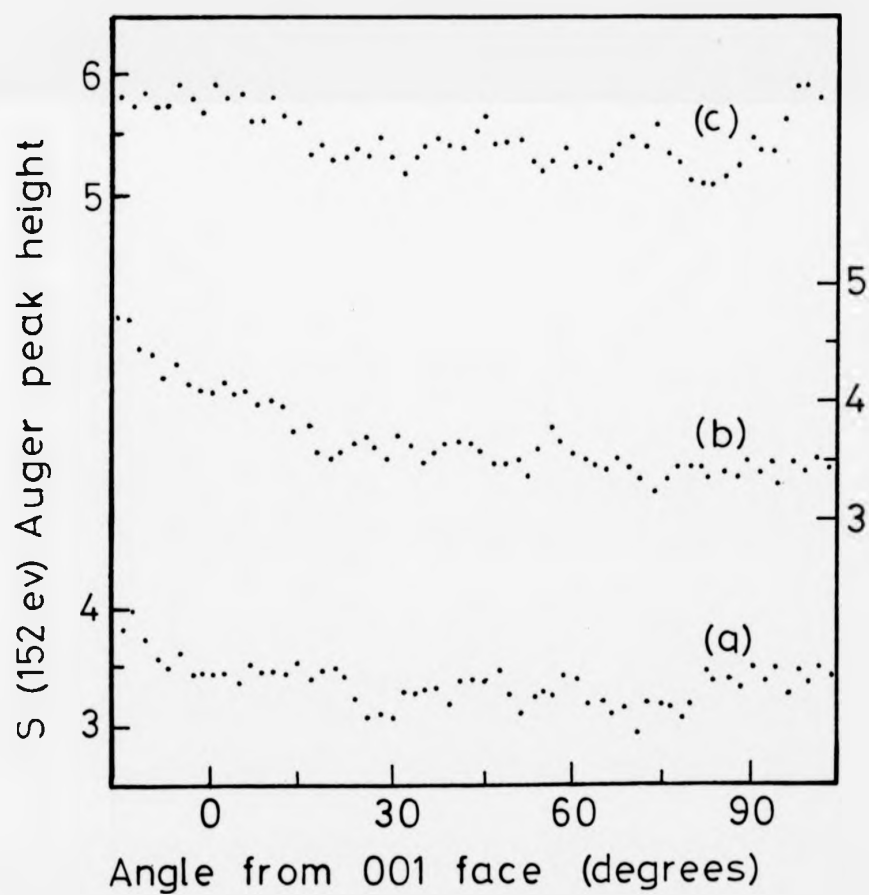


FIG. 7.1 Sulphur coverage on copper at increasing sulphur exposures.  
(c) is the coverage at saturation.

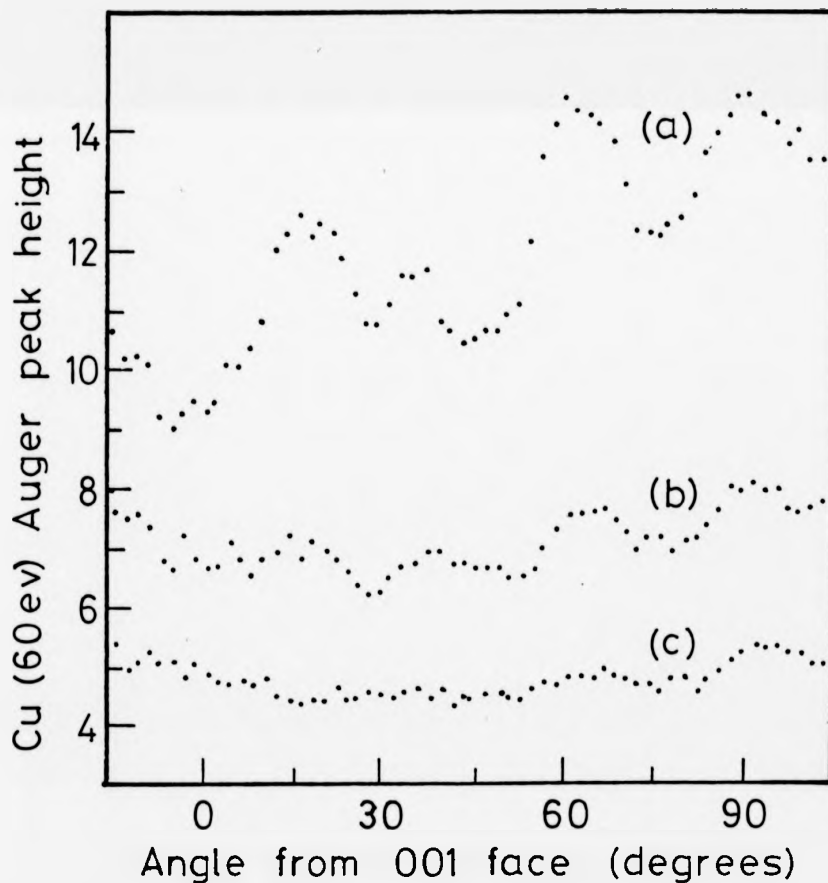
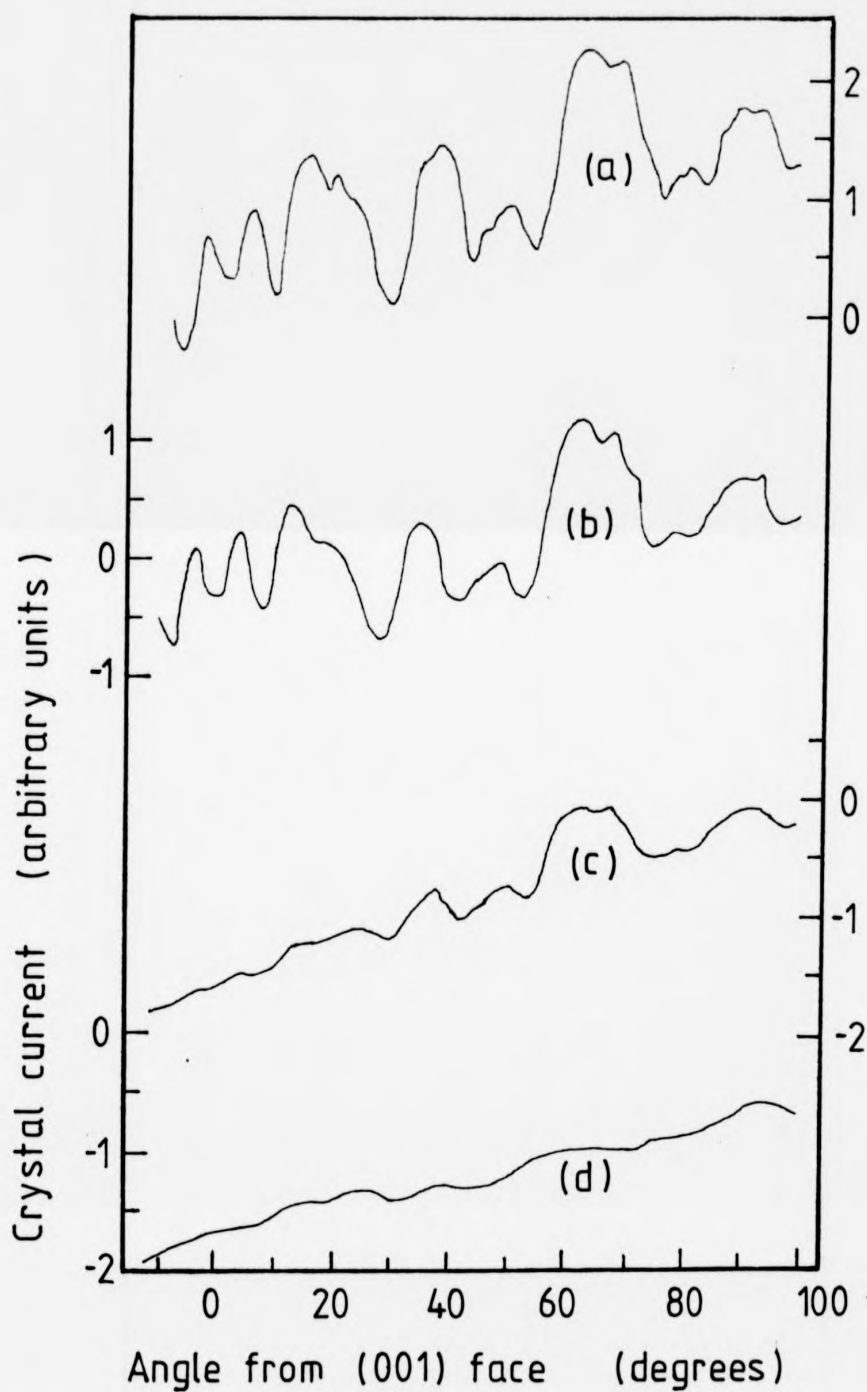
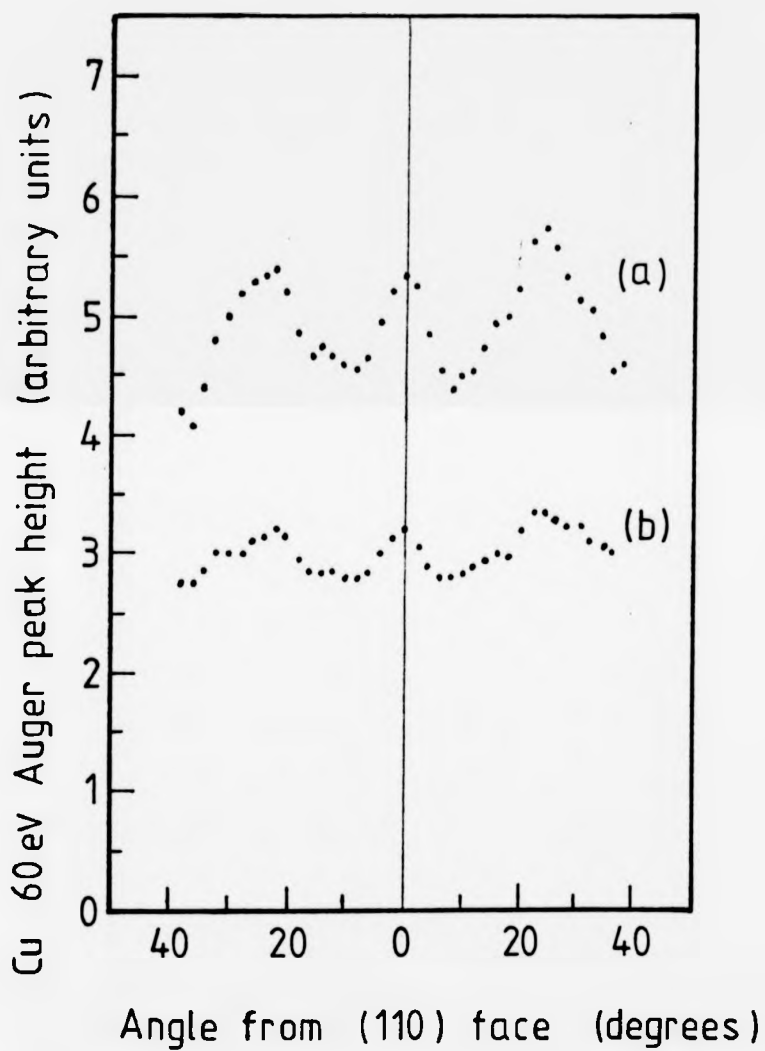


FIG. 7.2 Copper Auger peak heights after increasing sulphur exposures. Measurements taken at the same time as the sulphur measurements in fig. 7.1. (c) corresponds to the highest coverage (saturation).



**FIG. 7.3** Crystal current from a copper cylinder exposed to increasing amounts of sulphur. (d) corresponds to the highest sulphur coverage.



**FIG. 7.4** 60eV copper Auger peak from a copper cylinder .  
(a) clean cylinder; (b) cylinder exposed to  $10^{-4}$  L of oxygen.

The amorphous layer that builds up on the surface of the cylinder is not purely sulphur. The 60eV copper Auger peak never disappears, in fact as the sulphur exposure is increased, the copper Auger peaks tend to an equilibrium value. In one experiment such a large exposure was used that the surface of the cylinder was covered in a visible black compound. The copper Auger peaks were still clearly visible at this level of exposure. This suggests that even at room temperatures an amorphous sulphide layer forms on the crystal. The constant ratio of the sulphur to copper Auger peak heights implies that a compound of constant composition is formed. The actual ratio of the S 152eV to the Cu 60eV at high coverages was approximately 1.1 : 1, and this is consistent with the compound being  $\text{Cu}_2\text{S}$ . This situation is very similar to that found by Schwaha et al.<sup>17</sup> for sulphur on the (111) face of silver. Using a similar solid state cell they found that sulphur adsorbed on the (111) face of silver at room temperature with a sticking factor near unity. A compound of constant sulphur to silver ratio formed, rather than a thick layer of pure sulphur.

A further experiment was done at a low exposure of sulphur to see if there was any anisotropy in the adsorption at low coverages (figure 7.5). Even at low coverages, the only discernible variations are the broad variation due to the eccentricity of rotation of the crystal, and possibly a small variation arising from the Kikuchi type electron channelling effect.

The effect of heating the cylinder after it had been covered in sulphur can be seen in figure 7.6. The electron channelling variations in the copper 60eV Auger peak are clearly visible on the clean cylinder (b). These variations disappear when the crystal is



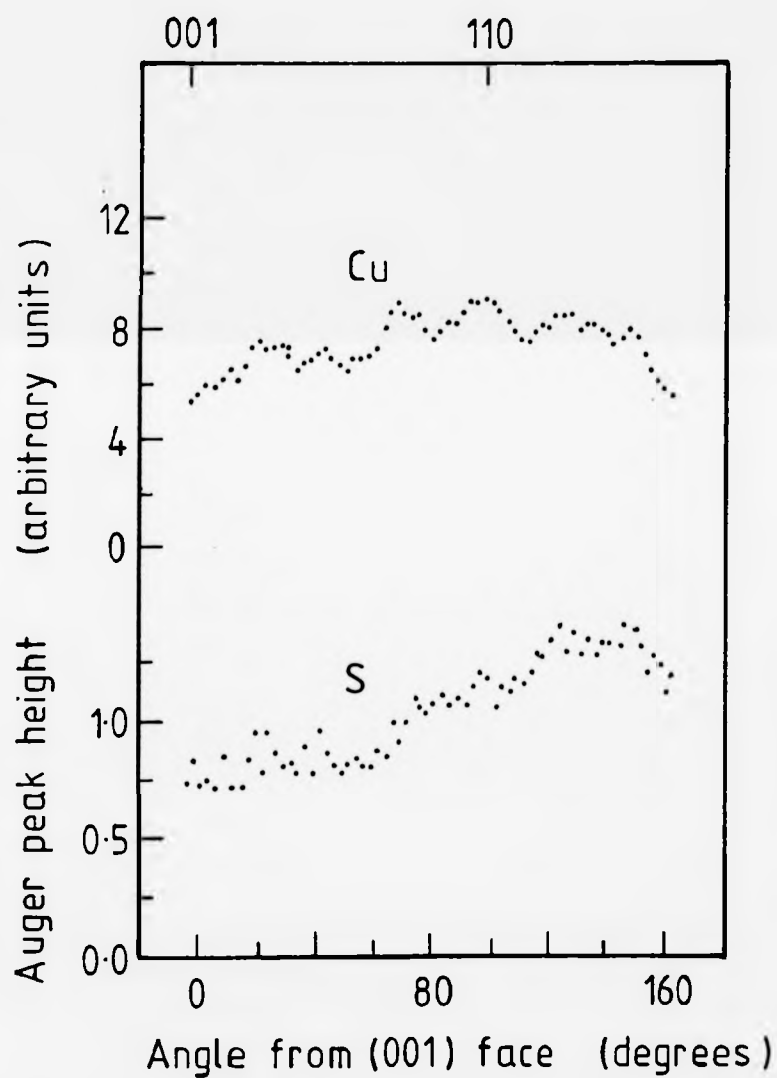
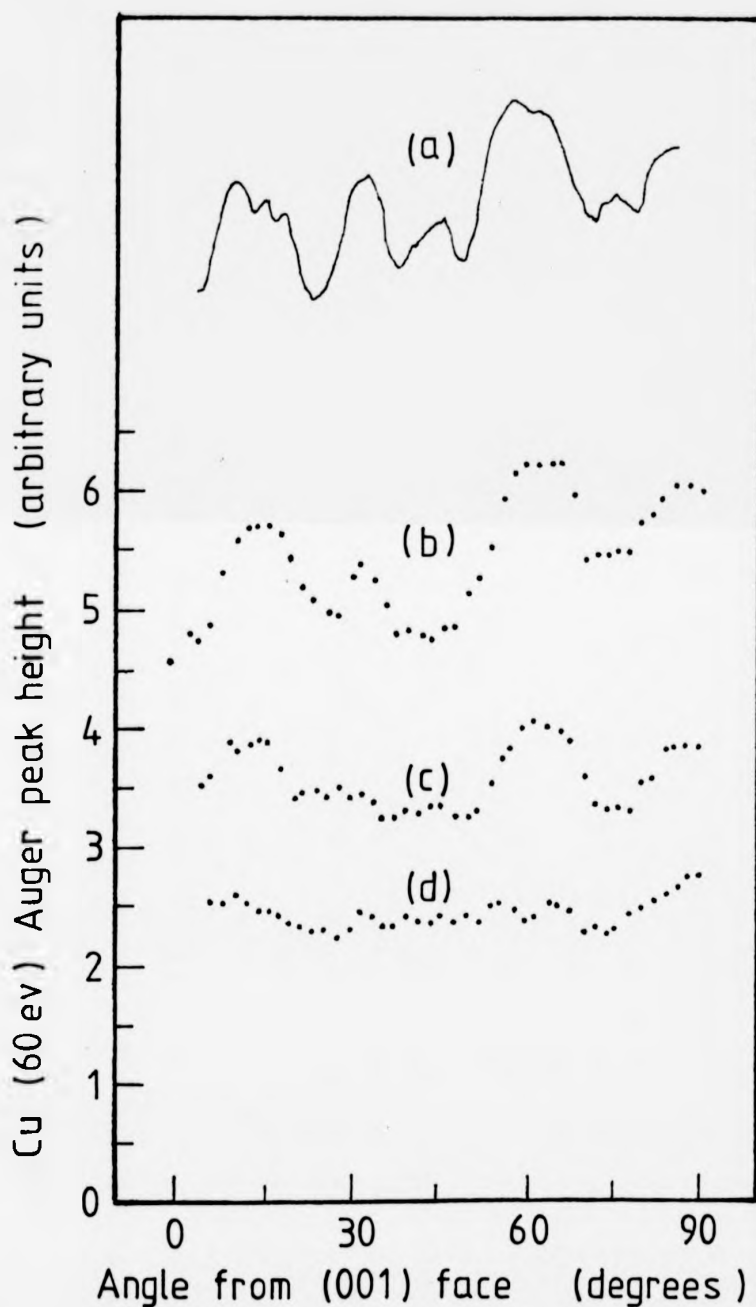


FIG. 7.5 S 152eV and Cu 60eV Auger peak heights at low sulphur exposures.



**FIG. 7.6** The effect of sulphur coverage on the 60eV Cu Auger peak.  
 (a) Crystal current from a clean cylinder (shown for reference).  
 (b) Cu peak from a clean cylinder. (c) Cu peak from a cylinder covered in sulphur then heated to 500°C for 30 minutes. (d) Cu peak from a sulphur covered cylinder.

exposed to sulphur (d), but reappear after the crystal has been heated (c) .

The adsorption of sulphur on copper can be summarised as follows:

- 1) Sulphur adsorbs isotropically i.e. with equal sticking factor on all faces on the cylinder.
- 2) An amorphous sulphide (probably  $\text{Cu}_2\text{S}$ ) forms on the cylindrical crystal.
- 3) As more sulphur is adsorbed, the sulphide grows uniformly on all faces of the cylinder. Layers of pure sulphur do not build up on the surface.

#### 4) Sulphur on nickel

The segregation of sulphur to nickel surfaces has been widely studied using LEED<sup>19,20</sup>, AES<sup>19,21-23</sup>, microhardness measurements and radioactive tracing<sup>18</sup>, and angle resolved UV photoemission<sup>24</sup>. The adsorption of sulphur on nickel surfaces has also been studied using the dissociative adsorption of  $H_2S$  as a means of producing surface sulphur layers on nickel.<sup>24,25</sup>

Floreen and Westbrook<sup>18</sup> showed that sulphur is strongly segregated to grain boundaries in polycrystalline nickel. This segregation causes a local increase in the microhardness of the grain boundary. Sickafus<sup>19</sup>, and then Riwan<sup>20</sup>, studied the segregation of sulphur to the (110) face of nickel in detail. Riwan showed that the  $c(2 \times 2)$  structure observed by Sickafus was not the final structure, as further segregation could take place.

The  $c(2 \times 2)$  structure was also observed by Perdereau & Oudar<sup>25</sup> in their adsorption studies. They observed a similar sequence of events on each of the three major low-index faces. Initially a preliminary adsorption state occurs with localisation of the sulphur atoms at sites of maximum coordination of the metal. This state is transformed by reconstruction into a two dimensional sulphide compound. Demuth et al.<sup>26</sup> have done a detailed analysis of experimental LEED data which confirms that in the initial stages of adsorption (or segregation) the sulphur atoms sit in high coordination sites in the atomic hollows of the surface.

#### 4) Sulphur on nickel

The segregation of sulphur to nickel surfaces has been widely studied using LEED<sup>19,20</sup>, AES<sup>19,21-23</sup>, microhardness measurements and radioactive tracing<sup>18</sup>, and angle resolved UV photoemission<sup>24</sup>. The adsorption of sulphur on nickel surfaces has also been studied using the dissociative adsorption of  $H_2S$  as a means of producing surface sulphur layers on nickel.<sup>24,25</sup>

Floreen and Westbrook<sup>18</sup> showed that sulphur is strongly segregated to grain boundaries in polycrystalline nickel. This segregation causes a local increase in the microhardness of the grain boundary. Sickafus<sup>19</sup>, and then Riwan<sup>20</sup>, studied the segregation of sulphur to the (110) face of nickel in detail. Riwan showed that the c(2x2) structure observed by Sickafus was not the final structure, as further segregation could take place.

The c(2x2) structure was also observed by Perdereau & Oudar<sup>25</sup> in their adsorption studies. They observed a similar sequence of events on each of the three major low-index faces. Initially a preliminary adsorption state occurs with localisation of the sulphur atoms at sites of maximum coordination of the metal. This state is transformed by reconstruction into a two dimensional sulphide compound. Demuth et al.<sup>26</sup> have done a detailed analysis of experimental LEED data which confirms that in the initial stages of adsorption (or segregation) the sulphur atoms sit in high coordination sites in the atomic hollows of the surface.

### 5) Results and discussion : S on Ni

As with the results for sulphur adsorption on copper, it was not possible to obtain a reliable measure of the sulphur exposure. The experiments were therefore rather limited as it was not possible to obtain, for example, sticking coefficients. A further limitation to the experimental accuracy has been pointed out by Coad & Riviere.<sup>21</sup> They showed that the amplitude of the differentiated Auger spectrum of sulphur on a nickel surface was not as reliable a measurement of the amount of sulphur present as the integrated area under the peak. However, bearing in mind the experimental limitation to the time available for collecting data, all measurements have been done using the derivative of the Auger peaks.

The broad trend of the behaviour is similar to the previous case of sulphur adsorption on copper. As adsorption proceeds, the sulphur to nickel Auger peak height ratio increases and then levels off at a constant saturation value. Further exposure does not then increase the S (152) eV Auger peak height. Results from an experiment involving three successive sulphur exposures are shown in figure 7.7. As with copper, the sulphur peak height is almost constant around the cylinder at all exposures.

However, at low exposures, the adsorption is slightly anisotropic round the crystal. This can be seen in figure 7.8. The high apparent noise level is due to the small signal being measured. At this stage the S 152eV Auger peak is of the order of 1/30th of the Ni 61eV peak. This anisotropy extends to a slightly higher sulphur coverage. In figure 7.9 the ratio of the sulphur to nickel peak heights is plotted at an exposure corresponding to a sulphur coverage of the order of three times as great as that in figure 7.8. The anisotropy is not as pronounced as for oxygen on nickel or copper; however it is certainly more marked than for the case of sulphur on copper when

##### 5) Results and discussion : S on Ni

As with the results for sulphur adsorption on copper, it was not possible to obtain a reliable measure of the sulphur exposure. The experiments were therefore rather limited as it was not possible to obtain, for example, sticking coefficients. A further limitation to the experimental accuracy has been pointed out by Coad & Riviere<sup>21</sup>. They showed that the amplitude of the differentiated Auger spectrum of sulphur on a nickel surface was not as reliable a measurement of the amount of sulphur present as the integrated area under the peak. However, bearing in mind the experimental limitation to the time available for collecting data, all measurements have been done using the derivative of the Auger peaks.

The broad trend of the behaviour is similar to the previous case of sulphur adsorption on copper. As adsorption proceeds, the sulphur to nickel Auger peak height ratio increases and then levels off at a constant saturation value. Further exposure does not then increase the S (152) eV Auger peak height. Results from an experiment involving three successive sulphur exposures are shown in figure 7.7. As with copper, the sulphur peak height is almost constant around the cylinder at all exposures.

However, at low exposures, the adsorption is slightly anisotropic round the crystal. This can be seen in figure 7.8. The high apparent noise level is due to the small signal being measured. At this stage the S 152eV Auger peak is of the order of 1/30th of the Ni 61eV peak. This anisotropy extends to a slightly higher sulphur coverage. In figure 7.9 the ratio of the sulphur to nickel peak heights is plotted at an exposure corresponding to a sulphur coverage of the order of three times as great as that in figure 7.8. The anisotropy is not as pronounced as for oxygen on nickel or copper; however it is certainly more marked than for the case of sulphur on copper when

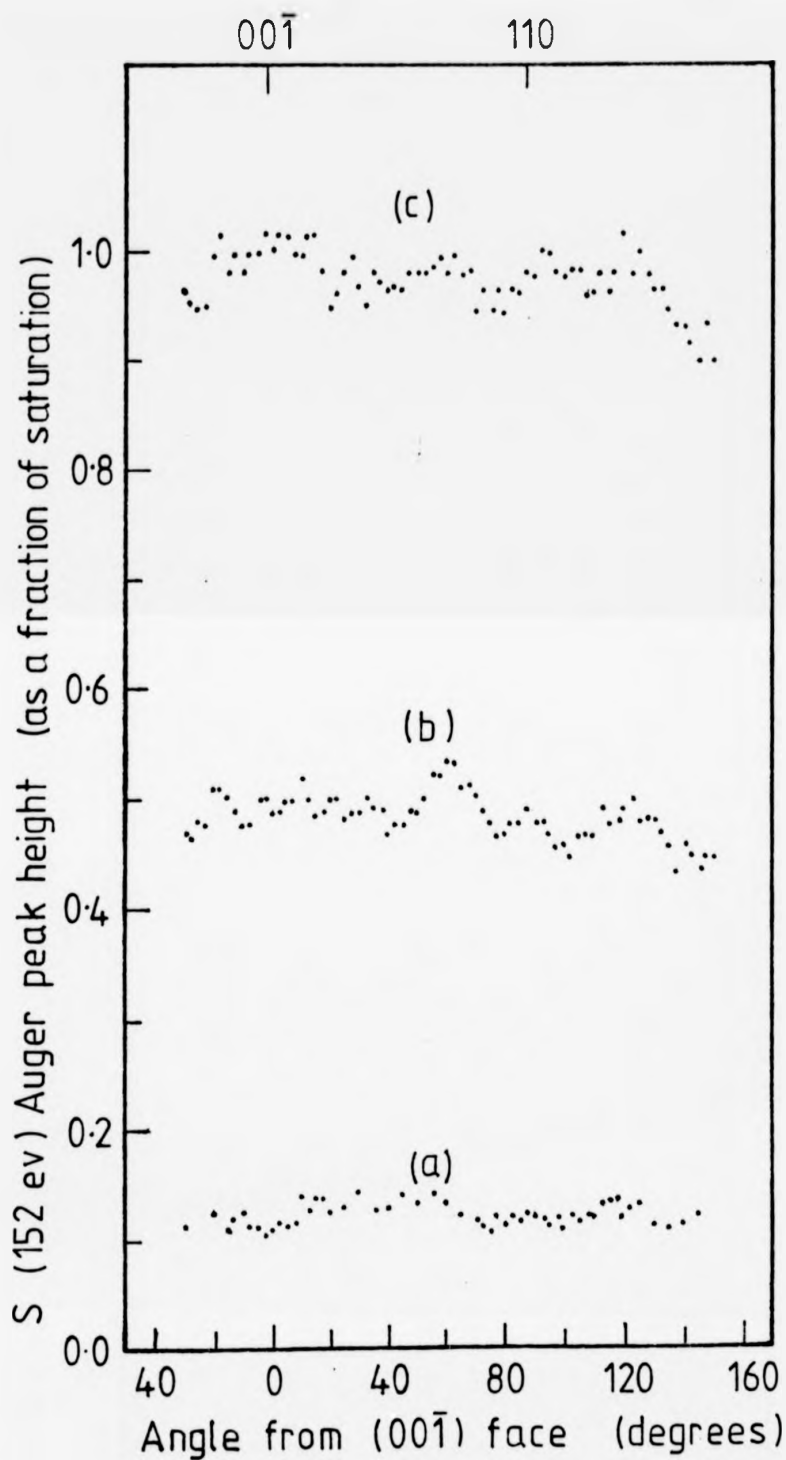


FIG. 7.7 Sulphur coverage on nickel. (a), (b), & (c) correspond to increasing sulphur exposures.



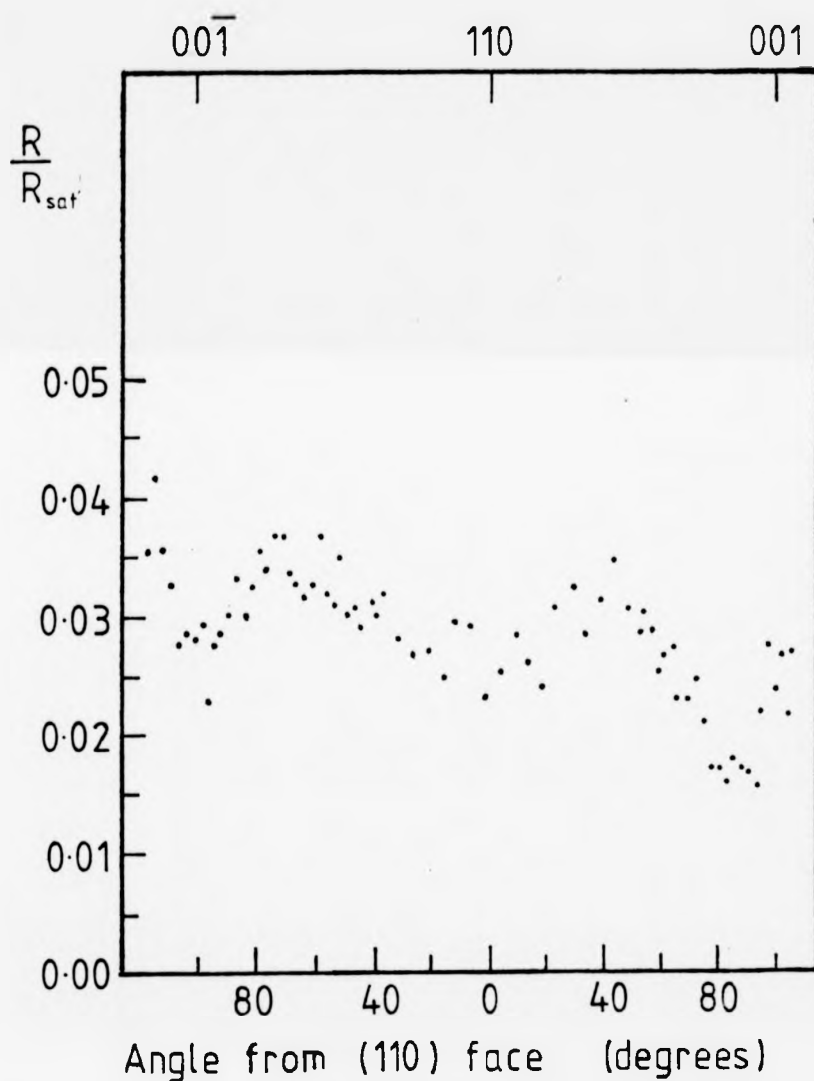


FIG. 7.6 Sulphur coverage on nickel after a small exposure to sulphur.  $R$  is the ratio of the peak heights of the S 152eV and Ni 61eV Auger peaks.

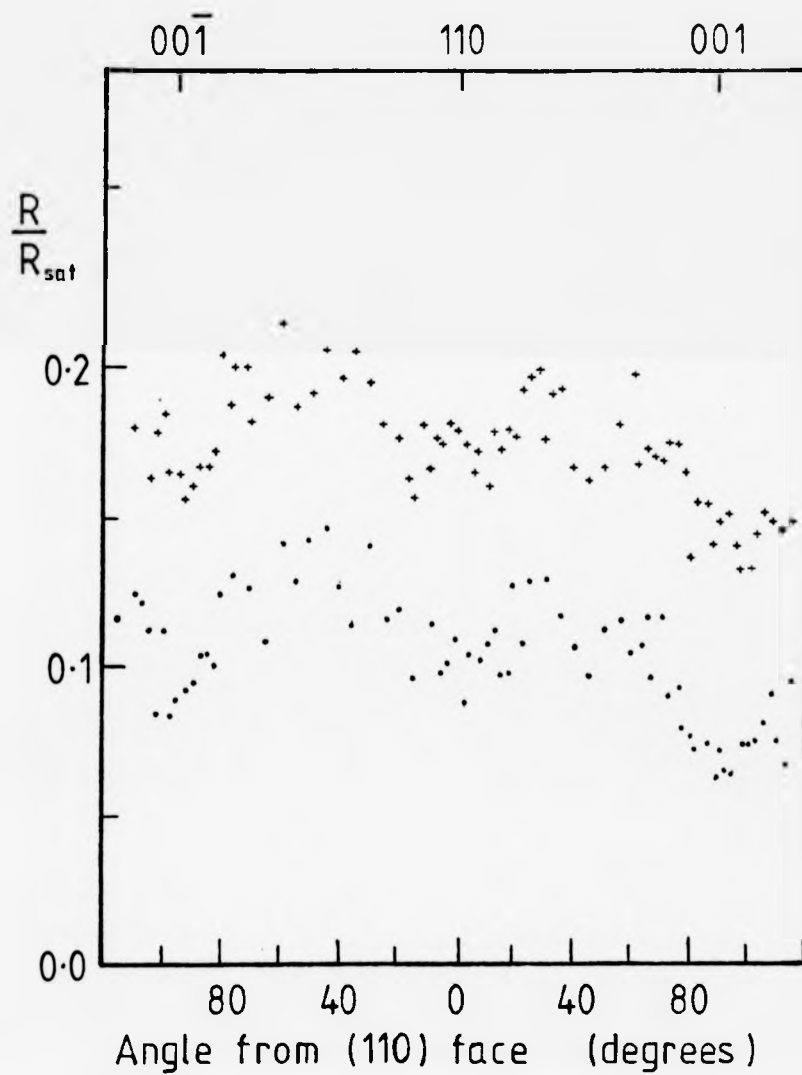


FIG. 7.9 Sulphur coverage on nickel.  $R$  is the ratio of the peak heights of the S152eV and Ni 61eV Auger peaks.

no anisotropy was discernible. The sulphur peak is at a minimum at the (001) and (110) faces. There is also a broad maximum in the region of the (111) face. This contrasts with the adsorption of oxygen on nickel where minima are found on the (111) and (001) faces, and maxima are found on the (110) and (113) faces.

As with the adsorption of sulphur on copper, adsorption of sulphur on nickel leads eventually to the formation of an amorphous bulk sulphide. This amorphous sulphide layer attenuates the electron channelling pattern from the bulk nickel crystal. This can be seen clearly in figures 7.10 and 7.11 which show the effect of increasing sulphur exposures on the Ni 61eV Auger peak and the elastically reflected electron peak. The complete disappearance of all structure in, for example, the elastic peak plot, suggests that the sulphide is completely amorphous and does not grow epitaxially on any face. Furthermore, the fact that at higher coverages growth is isotropic also suggests that the bulk sulphide phase is amorphous. If it were not completely amorphous, growth on certain faces might be favoured leading to anisotropy in the plot of the S 152 eV Auger peak height.

This behaviour contrasts with the results of Perdereau & Oudar<sup>25</sup> for the dissociative adsorption of  $H_2S$  on nickel. In their study a two dimensional sulphide formed at saturation. Further exposures to  $H_2S$  did not result in further adsorption or the formation of a bulk sulphide.

As with sulphur on copper, the ratio of the S 152 eV to the Ni 61eV Auger peaks tends to a constant value ( about 1.75 ). The ratio of the concentrations of sulphur to nickel can be roughly calculated as was done for sulphur on copper by comparing the measured Auger peaks with standard Auger peaks.<sup>27</sup> The value of the sulphur concentration found by this method (39% a.o.) is reasonably close to the value that would be expected (33% a.o.) if the sulphide

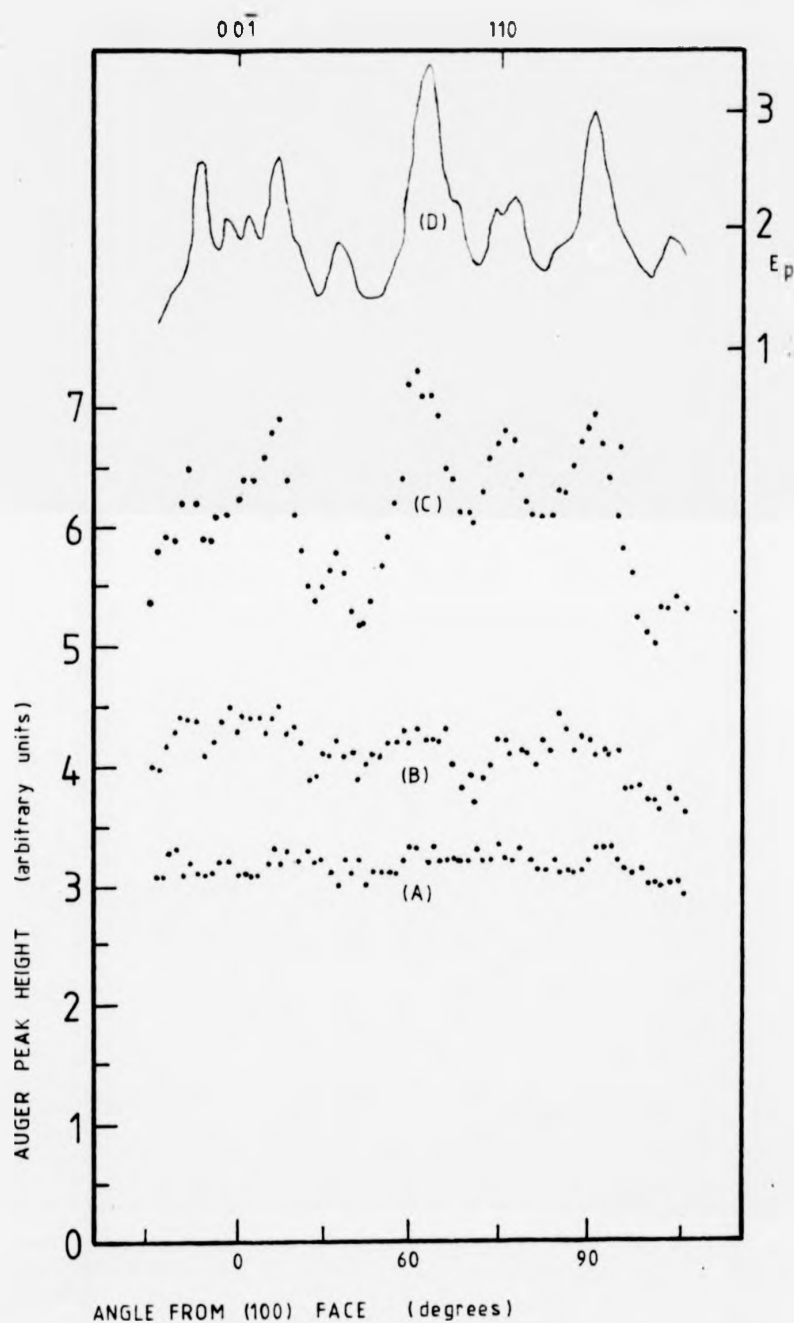


**FIG. 7.10** The effect of sulphur on the 61eV Ni Auger peak. (c) Ni Auger peak from a clean sample. (b) & (a) show the Ni peak from a sample exposed to increasing amounts of sulphur. (d) shows the elastic peak from a clean sample for comparison.

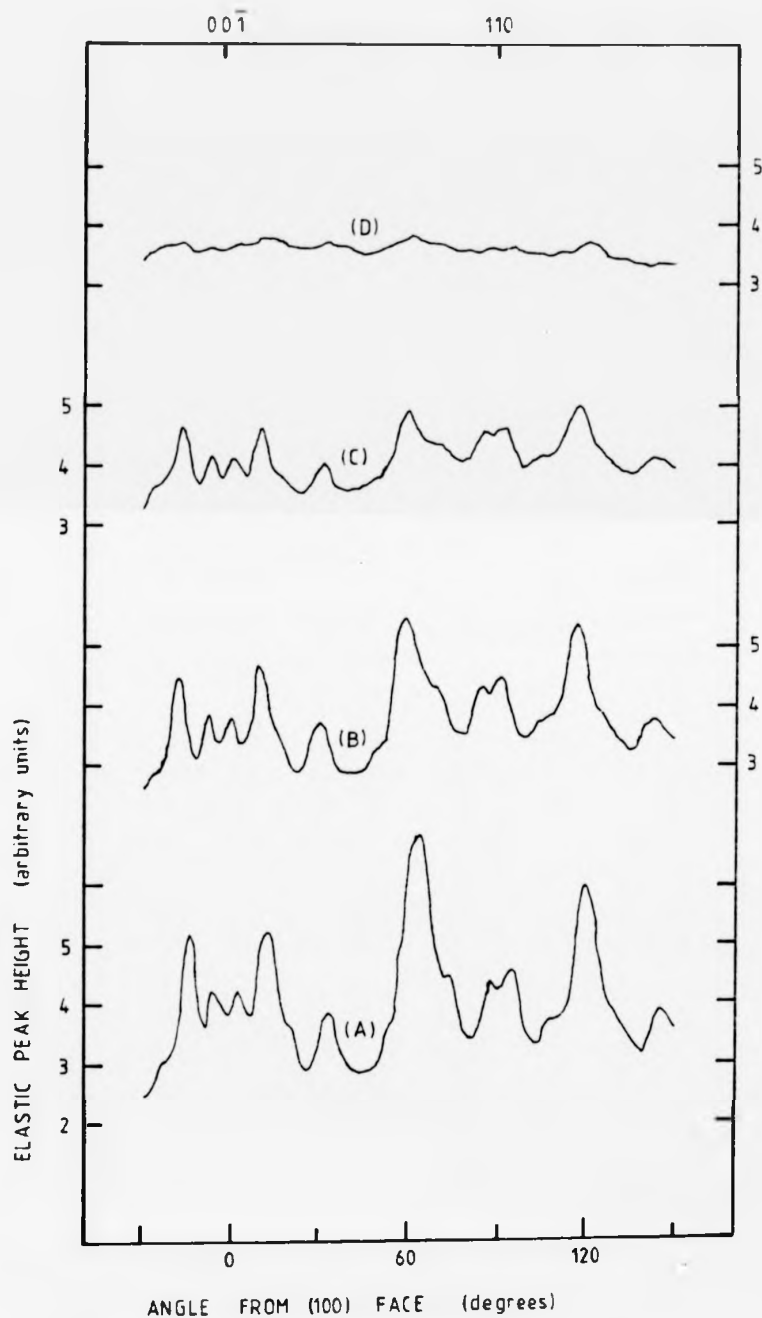


**FIG. 7.11** The elastic peak from a nickel sample exposed to increasing amounts of sulphur. (a) is the peak from a clear sample, (d) is the peak from a sample with a saturation coverage.

was in fact  $\text{Ni}_2\text{S}$ .

In summary then, the adsorption of sulphur on nickel is seen to proceed in three stages:

- 1) At low coverages adsorption occurs anisotropically. Adsorption is slowest on the (001) and (110) faces, but the difference between faces is not large.
- 2) At intermediate coverages a bulk sulphide grows amorphously. As the sulphide layer thickens, the ratio of the S 152eV to the Ni 61eV Auger peaks approaches a constant value.
- 3) At high coverages a bulk sulphide of constant composition (probably  $\text{Ni}_2\text{S}$ ) grows amorphously on all faces. the Auger peak ratio remains constant.

#### CHAPTER 7: REFERENCES

1. Y. N. Trehan & A. Goswami, Trans. Faraday Soc. **55** (1959) 2162.
2. J. L. Domange & J. Oudar, Surf. Sci. **11** (1968) 124.
3. J. Oudar, J. Vac. sci. Technol. **9** (1972) 657.
4. J. L. Domange, J. Vac. sci. Technol. **9** (1972) 682.
5. J. M. Koison & J. L. Domange, Surf. Sci. **67** (1977) 336.
6. H. P. Bonzel, Surf. Sci. **27** (1971) 387.
7. O. J. Cain & R. W. Vook, Thin Solid Films **58** (1979) 209.
8. R. P. Elliott, "Constitution of Binary alloys, 1st supplement", McGraw-Hill, New York (1965).
9. L. A. Harris, J. Appl. Phys. **39** (1968) 1419.
10. L. H. Jenkins & M. F. Chung, Surf. Sci. **74** (1971) 125.
11. B. Singh, R. W. Vook & E. A. Knabbe, J. Vac. sci. Technol. **17** (1980) 29.
12. G. E. Moya-Gontier & F. Moya, Scripta Met. **8** (1974) 153.
13. G. E. Moya-Gontier & F. Moya, Scripta Met. **9** (1975) 307.
14. D. McLean, "Grain boundaries in Metals", Oxford, Clarendon Press (1957).
15. S. P. Clough & D. F. Stein, Scripta Met. **9** (1975) 1163.
16. J. Oudar, Compt. Rend. **249** (1959) 259.
17. K. Schwaha, M. D. Spencer & R. L. Lambert, Surf. Sci. **81** (1979) 273.
18. S. Floreen & J. H. Westbrook, Acta Met. **17** (1969) 1175.
19. E. N. Sickafus, Surf. Sci. **19** (1970) 181.
20. R. Riwan, Surf. Sci. **27** (1971) 267.
21. J. P. Coad & J. C. Rivière, Proc. R. Soc. Lond. A **331** (1972) 403.
22. E. N. Sickafus & F. Steinrissler, J. Vac. sci. Technol. **10** (1973) 43.
23. S. Broz, C. Koziol & J. Kolaczkiwicz, Vacuum **26** (1975) 61.
24. T. T. Anh Nguyen & R. C. Cinti, Surf. Sci. **68** (1977) 566.
25. M. Perdereau & J. Oudar, Surf. Sci. **20** (1970) 80.

26. J. E. Demuth, D. W. Jepsen & P. A. Marcus, Phys. Rev. Lett. 32  
(1974) 1182.

27. "Handbook of Auger electron spectroscopy", 2nd Edn. Physical  
Electronic Industries Inc., Minnesota (1976).



## CHAPTER 8 : CONCLUSION

The advantages of using a single crystal to study the influence of surface structure on the reactivity of copper and nickel surfaces have been clearly demonstrated by the work presented in this thesis. The disadvantages of using a polycrystalline sample are that determining the crystallographic orientation of individual grains is not easy, and the faces that are present on a random sample of grains are generally complex faces of high Miller index. The advantage of a hemispherical crystal (that all crystallographic orientations are present at the surface) is outweighed by the disadvantage of the difficulty that was found in accurately positioning the electron beam on the sample.

The compromise of using a cylindrical sample turns out to be a good one. The problem of determining the exact surface orientation that is being sampled at any instant by the electron beam can be solved by using the symmetry of the results. Furthermore, by using a cylindrical crystal with a  $\langle 110 \rangle$  axis ( a method developed by Kramer<sup>1</sup> ), all three major low index faces were present on the same sample. Furthermore, the  $\langle 110 \rangle$  axis cylinder has the property that the surface structure varies round the crystal in a well-determined manner. The influence of surface structure can thus be easily studied using such a sample.

The four basic systems provided by adsorbing oxygen or sulphur on copper or nickel cylinders are influenced in different ways by the variation in the surface structure round the crystal cylinders. At one extreme, oxygen adsorption on copper is highly anisotropic; the reaction of oxygen onto a copper surface does not proceed past the chemisorption stage to a bulk oxidation phase (chapter 5). At the other extreme, the adsorption on copper of  $S_2$  molecules from a

## CHAPTER 8 : CONCLUSION

The advantages of using a single crystal to study the influence of surface structure on the reactivity of copper and nickel surfaces have been clearly demonstrated by the work presented in this thesis. The disadvantages of using a polycrystalline sample are that determining the crystallographic orientation of individual grains is not easy, and the faces that are present on a random sample of grains are generally complex faces of high Miller index. The advantage of a hemispherical crystal (that all crystallographic orientations are present at the surface) is outweighed by the disadvantage of the difficulty that was found in accurately positioning the electron beam on the sample.

The compromise of using a cylindrical sample turns out to be a good one. The problem of determining the exact surface orientation that is being sampled at any instant by the electron beam can be solved by using the symmetry of the results. Furthermore, by using a cylindrical crystal with a  $\langle 110 \rangle$  axis ( a method developed by Kramer<sup>1</sup> ), all three major low index faces were present on the same sample. Furthermore, the  $\langle 110 \rangle$  axis cylinder has the property that the surface structure varies round the crystal in a well-determined manner. The influence of surface structure can thus be easily studied using such a sample.

The four basic systems provided by adsorbing oxygen or sulphur on copper or nickel cylinders are influenced in different ways by the variation in the surface structure round the crystal cylinders. At one extreme, oxygen adsorption on copper is highly anisotropic; the reaction of oxygen onto a copper surface does not proceed past the chemisorption stage to a bulk oxidation phase (chapter 5). At the other extreme, the adsorption on copper of  $S_2$  molecules from a

molecular beam does not start with <sup>an</sup> anisotropic chemisorption phase; the reaction goes straight to <sup>a</sup>bulk "sulphidation" phase which occurs isotropically round the crystal (chapter 7).

The behaviour of nickel is quite different. The oxygen chemisorption phase appears to start isotropically, with an initial sticking factor of unity; however the coverage at the end of the chemisorption phase is different on different faces. After the chemisorption phase, an oxidation phase proceeds at a rate which depends strongly on the structure of the substrate surface (chapter 6). When sulphur segregates to a nickel surface (chapter 3), or adsorbs on a nickel surface (chapter 7), there does appear to be a slight variation in the amount of sulphur that segregates or chemisorbs on different faces. In the case of adsorption from a molecular  $S_2$  beam, adsorption of sulphur proceeds past the chemisorption phase into a bulk "sulphidation" phase. As with copper, the bulk sulphide that forms is amorphous, and would consequently be expected to grow isotropically, as is observed. Experiments at raised temperatures (chapter 3) have also shown the equivalence of results obtained in adsorption and segregation experiments.

One major problem, that could only be solved by further work on these types of samples, is the lack of structural information to complement the AES data. This is important because the interpretation of the results in this thesis is based on the assumption that the cylinders were perfect cylinders with no surface defects or facets. The importance of complementary structural information was emphasised by Blakely<sup>2</sup> who noted that the presence of carbon and sulphur on stepped nickel surfaces could induce changes in the morphology of the surface compared with the clean surface. The U.H.V. chamber used in this study had no facilities (e.g. LEED) for determination

of surface structure, and so the presence of such morphological effects could not be ruled out.

This is particularly the case for the oxygen adsorption experiments. In these experiments the essentially linear variation in the oxygen coverage round the cylinder could have been caused by facetting. In that case a "face" intermediate between (say) the (110) and (111) faces might have consisted of (110) and (111) facets, the ratio of the size of the facets depending on the angle of the face with respect to the (110) and (111) faces.

No such facets were observed under an optical microscope, but there was no evidence to conclusively show whether such facets did or did not exist on a sub-microscopic scale. The ability to settle this question by examining the surface structure (using LEED or RHEED for example) would have greatly enhanced the value of this work.

Finally, it is possible to speculate (for the case of oxygen chemisorption on copper) as to what would happen on an arbitrary face. This would enable predictions to be made about the variation in the chemisorption rate over a spherical crystal of the type studied by Young, Cathcart & Gwathmey<sup>3</sup> in the oxidation regime.

In chapter 5 the sticking factor of a face in the  $\langle 110 \rangle$  zone was related to the proportion of that face that could be classed as "rough" as compared with "smooth". In the  $\langle 110 \rangle$  zone, faces contain straight steps, but not kinked steps. The "roughness" of an arbitrary face was then considered as a function of the density of straight steps in that face. However on a truly arbitrary face we must also consider the effect of kinked steps, steps that are in some sense "rougher" than the straight edged steps that we have been considering up to now.

This can be done by looking at the maximum site coordination at a particular face. Using the notation of Sanders<sup>4</sup> the coordination

of a site is  $B_i$ , where  $i$  is the number of surface atoms an adatom can bond to.

Every face will contain sites involving one or two substrate atoms ( $B_1$  and  $B_2$  sites). The (111) face (the smoothest face) also contains  $B_3$  sites, but no sites with  $i$  greater than 3. Similarly the (100) face contains  $B_4$  sites, but no sites with  $i$  greater than 4. The "rough" (110) surface contains  $B_5$  sites, the highest coordination sites that are present in the  $\langle 110 \rangle$  zone. Increasing coordination (increasing  $i$ ) can thus be seen as a measure of increasing surface "roughness".

The problem of predicting what will happen at an arbitrary face can thus be thought of as the problem of predicting what will happen at a face containing  $B_6$  sites, as this is the only type of site present on a well-ordered f.c.c. surface that is not represented on faces in the  $\langle 110 \rangle$  zone (the  $B_6$  site is of course the kinked-step site mentioned earlier).

The behaviour of a  $B_6$  site can be predicted by considering the results presented in figure 8.1. This figure contains measurements for the initial sticking factor of oxygen on copper from this work and from the references quoted in chapter 5. The horizontal axis is the maximum site coordination that is present on a particular face ( $B_3$  therefore corresponds to a (111) face,  $B_4$  to a (100) face, and  $B_5$  to a (110) face). The ranges of the initial sticking factors from the references quoted in chapter 5, plus the sticking factors measured in this work are shown as the three vertical bars.

The effect on the initial sticking factor of increasing the site coordination is apparent. It would not seem too unreasonable to extrapolate the graph to a  $B_6$  site. In fact the maximum sticking factor that a  $B_6$  site could have is unity (i.e.  $\log S_0 = 0$ ), and this value is shown in figure 8.1 as a circled dot. This appears to

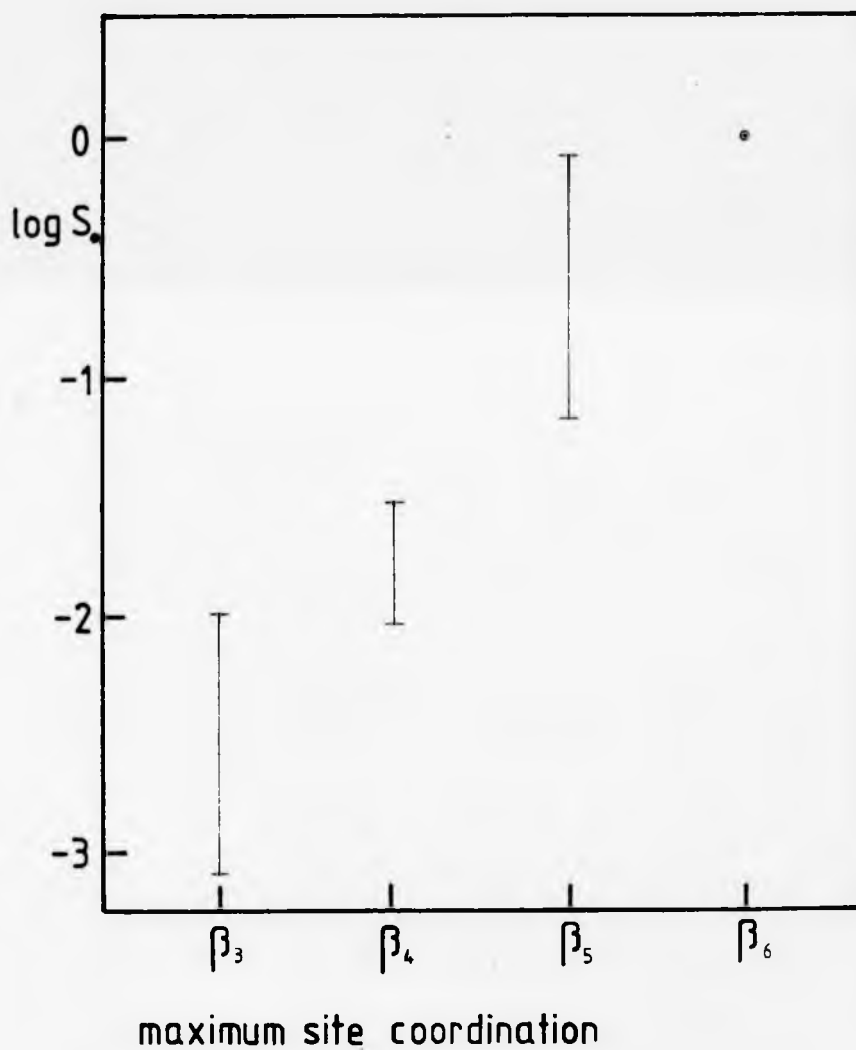


FIG. 6.1 Initial sticking factor as a function of site coordination.

be a reasonable extrapolation of the linear trend of results from  $B_3$ ,  $B_4$  and  $B_5$  sites. This is of course assuming a relationship of the form:

$$S_o = Ae^{Bi}$$

where A and B are constants, and i is the site coordination number.

To predict the sticking factor of an arbitrary face the proportion of sites of different coordination on that face must first be calculated. The average sticking factor of that face may then be calculated from the sticking factors of the various sites present, and from the proportion of the various sites that are present. This method is of course similar to the method used in chapter 5 for the calculation of the oxygen coverage on the cylindrical crystal. In principle then, it is possible to predict the initial sticking factor for all the faces of a spherical crystal, as used in the pioneering experiments of Gwathmey and coworkers.

#### CHAPTER 8: REFERENCES

1. H. M. Kramer, E. Langer & E. Bauer. Proc. 4th Internat. Conf. Solid Surfaces and 3rd ECOSS, Cannes (1980). "Le Vide, Les Couches Minces", 1, 217.
2. J. L. Blakely. Report 2891, Materials Science Centre, Cornell University, New York (1977). Paper presented at 3rd Internat. Summer Inst. in Surf. Sci., University of Wisconsin, Milwaukee (1977).
3. F. W. Young, J. V. Cathcart & A. T. Gwathmey, Acta Met. 4 (1956) 145.
4. J. V. Sanders. Proc. 2nd Internat. Conf. on Solid Surfaces (1974), Japan. J. Appl. Phys., Suppl. 2, Pt. 2 (1974) 479.
5. J. F. Nicholas, "An atlas of models of crystal surfaces", Gordon & Breach, Science Publishers, New York (1965).



#### APPENDIX A

##### Integration of the Equation for the Sticking Factor

An equation for the sticking factor of the form:

$$S = S_0(1 - 2\theta)^2 \quad \dots 1$$

can be used to derive an equation relating the coverage  $\theta$  to the exposure  $E$ .  $\theta$  and  $E$  will generally be measured in monolayers and Langmuirs respectively.

The rate of change of coverage is given by:

$$\frac{d\theta}{dt} = CSp$$

where  $C$  is a constant and  $p$  is the pressure measured in torr.

Substituting for the sticking factor from equation 1 gives:

$$\frac{d\theta}{dt} = C'S_0(1 - 2\theta)^2$$

which, on rearranging becomes:

$$P = \frac{1}{C'S_0(1 - 2\theta)^2} \frac{d\theta}{dt}$$

Integrating both sides gives:

$$\int_0^t P dt = \frac{1}{C'S_0} \int_0^\theta \frac{1}{(1 - 2\theta)^2} d\theta \quad \dots 2$$

The left-hand side of equation 2 is, by definition, the exposure  $E$ ; equation 2 is therefore equivalent to:

$$E = \frac{1}{2C'S_0(1 - 2\theta)} + b \quad \dots 3$$

where  $b$  is a constant. To find  $b$  we apply the condition that the coverage will be zero when the exposure is zero. Substituting these values for  $E$  and  $\theta$  in equation 3 gives:

$$0 = \frac{1}{2C'S_0} + b$$

$$\text{i.e.} \quad b = -\frac{1}{2C'S_0}$$

Substituting this value in equation 3 gives;

$$E = \frac{1}{2CS_0(1 - 2\theta)} - \frac{1}{2CS_0}$$

Multiplying each side by  $CS_0$  gives:

$$CS_0 E = \frac{1}{2(1 - 2\theta)} - \frac{1}{2}$$

$$\text{i.e.} \quad CS_0 E = \frac{\theta}{1/2 - \theta} \quad \text{where } C = 2C' \quad \dots 4$$

This is the form of the equation quoted as equation 5.2.

Equation 4 can be rearranged by multiplying each side by  $(0.5 - \theta)$  to get:

$$CS_0 E(0.5 - \theta) = \theta$$

Collecting terms in  $\theta$ :

$$\theta(1 + CS_0 E) = \frac{CS_0 E}{2}$$

$$\therefore \theta = \frac{CS_0 E/2}{CS_0 E + 1}$$

$$\therefore \theta = \frac{1/2}{1 + \frac{1}{CS_0 E}}$$

This is the form of the equation quoted as equation 5.7.

## APPENDIX B

### Integration of Equation 5.9

The integration of equation 5.9 to obtain an expression relating coverage to exposure can be split into two cases:

- A. Faces intermediate between the (001) and (113) faces.
- B. Faces either between the (111) and (110) faces, or between the (111) and (113) faces.

These two cases will be treated separately.

#### 1. Faces Between the (001) and (113) Faces

Equation 5.9 is:

$$\frac{d\theta}{dt} = P \sum_i \alpha_i' c_i s_i \quad \dots 5.9$$

For faces between the (001) and (113) faces,  $i$  takes the values 1 and 2.

The sticking factors are given in equation 5.6:

$$s_1 = s_{01}(1 - 2\theta)^2$$

$$s_2 = s_{02}(1 - 2\theta)^2$$

Substituting these into equation 5.9 gives:

$$\frac{d\theta}{dt} = P \left\{ \alpha_1' c_1 s_{01} (1 - 2\theta)^2 + \alpha_2' c_2 s_{02} (1 - 2\theta)^2 \right\}$$

$$\text{i.e.} \quad \frac{d\theta}{dt} = P(\alpha_1' c_1 s_{01} + \alpha_2' c_2 s_{02})(1 - 2\theta)^2$$

This is the same equation as the equation that has been integrated in Appendix A, except that the constants  $CS_0$  have been replaced by  $(\alpha_1' c_1 s_{01} + \alpha_2' c_2 s_{02})$ . From Appendix A, the integrated equation will therefore be:

$$\theta = \frac{1}{2} \left\{ 1 + \frac{1}{E(\alpha_1' c_1 s_{01} + \alpha_2' c_2 s_{02})} \right\}^{-1}$$

This is the form of the equation quoted as equation 5.11.

#### 2. Faces Between the (111) and either the (113) or (110) Faces

The form of the equations for both these cases is the same, so only the case of faces between the (111) and (110) faces will be treated. For these faces  $i$  takes the values 3 and 4, so that equation 5.6 gives:

$$S_3 = S_{03}$$

$$S_4 = S_{04} (1 - 2\theta)^2$$

Equation 5.9 becomes:

$$\frac{d\theta}{dt} = P \left\{ \alpha_3 C'_3 S_{03} + \alpha_4 C'_4 S_{04} (1 - 2\theta)^2 \right\}$$

$$\text{i.e.} \quad \frac{d\theta}{dt} = P \alpha_4 C'_4 S_{04} \left\{ (1 - 2\theta)^2 + \frac{\alpha_3 C'_3 S_{03}}{\alpha_4 C'_4 S_{04}} \right\}$$

$$\text{Let} \quad \delta = \frac{\alpha_3 C'_3 S_{03}}{\alpha_4 C'_4 S_{04}}$$

$$\text{Then} \quad \frac{d\theta}{dt} = P \alpha_4 C'_4 S_{04} \left[ (1 - 2\theta)^2 + \delta \right]$$

On rearranging and integrating, this becomes:

$$\int_0^\theta \frac{1}{(1 - 2\theta)^2 + \delta} d\theta = \alpha_4 C'_4 S_{04} \int_0^t P dt$$

$$= \alpha_4 C'_4 S_{04} E \quad \dots 1$$

To integrate the left-hand side of the above equation, we utilise the fact that  $\delta$  is small to obtain a Taylor expansion as follows:

Let  $X = (1 - 2\theta)^2$  and let  $F(X) = 1/X$ .

$$\text{Then } F'(X) = -1/X^2 \text{ and } \int_0^\theta \frac{1}{(1 - 2\theta)^2 + \delta} d\theta = \int_0^\theta F(X + \delta) d\theta$$

$$\text{and } F(X + \delta) = \frac{1}{X + \delta} = F(X) + \delta F'(X) + \frac{\delta^2}{2!} F''(X) + \dots$$

$\delta$  is less than 0.01, so that the third and higher terms in the above expansion are negligibly small. Thus:

$$\int \frac{1}{(1 - 2\theta)^2 + \delta} d\theta = \frac{1}{2} \int \frac{1}{(1 - 2\theta)^2} d\theta - \frac{\delta}{2} \int \frac{1}{(1 - 2\theta)^4} d\theta \dots 2$$

This approximation will only be valid when  $\delta$  is much smaller than  $(1 - 2\theta)^2$ , i.e. when  $\theta$  is smaller than  $1/2$ . As we are only considering the case when  $\theta$  is less than 0.35, this approximation is reasonable.

Substituting equation 2 into equation 1 gives:

$$\alpha_{44}^{C_4S_{04}} E = \int_0^{\theta} \frac{1}{(1-2\theta)^2} d\theta - \delta \int_0^{\theta} \frac{d\theta}{(1-2\theta)^4} \\ = \frac{1}{1-2\theta} - \frac{\delta}{3(1-2\theta)^3} + b$$

where  $b$  is a constant of integration, and  $c = 2c'$

Applying the condition that  $\theta = 0$  when  $E = 0$  gives:

$$b = \frac{\delta}{3} - 1$$

$$\text{Thus } E \alpha_{44}^{C_4S_{04}} = \frac{1}{1-2\theta} - \frac{\delta/3}{(1-2\theta)^3} + \delta/3 - 1$$

This is the form of equation quoted as equation 5.12.

This equation is exactly the same for faces between the (111) and (113) faces, except that the index  $i = 4$  is replaced by  $i = 2$  to give:

$$E \alpha_{22}^{C_2S_{02}} = \frac{1}{1-2\theta} - \frac{\delta/3}{(1-2\theta)^3} + \delta/3 - 1$$

$$\alpha_4 C_4 S_{04} E = \int_0^\theta \frac{1}{(1-2\theta)^2} d\theta - \delta \int_0^\theta \frac{d\theta}{(1-2\theta)^4} \\ = \frac{1}{1-2\theta} - \frac{\delta}{3(1-2\theta)^3} + b$$

where  $b$  is a constant of integration, and  $c = 2c'$

Applying the condition that  $\theta = 0$  when  $E = 0$  gives:

$$b = \frac{\delta}{3} - 1$$

Thus 
$$E \alpha_4 C_4 S_{04} = \frac{1}{1-2\theta} - \frac{\delta/3}{(1-2\theta)^3} + \delta/3 - 1$$

This is the form of equation quoted as equation 5.12.

This equation is exactly the same for faces between the (111) and (113) faces, except that the index  $i = 4$  is replaced by  $i = 2$  to give:

$$E \alpha_2 C_2 S_{02} = \frac{1}{1-2\theta} - \frac{\delta/3}{(1-2\theta)^3} + \delta/3 - 1$$

**REPRODUCED  
FROM THE  
BEST  
AVAILABLE  
COPY**